

Force generation at microtubule ends:
An *in vitro* approach to cortical interactions

Liedewij Laan

**Force generation at microtubule ends:
An *in vitro* approach to cortical interactions**

PROEFSCHRIFT

TER VERKRIJGING VAN
DE GRAAD VAN DOCTOR
AAN DE UNIVERSITEIT LEIDEN,
OP GEZAG VAN DE RECTOR MAGNIFICUS
PROF. MR. P.F. VAN DER HEIJDEN,
VOLGENS BESLUIT VAN HET COLLEGE VOOR PROMOTIES
TE VERDEDIGEN OP WOENSDAG 10 JUNI 2009
TE KLOKKE 15.00 UUR

DOOR

LIEDEWIJ LAAN

GEBOREN TE HENGELLO (O) IN 1980

Promotiecommissie:

Promotor: Prof. dr. M. Dogterom
Overige leden: Prof. dr. R. D. Vale (University of California San Francisco, USA)
Dr. S. Grill (MPI-CBG/MPI-PKS, Dresden, Germany)
Prof. dr. R. H. Medema (Universiteit Utrecht)
Prof. dr. C. Dekker (Technische Universiteit Delft)
Prof. dr. H. Schiessel
Prof. dr. T. Schmidt
Prof. dr. J. M. van Ruitenbeek

*Force generation at microtubule ends:
An in vitro approach to cortical interactions*

©2009 by Liedewij Laan. All rights reserved.

Cover: Laura van Uitert

The work described in this thesis was performed at the FOM Institute for Atomic and Molecular Physics (AMOLF), Science Park 113, 1098 XG Amsterdam. This work is part of the research programme of the ‘Stichting voor Fundamenteel Onderzoek der Materie’ (FOM), which is financially supported by the ‘Nederlandse Organisatie voor Wetenschappelijk Onderzoek’ (NWO). It is also partly funded by the Human Frontiers Science Program.

ISBN: 978-90-77209-33-2

A digital version of this thesis can be downloaded from <http://ub.leidenuniv.nl>. Printed copies can be obtained by addressing the library at the FOM institute for Atomic and Molecular Physics (AMOLF): library@amolf.nl, Science Park 114, 1098 XG, Amsterdam, the Netherlands.

Printed in the Netherlands by Ponsen & Looijen BV graphical company, Wageningen.

What I cannot create, I do not understand,
Richard Feynman

This thesis is partly based on the following articles:

Marileen Dogterom, Julien Husson, Liedewij Laan, E. Laura Munteanu, Christian Tischer
Microtubule forces and organization, (Chapter 1, 3, 5)
Cell motility / ed. P. Lenz. - New York : Springer, - pp. 93-115
(Springer series in Biological and Medical Physics, Biomedical Engineering) (2007)

Liedewij Laan and Marileen Dogterom
In vitro assays to study force generation at dynamic microtubule ends, (Chapter 2)
(*in preparation: invited contribution to Methods in Cell Biology*)

Julien Husson, Liedewij Laan, Marileen Dogterom
Force-generation by microtubule bundles, (Chapter 3)
Biophysical Reviews and Letters, in press (2009)

Liedewij Laan*, Julien Husson*, E. Laura Munteanu, Jacob W. J. Kerssemakers, Marileen Dogterom
Force generation and dynamic instability of microtubule bundles, (Chapter 3)
Proc Natl Acad Sci USA, **105**:8920-8925 (2008)
(*equal contribution)

Liedewij Laan, Julien Husson, Martijn van Duijn, Ronald D. Vale, Samara L. Reck-Peterson, Marileen Dogterom
'Cortex'-attached dynein regulates and pulls on shrinking microtubule ends *in vitro*, (Chapter 4)
(*under review*)

Liedewij Laan, Nenad Pavin, Guillaume Romet-Lemonne, Frank Jülicher, Marileen Dogterom
Reliable centering of dynamic MT asters in microfabricated chambers by pulling forces, (Chapter 5)
(*in preparation*)

Peter Bieling*, Liedewij Laan*, Henry Schek, E. Laura Munteanu, Linda Sandblad, Marileen Dogterom, Damian Brunner, Thomas Surrey
Reconstitution of a microtubule plus-end tracking system *in vitro*, (Chapter 6)
Nature **450**, 1100-1105 (2007)
(*equal contribution)

Other papers by this author:

E. Laura Munteanu, Liedewij Laan, Damian Brunner, Thomas Surrey, Marileen Dogterom
Regulation of microtubule dynamics, *in vitro*, by the autonomous microtubule-end tracker Mal3,
(*to be submitted*)

Liedewij Laan, Laura Munteanu, Jacob Kerssemakers, Marileen Dogterom
Meten aan microbuisjes met moleculaire resolutie,
Nederlands Tijdschrift voor Natuurkunde **72** 388-391 (2006) (Dutch physics journal)

Jacob W. J. Kerssemakers, E. Laura Munteanu, Liedewij Laan, Tim Noetzel, Marcel Janson and Marileen Dogterom
Assembly dynamics of microtubules at molecular resolution,
Nature **442**, 709-712 (2006)

Contents

Introduction	9
1.1 <i>Internal organization of the cell</i>	10
1.2 <i>Microtubules in cellular organization.....</i>	12
1.3 <i>Force generation in cellular organization</i>	18
1.4 <i>Thesis outline</i>	27
Mimicking microtubule interactions at the cell boundary with functionalized microfabricated structures	29
2.1 <i>Microfabrication.....</i>	30
2.2 <i>Activation of gold barriers</i>	37
2.3 <i>Assays with microfabricated structures.....</i>	39
2.4 <i>Acknowledgements.....</i>	45
Force generation and dynamic instability of microtubule bundles	47
3.1 <i>Introduction</i>	48
3.2 <i>Measurement of bundle forces and dynamics</i>	49
3.3 <i>Simulations on microtubule bundle dynamics.....</i>	55
3.4 <i>Discussion.....</i>	57
3.5 <i>Materials and Methods.....</i>	60
3.6 <i>Acknowledgements.....</i>	62
‘Cortical’ dynein regulates and pulls on dynamic microtubule ends <i>in vitro</i>.....	63
4.1 <i>Introduction</i>	64
4.2 <i>Fluorescence microscopy experiments.....</i>	64
4.3 <i>Optical trap experiments</i>	70
4.4 <i>Discussion.....</i>	75
4.5 <i>Materials and Methods.....</i>	79
4.6 <i>Acknowledgements.</i>	84

Reliable centering of dynamic microtubule asters in microfabricated chambers by pulling forces	85
5.1 <i>Introduction</i>	86
5.2 <i>Experimental results</i>	87
5.3 <i>Theory</i>	91
5.4 <i>Comparison of experiments and theory</i>	97
5.5 <i>Discussion</i>	98
5.6 <i>Materials and methods</i>	100
5.7 <i>Acknowledgements</i>	103
Reconstitution of a microtubule plus-end tracking system in vitro	105
6.1 <i>Introduction</i>	106
6.2 <i>Results on end-tracking in vitro</i>	106
6.3 <i>Discussion</i>	117
6.4 <i>Materials and Methods</i>	120
6.5 <i>Acknowledgements</i>	128
Concluding remarks and additional research directions	129
7.1 <i>Positioning processes based on microtubule pulling forces</i>	130
7.2 <i>Regulation of microtubule dynamics by a combination of force and +TIPs</i> ...	131
7.3 <i>Microtubule capture by non-motor proteins</i>	134
7.4 <i>Towards the role of MT-based transport in cortical pattern formation</i>	139
7.5 <i>Acknowledgements</i>	146
Bibliography	147
Summary	163
Samenvatting	167
Dankwoord	173
Curriculum Vitae	175

Chapter I:

Introduction

Biopolymers are essential for cellular organization. They bridge the cell interior forming a framework that is used as a reference frame for different cellular organelles. Interestingly this framework, called the cytoskeleton, is not static but constantly reorganizes. The dynamics of the cytoskeleton allow the cell to rearrange its interior for various processes such as cell division. This dynamic reorganization relies, at least partly, on forces that arise from assembly and disassembly of the cytoskeletal biopolymers. In many cases, these forces are generated when biopolymers interact with the cell boundary. Most cells contain three different biopolymers, microtubules, actin and intermediate filaments. This thesis focuses on force generation by microtubules that interact with opposing barriers. The following introduction chapter focuses on microtubules and their dynamic properties. Section 1.1 describes the properties of microtubules and their role in cellular organization. Section 1.2 explains how microtubule assembly and disassembly lead to force generation. Section 1.3 discusses the role of these forces in cellular processes. Section 1.4 finally gives an outline of this thesis.

1.1 Internal organization of the cell

The cell is the fundamental building block of every living organism. Typically more developed organisms consist of many different cell types. All perform their own function to ensure proper organization of the complete organism. For example muscle cells contract, nerve cells send and transmit signals, white blood cells are part of the immune systems and protect against diseases, etc. [12]. These different cell types may appear quite different at first sight, however the fundamental machineries that build up eukaryotic (plant and animal) cells are largely conserved throughout the different cell types (Fig. 1.1). A typical eukaryotic cell contains a nucleus, where the DNA is stored, mitochondria where ATP production takes place, membrane compartments where proteins are translated and folded, and a cytoskeleton that gives structure to the cell, etc. [12]. All of these components need to be highly organized and regulated both spatially and temporally. For example, most cells not only perform their specific function, but also periodically divide, which requires a complete reorganization of the cellular interior (Fig. 1.2). Tight regulation in cell division is essential. For example, before segregation occurs, the DNA first has to be duplicated and then properly

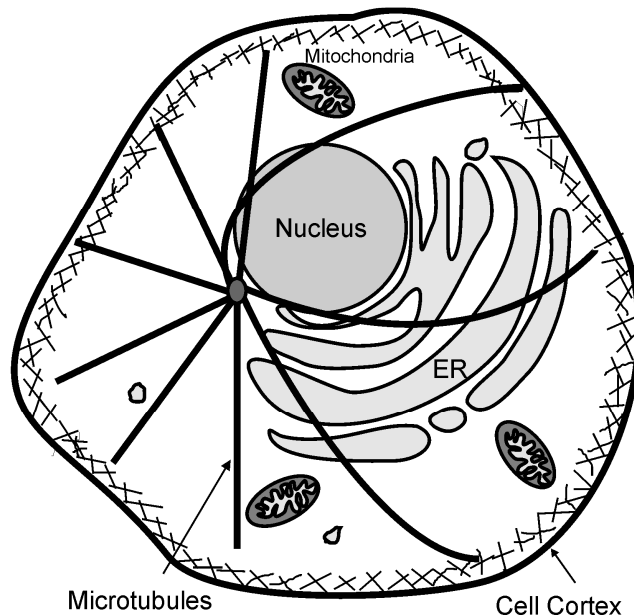


Figure 1.1

Simplified cartoon of the internal organization of a cell. The nucleus is positioned in the center by microtubules that radiate from the nucleus to the cell periphery. Microtubules and actin at the cell cortex form together an important part of the cytoskeleton. The endoplasmic reticulum (ER) is located close to the nucleus, and mitochondria can be found throughout the cytoplasm.

distributed over the two new cells.

From a physicist's perspective it is quite intriguing that cells are so highly organized. Cells are small compartments, tens of microns in size. The molecular building blocks of cells, proteins, are on the order of tens of nanometers. They stochastically move through the cell, due to thermal motion. So how can a cell organize its interior on the micrometer length scale, using stochastically moving small nanometer-sized building blocks? Moreover how can these tiny blocks rapidly and dramatically reorganize the cell interior throughout the cell cycle? One of the important machineries the cell exploits for this highly ordered cellular organization is

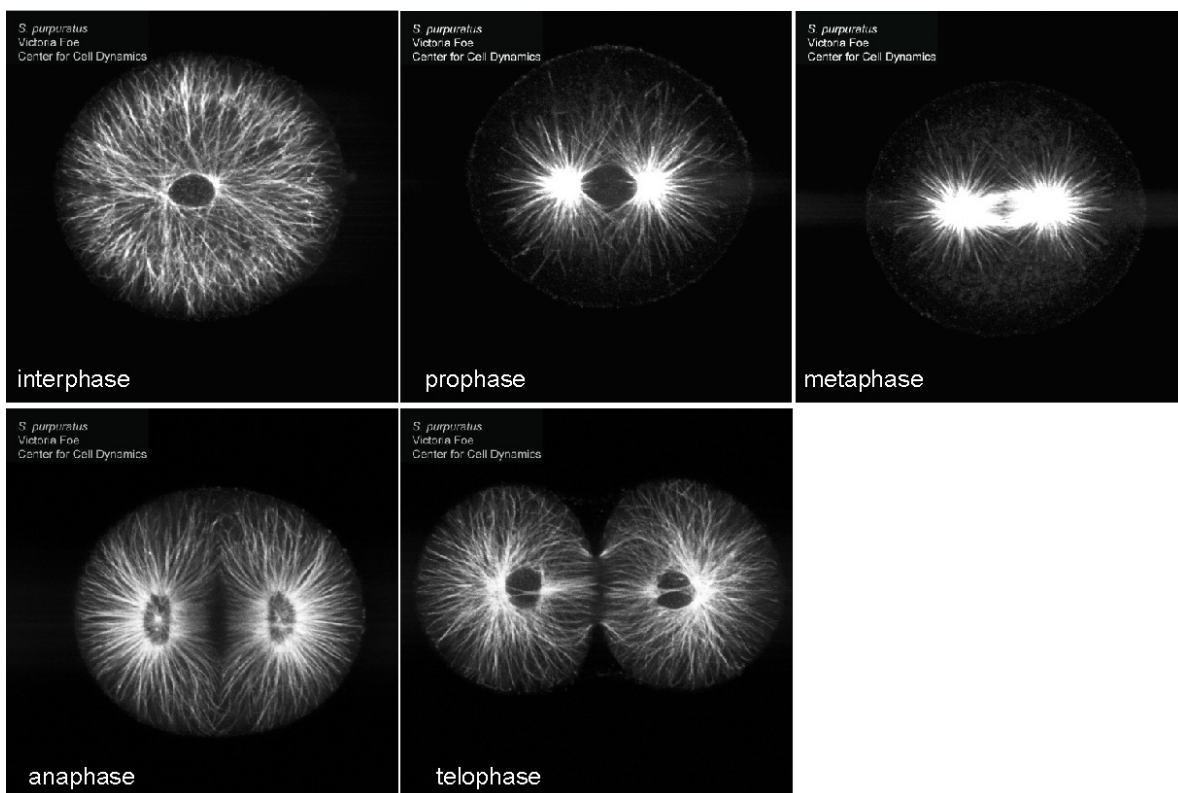


Figure 1.2

MTs are highly organized in space and time and dramatically reorganize during mitosis. In interphase MTs grow out from the cell center towards the cell periphery. In prophase the mitotic spindle forms. In metaphase the chromosomes (condensed DNA) are positioned by the mitotic spindle at the equator, followed by anaphase, where the chromosomes are segregated towards the spindle poles. In telophase cytokinesis takes place and the microtubules reform in an astral array. MTs are stained with antibody staining in *S. purpuratus* cells. Images made by Vitoria Foe from the Center of Cell Dynamics, University of Washington, Friday Harbor.

<http://www.celldynamics.org/celldynamics/research/cytokinesis/index.html>

the cytoskeleton. The cytoskeleton is defined as “the internal mechanical framework of a cell, composed of a network of protein filaments and extending throughout the fluid of the cell (the cytosol)”. It has the remarkable ability to dramatically reorganize in a short time period, for example during cell division (Fig. 1.2). At the same time the cytoskeletal protein filaments bridge the difference in length scale between individual proteins and cells, and generate forces necessary for proper organization [17]. The cytoskeleton consists of three different filaments, microtubules (MTs), actin, and intermediate filaments.

The work, presented in this thesis, focuses on cellular organization by forces generated by MTs, which will be the main subject of this introduction. First, MTs are introduced and the regulation of MTs to form dynamic structures within cells is discussed. Next the force generation mechanisms responsible for cellular organization are described.

1.2 Microtubules in cellular organization

MTs play many different roles in cellular organization [12]. During cell division a large dynamic array of MTs, called the mitotic spindle [18], functions to physically segregate the chromosomes. In non-dividing cells, MTs organize organelles in the cytoplasm [19, 20]. In migrating cells MTs play an important role in cellular polarization that leads to directed movement [21]. In addition, MTs form a track for motor proteins that distribute membrane organelles throughout the cell. Motor proteins, like kinesin and dynein [22, 23], are mechanochemical ATPases that translate directionally along MTs. ATP hydrolysis induces a conformational change that allows the protein to step along the MT against an opposing force, such as viscous drag in the cytoplasm, up to several pN [24].

1.2.1 Microtubules

MTs self-assemble from $\alpha\beta$ tubulin hetero-dimers into long protofilaments that form hollow protein tubes [17]. They are 25 nm in diameter with a variable length. The $\alpha\beta$ subunits align end to end, imposing a polarity on the MT (Fig. 1.3A). The MT polarity is reflected in a plus- and a minus-end that have different properties. The end with the β subunit outwards is the plus-end, which grows fast and is dynamic. The other end, the minus-end, grows slowly and is much less dynamic [25]. *In vitro*, MTs consist of 9-17 protofilaments, but *in vivo* MTs typically contain 13 protofilaments [26, 27]. On

the lengths scale of a cell (10-50 μm) MTs are quite stiff, because they have a persistence length of several mm [28].

MTs are dynamic structures, they possess a property called “dynamic instability”, introduced by Mitchison and Kirchner in 1984 [29, 30]. Dynamic instability is the intrinsic ability of MTs to rapidly switch between a growing and a shrinking state, events that are termed catastrophes and rescues [17] (Fig. 1.3AB). The energy source driving this out of equilibrium process is the hydrolysis of guanosine-5'-triphosphate (GTP). Tubulin has a GTP binding site and polymerizes in a GTP-bound state. With a slight delay the GTP in the MT gets hydrolyzed into GDP (guanosine-5'-diphosphate). After depolymerization the GDP-bound tubulin returns to the dimer state and exchanges the GDP to GTP in solution [17]. Experiments with a non-hydrolysable

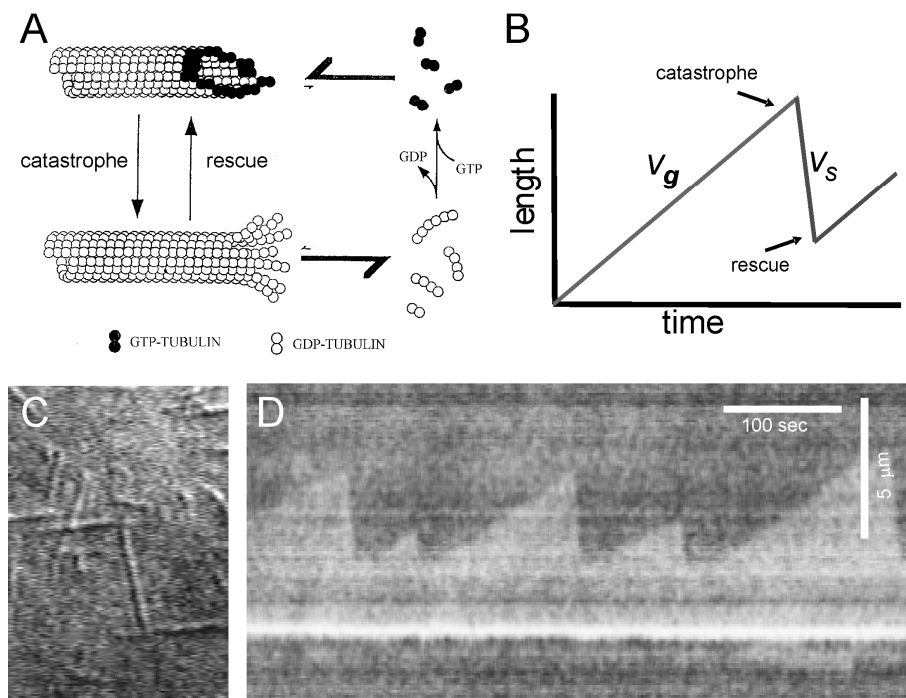


Figure 1.3

Microtubules are dynamic protein polymers. (A) Cartoon, taken from Inoue and Salmon [3], that shows the growing and the shrinking state of MTs and the role of GTP hydrolysis. (B) Graph that schematically shows the dynamics describing dynamic instability: growth (with velocity v_g), shrinkage (with velocity v_s), the switching from growth to shrinkage (catastrophe), and the switching from shrinkage to growth (rescue). (C) Differential interference contract (DIC) image of MTs grown from purified tubulin. (D) Kymograph of the dynamics of a MT in (C), which shows MT growth followed by fast shrinkage. MTs are grown from a stabilized seeds, and therefore do not shrink away completely.

homolog of GTP, guanylyl 5'-b,guethylene-diphosphonate (GMPCPP), showed that the hydrolysis of GTP is necessary for dynamic instability [31]. MTs that grow in the presence of GMPCPP do not switch to the shrinking state.

What is the role of GTP hydrolysis in dynamic instability? It is believed that some of the energy that is released by GTP hydrolysis deforms the tubulin dimer from a relatively straight to a more bent state [32]. In the (not-yet-proven) current view, the end of a growing MT is in the GTP-bound state (Fig. 1.3A). This tubulin serves as a stabilizing cap for the rest of the MT that consists of GDP-bound tubulin. The GDP-bound tubulin cannot relax to its preferred conformation because it is constrained in the MT lattice. The continuous addition of new GTP-bound tubulin ensures the maintenance of the GTP cap and thus the persistence of growth. Theoretical models show that a relatively short or even incomplete cap can stabilize a MT, by just accounting for the bending of the GDP-bound tubulin and the elasticity of the MT [33, 34]. However, a complete description of MT dynamics and mechanics is still missing.

The growth process of MT polymerization is another unresolved process. There is evidence from electron microscopy studies that MTs grow as an extended sheet that closes during growth, so-called “seam closure” [32, 35]. Recent high-resolution dynamic experiments with optical tweezers cannot yet resolve this issue, but do give new insight into the MT growth process [5, 36]. Some data and theoretical models suggest that the GTP cap at the tip is very dynamic and that mini-catastrophes regularly occur, but rarely result in a “real” catastrophe [36, 37]. Other experiments indicate that MTs grow by the addition of dimers and oligomers that pre-form in solution [5]. The MT-tip structure during shrinkage is believed to be quite different from the tip structure during growth. The tubulin dimers at the end of the shrinking MT are in the GDP-bound state, and are free to bend outwards, like ‘rams horns’, and subsequently dissociate (probably as oligomers) from the MT (Fig. 1.3A) [38].

What triggers the switching from one state to the other? Recent experiments suggest that rescues, switches from the shrinking to the growing state are induced by remnant GTP-bound tubulin in the lattice [39]. There is no explicit experimental data yet on the mechanism of catastrophe. Theoretical models propose that stochastic fluctuations of the end structure lead to switching between the two states [33, 34, 37]. Additional high spatial and temporal resolution experiments will be necessary to resolve the molecular mechanisms underlying dynamic instability.

Dynamic instability can be described by four parameters (Fig. 1.3BCD), the growth velocity, v_g , the shrinkage velocity, v_s , the catastrophe time, the average time the MT spends in the growing state until a catastrophe, T_{cat} , and the rescue time, the average

time a MT spends in the shrinkage state until a rescue, T_{res} . These parameters are intrinsic to MTs. The growth velocity of a MT *in vitro* is typically of the order of 1-5 $\mu\text{m}/\text{min}$. The shrinkage velocity is an order of magnitude larger, 10-50 $\mu\text{m}/\text{min}$. The catastrophe time *in vitro* is highly dependent on tubulin concentration and temperature [40] and can vary from several seconds up to hours [25]. Rescues are rarely observed *in vitro* and therefore usually only a lower bound of the rescue time can be calculated [41].

The parameters of dynamic instability *in vitro* can be regulated by temperature or tubulin concentration [40], but a cell can not easily manipulate these parameters on a short time scale. Nevertheless in a cell the dynamic instability parameters are quite variable and quite different from *in vitro* experiments. MTs tend to grow much faster and undergo more catastrophes and rescues [42]. In recent years it has become clear that cells exploit a large variety of proteins to regulate the parameters of dynamic instability both globally (section 1.2.2) and locally (1.2.3) to properly organize the MT cytoskeleton.

1.2.2 +TIPs track microtubule ends and regulate parameters of dynamic instability

To regulate MTs spatially and temporally, the cell uses a large set of MT associated proteins (MAPs) to perform many different functions. Some proteins, such as tau and MAP2, bind along the MT lattice, to mechanically strengthen the MT [43]. Other proteins, like Op18, target free tubulin in solution to regulate MT dynamics [44]. Since the discovery of CLIP170 [45], which was shown to localize at the ends of growing MTs, many MAPs have been shown to specifically track growing MT ends, so-called +TIPs [44, 46-49] (Fig. 1.4). Different +TIPs have different effects on MT dynamics and therefore can be used by the cell as a toolbox for MT regulation [50]. In *in vitro* experiments physiological MT dynamics indeed can be reconstituted [51] with two different +TIPs: XMAP215 [52] that enhances the MT growth velocity [5, 53] and the kinesin MCAK that removes the GTP cap and triggers catastrophes [54]. Also other reconstituted systems, as described in chapter 6, show how the antagonizing effect of different proteins can re-enact more physiological MT dynamics. For example the +TIP EB1 stabilizes MT dynamics *in vivo*, while *in vitro* experiments have shown that EB1 induces catastrophes [41, 55-57]. The answer to this contradiction lies in another function of EB1. EB1 itself autonomously end-tracks, however it also recruits other proteins to the MT end that have their own effect on MT dynamics [55, 58]. In *S. pombe* the CLIP170 homolog Tip1 that needs both the EB1-homolog Mal3 and the

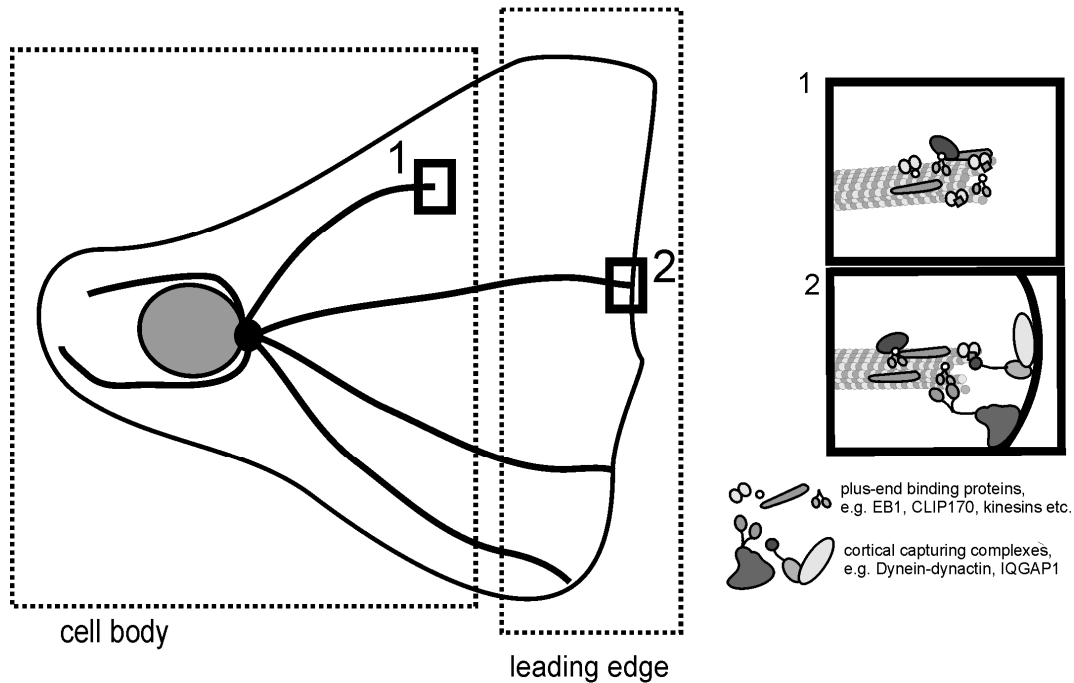


Figure 1.4

Cartoon of MT organization in a migrating cell. MTs are globally regulated by cytoplasmic plus-end binding proteins in the cell body. At the cortex of the leading edge, MTs are locally regulated by interactions between dynamic MTs, +TIPs and cortical proteins.

kinesin Tea2 to end-track [56], indeed partly antagonizes the destabilizing effect of Mal3 in *in vitro* experiments, similar to the *in vivo* situation [59].

Recently more and more mechanisms of MT regulation have been discovered [60, 61]. For example, *in vivo* as well as *in vitro* it has been shown that plus-end tracking kinesin-8 motor proteins [62-65] regulate MT dynamics in a MT-length dependent manner. A longer MT can collect more motors along its length, and because the motor walks faster than the MT grows, the concentration of kinesin-8 is higher at the end of a longer MT [65].

1.2.3 Microtubules are locally regulated at the cortex

MTs are globally regulated by +TIPs while growing through the cytoplasm. The cell also exploits local mechanisms to regulate MT dynamics. Biochemical gradients that are present can spatially organize the MT array [66]. In addition proteins, that are specifically localized at the cell cortex, can locally regulate the dynamics of MTs (Fig. 1.4, detail 2). +TIPs have been shown to participate in this regulation of MT dynamics

at cortical sites [67]. In addition, forces generated at the cortex regulate MT dynamics (section 1.3 and 1.4). This section focuses on three different mechanisms of MT-cortex interactions relevant to this thesis and describes their role in cellular organization.

Mechanism 1: The induction of MT catastrophes at the cell cortex.

In *S. pombe* cells the MT cytoskeleton has important functions in cellular polarization. MTs induce cortical polarity by transporting Tea1, a protein essential for polarized cell growth, at their plus-ends [68]. MTs deliver Tea1 specifically to the membrane linker protein Mod5 at the cell pole [69]. Because MTs release Tea1 after catastrophe, it is important that MT catastrophe is well regulated throughout the *S. pombe* cell: the catastrophe rate is low in the cytoplasm and strongly enhanced at the cell ends, where Tea1 needs to be delivered [64, 70]. Several mechanisms have been proposed for this tight regulation. Brunner et al suggested that Tip1 that travels with Tea1 at the MT end, stabilizes MTs in the cytoplasm, but rapidly dissociates from the MT end, after it hits the cell boundary, possibly through local regulation by other proteins [70]. Other papers show that force, generated by MT polymerization against the cell end, slows down MT growth [64, 71]. This reduction in MT growth velocity could directly regulate MT dynamics, as has been shown *in vitro* [72]. In addition it has been speculated that the catastrophe enhancing kinesin-8 motor protein preferentially accumulates at the ends of slow growing MTs, resulting in a higher catastrophe rate [64].

Mechanism 2: Capture and stabilization of MTs at the cell cortex.

During cell migration the MT cytoskeleton is polarized. Minus-ends are concentrated at the centrosomes and plus-ends contact the actin rich leading edge and focal adhesions in the rear of the cell (Fig. 1.4) [73]. This asymmetric MT array is essential for the directionality of cell motility. Removing the MT cytoskeleton reduces the directionality dramatically [74, 75]. *In vivo* studies suggest that MTs are captured and stabilized at the leading edge by interaction with cortical proteins [76]. One example of these cortical proteins is IQGAP1 [77], an actin binding protein, that interacts with the +TIP CLIP170 [45] to capture MTs. IQGAP1 is a large protein with binding sites for many proteins [78], among which are actin [79] and CLIP170 [80]. The mechanism by which IQGAP1 can capture MTs through CLIP170 is still a completely open question. CLIP170 binds transiently to the MT end, and dissociates from the MT end relatively fast after arriving at the cortex. This makes it a less likely candidate for a role in long term capture at the cortex. Possibly IQGAP1 initially captures MTs through CLIP170 at the leading edge, however the subsequent stabilization and

maintenance at the leading edge is performed by another capturing mechanism. Several other capturing mechanisms using other +TIPs and other cortical proteins have been identified [76], however the mechanisms of all these different possible capturing processes still remain to be clarified.

Mechanism 3: Generation of pulling forces by proteins at the cortex and shrinking MTs.

S. cerevisiae cells use two different subsequent mechanisms to generate pulling forces at the cortex that contribute to the positioning of the nucleus. Before the onset of anaphase the nucleus migrates to the mother-neck junction. Genetic studies have shown that the forces necessary for this process are generated by MTs with the +TIP Bim1 (the EB1 homolog in *S. cerevisiae*) and the +TIP kinesin Kar9 that together interact with Kip3, a depolymerizing kinesin at the cortex [81, 82]. The mechanism of this interaction is still to be resolved.

After the nucleus is positioned at the bud neck, MTs grow into the bud. When MTs hit the cortex, pulling forces are generated that pull the nucleus into the bud. These forces are generated by the minus-end directed motor protein dynein that is initially carried at the plus-end of the growing MT. After contact with the cortex, dynein is anchored to the cortical membrane protein Num1 and generates pulling forces on the MT [83, 84]. In addition to generating pulling forces, dynein also appears to regulate MT dynamics [7]. Again, the mechanism of force generation is not yet clear, although both lateral and end-on interaction between the MT and dynein are thought to be important.

The generation of pulling forces by dynein at the cortex is a mechanism used by many different cells [83]. In *S. pombe* cells during meiotic preprophase dynein interacts both laterally and end-on with dynamic MTs to generate nuclear oscillations important for homologous recombination [9, 85, 86]. In fibroblasts, dynein presumably also localizes both laterally and end-on to the MT to position the centrosome [20]. In the first cell stage *C. elegans* embryo dynein at the cortex only interacts end-on with the MT and is believed to be responsible for the positioning of the spindle [87] (discussed in more detail in section 1.3.6).

1.3 Force generation in cellular organization

Proper organization of the cellular interior relies on forces that are generated to position different organelles. In 1952, Shinya Inoué already showed that disassembly of MTs (at that time still referred to as protein fibrils) can generate enough force to

move the whole spindle through the cytoplasm to an anchoring site at the cell surface [3]. Subsequently, the assembly of MTs can generate forces that push the spindle again away from the anchoring site [3]. The next sections explain how MT based pushing and pulling forces are generated. In addition it is described how a collection of pushing and/or pulling force can organize the cellular interior.

1.3.1 Generation of pushing forces by growing microtubules

Several *in vitro* studies have directly shown that growing MTs can generate pushing forces [72, 88-90]. Thermodynamic arguments show that the free energy gain by incorporation of tubulin dimers in the MT can account for the energy needed for force generation [91, 92]. The energy released by the hydrolysis of GTP is considered unnecessary for force generation by MT assembly. However GTP hydrolysis is the main driving energy for force generation by shrinking MTs as explained in section 1.3.3. The mechanism for force generation by pushing lies essentially in the mechanism of MT growth itself. MT growth is the result of tubulin assembly at the end of the MT. The net assembly rate is given by:

$$\frac{dn}{dt} = k_{on} C_T - k_{off} \quad (1)$$

Where n is the number of subunits incorporated in the MT, k_{on} is the on-rate, k_{off} is the off-rate and C_T is the GTP-tubulin concentration. We can rewrite this as a growth velocity v by multiplying with the added MT length per subunit which is δ , the dimer length (8 nm), divided by the number of protofilaments (13) in the MT:

$$v = \delta (k_{on} C_T - k_{off}) \quad (2)$$

Thermodynamic arguments state that, in equilibrium, the ratio between the on-rate and the off-rate are related to the gain in free energy, ΔG , upon addition of one monomer, in the following way [91, 93]:

$$\frac{k_{on} C_T}{k_{off}} = \exp\left(\frac{\Delta G}{k_b T}\right) \quad (3)$$

Where k_b is Boltzmann's constant and T the absolute temperature. ΔG is different for the growing and shrinking states of MTs, but in this section we only consider the growing state. Let us imagine a simplified MT growing against a barrier that is pushed with a force F against the MT as shown in figure 1.5. To add a dimer of size δ , work has to be performed equal to $F\delta$. This will lower the free energy gain by $F\delta$:

$$\Delta G^* = \Delta G - F\delta \quad (4)$$

By substituting equation (2) and (3) into equation (1) and assuming that the off-rate is not affected by force (supported by experimental data [72, 88, 90, 94]) one can rewrite equation (1) as:

$$v = \delta \left(k_{on} C_T \exp\left(\frac{-F\delta}{k_b T}\right) - k_{off} \right) \quad (5)$$

This equation shows how an opposing force affects the velocity of polymerizing MTs. It also gives, by putting the velocity in equation (5) to zero, the stall force for a MT:

$$F_{stall} = \frac{k_b T}{\delta} \ln\left(\frac{k_{on} C_T}{k_{off}}\right) \quad (6)$$

A more mechanistic explanation of force generation by a growing MT arises from the Brownian ratchet model [95, 96]. In the simplest Brownian ratchet model the MT is described as a linear array of dimers (Fig. 1.5). The MT grows and pushes against a rigid barrier. Thermal fluctuations create gaps between the MT and the opposing barrier. If the fluctuation is large enough, a new tubulin dimer can be added. The new dimer inhibits the barrier from returning to its original position, and therefore the barrier has moved over a distance of the length of the tubulin dimer. Because the barrier is exerting an opposing force the addition of the tubulin dimer performs work (Fig. 1.5). In its simplest form, this model reproduces the same force velocity relation as shown in Eq. 5 [88, 90].

The effect of force on the growth velocity has been measured experimentally [88, 90, 94]. MTs were grown from a stabilized MT seed, attached to a glass surface, against a rigid glass barrier. When the MTs hit the barrier, they continued to grow and buckled. The growth velocity and the generated force were determined from the shape of the

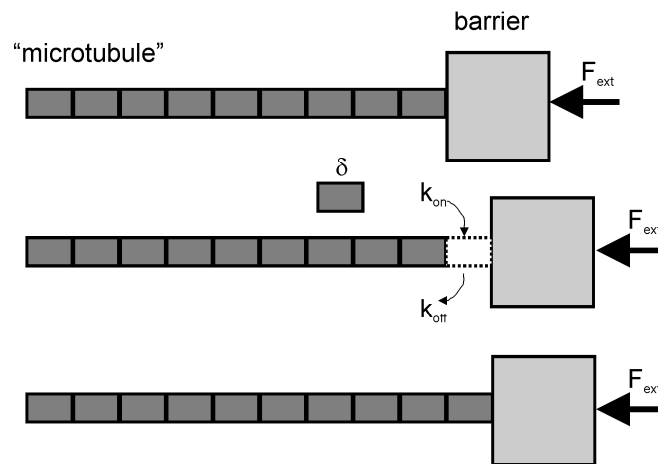


Figure 1.5

Cartoon explaining the Brownian ratchet model. Thermal fluctuations of the MT relative to the barrier occasionally open a gap large enough for the addition of a new tubulin dimer. After addition of the tubulin dimer the barrier cannot move back to its original position, so it moved over the length δ of a tubulin dimer. If the barrier exerts an opposing force F_{ext} than the assembly process performed work. Figure adapted from [6].

buckled MT. These experiments have shown that force indeed slows down the MT growth velocity in an approximately exponential manner, as described in equation (5). The stall force however can not be determined from these experiments. The slope of the force-velocity curve is very shallow at high forces which makes it impossible to determine the stall force from the force-velocity curve with a reasonable accuracy [88, 94]. Experiments where the MT polymerization forces are measured with an optical trap [5, 97], as described in chapter 3, should realize a more precise measurement of the stall force.

The above described buckling experiments were also performed to measure the effect of force on the catastrophe time. Surprisingly an opposing force only reduces the catastrophe time by limiting the growth velocity. Reduction of the growth velocity by reduced tubulin concentration yields a similar decrease in catastrophe time [72].

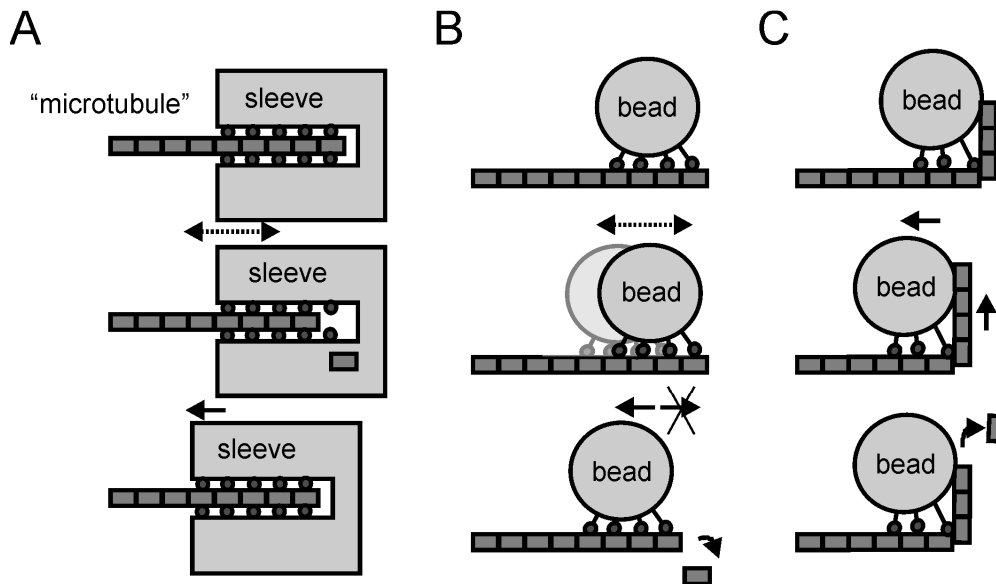


Figure 1.6

Cartoons of possible mechanisms underlying force generation by MT shrinkage. (A) Cartoon of the Hill model [1]. A MT is located in a sleeve. It is thermodynamically favorable to have many connections between the sleeve and the MT. After the dimer dissociates from the end, one connection is lost. Diffusion will move the sleeve along the MT to generate more binding sites. (B) Cartoon of the model explaining the tracking by a bead of a shrinking MT by a ratchet model. The bead diffuses along the MT, however unbinding from the end of the MT is not allowed. After the last dimer disassembles, the bead cannot diffuse anymore to the end position, and therefore has moved. (C) Cartoon of the model that takes protofilament bending into account: “the conformational wave model”. The outward bending protofilament exerts a power stroke on the bead, which pushes it forward; in addition the bead also performs biased diffusion similar to (B).

1.3.2 Generation of pulling forces by shrinking microtubules

The generation of force by disassembling MTs has also been shown in several *in vitro* experiments [98-101]. Since the first experiments, different theories have been developed to describe the force generation mechanism. In all these models the hydrolysis of GTP is the free energy source for force generation. A complication of describing pulling forces by MT depolymerization is that it is difficult to specify a device that allows an object to follow the end of a shrinking MT, without losing its mechanical connection.

The oldest model by Hill and Kirchner [1, 92] assumes that the depolymerizing MT is held in a sleeve or channel (Fig. 1.6A). The MT is held in the sleeve by

attractive forces between the MT and the wall of the sleeve. Tubulin is lost at the end of the sleeve. If diffusion is fast enough and the individual binding sites are relatively weak, the energetic preference to have many interactions between the sleeve and the MT creates a biased diffusion that pulls the MT into the sleeve, while it shrinks. More recent models are connected to experiments where beads coated with motor proteins can follow the end of a shrinking MT in the absence of ATP [101]. A ratchet-based model (Fig. 1.6B) assumes that the bead cannot fall off the end of the MT. Hence biased diffusion results in tracking of the disassembling MT by the bead, similar to the sleeve model. GTP hydrolysis induces dissociation of tubulin from the end of the MT. Yet another model, the “conformational wave model” [100] proposes that the conformational change in the MT due to GTP hydrolysis also produces work. The outward curling protofilaments generate a power stroke that can directly push a bead forward (Fig. 1.6C). This model is supported by elegant *in vitro* experiments, where a bead was attached to a MT via biotin-streptavidin linkage and held in an optical trap. When the shrinking MT passed the attached bead, movement of the bead was detected and a considerable force, of up to a pN, was measured [99].

1.3.3 Proteins can couple to a shrinking microtubule.

Since the first *in vitro* experiments showed that beads, coated with motor proteins, can follow a shrinking MT, several proteins, including other motor proteins [102, 103] have been discovered that can track a shrinking MT *in vitro*. In all these (and the following) experiments the proteins were attached to a bead, enforcing lateral contact between the protein and the MT.

The first non-motor protein example is the DAM1 complex. The DAM1 complex is the critical MT binding component at the kinetochore in *S. cerevisiae* [104]. It forms a ring around MTs and follows the shrinking MT end [105]. Optical trap experiments show that the DAM1 complex can harness the force generation of a shrinking MT, by moving with it against an opposing force of up to 3 pN [106, 107]. Interestingly, exerting a force on the DAM1 complex alters MT dynamics. Shrinkage is slowed down and the rescue rate is enhanced [107, 108]. This gives rise to the speculation that straightening the outward curling protofilaments slows down shrinkage. Shrinkage would be slowed down, because the protofilaments must overcome the force applied by the DAM1 complex, before they peel away from the protofilament.

Recently, another non-motor kinetochore complex, the NDC80 complex, has also been shown to track shrinking MT ends against an opposing force [109, 110]. The

NDC80 complex consists of four subunits with one binding site for the MT and does not form a ring. Ensembles of the order of ten NDC80 complexes are necessary for persistent end tracking. Individual NDC80 complexes cannot track depolymerizing MT ends, instead they exhibit one-dimensional diffusion along the MT. The authors explain the coupling of the NDC80 complex to the shrinking MT by biased diffusion as described in the Hill model, however without the necessity of the formation of a sleeve [110].

1.3.4 Cellular organization by microtubule pushing forces

The following examples are specific *in vivo* cases, where positioning processes purely depend on MT pushing forces. In *S. pombe* cells, during interphase, the nucleus needs to be properly positioned, because the nuclear position determines the position of the contractile ring responsible for cytokinesis [111]. MTs are the crucial players in nuclear positioning. They grow from a site attached to the nucleus to the cell ends, where they generate pushing forces that center the nucleus (Fig. 1.7A) [71]. The presence of pushing forces on the nucleus was shown by correlating deformations of the nuclear membrane with MT dynamics. Moreover when the nucleus was displaced by optical tweezers it returned to the cell center by MT pushing forces against the cell ends [112]. Detailed computer simulations of the fission yeast cell also show that MT pushing forces can bring a displaced nucleus back to the center [113]. MT pushing forces are also important during mitosis. Astral MTs align the mitotic spindle with the long cell axis by pushing against the cell edges [85, 114]. Alignment of the spindle is required for movement of the daughter nuclei towards the cell ends, as far away as possible from the division plane.

The mechanism underlying positioning by pushing forces has been studied in theory and in *in vitro* experiments. In these experiments positioning processes due to MT pushing forces were studied in microfabricated chambers [115, 116]. A bead was coated with stabilized MT seeds, serving as a MT organizing center, and followed over time. These experiments showed that simple MT pushing forces can center a MT organizing center as long as the MTs undergo enough catastrophes, as was also predicted in theoretical calculations [117]. If the MTs do not regularly undergo catastrophes they become longer, and eventually buckle, which leads to failure of the positioning process. Long MTs buckle more easily, because the force necessary to buckle a MT, scales with the MT length, $f_b \sim k_b T L_p / L^2$ [118], where k_b is the Boltzmann constant, T is the temperature, L_p is the persistence length, and L the MT length. Given that the persistence length of a MT is typically $25 \text{ pN} \cdot \mu\text{m}^2$ [28, 119], a

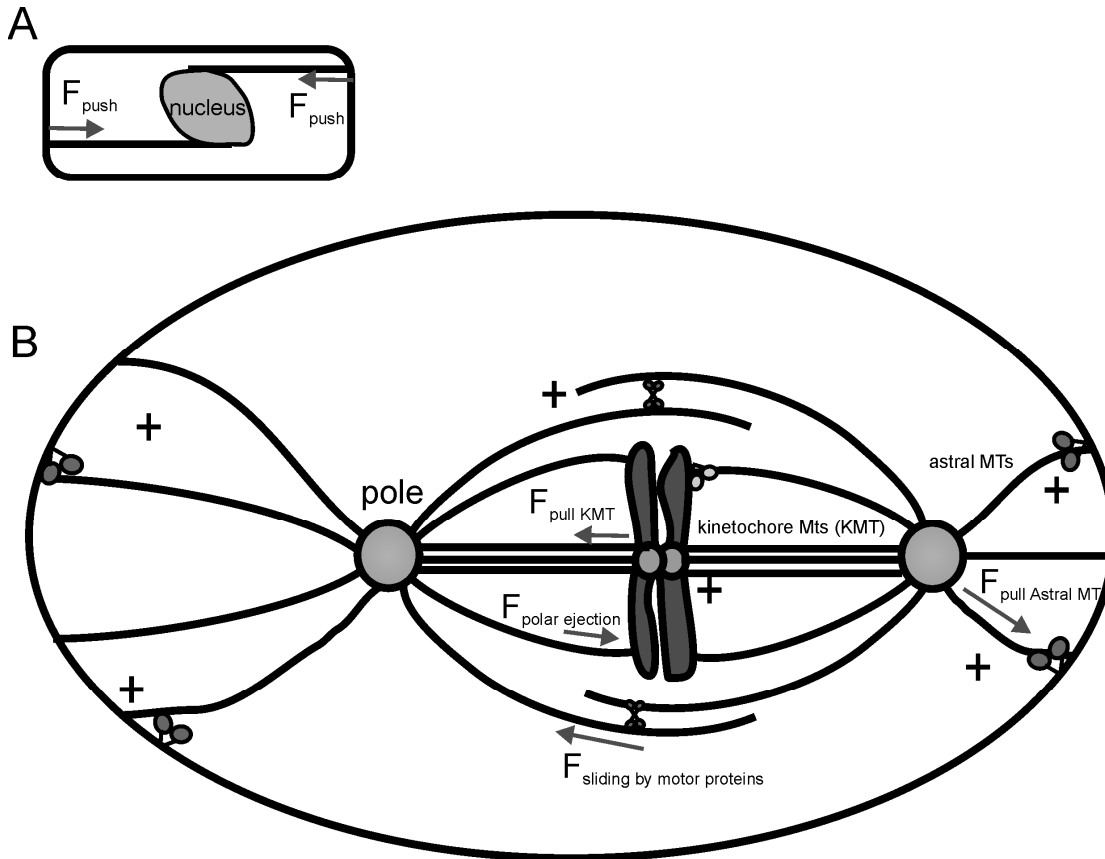


Figure 1.7

Force generation organizes the cellular interior. (A) Cartoon of a *S. pombe* cell. The nucleus is positioned by pushing forces, generated by MTs that grow from the nucleus towards the cell ends. Deformations of the nucleus reveal the generation of pushing forces. (B) Cartoon of the spindle in a first cell stage *C. elegans* embryo. The spindle is positioned by a combination of pushing and pulling forces generated at the cell cortex. The spindle is organized by a delicate balance between polar ejection forces from MTs that impinge upon the chromosomes and in addition occasionally interact with chromokinesins, and poleward forces due to MT depolymerization at the kinetochore.

MT with a length of $1 \mu\text{m}$ will buckle at $\sim 500 \text{ pN}$, however a MT with a length of $22 \mu\text{m}$ will already buckle at a force of $\sim 1 \text{ pN}$.

1.3.5 Cellular organization by a combination of microtubule pushing and pulling forces

In several systems, a combination of pushing and pulling forces is thought to be essential for proper organization [76]. The best studied, but probably also most

complex example, is the mitotic spindle. In the mitotic spindle a complex interplay between several mechanisms leads to proper chromosomal alignment and segregation [12]. The details of the mechanisms appear to differ in different systems, however the idea that a balance of antagonistic forces contributes to mitosis is thought to be more general [120, 121]. The forces organizing the spindle are generated by the interplay between multiple molecular motors and dynamic MTs (Fig. 1.7B). Motor proteins generate forces by cross-bridging and sliding MTs relative to adjacent MTs or other structures [120, 122]. In addition they couple the motion of cellular objects to MT growth and shrinkage (Fig. 1.7B). Force generation by dynamic MTs also plays a role. Pushing forces are believed to contribute to the generation of polar ejection forces [123]. Polar ejection forces are responsible for the movement of chromosomes away from the cell poles. Astral MTs that grow from the centrosome impinge upon the chromosomes and generate a pushing force. Additionally chromokinesins, plus-end directed motor proteins, located at the chromosomes, contribute to the generation of polar ejection forces by pulling on these MTs [124, 125]. The antagonistic forces that drive chromosomes towards the poles are, at least partly, due to MT pulling forces at the kinetochore [126]. Kinetochore MTs form bundles that are attached with their minus-end at the pole (centrosome) and with their plus-end at the kinetochore. In anaphase, during progression towards the poles, the MT plus-ends shrink while pulling the kinetochores towards the poles [126]. MT pulling forces also contribute to the positioning and segregation of the spindle poles, by interaction of astral MTs with motors at the cell cortex [120] (Fig. 1.7B).

How all these different forces and mechanisms lead to the formation and maintenance of the spindle is still an open question. However, *in vitro* experiments and computational models have been more and more successful in reproducing fundamental dynamic properties of the mitotic spindle [127-134], revealing our progress in understanding mechanisms underlying the behavior of the mitotic spindle.

MT-based pushing and pulling forces not only contribute to spindle formation, but they also play an important role in the positioning of the mitotic spindle in the cell. A classical example is the first cell stage *C. elegans* embryo. In a *C. elegans* embryo, the position of the spindle determines the cell division axis. In the first cell cycle the spindle moves towards the posterior end of the cell, resulting in asymmetric cell division (Fig. 1.7B). During this movement the spindle oscillates perpendicular to the cell axis. Laser cutting experiments revealed that pulling forces are critical for the positioning of the mitotic spindle [10, 135]. After cutting the poles of the spindle in small pieces, they moved towards the cell cortex, revealing the presence of pulling forces.

So why are pulling forces exploited in this system? Several theoretical studies have been developed to describe the oscillations and positioning of the spindle in *C. elegans* embryos [136-139]. All these models include pushing forces in addition to pulling forces. In these models pushing forces produce the main centering mechanism (see previous section). Pulling forces have been assigned different roles in the positioning process. One model predicts that an inhomogeneous distribution of pulling force generators induces the asymmetric positioning of the spindle [136]. In other models, pulling forces drive spindle oscillations [137, 139]. Experiments have shown though that oscillations are not necessary for asymmetric cell division of the first cell stage *C. elegans* embryo [87].

These experimental findings led to speculations about the different roles of pushing and pulling forces [6, 8]. Possibly the size of a system matters: in large systems (like *C. elegans*), MTs need to be long and cannot generate large pushing forces due to buckling. Only in small systems (like *S. pombe*), MT pushing is efficient, even though the actin network might strengthen MTs by giving lateral support, allowing for more efficient pushing in larger cells [140]. Another factor may be the symmetry of the system. In *C. elegans* the spindle needs to be asymmetrically positioned. In interphase in mammalian cells the large nucleus prevents the formation of an isotropic MT array around the centrosome [76]. Both systems include pulling forces. All together the fundamental role of pulling forces still remains to be clarified.

1.4 Thesis outline

The work presented in this thesis focuses on the role of MTs in cellular organization. It in particular deals with different mechanisms of MT force generation and the regulation of MT dynamics by these generated forces. Although most recent research has focused on the biochemical regulation of MT dynamics, MTs are also physically regulated; *in vivo* MTs regularly grow into physical boundaries, like the cell cortex or cellular organelles, where pushing and pulling forces are generated. In this thesis these interactions with physical boundaries are assessed in minimal *in vitro* experiments that allow for the systematic analysis of isolated mechanisms. In addition, simple computer simulations and mathematical modeling are performed to explain the experimental findings and to investigate the consequences of the experiments for other *in vitro* and *in vivo* systems.

Chapter 2 details the various *in vitro* assays that we use to study the interaction of dynamic MTs with physical boundaries. These boundaries are rigid barriers made with microfabrication techniques.

Chapter I

In chapter 3 we study the effect of an opposing force on the dynamics of a MT bundle with an optical trap. We show that in a bundle of MTs the maximum force that can be generated scales with the number of MTs in the bundle. Additionally we find that an opposing force couples MT dynamics in the bundle, resulting in catastrophes of the complete bundle. We can reproduce this mechanism in simple computer simulations.

Chapter 4 describes the interaction of dynamics MT ends with a dynein-coated barrier that mimics the end-on interaction of MT ends with dynein at the cell cortex or the kinetochore. We find that the interaction of dynein with dynamic MT ends can generate pulling forces, as has been long hypothesized. Moreover we show that dynein, only if it is attached to a growth opposing barrier, can regulate MT dynamics. Interestingly, our data are consistent with many *in vivo* observations.

In chapter 5, we study the implication of pulling forces on cellular positioning processes. We specifically attach dynein to the wall of a microfabricated chamber to show that pulling forces can improve the centering of dynamic MT asters in a confining microfabricated chamber compared to purely pushing based mechanisms. Additionally, we present a new model that explains this improved centering by pulling forces.

Chapter 6 presents experiments that study the end-tracking mechanisms of different +TIPs and their effect on MT dynamics *in vitro*. We show that Mal3 can autonomously track both dynamic MT ends and acts as a loading factor for Tip1 and the kinesin Tea2, which specifically track the MT plus-end.

Finally chapter 7 contains considerations for future research and preliminary data for a few additional research directions. In section 7.1 two possible future experiments, inspired on the theory developed in chapter 5, are described. In section 7.2, the combined effect of force and +TIPs on MT dynamics is discussed. Section 7.3 describes an assay to study MT capture to a physical barrier by the interaction of the +TIP CLIP170 and the cortical protein IQGAP1. With this assay we hope to shed light on the mechanisms of MT capture by non-motor proteins. Section 7.4 presents the progress in the development of an *in vitro* assay to study the role of transport of proteins at the ends of dynamic MTs in the formation of dynamic protein patterns at the cellular cortex.

Chapter II:

Mimicking microtubule interactions at the cell boundary with functionalized microfabricated structures

The cell is a very complex environment. Many processes occur simultaneously in a small confining space and are often entangled. Therefore, in most cases it is impossible to perturb only one specific process. These problems can be circumvented by isolating the components that contribute to a specific cellular process, from their environment. Experiments that aim to create such a minimal system in which only the fundamental properties of a specific cellular process are maintained are so-called in vitro experiments. In this thesis we use in vitro experiments to study how microtubule (MT) interactions with the cell boundary play a role in cellular organization. In our minimal systems, (functionalized) microfabricated barriers mimic cell boundaries. In carefully designed experiments we grow MTs against these microfabricated structures to study the specific cellular process we are interested in.

In this chapter different methods and assays are described necessary to realize these in vitro experiments. Section 2.1 describes the microfabrication techniques. Section 2.2 describes how proteins can be specifically attached to these microfabricated structures, to be able to mimic cortical interactions. In section 2.3 is explained how these functionalized microfabricated structures are incorporated in assays, and the details of the assays themselves are discussed.

2.1 Microfabrication

In this section four different microfabricated structures (Fig. 2.1) with their accompanying fabrication procedures are described. Every microfabricated structure has specific features designed for a specific experiment. In figure 2.1A a cartoon of a MT growing against a glass barrier is drawn (microfabrication described in section

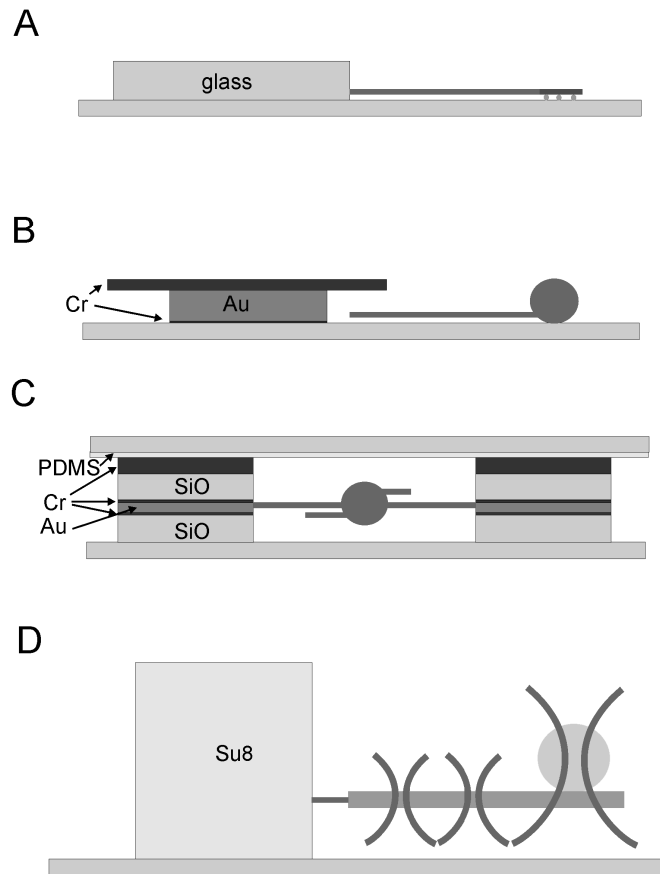


Figure 2.1

Cartoons of assays exploiting microfabricated structures (side views). (A) MTs grow from stabilized MT seeds against glass barriers as described in chapter 7. (B) MTs growing from centrosomes against gold barriers, consisting of a sandwich made of a thin chromium layer, a gold layer and a thick chromium layer, as described in chapters 4 and 7. (C) Centrosome positioning in a microfabricated chamber, consisting of a sandwich made of a glass layer, a thin chromium layer, a gold layer, a thin chromium layer, a glass layer and a thick chromium layer, sealed with a PDMS layer, as described in chapter 5. (D) Axoneme-bead construct in an optical trap positioned against a barrier consisting of SU-8 photo resist, as described in chapters 3 and 4.

2.1.1). These glass barriers are used in the experiments described in chapter 7, where our goal is to study the combined effect of force and +TIPs on MT dynamics. In these experiments MTs are grown against $\sim 1.5 \mu\text{m}$ high glass barriers from surface-attached stabilized MT seeds. In this assay the glass barriers need to be high and straight enough to prevent MTs from growing over the barriers.

In figure 2.1B (microfabrication described in section 2.1.2) a cartoon of a MT growing from a surface-attached centrosome against a gold barrier is shown, as used in the experiments in chapter 4 and 7. The barriers are $\sim 1.5 \mu\text{m}$ high and made of gold to allow for specific attachment of proteins to the barrier via thiol-chemistry. A thin layer of chromium between the gold layer and the coverslip ensures good adhesion of the gold layer. The chromium overhang on top provides an extra feature to prevent MTs from growing over the barrier and enforces end-on contact between the MT and the barrier. The goal of these experiments is to study the interaction of dynamic MT ends with barrier-attached proteins, mimicking MT-cortex interactions.

Figure 2.1C (microfabrication described in section 2.1.3 and 2.1.4) shows a cartoon of a centrosome that is freely moving in a microfabricated chamber (chapter 5). The experiment is designed to study MT-based positioning processes due to pushing and pulling forces in confining geometries. Pulling forces are introduced in the experiment by specifically attaching dynein molecules to a gold layer in the chamber wall. By varying the thickness of this gold layer the amount of dynein on the wall and thus the magnitude of the pulling forces can be varied. The gold layer is constructed between two chromium layers for proper adhesion and two glass layers, which allow for the generation of pushing forces due to MT polymerization and elastic restoring forces. The chromium layer on top is a result of the fabrication process. The complete chamber wall is $\sim 2.5\text{-}2.7 \mu\text{m}$ high.

Figure 2.1D (microfabrication described in section 2.1.5) shows a cartoon of SU-8 barriers that are used in optical trap experiments (chapters 3 and 4). In this experiment MT dynamics can be measured as well as MT based pushing and pulling forces. MTs are grown from an axoneme attached to a bead held in an optical trap against a SU-8 barrier. The barrier is approximately $7 \mu\text{m}$ high. The construct is positioned approximately 4 bead radii ($\sim 4 \mu\text{m}$) above the bottom surface (where the viscosity of the medium is constant [141]). The additional $3 \mu\text{m}$ of the barrier prevent the MTs from growing over the barrier.

2.1.1 Fabrication of glass barriers (Fig. 2.1A)

Coverslips, cleaned in chromosulphuric acid (Sigma), were coated with $\sim 1.5 \mu\text{m}$ silicon monoxide in a home-built evaporation chamber. S1813 photo resist (Sigma) was spincoated on top and afterwards soft-baked. The samples were exposed to ultraviolet light through a chromium mask, post-exposure baked, and developed in MF319 developer. The sample was

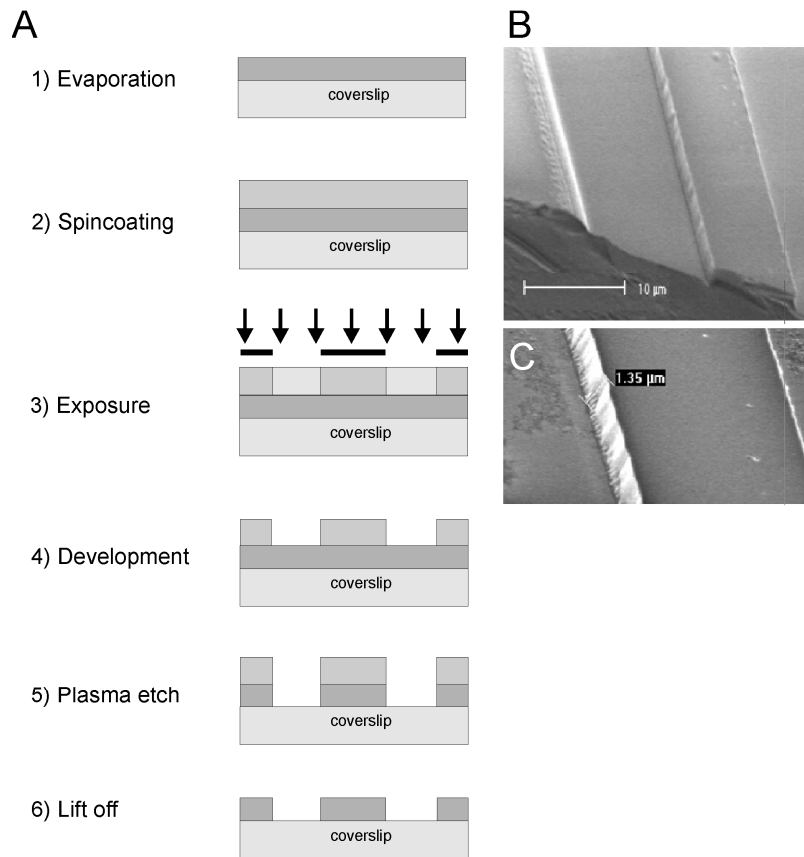


Figure 2.2

Fabrication process of glass barriers. (A) Steps taken in the fabrication process as explained in the text. (B) A low magnification scanning electron micrograph (SEM) image of the glass-barriers. (C) Higher magnification SEM image of the glass barriers.

plasma-etched in a mixture of a CHF_3 -/ SF_6 -/Argon- plasma in the Oxford Plasma Plasmalab 80+ ICP plasma-etcher, and the remaining photo resist was removed by sonication in acetone, resulting in 1.5 μm high silicon mono-oxide barriers on a coverslip (Fig. 2.2).

2.1.2 Fabrication of gold barriers (Fig. 2.1B)

Clean coverslips were coated with a sandwich of a thin chromium layer (5 nm), gold (700 nm), and a thick chromium layer (150 nm) in a home-built evaporation chamber. Afterwards the samples were coated with hexamethyldisilazane (HMDS) using evaporation under vacuum for 1 hour. HMDS created a good contact between chromium and the S1813 photo resist that was spincoated on top and afterwards soft-baked. The samples were exposed to ultraviolet light through a chromium mask, post-exposure baked, and developed in MF319 developer. The samples were subsequently immersed in chromium etchant, acetone, to remove the photo resist, gold etchant, and finally they were very briefly immersed in chromium etchant again, to remove the thin layer of chromium on the bottom, but to keep the thick layer of chromium on top. This fabrication process resulted in a pattern of gold barriers with an overhang of chromium on top (Fig. 2.3).

2.1.3 Microfabricated chamber fabrication (Fig. 2.1C)

Clean coverslips were coated with a sandwich of chromium (5 nm), gold (100 or 700 nm), chromium (5 nm), silicon mono-oxide (1200 or 900 nm) and chromium (400 nm), in a home-built evaporation chamber. Afterwards the samples were coated with hexamethyldisilazane (HMDS) using evaporation under vacuum for 1 hour. Subsequently S1813 photo resist was spincoated on top and afterwards soft-baked. The samples were exposed to ultraviolet light through a chromium mask, post-exposure baked, and developed in MF319 developer. The samples were subsequently immersed in chromium etchant and acetone, to remove the photo resist, resulting in a pattern of chambers in the top chromium layer. Subsequently the samples were plasma-etched in a mixture of a CHF_3 -/ SF_6 -/ Argon- plasma in the Oxford Plasma Plasmalab 80+ ICP plasma-etcher. The results were microfabricated chambers that consisted of a sandwich of 1200/900 nm glass, 5 nm chromium, 100/700 nm gold, 5 nm chromium, 1200/900 silicon mono-oxide, and ~100 nm chromium. To remove possible contamination of the plasma on the gold layer the process was ended with 15 minutes exposure to oxygen plasma. Afterwards the samples were checked for defects

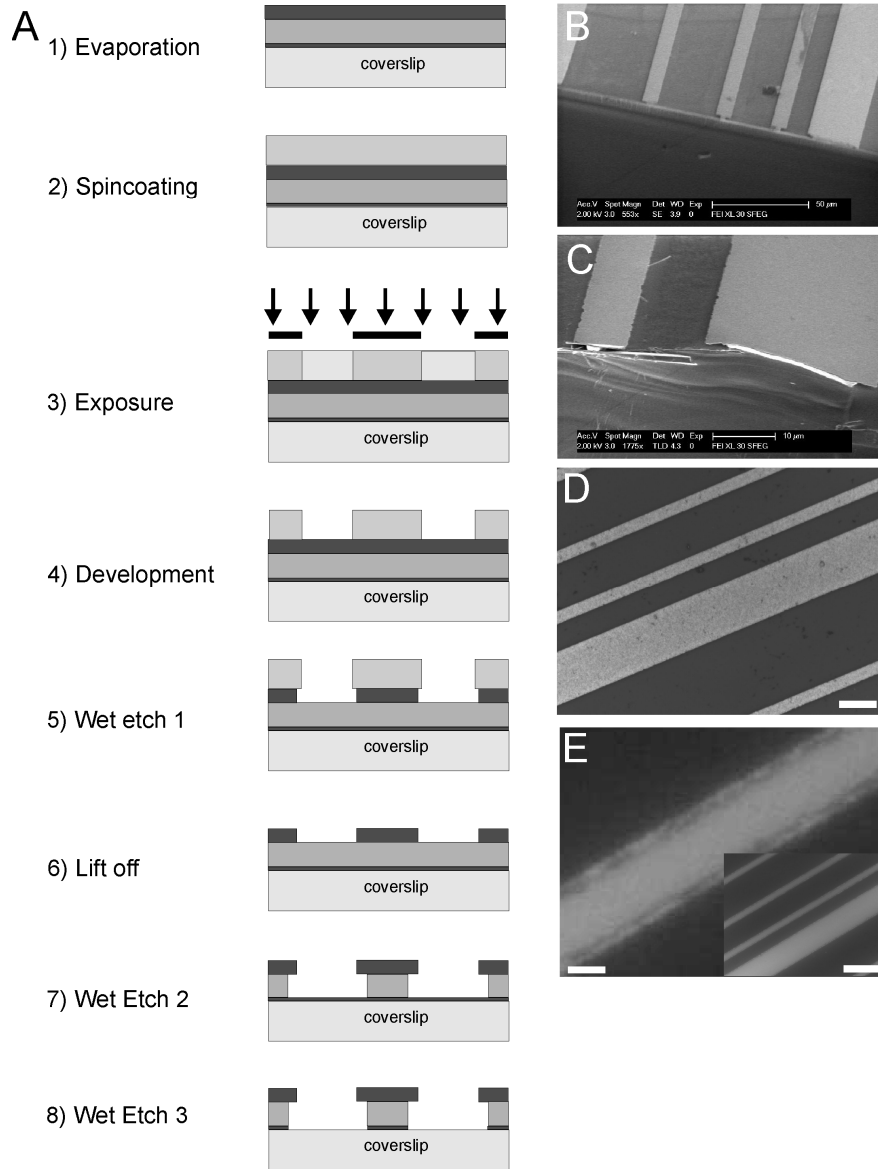


Figure 2.3

Fabrication process of gold barriers. (A) Steps taken in the fabrication process as explained in the text. (B) A low magnification scanning electron micrograph (SEM) image of the gold barriers. (C) Higher magnification SEM image of the gold barriers with the chromium overhang on top. (D) Reflected light bright field image of the barriers, image taken from above, such that the chromium is shown. Scale bar indicates 30 μm . (E) inset: Reflected light bright field image of the barriers, image taken from below. Scale bar indicates 30 μm . The large image is a high magnification of one small barrier, showing the gold layer and the chromium overhang. Scale bar indicates 3 μm .

Mimicking cortical interactions with microfabricated structures

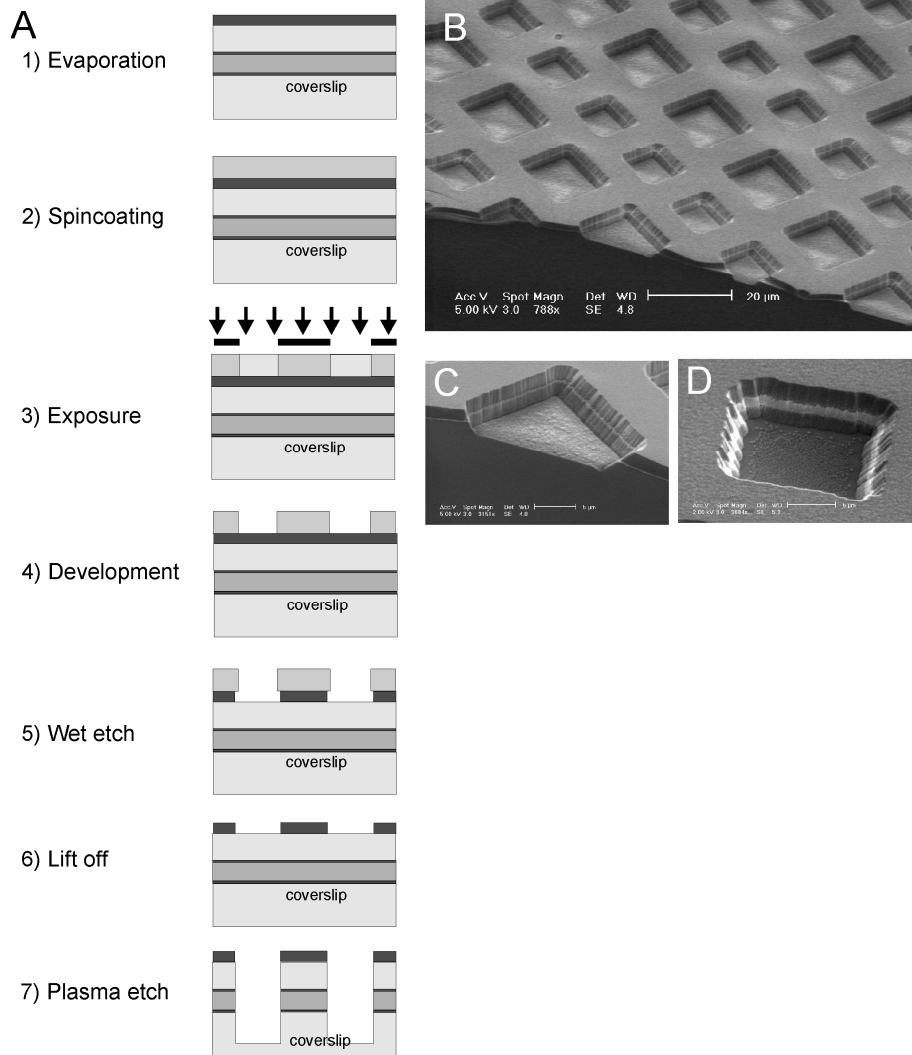


Figure 2.4

Fabrication process of microfabricated chambers. (A) Steps taken in the fabrication process as explained in the text. (B) A low magnification scanning electron micrograph (SEM) image of the microfabricated chambers. (C) Higher magnification SEM image of microfabricated chambers with a 100 nm gold layer. (D) Higher magnification SEM image of microfabricated chambers with a 700 nm gold layer.

in a FEI XL30 SFEG electron microscope. The microfabricated chambers were ~ 2.6 μm deep, and of two sizes: 10 and 15 μm -wide square chambers, with either 100 or 700 nm thick gold layers (Fig. 2.4).

2.1.4 Fabrication of PDMS lids

The microfabricated chambers (section 2.1.3) were closed with a polydimethylsiloxane (PDMS) lid to achieve good sealing. The PDMS layer was fabricated on a 24x60 mm coverslip, by firmly squeezing a droplet of PDMS between a piece of transparency slide and the coverslip. The PDMS was cured in a 100 °C oven for 1 hour. Afterwards the transparency slide was removed, leaving a ~80 µm flat layer of PDMS on the coverslip. The PDMS layer together with the coverslip was thin enough to allow for microscopic observation with a high magnification oil immersion objective through the microfabricated chamber, looking from either side. The PDSM coverslips were stored in a closed box for approximately 1 week.

2.1.5 Microfabricated chambers for optical trap experiments (Fig. 2.1D)

Clean coverslips were spincoated with SU-8 negative tone photoresist (Microchem) to produce a 7 µm-thick layer, which was then soft-baked. The coverslips were exposed to UV light and post-exposure baked. The illuminated areas were developed (XP SU8-developer, microchem) and hard-baked, leaving 7 µm-high chambers of 40 by 80 µm separated by 20 µm-wide barriers (Fig. 2.5).

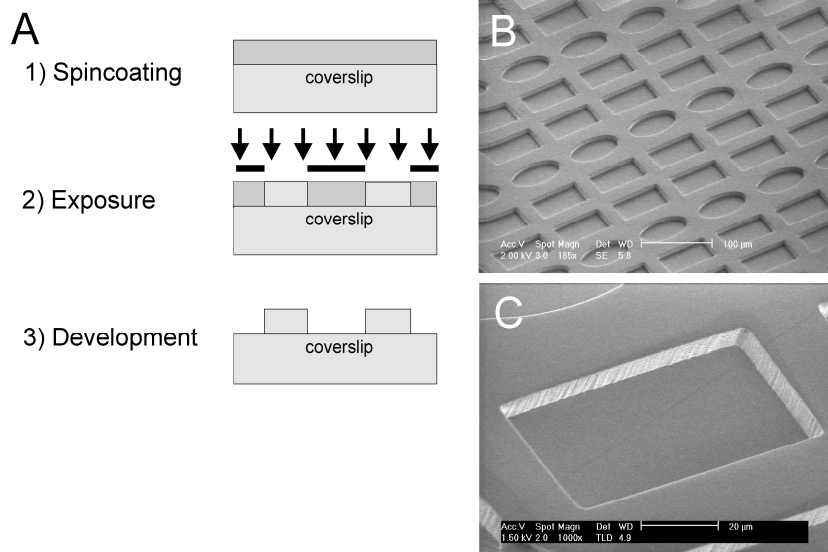


Figure 2.5

Fabrication process of SU-8 chambers. (A) Steps taken in the fabrication process as explained in the text. (B) A low magnification scanning electron micrograph (SEM) image of the SU-8 chambers. (C) Higher magnification SEM image of the SU-8 chambers.

2.2 Activation of gold barriers

2.2.1 Biotinylation of gold barriers

The gold barriers were specifically labeled with biotin using thiol-chemistry [142] (Fig. 2.6 A). The slide with gold barriers was cleaned with ethanol, immersed in 200 mM 11-mercapto-1-undecanoic acid in ethanol for 3 hours, rinsed with ethanol, immersed in 100 mM 1-ethyl-3-(3-(dimethylamino)propyl)carbodiimide (EDAC) and 200 mM pentafluorophenol (PFP) in ethanol for 20 minutes, rinsed with ethanol, immersed in 0.1 mM biotin-PEO-LC-amine, and finally rinsed with ethanol. To remove non-specific interactions of the thiol-groups with glass surfaces the slides were sequentially immersed in 2 M NaCl for 7 minutes, 0.1% tween in milliQ for 15 minutes, 0.1% tritonX for 7 minutes, and thoroughly rinsed with milliQ water. The slides were stored in ethanol and could be used for several weeks. The attachment of biotin to gold was tested by evaluating the specific binding of fluorescent streptavidin to gold structures. Microfabricated chambers with a thin layer of gold in their walls (as described in section 2.1.3) were exploited for this test (Fig. 2.6C). In figure 2.6D bright field reflection microscopy and fluorescence microscopy images (inset) show the microfabricated chambers that were incubated with fluorescent streptavidin. Streptavidin only attached to the gold line in the walls. Figure 2.6 E shows a y-projection (side-view) of a z-stack of three microfabricated chambers incubated with fluorescent streptavidin. Images were made with spinning disk confocal fluorescent microscopy. The dotted line shows the top and the bottom of the microfabricated chambers. There is a clear fluorescent signal from the middle of the microfabricated chamber (the total chamber height is $\sim 2.6 \mu\text{m}$). The height of this fluorescent signal reveals the z-resolution of our spinning disk confocal fluorescence microscope which is approximately $\sim 1 \mu\text{m}$.

2.2.2 Attachment of biotinylated proteins to biotinylated gold barriers

Proteins of choice were specifically attached to a gold surface via biotin-streptavidin linkage and thorough blocking of the other surfaces. The glass surfaces were blocked with 0.2 mg/ml PLL-PEG (SurfaceSolutions, Switzerland) for 5 minutes, rinsed with MRB80, blocked with 1 mg/ml κ -casein in MRB80 for 5 minutes, and rinsed. Subsequently a multilayer (to enhance the number of binding sites) of biotinylated-BSA and streptavidin was formed [142] on the gold barrier (Fig. 2.6 B). A streptavidin mix (0.5 mg/ml streptavidin, 1 mg/ml κ -casein, 5 mg/ml BSA in MRB80) and a

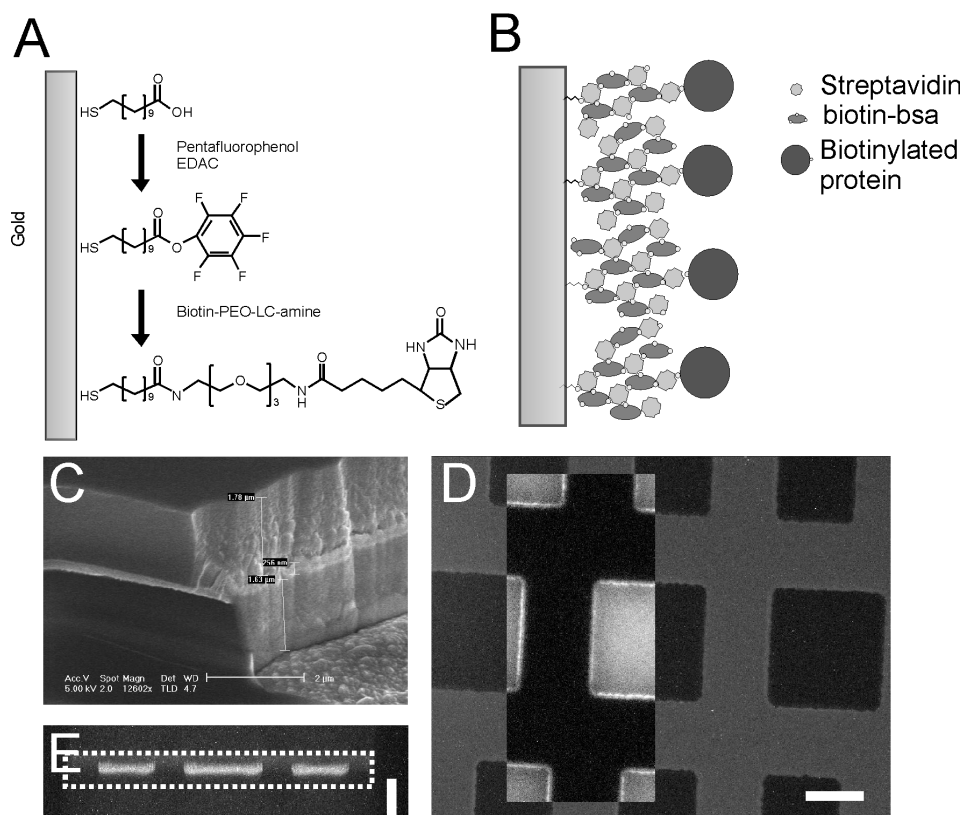


Figure 2.6

Activation of gold barriers. (A) Cartoon of the chemical process involved in biotinylation of the gold barrier. (B) Cartoon of a streptavidin-biotin-BSA layer assembled on a 100 nm gold layer. (C) SEM image of a sidewall of a microfabricated chamber. (D) Reflected light bright field image of the microfabricated chambers. Scale bar indicates 10 μm . The inset is a fluorescence image which shows the specific attachment of fluorescent streptavidin to the gold layer in the microfabricated chamber walls. (E) Y-projection of a z-stack of spinning disk confocal fluorescence images of the same microfabricated chambers as in C and D. The white, dotted square shows the top and the bottom of the microfabricated chambers. Scale bar indicates 3 μm .

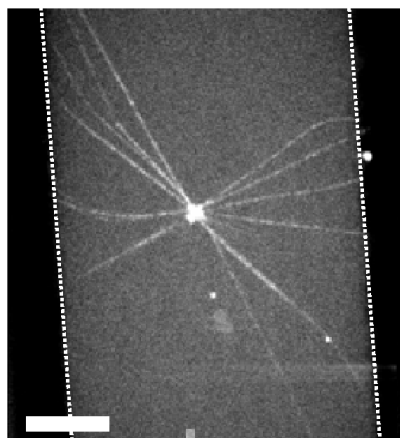
biotinylated-BSA-mix (1.5 mg/ml biotinylated-BSA, 1 mg/ml κ -casein, 5 mg/ml BSA in MRB80) were sequentially introduced and incubated for 5 minutes to create a multilayer with 3 layers of streptavidin and 2 of biotinylated-BSA. Afterwards the biotinylated protein was introduced (biotinylated protein, 1 mg/ml κ -casein, 5 mg/ml BSA in MRB80) for 5 minutes (in the case of control experiments without biotinylated protein, this step was left out).

2.3 Assays with microfabricated structures

We used our microfabricated structures in four different assays that are described in this section. In the first assay (2.3.1) MTs are growing from surface-attached nucleation sites against functionalized gold barriers (section 2.1.2). In chapter 4 we exploit gold barriers to study the interaction of dynamic MT ends with barrier-attached dynein. In chapter 7 MTs are grown against gold barriers to study the capture of MTs by IQGAP1. In the second assay (section 2.3.2) MTs are grown against glass barriers (section 2.1.1) to study the combined effect of MT polymerization forces and +TIPs on MT dynamics, as described in chapter 7. In section 2.3.3 the third assay to study positioning processes due to MT pushing and pulling forces, as exploited in chapter 5, is described. Finally fourth assay is the optical trap assay to measure MT dynamics as well as MT pushing and pulling forces, used in chapters 3 and 4, and described in section 2.3.4.

2.3.1 Assay of microtubules growing against functionalized barriers

Microscope slides were cleaned in chromosulphuric acid. A 20 μ l-flow cell was constructed by drawing two parallel lines of vacuum grease approximately 5 mm apart on a clean microscope slide, and mounting a coverslip containing barriers that were biotinylated as described in section 2.2.1 on top. A solution of centrosomes in MRB80 was flown in and incubated for 5 minutes in order to let centrosomes non-specifically adhere to the glass surfaces. Centrosomes that did not stick to the surface were washed out by rinsing with two flow cell volumes of MRB80. Subsequently the barriers were functionalized with a biotinylated protein (dynein in chapter 4 and IQGAP1 in chapter 7) as described in section 2.2.2. The flow cell was rinsed with MRB80 and the final tubulin mix was introduced (variable tubulin/rhodamine tubulin concentration (Cytoskeleton, Denver), 1 mM GTP, 1 mM ATP, 0.8 mg/ml κ -casein, 0.1% methyl cellulose (4000cP), and an oxygen scavenger system in MRB80). The flow cell was sealed and examined at 25°C using spinning disk confocal microscopy (Fig. 2.7). Movies were made with 561 nm laser light with a time lag of 3 seconds and 300 ms exposure, on a Leica microscope with a 100x 1.3 NA oil immersion objective equipped with a spinning disk confocal head from Yokogawa and a cooled EM-CCD camera (C9100, Hamamatsu Photonics).



top view

Figure 2.7

Spinning disk confocal fluorescent image of MTs growing from a centrosome against a functionalized gold barrier. The white dotted lines show the edges of the microfabricated barriers. Scale bar indicates 10 μm .

2.3.2 Assay of microtubules growing against glass barriers

This assay is essentially the same as the previously described one (section 2.3.1). In this case the steps involving thiol-chemistry and biotin streptavidin linkage are left out. In addition, MTs are nucleated from biotinylated stabilized GMPCPP MT seeds, instead of from centrosomes. The seeds are attached to a PLL-PEG-biotin surface via biotin-streptavidin linkage. PLL-PEG-biotin replaces PLL-PEG for surface blocking.

2.3.3 Optical trap experiments

2.3.3.1 Optical trap set-up

The optical trap set-up [143, 144] consisted of an infrared trapping laser (1064 nm, Nd:YVO₄, Spectra-Physics, USA, CA), which was focused into the sample by a 100x /1.3 NA oil immersion objective. The laser beam was time-shared using acousto-optical deflectors (AODs) (IntraAction DTD-274HA6) to create a “key hole” trap consisting of a point trap and a line trap, as described earlier [5, 97]. A low-power red laser (633 nm, HeNe, 1125P, Uniphase) was superimposed after the AODs on the IR beam. Before or after every experiment, the red laser light was focused on a bead

trapped in the point trap, and imaged onto a quadrant-photodiode for stiffness calibration. The stiffness of the point trap was determined by analysis of the power-spectrum of the thermal fluctuations of the bead. Typically, trap stiffnesses in the range of 0.03-0.12 pN/nm were used.

2.3.2.2 Optical trap assay

A clean coverslip with microfabricated SU-8 chambers (as described in 2.1.5) was built into a flow system, which consisted of a channel cut in parafilm squeezed between a microscope slide and a coverslip. In order to block the surface of the chambers, first a 0.2 % agarose solution at 70°C was flown in. The agarose was blow-dried by connecting a pump to the channel for a few minutes. Afterwards, a 0.1% Triton X100 solution was flown through to prevent bubble formation in the flow cell. A second blocking step was done by incubating the flow system for 10 min with a 0.1 mg/ml κ -casein solution in MRB80. Finally the flow cell was rinsed with 100 μ l of MRB80. The experiment started by flowing in axonemes and beads. Axonemes were purified from sea urchins according to [145]. First a bead was trapped in the point trap. Then an axoneme was caught in the line trap and non-specifically stuck to the bead [5]. This construct was subsequently positioned in front of a barrier in one of the microfabricated chambers. The experiment was performed with the axoneme relatively close to the barrier to keep the MTs short (less than one μ m). The force necessary to buckle these short MTs is much higher than the force that is maximally applied with the optical trap. Therefore the MTs were forced to stay in ‘end-on’ contact with the barrier during the experiment. Because the axoneme-bead construct was not infinitely stiff, the bead was moved from the trap center over a distance that was generally smaller than the motion of the axoneme tip away from the barrier. The conversion factor to relate bead displacement to displacement of the axoneme tip was measured by repeatedly pushing the barrier against the construct and plotting the subsequent bead displacement as a function of barrier displacement. After a first soft regime of approximately 50 nm, the conversion factor was constant over several hundreds of nm (Fig. 2.8) [5].

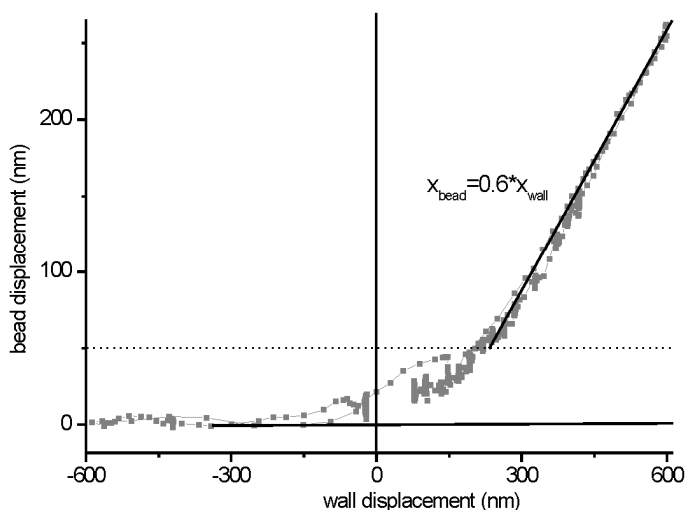


Figure 2.8

The stiffness of the axoneme-bead construct. The wall displacement is plotted against the bead displacement. The axoneme-bead construct shows an initial soft regime of approximately 50 nm, followed by a linear regime.

Afterwards, the tip of the axoneme was positioned approximately 100 nm away from the barrier. Next, the chamber was rinsed to remove left over beads and axonemes and afterwards the tubulin mix (with the addition of 0.1 mg/ml κ -casein, 1 mM GTP in MRB80) was added to trigger MT growth. In figure 2.9C a typical dataset of MT growth is shown: Initially there is no MT growth and the bead is positioned in the center of the trap. Then the MT starts to grow and pushes the bead out of the trap center. Eventually the MT undergoes a catastrophe and while the MT shrinks the bead moves back to the trap center. We could distinguish between plus- and minus-end growth because the plus-end is known to grow faster and to have more catastrophes [17]. Occasionally we obtained measurements with much slower growth and no catastrophes, which we attributed to minus-ends. Axonemes and beads were imaged using VE-DIC microscopy. During the experiments, the image stream was digitized at 1 Hz and the position of the bead was tracked online using a cross-correlation routine for live monitoring. Afterwards the recorded images were digitized at a frame rate of 25 Hz. This image stream was used to track the bead offline. The bead tracking was automated using home-written IDL software. The position of the bead was obtained with sub-pixel resolution down to 2-3 nanometers [146].

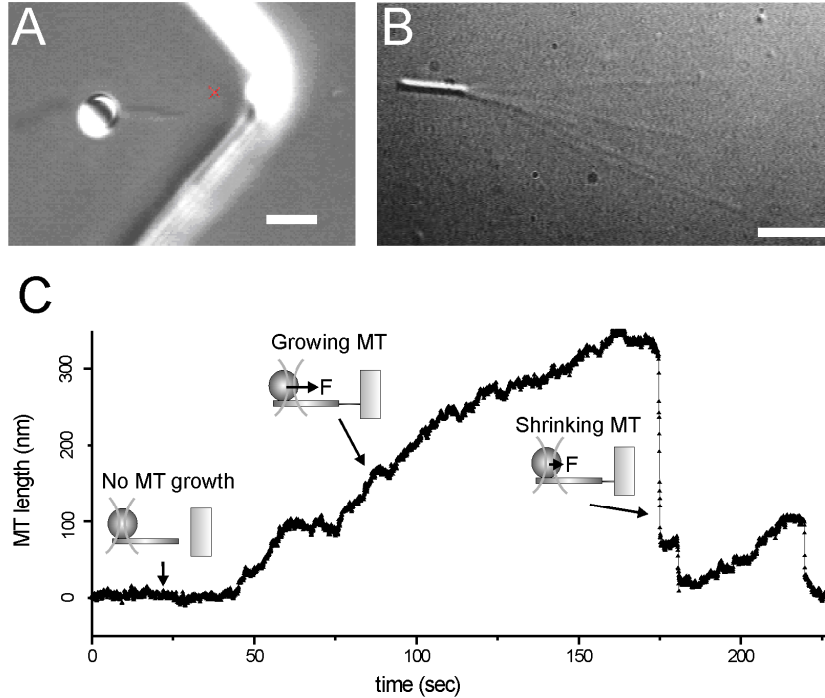


Figure 2.9

The optical trap experiment. (A) Video-enhanced differential interference contrast (VE-DIC) image of a construct, consisting of a bead held in the optical trap connected to an axoneme, positioned in front of a barrier. Scale bar indicates 2 μm . (B) VE-DIC image of MTs growing from an axoneme. The number of MTs growing from the axoneme can be controlled by varying the tubulin concentration and the temperature [2]. Scale bar indicates 3 μm . (C) Graph with a typical dataset of MT-length against time. Cartoons in the graph show the bead position relative to the trap position for different phases of the experiment.

2.3.4 Assay with functionalized microfabricated chambers

A microfabricated chamber coverslip was fabricated as in section 2.1.4. and activated as described in section 2.2.1. The microfabricated chambers and the PDMS lid (fabricated as in section 2.1.5) were immersed in a mix of κ -casein (2 mg/ml) and BSA (5 mg/ml) in MRB80 (80 mM K-Pipes, 4 mM MgCl_2 , 1 mM EGTA, pH = 6.8) for 15 minutes. Afterwards both surfaces were blow-dried using a N_2 -flow. The PDMS coverslip and the microfabricated chamber coverslip were incorporated into a temporary flowcell, with Teflon-tape as a spacer and a metal block as a weight on top

Chapter II

of the flowcell to keep the two coverslips tightly together. The flowcell was filled with a solution of κ -casein (2 mg/ml) and BSA (5 mg/ml) in MRB80 for 10 minutes, for extra blocking. Then the biotinylated protein was introduced as described in section 2.2. The sample was rinsed with MRB80. Before the tubulin solution was introduced, the sample was placed on a metal block of 4°C to prevent MT growth. The tubulin solution (centrosomes, 22 μ M tubulin, 1.6 μ M Rhodamine tubulin, 1 mM GTP, 1 mM ATP, an oxygen scavenger system, 0.5 mg/ml κ -casein, and 16% sucrose in MRB80) was introduced in the flowcell, and left to mix by diffusion for 4 minutes. Afterwards the Teflon tape was carefully removed and the PDMS coverslip was firmly pressed on the microfabricated chamber coverslip for 2 minutes to create good sealing of the microfabricated chambers. The edges of the microfabricated chamber coverslip were sealed with hot candle wax. The flowcell was sealed and examined at 25°C using spinning disk confocal microscopy. The sample was imaged through the PDMS layer and therefore it could easily be checked whether the microfabricated chambers were well-sealed (Fig. 2.10). Only asters located in well-sealed microfabricated chambers were considered for further analysis. Movies were made with 561 nm laser light with a time lag of 3 or 5 seconds and 300 ms exposure, on a Leica microscope with a 100x 1.3 NA oil immersion objective equipped with a spinning disk confocal head from Yokogawa. Due to bleaching problems individual asters could not be imaged longer than approximately 15 minutes, but by sequentially imaging different asters, the positioning process could be monitored over ~3 hours.

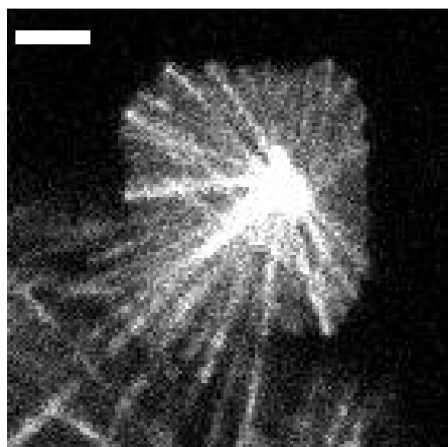


Figure 2.10

Spinning disk confocal fluorescence image of an incompletely sealed microfabricated chamber. The left-bottom corner was not well sealed and therefore the MTs could grow between the walls and the PDMS. Scale bar indicates 5 μ m.

2.4 Acknowledgements

I would like to thank Chris Rétif for his advice on microfabrication, Henk Bar for his help with microfabrication, Martijn van Duijn and Guillaume Romet-Lemonne for setting up the thiol-chemistry assay and initiating the project, Jacob W. J. Kerssemakers, E. Laura Munteanu, and Julien Husson for developing and help with the optical trap assay, Matt Footer (J. Theriot laboratory) for the axoneme purification, and Clause Celati (M. Bornens laboratory) for help with the centrosome purification.

Chapter III:

Force generation and dynamic instability of microtubule bundles

Individual dynamic microtubules can generate pushing or pulling forces when their growing or shrinking ends are in contact with cellular objects such as the cortex or chromosomes. These microtubules can operate in parallel bundles, for example when interacting with mitotic chromosomes. Here we investigate the force generating capabilities of a bundle of growing microtubules, and study the effect that force has on the cooperative dynamics of such a bundle. We used an optical tweezers set-up to study microtubule bundles growing against a microfabricated rigid barrier in vitro. We show that multiple microtubules can generate a pushing force that increases linearly with the number of microtubules present. In addition, the bundle can cooperatively switch to a shrinking state, due to a force induced coupling of the dynamic instability of single microtubules. In the presence of GMPCPP, bundle catastrophes no longer occur, and high bundle forces are reached more effectively. We reproduce the observed behavior with a simple simulation of microtubule bundle dynamics that takes into account previously measured force effects on single microtubules. Using this simulation, we also show that a constant compressive force on a growing bundle leads to oscillations in bundle length that are of potential relevance for chromosome oscillations observed in living cells.

This chapter has been published:

Liedewij Laan*, Julien Husson*, E. Laura Munteanu, Jacob W. J. Kerssemakers, Marileen Dogterom
Force-generation and dynamic instability of microtubule bundles,
Proc Natl Acad Sci USA, **105**:8920-8925 (2008) (*equal contribution)

3.1 Introduction

Microtubules (MTs) are dynamic cytoskeletal polymers that constantly switch between growing and shrinking states in a process termed dynamic instability [147]. They are able to generate pushing forces during their assembly process, and pulling forces during their disassembly process [3, 148]. Pushing forces have been shown to contribute, for example, to nuclear positioning in fission yeast [71], while both MT pushing and pulling forces have been implicated in chromosome motion during mitosis [17]. The force that a single growing MT can generate, and the effect that this force has on the assembly dynamics of the MT, has been studied in detail in *in vitro* experiments [5, 56, 72, 90, 149]. It has been shown that the growth velocity decreases, and the catastrophe frequency (the rate at which MTs switch from growth to shrinkage) increases, as the compressive force on the MT end increases. This implies that growing MTs interacting with obstacles in cells, such as the cell cortex or chromosomes, are expected to enhance their probability of switching to a shrinking state due to compressive forces that are generated in these situations. In this way, force can provide a regulation mechanism to the cell to (locally) control MT dynamics [50].

Often MTs do not operate alone, but work together in bundles. In particular in the case of mitosis, MTs that interact with the chromosomes grow in parallel bundles that could presumably generate collective forces on the chromosomes that greatly exceed the force generated by a single MT [150]. A subset of these MTs associates with specialized attachment sites on the chromosomes called kinetochores [151]. During anaphase, shrinking kinetochore MT bundles are believed to produce pulling forces on the chromosomes that cause poleward motion [152]. During pro-metaphase and metaphase, poleward motion is alternated with anti-poleward motion, which is believed to be due to interactions of non-kinetochore MTs with motor proteins located on the chromosome arms [122] and/or pushing forces generated by the growth of MT bundles against kinetochores or chromosome arms [123]. It is however not known what the collective force generating capabilities of multiple growing MTs are, and thus how importantly these forces might contribute to the anti-poleward motion of chromosomes observed during mitosis.

In this chapter we ask how much force can be generated by multiple MTs that are growing in parallel from a common rigid base (without being otherwise crosslinked to each other). Do forces generated by single MTs add up in a linear fashion, and how are the dynamics of the single MTs and the bundle affected by the presence of a compressive force? In order to address these questions, we studied the

dynamics of a MT bundle under force in an *in vitro* experiment where MTs growing from pure tubulin pushed against a microfabricated rigid barrier. We used an optical tweezers set-up, as described in previous experiments on single MTs [5, 97]. We show that multiple MTs that grow in parallel can reach much higher forces than single MTs, and that the increase in force is linear with the number of MTs present. Surprisingly, we also observe cooperative catastrophes, i.e. relatively abrupt switches to the shrinking state of the entire MT bundle, even though the probability for spontaneous near-simultaneous catastrophes of all MTs in the bundle is negligible under our conditions. When we grow the bundle in the presence of GMPCPP, a slowly hydrolysable analogue of GTP [31], bundle catastrophes no longer occur and as a result the bundle reaches high forces more effectively. We can reproduce the observed behavior with a simple simulation of MT bundle dynamics that takes into account the force effects that have been measured for single MTs [72, 149]. Apparently, the otherwise independent dynamics of individual MTs can be coupled to each other due to the presence of a compressive force. Interestingly, when in the simulation we exert a constant compressive force on the growing bundle, we observe length oscillations similar to chromosome oscillations measured in *newt lung* cells during pro-metaphase [153].

3.2 Measurement of bundle forces and dynamics

In order to study the dynamics and force generation of a growing MT bundle *in vitro*, we used an optical tweezers technique that allowed us to grow multiple MTs from an axoneme, a naturally occurring rigid bundle of polarity aligned stabilized MTs, against a rigid microfabricated barrier [97, 154, 155] (Fig. 3.1A). The axoneme was non-specifically attached on one side to a bead. This construct was held in a key-hole trap, a time-shared optical trap that had a main trapping point to hold the bead and a weak line trap to align the axoneme (Fig. 3.1A). The construct was positioned halfway up a 7 μm -high sidewall of a microfabricated chamber (Fig. 3.1B) built into a flow system. When a solution containing tubulin and GTP was flown in, MT growth started. After growing MTs made contact with the barrier, further length increases of the MTs led to a displacement of the bead in the trap and a linearly increasing force on the MTs. By determining the position of the bead in the trap and the trap stiffness, we could measure the forces generated by the bundle of MTs over time. To keep the MTs short (less than one micrometer) and thus prevent them from buckling, we started the experiment with the axoneme very close to, or slightly pressed against the barrier and

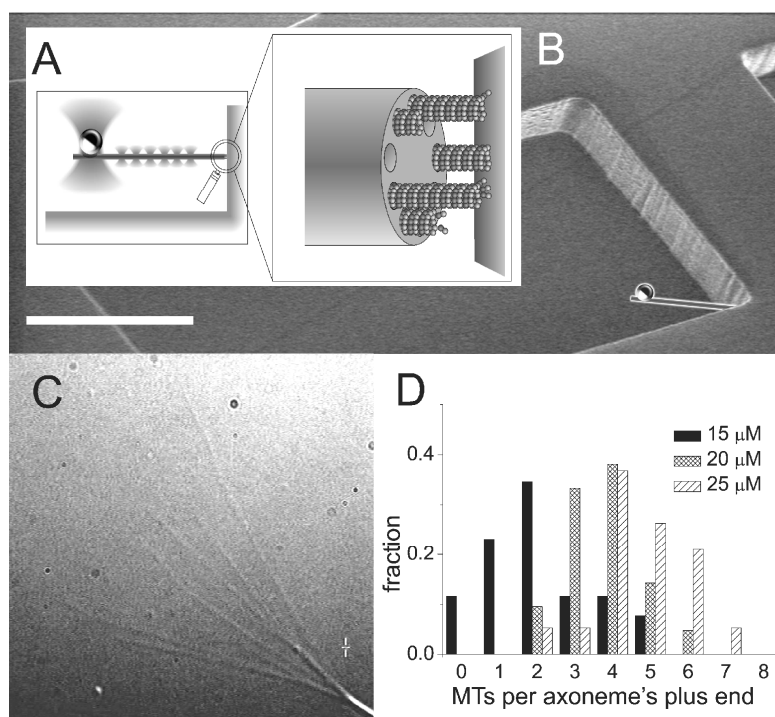


Figure 3.1

Experimental set-up. (A) Schematic picture of a MT bundle nucleated by an axoneme growing against a barrier. A construct made of a bead attached to the axoneme is maintained in position by a “key-hole” trap: a single strong trap holds the bead while many shallow traps form a line trap constraining the axoneme’s movement along a single direction. (B) Scanning electron micrograph of a micro-chamber, whose corner is used as a rigid barrier. A schematic construct (drawn to scale) is superimposed on the micrograph. Scale bar is 20 μm . (C) Video-enhanced differential interference contrast (DIC) image of an axoneme from which several MTs are growing. (D) Histograms of the number of MTs observed per axoneme, for different tubulin concentrations at 27° C.

chose a relatively high trap stiffness so that MTs would stall before they would grow too long [149].

The axonemes we used had 9-11 nucleation sites for MTs (as determined from EM pictures; data not shown). The average number that was nucleated could be tuned by varying the tubulin concentration and the temperature. We first characterized the nucleation properties by sticking axonemes to the surface of a flow cell and by growing MTs at different temperatures and tubulin concentrations (see section 3.4.2). We counted the number of MTs per axoneme in the first 5 to 10 minutes of the experiment, assuming that the end with the most MTs was the plus-end (Fig. 3.1C). MT plus-ends grow much faster than minus-ends, so the corresponding end of an axoneme has more and longer MTs [25]. To verify this, we occasionally introduced

beads coated with kinesin molecules into our samples [156]. When placed on an axoneme, these beads always moved to the side with the most MTs. In figure 3.1D three histograms are shown with the number of MTs per axoneme at different tubulin concentrations at 27 °C. At a tubulin concentration of 25 μM the average number of MTs was 4.7 ± 1.2 , with a maximum of 9 per axoneme. However we expect this number to be an underestimate because we could not detect MTs shorter than approximately 1 μm . When raising the concentration or temperature further, to get an average number close to the maximal number of nucleation sites, spontaneous nucleation of MTs occurred, which would have been a problem in the trap experiment. We decided to perform our trap experiments at 28°C with an initial tubulin concentration of 25 μM . We estimate that mixing in the flow cell diluted the tubulin down to about 20 μM (corresponding to an average number of MTs around 4 in figure 3.1D).

In figure 3.2A, four traces of plus-end MT bundle growth are shown. We could distinguish between plus- and minus-end growth because the plus-end grew faster and had catastrophes. Occasional measurements with much slower growth and no catastrophes, which we attribute to minus-ends, are not shown. When focusing on the first dataset in figure 3.2A (upper trace), it appears that indeed several MTs are growing together. First a MT starts growing at $t \sim 25$ s until it reaches a force of 2.8 ± 0.7 pN, stalls and has a catastrophe at $t \sim 105$ s. Given the conditions and previous results on single MT force generation, we attribute this event to the growth of a single MT. At $t \sim 155$ s, a new MT starts to grow. In this case no catastrophe is observed before $t \sim 295$ s and forces up to 20 ± 5 pN are reached. This force is significantly higher than the force generated by a single MT, and we thus attribute this event to multiple MTs growing together in a bundle. If we assume that MTs can add up their forces linearly, there must be around 7 MTs growing together in the bundle, close to the maximum number of nucleation sites on the axoneme. Interestingly, the MT bundle switches to an apparent shrinking state at $t \sim 295$ s, an event that is reminiscent of catastrophe events that are normally observed for single MTs. Measurements were stopped when all tubulin had flown through the experimental chamber. In some cases (lower trace in figure 3.2A), the measurement was stopped because the construct got stuck to the barrier (due to a non-specific interaction). We detected this by translating the barrier away from the trap after the force had reached an apparent static plateau.

Figure 3.2B shows a histogram of the data collected from nine force traces taken under as much as possible similar experimental conditions, representing a total measurement time of approximately 3300 seconds. This included three traces where

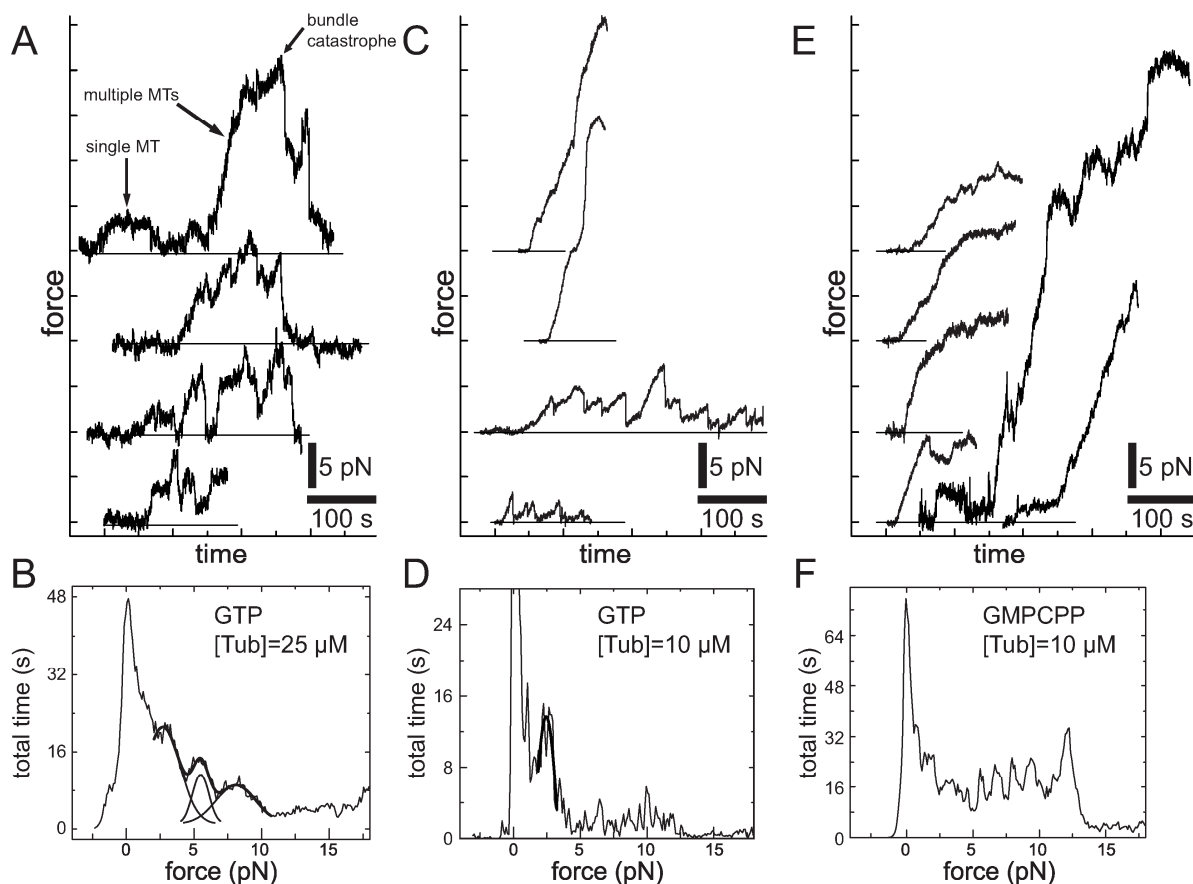


Figure 3.2

Force generation by growing MT bundles in the presence of GTP and GMPCPP. (A) Force traces as a function of time for a tubulin concentration of 25 μM in the presence of GTP. For clarity, the three upper curves were shifted upward by 10 pN, 20 pN, and 30 pN respectively. Horizontal lines indicate the zero-force level in each case. Arrows in the upper trace indicate growth of a single MT, followed by the growth of a bundle consisting of multiple MTs. (B) Histogram of measured forces for nine traces obtained under similar conditions. The three lower curves from A were used, as well as six extra curves not shown here. A 0.1 pN force binning was used. In addition to the peak at zero-force, three almost equally-spaced peaks are observed at higher forces. The center positions of these peaks were estimated by simultaneously fitting the sum of three Gaussian distributions to the histogram between 2 and 11 pN. The Gaussian distributions, as well as their sum, are superimposed onto the histogram. (C) Similar to A for a tubulin concentration of 10 μM . (D) Histogram of forces obtained from 4 traces shown in C. A Gaussian distribution was fitted to the histogram between 1.4 and 3.2 pN, in order to estimate the (single) peak position centered around 2.4 pN. (E) Similar to C in the presence of GMPCPP. (F) Histogram of forces obtained from 12 traces such as shown in E. No clear $\sim 3\text{pN}$ -spaced peaks can be observed in this histogram (see Fig. 3.3).

the force reached up to ~ 40 pN, which we attribute to the presence of probably two bundled axonemes, which together can nucleate more than 11 MTs. The histogram shows the total amount of time the bundles spent at a given force. As expected, the histogram has a first peak at zero force, which simply represents the non-growing bundle undergoing thermal fluctuations around a zero-force average. In addition, the histogram shows three other peaks, whose center locations were determined by a simultaneous fit of three Gaussian distributions on a restricted force range (2 pN to 11 pN). The three peak positions, at 2.7 pN, 5.5 pN, and 8.1 pN, respectively, are approximate multiples of 2.7 pN. The 2.7 pN value can be compared to the maximum force developed during the single-MT event in the upper trace in figure 3.2A. As the peak locations observed in the histogram in figure 3.2B correspond to multiples of the maximum force developed by a single MT, we attribute these peaks to the maximum force generated by a bundle made of one, two or three MTs, respectively. One expects that close to its maximum reachable force, a bundle grows slower or stalls, thus increasing the amount of time it spends at that force. For forces higher than 10 pN, no clear peaks are distinguishable anymore in the histogram. This is likely the result of the reduced statistics at higher forces (high forces are reached less frequently, due to bundle catastrophes, see also figure 3.3A), as well as the presence of experimental error, which broadens the force distribution. The main experimental error comes from

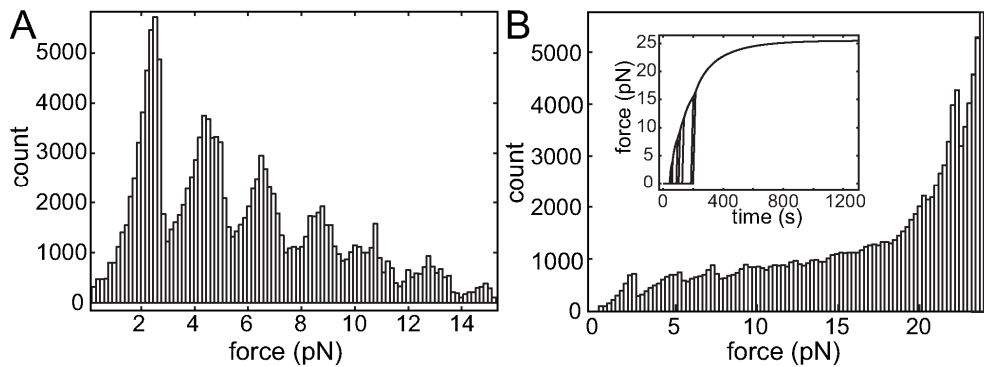


Figure 3.3

(A) Histogram obtained by adding simulated force traces generated by a GTP bundle for a relatively high catastrophe rate (10 times higher than for the simulation in Figure 3.4). The histogram shows clearly equally spaced peaks, similar to the experimental histogram in Figure 3.2A. (B) Histogram obtained by adding simulated force traces generated by a GMPCPP-MT bundle, corresponding to a zero catastrophe rate. Because the nucleation is high enough and there are no catastrophes, individual stalling events are observed much less frequently, which results in less obvious peaks in the histogram. *Inset*: Example of such a force vs time trace, showing no catastrophe and only stalling at the maximal force.

the fact that the trap stiffness has to be determined for each individual experiment, introducing an error up to ~20% between forces measured in different experiments (due to variable bead sizes). One therefore expects that at high forces the absolute error becomes comparable to the spacing between peaks.

Even though the number of experiments we combined in a single force histogram was limited to nine, both the observed histogram peaks and the maximum forces reached in individual cases are clearly consistent with a linear addition of single-MT maximum forces: a bundle made of N MTs appears to generate a maximum force N times higher than the single-MT maximum force. As a consequence, when a MT bundle reaches its maximum force, each MT in contact with the barrier feels a force that is equal to its own maximum (stall) force. The observation that a bundle can still experience an apparent catastrophe must mean that there is a finite chance that all MTs in the bundle switch within a small amount of time to a shrinking state. We propose that this is due to the fact that the catastrophe rate of individual MTs is highly force dependent [72]. When one of the MTs has a catastrophe, the force on the others increases which means the probability to also experience a catastrophe is expected to increase. This leads to what could be considered a force induced coupling of the dynamic instability of single MTs.

One would expect that the probability for the bundle to experience a catastrophe is not only affected by force, but also by the rate at which individual MTs experience a catastrophe in the absence of force. Since this rate is sensitive to the growth rate of MTs, and therefore the tubulin concentration [72], we repeated the bundle experiment in the presence of a lower concentration of tubulin (Fig. 3.2CD). We found that in this case catastrophes often occurred before high forces could be reached. Although in individual cases we still observed forces generated by multiple MTs (Fig. 3.2C), a histogram of the force data only revealed a clear peak corresponding to single-MT events (Fig. 3.2D). When, at the same low tubulin concentration, we inhibited catastrophes by adding GMPCPP instead of GTP[31], bundle catastrophe no longer occurred and forces corresponding to multiple MTs were again observed (Fig. 3.2EF). Note that in this case one would expect to observe maximum forces corresponding to the stall force of 9-11 MTs (the number of nucleation sites). In individual cases we indeed observed large forces. However, we had to terminate most of our measurements before this situation was reached, again because the construct got stuck to the barrier. Note also that in the GMPCPP case clear peaks due to stalling of individual MTs can only be expected if nucleation of subsequent MTs is slow. Instead, we observe a rather continuous, slightly increasing distribution of forces which is expected as a bundle of near-simultaneously nucleated

MTs slows down at increasing force (see Fig. 3.3B). This absence of clear peaks unfortunately prevents us from addressing whether the stall force of single MTs is influenced by GTP-hydrolysis.

3.3 Simulations on microtubule bundle dynamics.

To test whether the mechanism described above provides a plausible scenario for bundle catastrophes, we performed simple computer simulations of bundle dynamics that included previously measured effects of force on the dynamics of individual MTs [72, 149] (Fig. 3.4A; see Materials and Methods). The nucleation of new MTs from axonemes and the catastrophes of individual growing MTs were modeled as stochastic processes with Poissonian distributions. The growth itself was treated as a deterministic and continuous process. We simulated the experimental conditions by applying a linearly increasing force to the growing bundle to represent the spring-like character of the trap. We assumed that the force only acted on the MTs that were in contact with the barrier; the force that was exerted upon each MT was taken as the total force divided by the number of force sharing MTs in contact with the barrier [157]. In the simulation we tracked the length of the bundle as well as the individual MTs in the bundle (Fig. 3.4B), allowing us to study the effect of single MT behavior on the dynamics of the whole bundle. To compare the simulations and experiments we plotted the force generated by the bundle, which is linearly proportional to the length of the longest MTs in the bundle. In figure 3.4B the simulated dynamics of a MT bundle can be seen, while in figure 3.4C we zoom in on a specific event in order to visualize details in the growth curve that can be compared with experimental results (Fig. 3.4D). The MT bundle as a whole shows a force dependent growth velocity that depends on the number of MTs that are in contact with the barrier. Newly nucleated MTs grow faster than the MTs under force, and quickly reach the barrier. When a newly nucleated MT reaches the barrier, the bundle starts to grow faster (large black arrows in figure 3.4CD), whereas an individual MT catastrophe slows the bundle down (white arrows). The opposing force couples the dynamics of the MTs in the bundle. This cooperative behavior is most obvious just before the bundle as a whole undergoes a catastrophe. In figure 3.4C, the bundle has grown quite persistently until the first MT in the bundle has a catastrophe at ~280 sec. As a result, the force on the other MTs increases, their velocity goes down (and even becomes negative), and their probability to also have a catastrophe increases. Every new catastrophe in the bundle

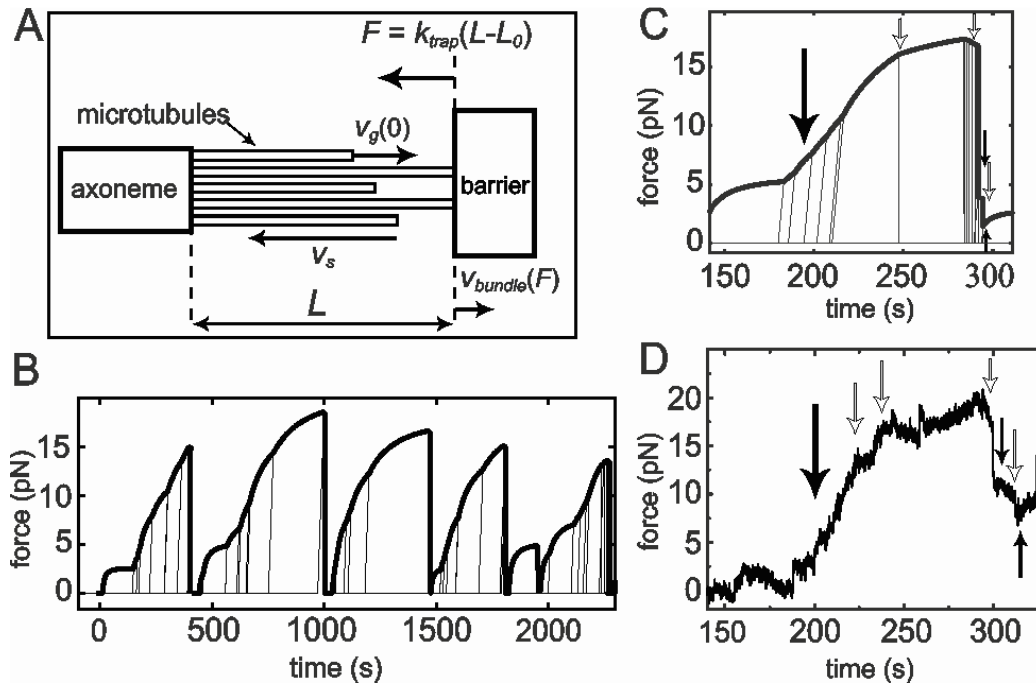


Figure 3.4

Simulations of MT bundle dynamics under force. (A) Schematic picture showing the geometry and some of the parameters used in the simulations. MTs grow from nucleation sites provided by an axoneme. Before they reach the barrier, their zero-force growth velocity is $v_g(0)$. When N MTs are in contact with the wall, each single MT is submitted to a force F/N , where F is the total force exerted on the MT bundle. F is proportional to the increase in bundle length $L-L_0$ and to the trap stiffness k_{trap} . After a MT undergoes a catastrophe, it shrinks with a velocity v_s . The bundle has a growth velocity $v_{bundle}(F)$. (B) Force trace generated by the simulations. The thick line represents the force generated by the bundle, which is proportional to the length of the longest MTs in the bundle. The thin lines show the dynamics of individual MTs that are not (yet) in contact with the barrier. Oblique thin lines represent growing MTs while vertical lines represent shrinking MTs. (C) Selected event from a simulated force trace. Arrows represent events to be compared with experimental data in D (see text). (D) Experimental force trace (same data as the top curve in Fig. 3.2A). Arrows represent events to be compared with the simulated growth event in C.

increases this probability even further, and a single catastrophe in the bundle can thus induce a cascade of catastrophes, resulting in a catastrophe of the entire bundle.

Qualitatively, this behavior is quite insensitive to the exact choice of parameters. For example, more MTs lead to higher forces and longer bundle catastrophe times. An increased individual catastrophe rate, or higher sensitivity of the catastrophe rate to

force, leads to shorter bundle catastrophe times. However, high forces and catastrophes of the entire bundle are always observed. Note that apparent rescues of the bundle are also observed. This is however not due to rescues of individual MTs, but the result of newly nucleated growing MTs catching up with a shrinking bundle at low force (small black arrows). Although in figure 3.4D we compare an experimental trace with a simulated trace (Fig. 3.4C) that was selected for its specific similarity to the experimental data, the simulated trace is quite representative of other simulated growth events, as can be seen by comparing figures 3.4B and 3.4C. The similarity between the experimental and simulation results suggests that the experimentally observed dynamic instability of MT bundles can indeed be explained as a force induced coupling of the dynamic instability behavior of single MTs.

3.4 Discussion

The combined results of our experiments and simulations show that the maximum forces MTs can generate linearly add up when growing in a parallel bundle. Sharing the force allows the MTs to show cooperative dynamic behavior in the form of bundle catastrophes. In practice, the maximum forces that are generated are a function not only of the number of MTs that can be nucleated, but also of the probability that individual MTs undergo catastrophes. One might argue that it is not very surprising that multiple biopolymers that grow together in a parallel bundle can share a force. In fact, for multiple protofilaments growing in parallel within a single MT, something similar has been predicted and observed [90, 157]. The difference however is that MTs in a bundle are only connected at their base and not crosslinked to each other in any other way. Therefore they have no direct way of influencing each others growth dynamics. A priori, it is therefore difficult to predict what level of cooperativity to expect. In the case of a parallel growing actin bundle we have in fact found evidence that the generated force is limited to the force generated by a single filament [158]. In that case the force seems to be carried by always the single longest filament whereas the identity of this filament constantly changes due to depolymerization events. The exact details of this apparently different behavior remain to be understood.

The measurements and simulations we presented so far were all on MT bundles growing against a spring-like force. However, the simulation also allowed us to study the dynamics of a MT bundle growing against a constant force. We found that if a constant small force was applied, the bundle as a whole experienced alternating collective catastrophes and apparent rescues resulting in oscillations around a constant

length (Fig. 3.5A). Interestingly, during chromosome positioning in mitosis, chromosomes also exhibit oscillatory motions, as measured for example by Skibbens *et al.* [153]. During mitosis, chromosomes first become mono-oriented (one of the two sister kinetochores associates with MT ends), then become bi-oriented (both sister kinetochores associate with MT ends), and eventually congress to the equator. In their paper Skibbens *et al.* show that chromosome oscillations observed during the mono- and bi-oriented phase are not sinusoidal but appear as a saw tooth pattern consisting of abrupt switches between constant opposite velocities. We could reproduce bundle oscillations that were reminiscent of the specific mono-oriented oscillations described by Skibbens *et al.* by making only a few changes to our simulations (see section 3.5 Materials and Methods for details). We set both v_s and $v_g(0)$ to the same value, since growth and shrinkage velocities are similar in magnitude *in vivo*. We increased the number of nucleation sites and the catastrophe rate, and assumed a constant small force applied on the bundle by the barrier. We found that the occurrence of oscillatory behavior is not very sensitive to the exact choice of the input parameters, as long as the force is small compared to the stall force of the MT bundle. For example, more MTs in

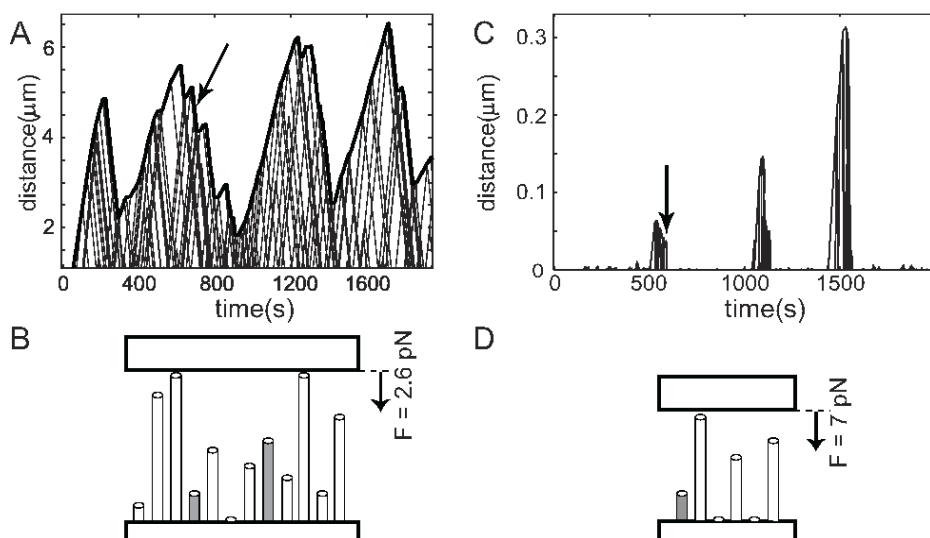


Figure 3.5

MT bundle oscillations. (A) Simulations of bundle growth under a small constant force reveal length oscillations that are reminiscent of chromosome oscillations observed by Skibbens *et al.* (14). See text and section 3.4.5 for a description of the simulation parameters used. Arrow indicates the time point corresponding to the sketch in B. (B) Situation sketch of the MT bundle shortly before an apparent rescue of a shrinking MT bundle. Grey tubes indicate growing MTs, white tubes indicate shrinking MTs. (C) Similar to A for a larger force and lower number of MTs (see section 3.4.5). In this case only short bursts of bundle growth are observed. (D) Situation sketch, similar to B, corresponding to the arrow in C.

the bundle lead to a longer average length around which the bundle oscillates and at a low catastrophe rate the bundle switches on average less frequently. The oscillations, however, remain. Only when either the number of MTs is too small and/or the force is too high, oscillations are no longer observed and short bursts of growth, similar to what we measure in our trap experiments, remain (Fig. 3.3CD).

In recent models describing chromosome oscillations, MT polymerization forces are considered to be negligible [129, 130, 159-161]. Our findings suggest that the cooperative polymerization dynamics of MT bundles may instead be worth considering as mechanism contributing to this phenomenon. Interestingly, Vandenbeldt *et al.* [162] studied kinetochore MT bundles and found that almost all bundles examined had a mixture of kinetochore MTs in the polymerizing and depolymerizing states. In our simulations the individual MTs in the bundle are also very dynamic although as a whole the bundle shows cooperative behavior (see Fig. 3.5AB). It is important to stress that the effects we describe may be relevant for both MTs in contact with the kinetochore and MTs pushing against the chromosome arms. It is also important to stress that in reality chromosome oscillations are undoubtedly the result of a more complex mechanism than is described here. For example, even mono-oriented kinetochores are often under tension [163] indicating that MTs generate pulling forces on the kinetochore at least some fraction of the time. Also, there is clear evidence that chromosome oscillations depend on the action of chromokinesins such as Kid [164]. Both effects are not considered here.

In summary, we have shown using a combination of experiments and simulations that MT bundles *in vitro* can reach forces much higher than the stall force of individual MTs, and can undergo force induced catastrophes of the complete bundle. We propose that MT bundles can reach these high forces by sharing the force, and that this sharing introduces coupling of their dynamic instability behavior. Additional results obtained using our simulations suggest that this mechanism may contribute to chromosome oscillations observed *in vivo*. In the future, it would be very interesting to perform similar experiments under more physiological conditions, for example in the presence of the MT crosslinker Xnf7 [165], which is believed to be involved in crosslinking kinetochore bundles during mitosis.

3.5 Materials and Methods

3.5.1 Materials.

Axonemes (a generous gift from Matt Footer) were purified from sea urchins according to [154] and stored following a method from Ref. [145], except that no glycerol was used. Their nucleating properties were characterized using Video-Enhanced Differential Interference Contrast (VE-DIC) microscopy (see section 3.5.2). Tubulin was purchased lyophilized from Cytoskeleton (Denver) and resuspended in MRB80 (80 mM K-Pipes, 4 mM MgCl₂, 1 mM EGTA, pH = 6.8).

3.5.2 Axoneme characterization using VE-DIC microscopy.

Coverslips and microscope slides were cleaned in chromosulphuric acid. A 20 µl-flow cell was constructed by drawing two parallel lines of vacuum grease approximately 5 mm apart on a clean microscope slide, and mounting a clean coverslip on top. A solution of axonemes in MRB80 (80 mM K-Pipes, 4 mM MgCl₂, 1 mM EGTA, pH = 6.8) was flown in and incubated for 5 minutes in order to let axonemes adhere to the glass surfaces. The concentration of the axonemes was tuned such that after preparation of the sample approximately 5 axonemes could be seen in a field of view of the microscope (35x25 µm²). Axonemes that did not stick to the surface were washed out by washing with two flow cell volumes of MRB80. The flow cell was blocked with 5 mg/ml BSA in MRB80 for 5 minutes. Afterwards the tubulin mix (10-25 µM tubulin, 5 mg/ml BSA, 1 mM GTP in MRB80) was introduced and the sample was sealed.

Samples were observed on an inverted microscope (DMIRB, Leica Microsystems, Rijswijk, The Netherlands) with a 100x 1.3 NA oil immersion objective by VE-DIC microscopy. The temperature in the sample was adjustable by a sleeve around the objective lens, which was controlled by thermoelectric coolers (Melcor). Images were recorded by a CCD camera (CF8/1, Kappa) and sent to an image processor (Argus 20, Hamamatsu). The resulting image stream was both recorded on a DVD and digitized online at a rate of 1 frame every 2 s. The number of MTs per axoneme was visually counted. The end of the axoneme with the most and longest MTs was considered the plus-end. For a few conditions this was confirmed with kinesin-coated beads that walk on the axoneme to the plus-end. Per condition at least 20 axonemes were counted.

3.5.3 Optical tweezers experiments

The optical tweezers set-up was as described in section 2.3.3.1. Barriers were fabricated according to section 2.1.5. The assay was performed as in section 2.3.3.2. We set the temperature in the experiments at 28°C.

3.5.4 Simulations.

Using MatLab, we simulated the dynamics of a parallel bundle of MTs nucleated by a surface with a fixed number of nucleation sites, growing against a barrier to which a load F was applied (Fig. 3.4A). MT growth and shrinkage were treated as deterministic processes with well-defined velocities, whereas nucleation and catastrophe events of individual MTs were treated as random processes. The parameters in the simulation were the nucleation rate of individual MTs, their average catastrophe time (T_c), and their growth (v_g) and shrinkage (v_s) velocities. The length L and growth velocity v_{bundle} of the bundle were defined as the length and velocity of the longest MT(s) in the bundle. The force exerted on the growing MT bundle was assumed to increase linearly with $L-L_0$ (L_0 being the bundle length upon first contact with the barrier) with a factor k_{trap} (the stiffness of the trap in our experiments), and assumed to be distributed evenly over all MTs in the bundle that are in contact with the barrier.

3.5.5 Simulations: force dependence and choice of parameters.

For simulations corresponding to our experiments, the number of nucleation sites was chosen to be 9. The nucleation rate was estimated from the experimentally observed number of MTs per axoneme using DIC microscopy. It was assumed that in the experiments steady state was not reached yet, since most experiments were done in the first 5-10 minutes. The nucleation rate ($4 \cdot 10^{-3} \text{ s}^{-1}$) was chosen so that the number of MTs was the same in experiments and simulation after 5-10 minutes. v_g in the absence of force was taken from experiments on freely growing MTs under the same conditions ($2.5 \text{ } \mu\text{m}/\text{min}$). Shrinkage is much faster than growth *in vitro*, so v_s was taken as infinite. We assumed for practical purposes that a force f encountered by an individual MT changed its growth velocity in the following way: $v_g(f) = C_1 \exp(-C_2 f) - C_3$ [149]. The constants were estimated from $v_g(0)$ and the

apparent stall force for one MT in our experiments (2.7 pN), and by taking C_2 from previous measurements (1.2 pN^{-1}) [149]. Note that Brownian ratchet-type theoretical models in fact predict slightly different functional forms for this force velocity curve [95, 157]. We assumed that the individual catastrophe time increases linearly with v_g with a small offset for $v_g=0$ as previously measured [72]. For growth velocities smaller than zero, which can occur when the force encountered by a growing MT suddenly rises above the stall force, T_c was chosen to scale with $1/v_g$. For simulations of bundle oscillations we modified the following parameters: 1) We assumed 15 nucleation sites, because the number of MTs at the kinetochore varies from 10 to 45 [151]. 2) We set both v_s and $v_g(0)$ to the same value ($2.0 \text{ }\mu\text{m}/\text{min}$), since growth and shrinkage velocities are similar in magnitude *in vivo*. Shrinkage was assumed to be force independent. 3) We increased the catastrophe rate by a factor of twelve, because *in vivo* MTs are more dynamic [17]. 4) We used a constant small force of 2.6 pN and then varied the nucleation rate until we could near-quantitatively reproduce the oscillatory behavior observed for chromosome oscillations (Fig. 3.5A). For figure 3.5C a smaller number of MTs (6) and a higher force (7 pN) were used.

3.6 Acknowledgements.

I would like to thank Julien Husson for performing the experiments together with me, E. Laura Munteanu and Jacob Kerssemakers for developing and maintaining the set-up, and Matt Footer (Theriot lab, Stanford, US) for isolation of the axonemes.

Chapter IV:

‘Cortical’ dynein regulates and pulls on dynamic microtubule ends *in vitro*.

*Pulling forces generated at the cellular cortex are important for the positioning of various intracellular organelles. These forces are believed to be due to the interaction between dynamic microtubules and cytoplasmic dynein, but the mechanism remains unclear. In this study, we have reconstituted the end-on attachment of dynein to dynamic microtubule ends in an *in vitro* system by attaching dynein molecules to a microfabricated barrier. We show that ‘cortical’ dynein, in the absence of any other factors, can capture microtubule ends, regulate their dynamics, and generate pulling forces up to several pN at shrinking microtubule ends, consistent with observations in living cells. Our results show that the functional behavior of cortical dynein critically depends on its mechanical attachment to a microtubule growth-opposing barrier.*

4.1 Introduction

Microtubules (MTs) are highly dynamic protein polymers that play essential roles in cellular organization [17]. Typically, MTs grow from a nucleating center near the middle of the cell towards the cell periphery, where they may interact with the cortex and generate pushing and/or pulling forces needed to position different organelles in the cell [6, 8, 166]. In situations where pulling forces are created, cytoplasmic dynein, a minus-end directed processive motor protein, has been implicated in forming the connection between the cell cortex and the MT cytoskeleton [7-11, 13, 14, 16, 17, 166, 167]. These apparent MT-dynein interactions sometimes involve sideways contacts between MTs and the cortex, as observed in dividing *Saccharomyces cerevisiae* cells, where motion of the nucleus into the bud neck is mediated by MTs gliding along the cortex in a dynein-dependent manner [7, 8]. In addition, there is increasing evidence that dynein can attach end-on to dynamic (shrinking) MT ends and that this complex can generate a pulling force. For example, the motion of the nucleus in *S. cerevisiae* during the very early and late stages of cell division appears to depend on end-on ‘capture and pull’ events (Fig. 4.1A) [7, 168]. End-on attachment of dynein to MTs at the cortex also produces nuclear motions during meiotic prophase in *Schizosaccharomyces pombe* (Fig. 4.1B)[8, 9], and the asymmetric positioning of the mitotic spindle during the first cell stage in *Caenorhabditis elegans* embryos (Fig. 4.1C, detail 1) [10, 11]. In addition, at kinetochores, cytoplasmic dynein has been suggested to interact end-on with MT ends to help regulate the poleward movement of chromosomes during mitosis (Fig. 4.1C, detail 2) [13-16]. For all these examples, it is unknown how dynein interacts with dynamic MT ends, and whether the activity of dynein is responsible for the regulation of MT dynamics [7, 9, 168] and the generation of pulling forces.

4.2 Fluorescence microscopy experiments

We sought to reconstitute the end-on attachment of dynein to dynamic MT ends in an *in vitro* system. In our assays, dynamic MTs grow against a microfabricated barrier, coated with a truncated dynein obtained from *S. cerevisiae* (GST-Dyn331, referred to herein as dynein [169]) that was purified and biotinylated. Recent experiments have shown that this truncated dynein exhibits processive minus-end-directed motility and stalls at a force (4.8 ± 1.0 pN) similar to full length dynein [169, 170]. In our first experiment, fluorescently-labeled MTs grew from a surface-attached centrosome

'Cortical' dynein regulates and pulls on dynamic microtubule ends in vitro

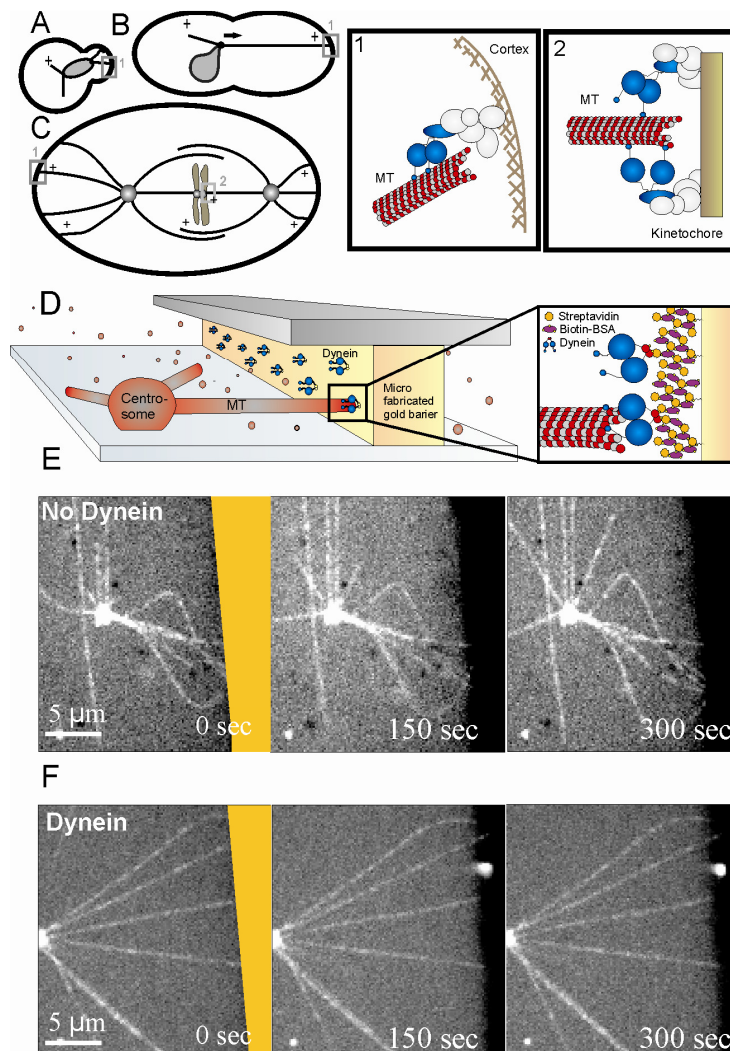


Figure 4.1

Cortical dynein captures dynamic MT ends, *in vivo* and *in vitro*. (A) In *Saccharomyces cerevisiae*, MTs interact with cortical dynein to move the nucleus into the budneck. In addition to sideways contacts, MT ends interact end-on with the cortex [7, 8] (detail 1). (B) During meiotic prophase in *Schizosaccharomyces pombe*, the nucleus migrates between the two cell poles due to interactions between cortical dynein and shrinking MT ends [9]. (C) In large mitotic spindles such as found in *C. elegans* embryos, MT ends interact with cortical dynein to contribute to (asymmetric) positioning of the spindle [10, 11]. In spindles, a similar end-on attachment between dynein and MT ends can be found at the kinetochore [13-16] (detail 2). (D) Schematic view of the interaction between dynamic MT ends and 'cortical' dynein *in vitro*. MTs grow from surface-attached centrosomes against a dynein-coated gold barrier. Dynein molecules are attached to the barrier via streptavidin and biotin-BSA (detail roughly drawn to scale). Imaging is performed from below, through the coverslip; therefore the MT end can be detected even when it contacts the barrier. (E, F) Time sequences of images of rhodamine labeled MTs growing from centrosomes against a barrier in the absence (E) and presence (F) of dynein. The position of the barrier is indicated in orange in the left images.

against a gold barrier (Fig. 4.1D).

By exploiting gold-specific-chemistry and good surface blocking, dynein can be attached specifically to the barrier through a biotin-streptavidin linkage [142]. Using spinning disk confocal microscopy, we followed individual MTs over time. In the absence of dynein at the barrier, most MTs continued to grow and buckled (Fig. 4.1E). Some MTs were observed to stall, but these rapidly underwent a catastrophe (a switch from growth to shrinkage; 4 events in 1110 sec) and lost contact with the barrier, as previously observed [88, 171]. In the presence of dynein, MTs stopped growing when their ends hit the barrier (Fig. 4.1F). In contrast to the situation without dynein, these MTs subsequently remained in a straight end-on conformation for long times before they were occasionally observed to shrink (4 events in 33320). MTs were never observed to make sideways contact with the dynein-coated barrier.

These experiments show that barrier-attached dynein stops MT growth and subsequently prevents MT shrinkage. However, they do not reveal whether dynein inhibits MT shrinkage by preventing catastrophes, or by preventing shrinkage itself. To test this, we performed a different experiment in which the bottom surface was coated with dynein molecules. In this case, growing MTs were pulled loose from the centrosome, and glided towards the barrier (Fig. 4.2). When these MTs hit the dynein-coated barrier, they quickly underwent a catastrophe, but the shrinking MT ends stayed in contact with the barrier. The subsequent shrinkage velocity was much slower ($3.4 \pm 0.9 \mu\text{m}/\text{min}$) than is normally the case for MTs in solution ($7.5 \pm 2.2 \mu\text{m}/\text{min}$) (Fig. 4.2, Table 4.1). The shrinkage velocity was also slower than the dynein gliding velocity ($7.8 \pm 2.1 \mu\text{m}/\text{min}$), which means that both MT shrinkage and dynein motion were slowed down by the dynein-MT connection. We thus conclude that barrier-attached dynein captures growing MT ends, induces catastrophes, and slows down or even stalls (Fig. 4.1F) subsequent shrinking of MTs.

To test whether dynein induces catastrophes by a putative depolymerizing activity, we also performed gliding experiments with MTs that were stabilized with GMPCPP, a slowly hydrolysable analogue of GTP. These stabilized MTs stopped moving along the bottom surface when they contacted the barrier, but shrinkage was never observed. An upper estimate for the shrinkage velocity is given by $0.2 \text{ nm}/\text{sec}$ (Fig. 4.3), which is much slower than the depolymerization velocity of $\sim 65 \text{ nm}/\text{sec}$ reported for the depolymerizing kinesin protein MCAK [54]. Thus, dynein can not effectively induce depolymerization of non-dynamic MTs stabilized with GMPCPP.

'Cortical' dynein regulates and pulls on dynamic microtubule ends in vitro


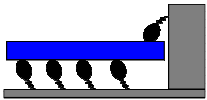
	Dynein (n)	Dynein AAA3E/Q (n)	
V_{gliding} [$\mu\text{m}/\text{min}$]	7.8 ± 2.1 (20)	0.22 ± 0.06 (16)	
	MT dynamics in the presence of dynein in solution		
	No Dynein (n)	Dynein (n)	Dynein AAA3E/Q (n)
V_{growth} [$\mu\text{m}/\text{min}$]	0.8 ± 0.3 (13)	0.8 ± 0.2 (12)	0.8 ± 0.3 (17)
V_{shrink} [$\mu\text{m}/\text{min}$]	8.1 ± 2.1 (12)	8.6 ± 3.5 (11)	8.1 ± 2.9 (14)
T_{cat} [sec]	900 ± 170 (29)	970 ± 160 (36)	910 ± 180 (27)
T_{res} [sec]	$T_{\text{res}} > 1100$ (0)	$T_{\text{res}} > 1530$ (0)	$T_{\text{res}} > 960$ (0)
	Dynamics of MTs (nucleated from a centrosome), gliding on a dynein-coated surface against a dynein-coated barrier		
	No Dynein, no barrier (n)	Dynein, no barrier (n)	Dynein, with barrier (n)
V_{growth} [$\mu\text{m}/\text{min}$]	1.3 ± 0.4 (38)	1.4 ± 0.6 (20)	
V_{shrink} [$\mu\text{m}/\text{min}$]	7.5 ± 2.2 (23)	7.7 ± 3.4 (16)	3.4 ± 0.9 (22)
T_{cat} [sec]	3100 ± 1000 (11)	2800 ± 750 (14)	
T_{res} [sec]	$T_{\text{res}} > 760$ (0)	90 ± 40 (8)	

Table 4.1

Dynein gliding speeds and dynamics of MTs interacting with dynein molecules. Dynein in solution does not affect MT dynamics. Even a dynein mutant that moves much slower than MTs shrink (dynein AAA3E/Q) has no effect on MT dynamics. MT dynamics are also not affected (apart from rescues) when MTs are gliding on a dynein-coated surface. Dynein that is attached to a growth-opposing barrier slows down MT shrinkage, similar as measured in the optical trap experiments (see Table 4.2).

The differences in MT growth and shrinkage velocities between the different assays are due to differences in tubulin concentration and temperature. Moreover the gliding experiments are done in the presence of methyl cellulose, which also affects MT dynamics (for details on the experimental conditions see Materials and Methods). The errors on the velocities are the weighted standard deviations. The error on the catastrophe or rescue time is the statistical error given by the catastrophe or rescue time divided by the square root of the number of observed events.

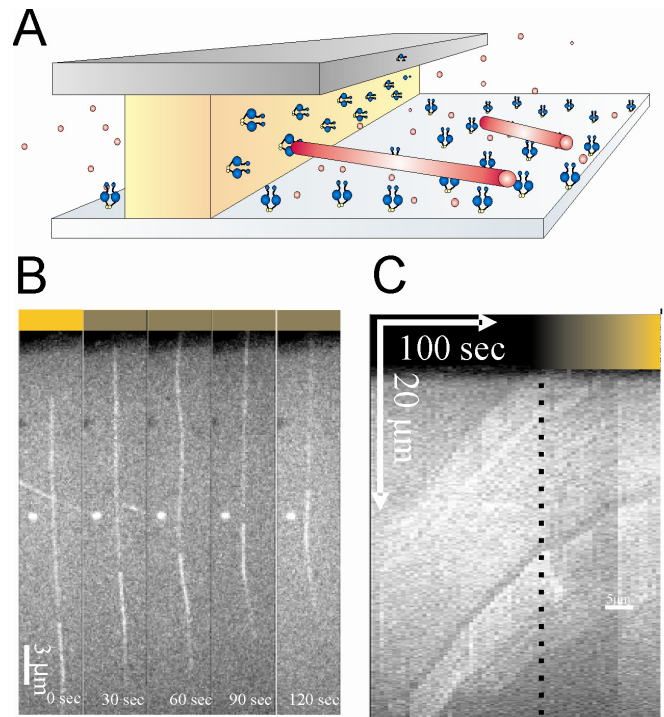


Figure 4.2

(A) Schematic view of the gliding experiment. Fluorescent dynamic MTs grow and glide on a dynein-coated surface against a dynein-coated gold barrier. (B) Time sequence of images of a MT gliding with its plus-end against the barrier. (C) Kymograph of the same MT. The speckles on the MT show that the growing MT first glides towards the barrier, then hits the barrier (dotted line) and buckles, rapidly undergoes a catastrophe, and then continues gliding at a lower speed while shrinking.

'Cortical' dynein regulates and pulls on dynamic microtubule ends in vitro

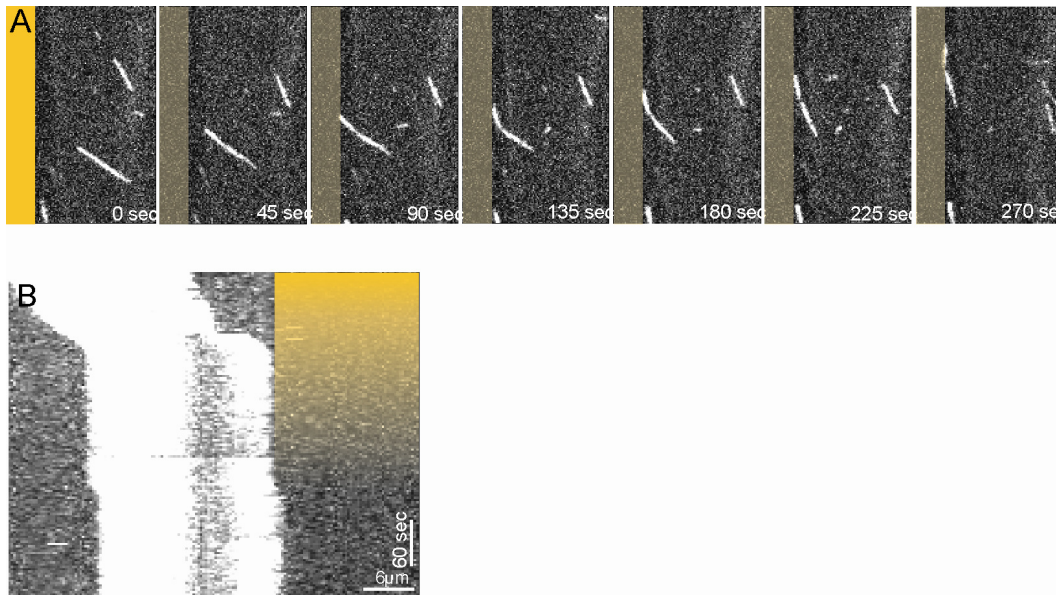
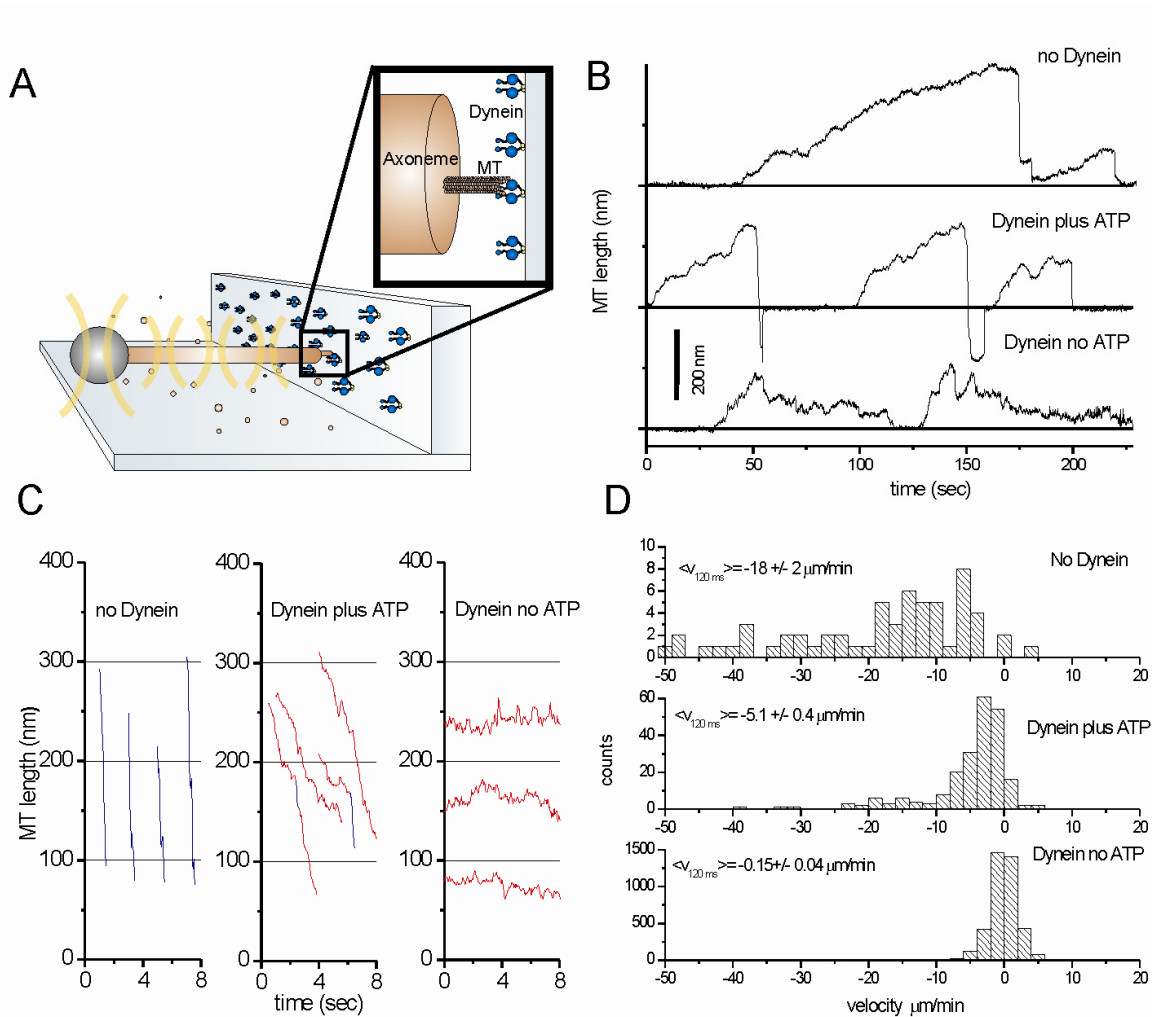


Figure 4.3

Barrier-attached dynein does not depolymerize GMPCPP MTs. (A) Time sequence of a GMPCPP-stabilized MT that glides on a dynein-coated surface against a dynein-coated barrier (Fig. 4.2). When the MT hits the barrier it buckles and eventually glides along the barrier (barrier is indicated in yellow). (B) Kymograph of a GMPCPP MT that glides against a barrier (barrier is indicated with faded yellow, to reveal the movement of the MT end). The first ~120 sec the MT glides towards the barrier. As soon as it hits the barrier it stops gliding but does not depolymerize. The movement of the MT after ~250 sec, we contribute to repositioning of the GMPCPP MT end on the barrier. All GMPCPP MTs we observed stopped moving against the barrier or started gliding along it. No depolymerization was observed.

**Figure 4.4**

‘Cortical’ dynein regulates MT dynamics. (A) Schematic view of the optical trap experiment. A bead-axoneme construct is held in a key-hole optical trap [5]. MTs grow from the axoneme against a dynein-coated barrier. Detail is roughly drawn to scale. (B) Optical trap data of growth and shrinkage of MTs against a bare barrier (upper trace), and against a dynein-coated barrier in the presence (middle trace) and absence (lower trace) of ATP (C) Shrinking events of the three different experiments. Fast shrinking events ($> 10 \mu\text{m}/\text{min}$; measured over 120 ms intervals) are indicated in blue, slow events ($< 10 \mu\text{m}/\text{min}$) in red. (D) Histograms of all shrinking velocities measured over 120 ms intervals (see also Table 4.2) (error in the average is the SE).

4.3 Optical trap experiments

We next used an optical trap to obtain more information about the contact between dynamic MT ends and dynein at the barrier, and to reveal whether pulling forces were generated. In this set-up, which was previously developed in our laboratory [5, 97], MTs grow from an axoneme-bead-construct, which is held in an optical trap and positioned in front of a barrier (Fig. 4.4A). When a growing MT reaches the barrier, the bead is pushed away from the barrier until the MT switches to a shrinking state (Fig. 4.5A). As the MT shrinks, the bead moves back to the center of the trap, after which contact between the shrinking MT and the barrier is lost. However, if dynein makes a physical attachment between the shrinking MT end and the barrier, a pulling force can be created that causes the bead to continue to move towards the barrier, beyond the center of the trap. Figure 4.4B shows typical sequences of MT growth and shrinkage events in the absence (top), and the presence of barrier-attached dynein,

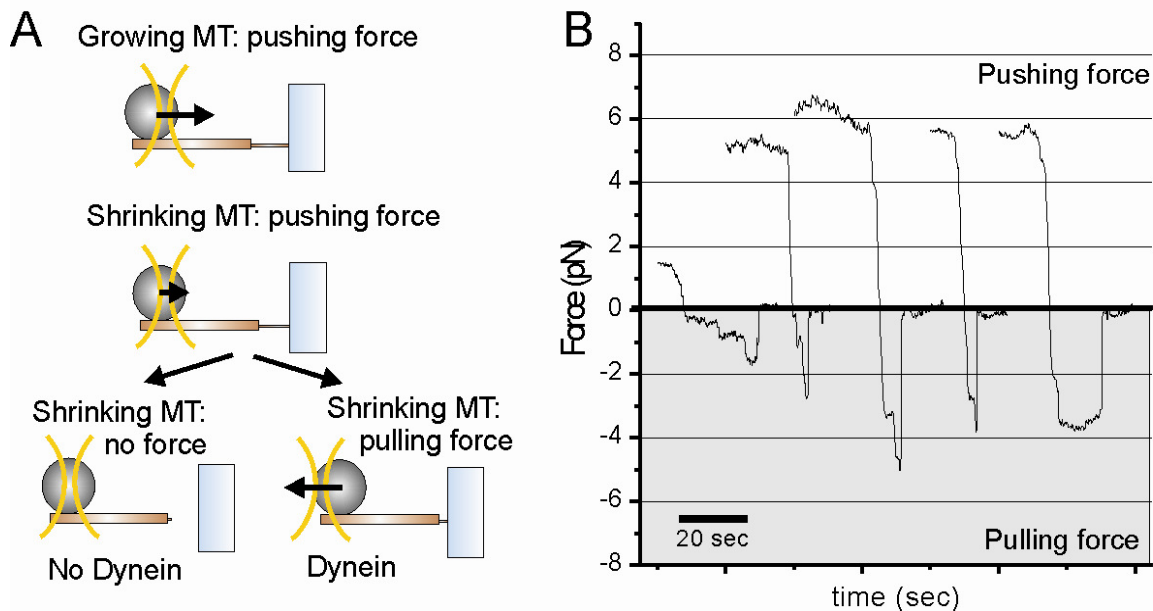


Figure 4.5

'Cortical' MT-dynein interactions generate pulling forces. (A) Cartoon that shows how MT growth and shrinkage without (left) and with (right) dynein at the barrier relate to bead movement in the trap and the generation of pushing/pulling forces. (B) Shrinking events where the dynein-MT interaction produces a pulling force (corresponding to negative forces, shaded in grey).

with and without the addition of ATP (middle and bottom). We again found that MTs shrink more slowly when pushed against a dynein-coated barrier ($5.1 \pm 0.4 \mu\text{m}/\text{min}$, SE) than against an uncoated barrier ($18 \pm 2 \mu\text{m}/\text{min}$, SE) (Fig. 4.4BCD). In the absence of ATP, which causes dynein to bind to MTs in a rigor state [170], the MT shrinkage was almost completely stalled ($0.15 \pm 0.04 \mu\text{m}/\text{min}$, SE).

The optical trap experiments confirm that barrier-attached dynein slows the MT shrinkage velocity. They also confirm that dynein increases the catastrophe frequency. even though catastrophes were observed both in the presence and absence of dynein due to compressive forces of the barrier on the MT end [171]. The average time that MTs spent growing before a catastrophe (the catastrophe time) against a dynein-coated barrier was $T_{\text{cat}} = 65 \pm 17 \text{ sec}$ (total time=974 sec, 6 exp). This was only slightly shorter than the time MTs spent growing against an uncoated barrier, $T_{\text{cat}} = 100 \pm 20 \text{ sec}$ (total time= 2708 sec, 4 exp). However, it is possible that this relatively modest difference is due to the fact that the time a MT needs to ‘find’ dynein molecules on the

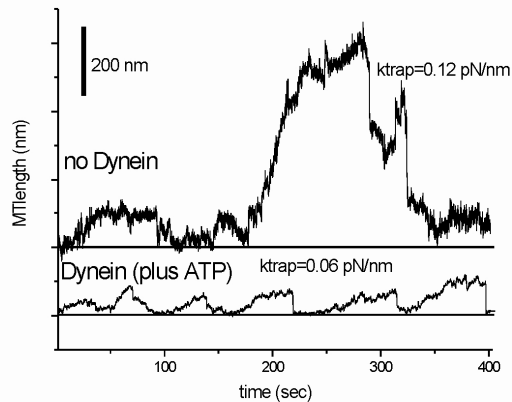


Figure 4.6

Dynein induces MT catastrophe if attached to a growth-opposing barrier. In this optical trap experiment MTs are grown at a higher tubulin concentration ($25 \mu\text{M}$) and at a higher temperature (29°C) than in Fig. 4.4. In this case multiple MTs are growing together in a parallel bundle. Because the multiple MTs share the applied force [2], they are expected to be more stable and undergo catastrophes less frequently. Without dynein on the barrier (top trace), the MTs grow indeed much longer before they (collectively) undergo a catastrophe, $\langle T_{\text{cat}} \rangle = 260 \pm 60 \text{ sec}$ (total time = 4748 sec, 8 exp). In the presence of dynein (bottom trace), the catastrophe time is still short, $\langle T_{\text{cat}} \rangle = 56 \pm 6 \text{ sec}$ (total time = 4854 sec, 3 exp) $k_{\text{trap}} = 0.06 \text{ pN}/\text{nm}$. This shows that dynein indeed induces catastrophes. Under these conditions we find again a reduced shrinkage velocity with dynein on the barrier, $v_{\text{shrink}} = 4.8 \pm 0.4 \text{ (SE)} \mu\text{m}/\text{min}$, compared to when there is no dynein present, $v_{\text{shrink}} = 15 \pm 0.7 \text{ (SE)} \mu\text{m}/\text{min}$.

barrier is similar to the catastrophe time against an uncoated barrier. In an attempt to separate these time scales, we increased the tubulin concentration and temperature in the experiment (Fig. 4.6). In this case, multiple MTs were growing in a parallel bundle, which resulted in very long (bundle) catastrophe times against an uncoated barrier, as individual MTs were influenced by the compressive force to a lesser extent ($T_{\text{cat}} = 260 \pm 60$ sec (total time = 4748 sec, 8 exp)) [2]. MTs growing against a dynein-coated barrier, however, still had a short catastrophe time ($T_{\text{cat}} = 56 \pm 6$ sec (total time = 4854 sec, 3 exp)). Thus, barrier-attached dynein clearly increases the MT catastrophe rate. individual MTs were influenced by the compressive force to a lesser extent ($T_{\text{cat}} = 260 \pm 60$ sec (total time = 4748 sec, 8 exp)) [2]. MTs growing against a dynein-coated barrier, however, still had a short catastrophe time ($T_{\text{cat}} = 56 \pm 6$ sec (total time = 4854 sec, 3 exp)). Thus, barrier-attached dynein clearly increases the MT catastrophe rate.

It is important to note that none of the effects on MT dynamics described so far were observed when dynein was present in solution instead of attached to a barrier (Table 4.1). Even a dynein mutant that moves much slower than the MT shrinks ($v_{\text{glide}} = 0.22 \pm 0.16$ $\mu\text{m}/\text{min}$) [172], had no effect on MT dynamics in solution (Fig. 4.7). Similarly, when dynamic MTs were gliding on a dynein-coated surface, no change in growth velocity, shrinkage velocity, or catastrophe time was observed. In this case, only the rescue frequency was increased (Table 4.1). This means that the effects on

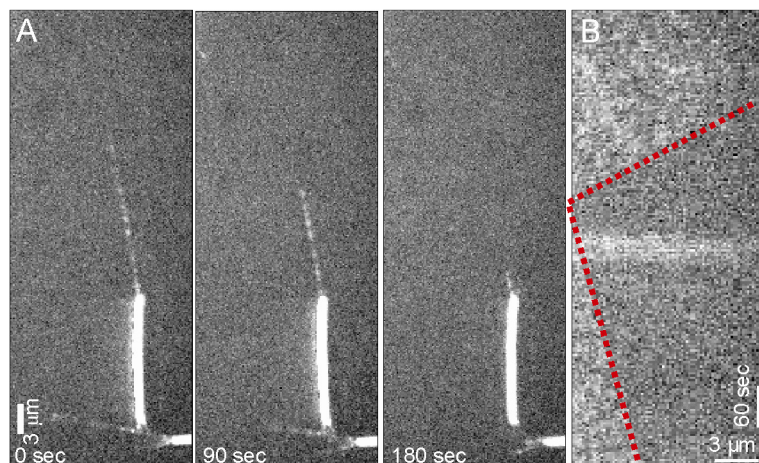


Figure 4.7

The slow moving dynein AAA3E/Q does not alter MT dynamics. We confirmed that dynein AAA3E/Q is present on the MT lattice using spinning disk confocal microscopy. (A) Time sequence of a shrinking MT, nucleated from an axoneme, decorated with dynein AAA3E/Q. (B) Kymograph of a growing and shrinking MT in the presence of dynein AAA3E/Q. The end of the MT is indicated with a red dotted line. No rescues or slow shrinkage are observed.

	Nr Exp	Nr Shrinkage events		V_{shrink} ($F > 0$) [$\mu\text{m}/\text{min}$]	F_{pull} , pN	V_{shrink} ($F < 0$) [$\mu\text{m}/\text{min}$]
		($F < 0$) MT-barrier connection lost	($F < 0$) MT-barrier connection persists			
No Dynein	4	21	0	18 ± 2	--	--
Dynein plus ATP	6	5	10	5.1 ± 0.4	2.0 ± 1.4	1.1 ± 0.33
Dynein no ATP	3	7	0	0.14 ± 0.04	--	--

Table 4.2

Dynamics of shrinking MTs in the optical trap experiment (Fig. 4.4). We analyzed the shrinkage events in which MT shrinkage allowed the bead to move all the way back to the zero-force position (excluding events where rescues occurred before). We counted the number of times the MT-barrier connection was lost after the zero-force position was reached and how many times the connection persisted, and thus a pulling force was generated. Only when dynein is present at the barrier and ATP is added, pulling forces are generated, with an average maximum force of 2 pN. As observed in the gliding experiments, barrier-attached dynein slows down MT shrinkage (especially when a pulling force is generated). In the absence of ATP, this effect is dramatically enhanced, and no pulling forces are detected. The error on the shrinkage velocity is de standard error. The error on the force is the standard deviation.

MT dynamics that we observe are critically dependent on the fact that dynein is mechanically attached to a growth-opposing barrier.

Finally, we exploited our optical tweezers set-up to determine whether the dynein-MT connection is able to generate a pulling force. Our experiments show that dynein can maintain the connection to a shrinking MT against pulling forces up to ~ 5 pN (with a mean force of 2.0 ± 1.4 pN; $n=10$) (Fig. 4.5B, Table 4.2). Note that in the presence of this pulling force, the MT shrinkage velocity is even slower than when the MT-dynein contact is under compression (Table 4.2, Fig. 4.8). In the absence of ATP, no detectable pulling forces are generated (Fig. 4.4B bottom), indicating that motor activity is needed for force generation (Table 4.2). It is possible, however, that motor

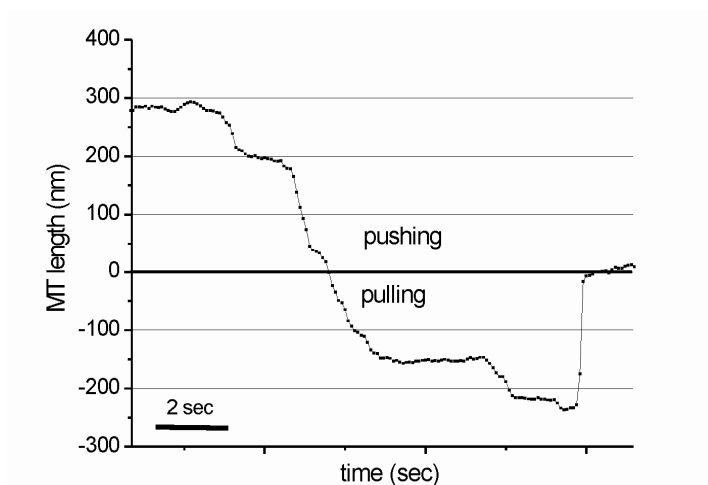


Figure 4.8

Detail of MT shrinkage in the presence of ATP against a dynein-coated barrier in our optical trap experiment. MT shrinkage against a pulling force is on average slower than against a pushing force (see also Table 4.2).

activity is only needed to maintain the dynamic connection between the barrier and the shrinking MT, as the work against the applied load (wholly or in part) may be performed by the depolymerizing MTs themselves [99] (Fig. 4.9).

4.4 Discussion

4.4.1 Stoichiometry of the microtubule-dynein interaction

We asked how many barrier-attached dynein molecules are needed to form a stable attachment and affect the dynamics of a MT end. Although we did not have the means to address this question directly, several observations suggest that the events that we observe may be due to only a few or even a single dynein-MT interaction. First, the maximum observed pulling forces of up to 5 pN never exceed the previously measured maximum forces for single dynein molecules [170] or shrinking MTs [99, 107]. If multiple dyneins were available to perform work, one might expect to (occasionally) observe higher forces. Of course, an alternative possibility is that in our set-up the connection between the MT and the motors breaks before higher forces can be reached. A second indication comes from a detailed analysis of the shrinkage events in our optical trap experiments (Fig. 4.4C). In the absence of dynein, only fast shrinkage events are observed. However, when attached to a dynein barrier, we observe periods of 'slow' ($< 10 \mu\text{m}/\text{min}$; indicated in red) and 'fast' ($> 10 \mu\text{m}/\text{min}$; indicated in blue) MT shrinkage, with occasional switches from slow to fast shrinkage (see also Fig.

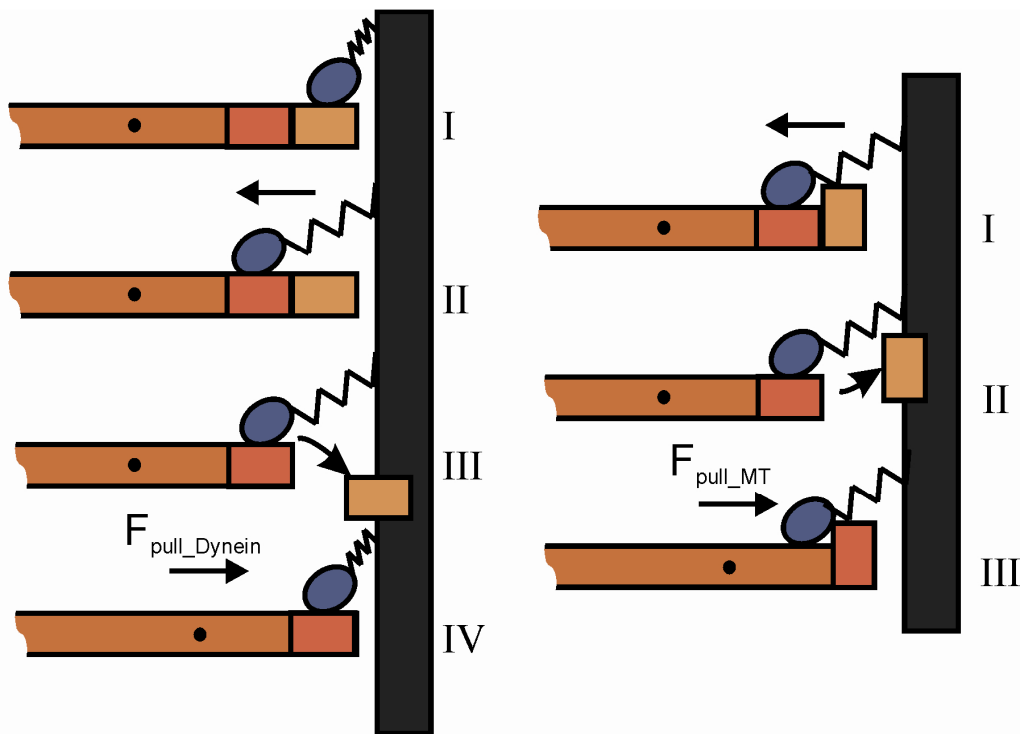


Figure 4.9

Cartoons that schematize the different ways the MT-dynein complex may generate a pulling force. See Fig. 4.11 in the main text for a general explanation of the coupling between dynein movement and MT shrinkage. A) In the first scenario, the power stroke of dynein generates the pulling force (state IV). The MT only needs to depolymerize such that dynein can move the MT end towards the barrier. B) In the second scenario, the outward curling of the protofilaments generates the pulling force (state III). Dynein needs to be able to move in response to the curling protofilaments but does not need to generate a force. In reality both mechanisms may contribute to the generation of force.

4.10). We postulate that such slow-to-fast switches reflect dynein detachment from the MT. This allows us to roughly estimate the off-rate of a dynein molecule from a shrinking MT end to be $0.10 \pm 0.07 \text{ sec}^{-1}$ (total time= 34.7 sec, 27 shrinkage events, 4 switches). This is of the same order of magnitude as the rate at which a single, processively moving dynein molecule dissociates from a MT, $0.04 \pm 0.07 \text{ sec}^{-1}$ [169]. Even though the experimental conditions are not directly comparable, one might expect a collection of dynein molecules to have a much lower effective off-rate. Together, these results suggest that it is likely that only a single dynein molecule is interacting with, and changing the dynamics of, a MT end.

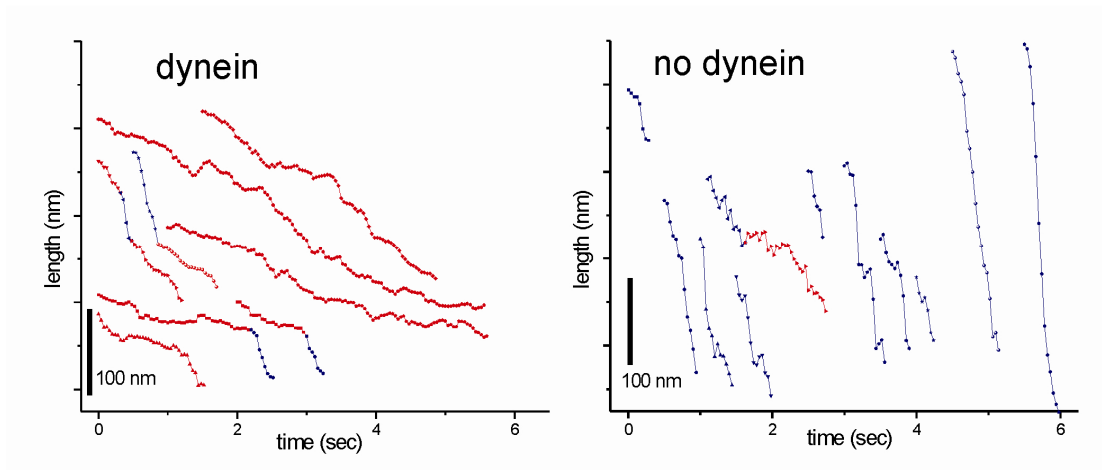


Figure 4.10

Shrinkage events in our optical trap experiment with dynein on the barrier (with ATP; left) and without dynein on the barrier (right). Shrinkage intervals with a velocity higher than 10 $\mu\text{m}/\text{min}$ (measured over 120 ms) are indicated in blue, shrinkage intervals with a velocity lower than 10 $\mu\text{m}/\text{min}$ are indicated in red. The data with dynein show clear switches in velocity

4.4.2 Mechanisms of the interaction between dynein and dynamic microtubule ends

Combining all our results, we propose that barrier-attached dynein and dynamic MT ends influence each other in the following way: growing MT ends that come into contact with dynein quickly switch to a shrinking state. This is not the result of a depolymerizing activity of dynein, but possibly the result of dynein pulling the growing MT end against the barrier. This would hinder further growth, which then triggers a catastrophe [171]. Dynein attached to what has now become a shrinking MT end cannot move at its preferred velocity (even in the absence of a pulling force), since motion has to be coordinated with MT shrinkage (Fig. 4.11). Without MT shrinkage, the MT end cannot move closer to the barrier, and as a result, dynein is unable to move towards the MT minus-end. MT shrinkage does not occur at the normal velocity, since it has to be coordinated with dynein stepping events: no shrinking can occur as long as dynein stays firmly attached to the MT end (we speculate that barrier-attached dynein inhibits shrinkage by mechanically preventing protofilaments from curling outwards,

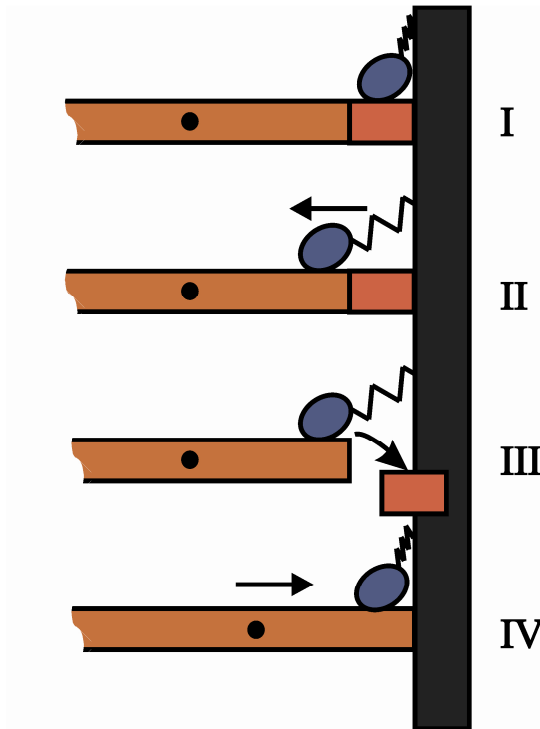


Figure 4.11

Cartoon of the coupling between MT shrinkage and dynein movement. I) Dynein is bound to the end of the MT and prevents shrinkage. The system is blocked in this state in the absence of ATP as the motor cannot move (see Fig. 4.4). II) Dynein has stepped away from the MT end. The system is blocked in this state for GMPCPP-stabilized MTs as the MT cannot shrink (see Fig. 4.3). III) The MT end shrinks. The system is blocked in this state if the MT cannot move towards the barrier (see Fig. 4.1). IV) MT end and dynein move together towards the barrier. This brings the system back to state I. This coupled MT shrinkage and dynein motion is able to generate a pulling force (see Fig. 4.9).

as has been proposed for the Dam1 complex [108]). This coupled motion of dynein and the shrinking MT is able to persist in the presence of a pulling force generated by the shrinking MT-dynein complex, albeit at a further reduced rate.

The fact that slow motion is still observed in the absence of ATP (Fig. 4.4), may be consistent with the observation that single dynein molecules, assisted by an external force, are able to move slowly in the absence of ATP [170]. Interestingly, when the MT itself is unable to move (Fig. 4.1F), dynein can apparently be locked in a configuration where it no longer can detach from the MT end (consistent with previous observations on stalled single dynein molecules [170]). This could also explain the

observation that dynein under tension can stabilize MT attachment at kinetochores [15]

4.4.2 *In vivo* relevance

Our results may explain several observations of how dynein affects dynamic MTs *in vivo*. In *S. cerevisiae*, MTs shrink at two times faster rates in mutants where dynein is not functional [168]. Similarly, during meiotic prophase in *S. pombe*, astral MTs shrink more than two times faster in dynein deletions compared to wild type cells [9]. Yamamoto et al. (11) propose that a MT-disassembling factor might be involved in this effect, but our study shows that dynein itself may be responsible for the regulation of MT dynamics. In both studies, the slower rates of MT shrinkage in wild type cells may result from the fact that a subset of MTs shrink slowly due to interaction with dynein at the cortex. In *C. elegans* embryos, MTs have also been shown to interact end-on with the cortex [138]. In this system, several theoretical models have been developed to describe how cortical force generators that interact with dynamic MTs position the mitotic spindle. Our results provide useful new input for these models, as their outcome depends on the details of the cortical force generator-MT interaction [11, 137, 138]. Finally, our results show that dynein, in addition to regulating MT dynamics and participating in the generation of pulling forces, can efficiently couple cargo to depolymerizing MTs. In this role, it may be important for connecting kinetochores to disassembling MTs during mitosis, as has been suggested for the DAM1 complex, and plus-end directed motors such as members of the kinesin-1 and kinesin-8 families [101, 102, 107].

4.5 Materials and Methods

Chemical reagents were obtained from Sigma, unless stated otherwise.

4.5.1 Biological Materials

The dynein constructs used in this study were the biotinylated GST-dynein331 construct (from now on referred to as dynein) as well as the GST-dynein331 E2488Q construct (from now referred to as dynein AAA3E/Q). They were both tested in a gliding assay using a simple flow cell. The gliding speeds found were 130 +/- 35 (29)

nm/sec for dynein, and 3.7 ± 2.7 ($n=16$) nm/sec for dynein AAA3E/Q, very similar to numbers described before [169, 172]. For dynein we also tested whether it binds in a rigor state to MTs when no ATP was present. To make sure that no residual ATP, coming from the dynein purification, was present, the sample was washed with several flow cell volumes of buffer after it was incubated with dynein. After these washes, MTs did bind to the surface of the chamber, but no MT gliding was observed. Axonemes (a generous gift from Matt Footer) were purified from sea urchins according to Ref. [154] and stored following a method from [145], except that no glycerol was used. Centrosomes were purified with generous help of Claude Celati from human lymphoblastic KE37 cell lines according to Ref. [173].

4.5.2. Assay on microtubule dynamics in the presence of freely floating dynein

Coverslips and microscope slides were cleaned in chromosulphuric acid. A 20 μ l-flow cell was constructed by drawing two parallel lines of vacuum grease approximately 5 mm apart on a clean microscope slide, and mounting a clean coverslip on top. A solution of axonemes in MRB80 (80 mM K-Pipes, 4 mM $MgCl_2$, 1 mM EGTA, pH = 6.8) was flown in and incubated for 5 minutes in order to let axonemes adhere to the glass surfaces. The concentration of the axonemes was tuned such that after preparation of the sample approximately 5 axonemes could be seen in a field of view of the microscope ($35 \times 25 \mu m^2$). Axonemes that did not stick to the surface were washed out by washing with two flow cell volumes of MRB80. The flow cell was subsequently blocked with 0.2 mg/ml PLL-PEG (SurfaceSolutions, Switzerland) in MRB80 for 5 minutes, rinsed with 10 flowcell volumes, blocked 1 mg/ml k-cas in MRB80 for 5 minutes and rinsed. Afterwards the tubulin mix (15 μ M tubulin (Cytoskeleton, Denver), 0.5 mg/ml κ -casein, 1 mM GTP, 1 mM ATP, and an oxygen scavenger system (20 mM glucose, 200 μ g/ml glucose oxidase, 400 μ g/ml catalase) in MRB80), optionally with 8 nM dynein or 8 nM dynein AAA3 E/Q, was introduced and the sample was sealed. Samples were observed on an inverted microscope (DMIRB, Leica Microsystems, Rijswijk, The Netherlands) with a 100x 1.3 NA oil immersion objective by Video-Enhanced Differential Interference Contrast (VE-DIC) microscopy. The temperature in the sample was adjusted by a sleeve around the objective lens, which was controlled by thermoelectric coolers (Melcor). Our experiments were done at 20°C. Images were recorded by a CCD camera (CF8/1, Kappa) and sent to an image processor (Argus 20, Hamamatsu). The resulting image stream was both recorded on a DVD and digitized online at a rate of 1 frame every 2 s. In the case of dynein AAA3 E/Q the samples were also examined using spinning disk

confocal microscopy (Fig. 4.7). Movies were made with a time lag of 3 seconds and 300 ms exposure, with 488 nm laser light on a Leica microscope with a 100x 1.3 NA oil immersion objective equipped with a spinning disk confocal head from Visitech (UK).

4.5.3 Data analysis assay of microtubule dynamics in the presence of freely floating dynein

For the analysis of MT dynamics, DIC data were collected from three independent experiments for every condition. The growth and shrinkage velocities (V_{growth} and V_{shrink}) were measured from manual fits to the growth/shrinkage parts of kymographs. The growth velocity was used to decide whether the MT studied was a plus-end or a minus-end. It is known that minus-ends grow much slower than plus-ends [25]. Only plus-ends were analyzed. The average velocity is the average over all events weighted with the time of the individual events. The error is the weighted standard deviation. The catastrophe time or rescue time (T_{cat} or T_{res}) was determined by dividing the total growth or shrinkage time by the total number of catastrophes or rescues observed. The error is the statistical error is given by the catastrophe or rescue time divided by the square root of the number of observed events.

4.5.4 Assay on microtubules growing from centrosomes against a dynein-coated barrier

Activated gold barriers (fabricated and activated as described in section 2.1.2 and 2.2) and were incorporated into a flow cell as in section 2.3.1. Biotintlated dynein was added as the biotinylated-protein at 8 nM. The specificity of dynein for the gold barriers was tested by adding stabilized MTs to this sample and checking for gliding. In between the barriers, no gliding of MTs was observed anymore under these conditions. The experiments were performed at 15 μM tubulin, 1 μM Rhodamine tubulin (Cytoskeleton, Denver)

4.5.5 Data analysis of microtubules growing from centrosomes against a dynein-coated barrier

We performed 5 experiments with dynein present and 3 without dynein at the barrier. The data of the experiments without dynein were also used to obtain the dynamic properties of MTs growing freely from centrosomes (no dynein, no barrier, see Table

1). The data were analyzed as described above for the assay on MT dynamics in the presence of dynein freely floating in solution. The catastrophe time of MTs in contact with the barrier was determined for MTs that stalled at the barrier (and remained straight) both in the presence and absence of dynein. The contact time at the barrier is defined as the total time that MTs spend at the barrier divided by the number of events in which the MT is observed to shrink away from the barrier. The error is the statistical error given by contact time divided by the square root of the number of observed events. For $n < 7$, only a lower bound is given.

4.5.6 Assay on dynamic microtubules gliding on a dynein surface against a dynein-coated barrier

This assay is very similar to the assay described in section 4.4.4, except that surface blocking was reduced, by not blocking with PLL-PEG and by reducing the κ -casein concentration in the different steps to 0.1 mg/ml. Reduced blocking allows non-specific binding of dynein to the surface. The presence of dynein was tested by adding stabilized MTs that were indeed observed to glide on the surface. Dynamic MTs were again nucleated by surface-attached centrosomes. However, at a certain MT length, the dynein on the surface pulled the MTs from the centrosome, which created freely gliding dynamic MTs. To create speckles on the MTs the rhodamine tubulin concentration was reduced to 0.5 μM . Otherwise, sample preparation and observation were as described for the previous experiment. We are certain that ends that interact with the barrier in this experiment are the plus-ends, because MTs glide with their plus-ends forward on a surface coated with minus-end directed motor proteins. In the case of GMPCPP MTs (Fig. 4.3), no tubulin was added, so the MTs did not grow. Otherwise the assay was the same.

4.5.7 Data analysis of dynamic microtubules gliding on a dynein surface against a dynein-coated barrier

MTs that were gliding against the barrier as well as MTs that were gliding freely were analyzed from 7 different experiments. For every MT the gliding velocity was determined by a manual fit to the movement of speckles on kymographs (Fig. 4.2). For every MT the elongation (growth plus gliding) velocity, or shortening (gliding plus shrinkage) velocity was determined using manual fits to a kymograph. The growth velocity and shrinkage velocity were determined by subtracting the gliding velocity from the elongation or shortening velocity. The average velocity is given by the

average over all events weighted with the time of the individual events. The error is given by the weighted standard deviation. The catastrophe time or rescue time (T_{cat} or T_{res}) was determined by dividing the total growth or shrinkage time by the total number of catastrophes or rescues observed. The error is the statistical error given by the catastrophe or rescue time divided by the square root of the number of observed events. For $n < 7$, only a lower bound is given. In the case of GMPCPP MTs, no MT shrinkage could be detected within the observation time (by analyzing the movement of speckled MTs). Therefore an upper estimate of the shrinkage velocity could be calculated by dividing the pixel size (110 nm) by the observation time (600 sec). This resulted in an upper estimate of the shrinkage velocity of 0.2 nm/sec.

4.5.8 Optical trap experiments

The optical tweezers set-up was as described in section 2.3.3.1. Barriers were fabricated according to section 2.1.5. The assay was performed as in section 2.3.3.2. However after the incubation with κ -cas, the flow cell was incubated with dynein, 15 nM for 20 minutes in the case of an experiment with dynein,. The flow cell was rinsed with 100 μ l of MRB80, to remove freely floating dynein and left over ATP. A gliding assay showed that under these conditions dynein was indeed present on the surface (in this experiment, dynein attached non-specifically to all surfaces including the barriers). In some experiments with dynein present, the axoneme-bead construct was placed at the bottom surface of the chamber at the end of the experiment to let it glide on the dynein on the bottom surface. The gliding of the construct on the surface allowed us to confirm that we were looking at plus-end dynamics. The temperature of the experiment was kept at 25°C.

4.5.9 Data analysis of optical trap experiments

MT length was plotted against time by multiplying the bead displacement with the conversion factor. Shrinking velocities were measured on shrinking events that were identified by eye (Table 4.2). On these events linear fits were made to a moving window of 4 frames (120 ms). The average shrinkage velocity was determined by averaging over all fits over all events from all experiments. The error is given by the standard error over all fits. In the case of experiments with dynein on the barrier with ATP, shrinking events above the zero position (center of the trap) and below zero were taken separately, because shrinking events below zero corresponded to shrinking against a pulling force. For the experiments with dynein on the barrier without ATP,

the whole event from the moment it started to shrink until the bead reached the zero position was taken into account (including stretches of apparent MT length increase).

The catastrophe time was averaged over all events, with the error given by the catastrophe time divided by the square root of the number of observed events. The catastrophe time of an individual event is given by the time between the moment the growth of the MT starts to move the bead out of the trap and the moment the MT undergoes catastrophe and starts to shrink.

The force was plotted against time by multiplying the bead position with the trap stiffness. The average maximum force was calculated by averaging the maximum force of the shrinking events that went below the zero bead position, with the error given by the standard deviation (Table 4.2). To determine the off-rate of dynein from the shrinking MT, we only evaluated the part where the MT was pushed against the barrier (Fig. 4.10).

4.6 Acknowledgements.

I would like to acknowledge Julien Husson for collaborating on the optical trap experiments, Martijn van Duijn for developing the gold-specific chemistry, Samara Reck-Peterson and Ron Vale for kindly giving us the dynein constructs and for helpful discussions, Matt Footer for kindly providing us with axonemes, Claude Celati for help with the centrosome purifications, E. Laura Munteanu and Jacob W.J. Kerssemakers for developing the optical trap set-up, Guillaume Romet-Lemonne for help with developing the microfabrication, Chris Rétif, Henk Bar, and Marco Seynen for technical support.

Chapter V:

Reliable centering of dynamic microtubule asters in microfabricated chambers by pulling forces

In living cells, dynamic microtubules interact with the cortex to generate pushing and/or pulling forces that position the organizing center correctly with respect to the confining geometry of the cell. The mechanisms by which pushing forces center organelles have been studied quite extensively in vivo, in vitro and in theoretical models. However the role of pulling forces in positioning processes is still poorly understood. We investigate the positioning by pulling forces relative to pushing forces in an in vitro experiment. Microtubule asters are grown in square microfabricated chambers. Pushing forces arise from microtubule growth and elastic restoring forces of the microtubule array. Pulling forces are introduced by specifically attaching the motor protein dynein to the chamber walls. Surprisingly we find that microtubule asters center in microfabricated chambers more reliably by a combination of pulling and pushing forces, than by pushing forces alone. To explain our data we have developed a theoretical model in which pulling forces center an aster due to a microtubule-growth-and-sliding induced anisotropic distribution of microtubules in the microfabricated chamber. If growing microtubules have a relatively low probability to bind to a motor, the microtubules will slide along the chamber wall, before a motor captures them. This sliding generates an anisotropic distribution of microtubules with most microtubules close to the corners of the microfabricated chamber. The subsequent net force generated by this microtubule distribution reliably centers the microtubule aster.

5.1 Introduction

Microtubules (MTs) play an important role in cellular organization. Through interactions with the cellular cortex pushing and/or pulling forces are generated that position various organelles in the cell [3, 6, 112, 168]. The centering mechanisms that pushing forces exploit to position organelles have been studied quite extensively *in vivo*, *in vitro*, and in theoretical models. In *Schizosaccharomyces pombe* cells in interphase, motions of the nucleus are directly correlated with dynamics of growing MTs interacting with the cell ends [71]. If in this system the nucleus is artificially displaced from the cell center MT pushing forces bring the nucleus back to the cell center [112]. In *in vitro* experiments it has been shown that simple pushing by freshly nucleated MTs, grown from a MT-nucleating bead or centrosome, allows a MT aster to find the geometrical centre of a confining geometry [116], provided the MTs have enough catastrophes [115], as was predicted in theoretical models [117].

Elegant *in vivo* experiments in first cell stage *Caenorhabditis elegans* embryos show that pulling forces also play an important role in positioning processes [10]. In these experiments the central spindle was removed by laser ablation and the relaxation of the spindle poles was monitored. The spindle poles moved towards the cell poles indicating the presence of pulling forces from the cortex on the spindle [10]. The role of these pulling forces in the positioning of the spindle is not yet understood. Several models have been developed to describe positioning processes due to pulling forces [138, 174]. These theoretical models predict that pushing forces are essential to generate centering in a system where pulling forces are also present. In the absence of pushing forces, pulling forces are suggested to be incapable of centering, because in the current models and speculations pulling forces contain no positional information [136-138], or contain positional information that leads to de-centering [6, 175]. Positional information that leads to de-centering arises from the time newly nucleated MTs take to arrive at the cortex after catastrophe. If the centrosome is de-centered it takes less time for MTs to grow back after catastrophe to the proximal site than to the distal site. This results in a higher average number of MTs in contact with the proximal site and thus in a net pulling force towards the proximal site, away from the center position.

In this study we experimentally investigate the role of pulling forces in MT-aster positioning processes. Are pulling forces indeed unstable and are pushing forces necessary for centering? What is the role of pulling forces in the positioning process? We address these questions in minimal *in vitro* experiments, as previously performed for the case of pushing forces [115, 116]. We use microfabricated

chambers to confine MT asters, and specifically attach minus-end directed motor proteins to the chamber walls, to introduce pulling forces on the aster. By varying the number of motor proteins on the chamber walls, the ratio of pushing to pulling forces in our system can be varied. We show that if pulling forces are present, in addition to pushing forces, MT asters center more efficiently in microfabricated chambers than if only pushing forces are present. This centering by pulling forces relies on geometrical effects: as MTs first push against the walls of the microfabricated chamber they actively redistribute their contact points with the wall before they attach to a motor protein. In a square geometry for example, most MTs slide to the corners. We use a simple mathematical model to show that a sliding-induced anisotropic distribution of MTs results in centering by pulling and pushing forces simultaneously.

5.2 Experimental results

Our minimal system consists of a dynamic MT aster, grown from a centrosome, confined in a microfabricated chamber (Fig. 5.1A). The top of the microfabricated chamber is sealed by firmly pressing a coverslip with a thin layer of PDMS on top (see chapter 2 for details). A gold layer, fabricated in the wall of the microfabricated chamber (Fig. 5.1B, Fig. 2.5), allows for specific binding of biotinylated dynein molecules via gold-specific chemistry and biotin-streptavidin linkage (Fig. 5.1A, Fig. 2.4) [142]. In our experiments, we use a truncated dynein obtained from *S. cerevisiae* (GST-Dyn331, referred to herein as dynein [170, 176]). As shown in chapter 4 this construct exerts pulling forces on shrinking MT ends. Pushing forces are generated by MT polymerization forces as well as by elastic restoring forces due to MT bending [88, 118]. By varying the thickness of the gold layer we vary the number of dynein molecules that are available for MT capture in the microfabricated chamber and thus vary the ratio of pushing to pulling forces.

We perform experiments with three different effective amounts of dynein bound to the sidewalls of the microfabricated chambers: 1) no dynein at the sidewalls, 2) dynein bound to a 100 nm thick gold layer, and 3) dynein bound to a 700 nm thick gold layer. We monitor if the MT aster is centered and if the MT aster is moving through the microfabricated chamber. We consider the centrosome centered in the microfabricated chamber if the centrosome is located within the 10% area in the middle of the microfabricated chamber. We consider a MT aster to be moving if it

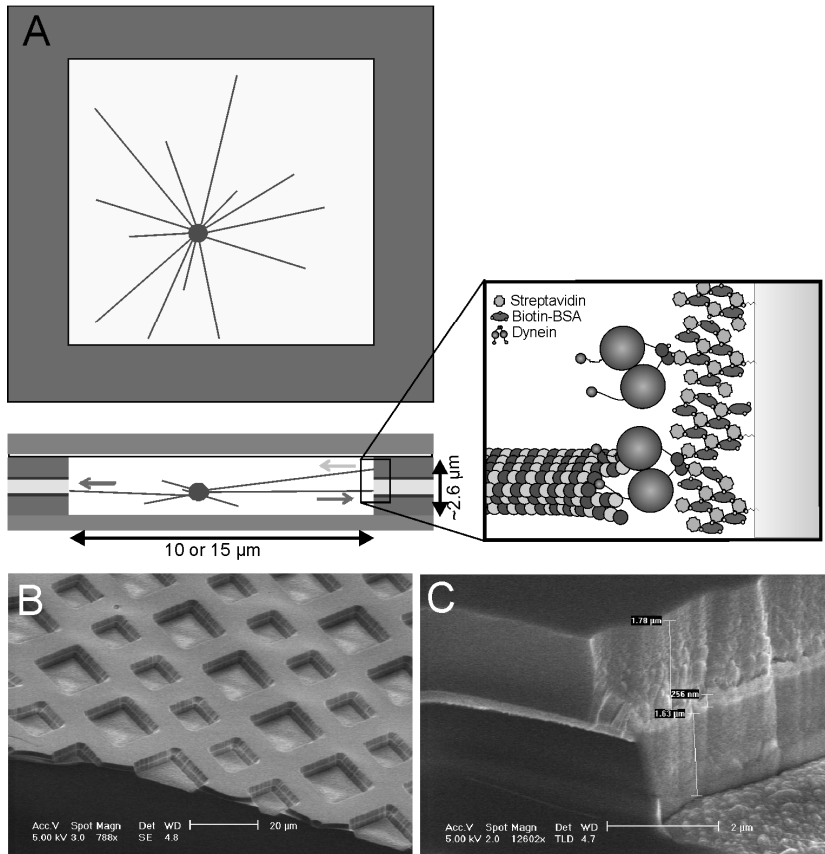


Figure 5.1

Experimental set-up. (A) Schematic picture of a MT aster confined in a microfabricated chamber with dynein motors specifically bound to the gold layer. Detail shows the attachment of dynein molecules to the gold layer via streptavidin and biotin-BSA (roughly to scale). (B) Scanning electron micrograph (SEM) image of the microfabricated chambers. (C) High resolution SEM image of a wall of a microfabricated chamber showing a 200 nm gold layer in between a layer of silicon mono-oxide and glass.

moves faster than 1 nm/sec; the slowest detectable movement (calculated by dividing the pixel size (165 nm) by the observation time of an aster (typically 150 sec)). Based on observation of these two parameters, we divide the positioning process into three regimes: (1) average MT length < d, (2) average MT length ~ d, and (3) average MT length > d, where d is the half-width of the microfabricated

Reliable centering of dynamic MT asters in microfabricated chambers by pulling forces

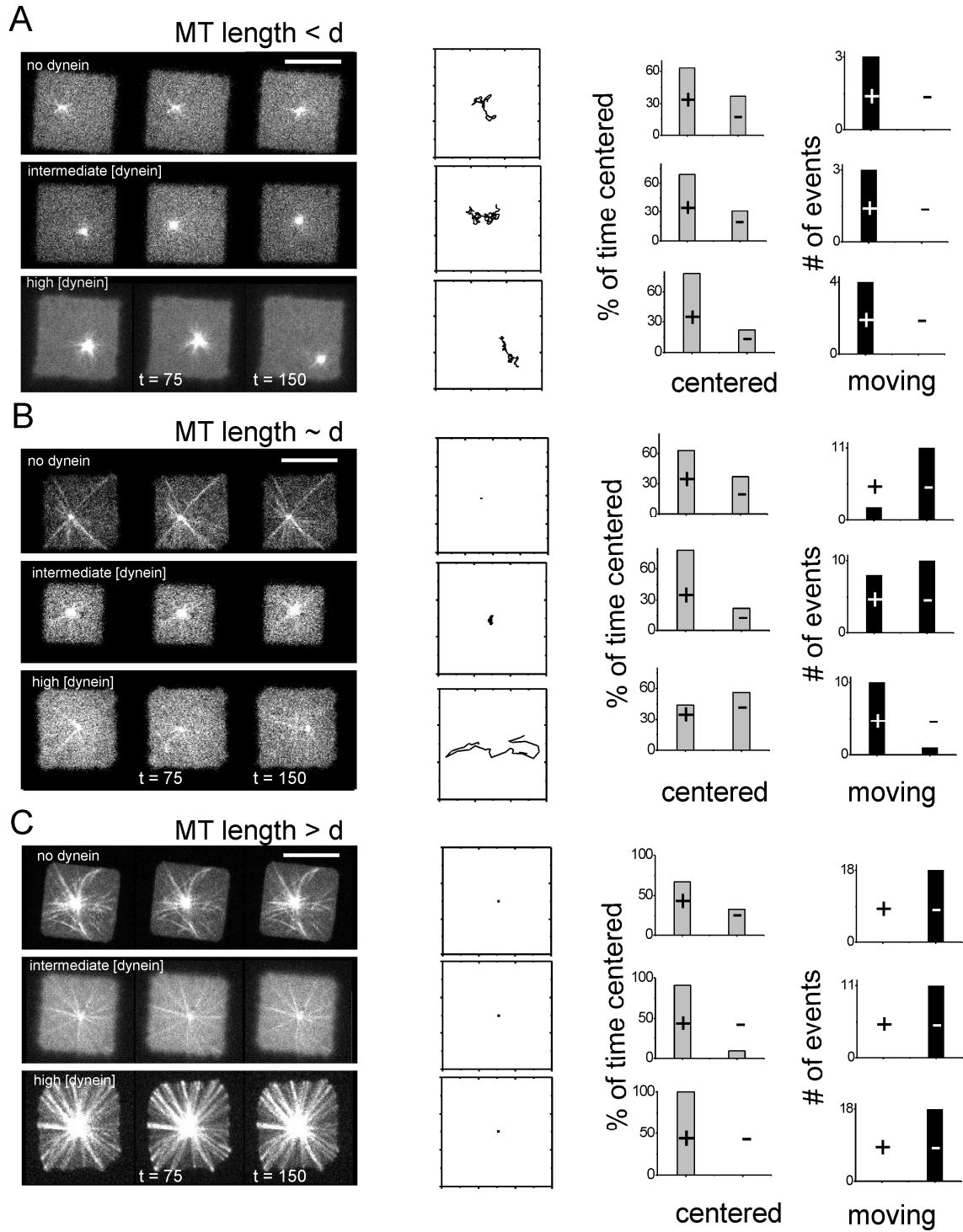


Figure 5.2

The positioning process of MT asters in microfabricated chambers. On the left, spinning disk confocal fluorescence images are shown of the positioning of MT asters with short (A), intermediate (B), and long MTs (C) in microfabricated chambers. For every MT aster length, data are shown without dynein, with intermediated dynein amounts, and high dynein amounts on the microfabricated chamber walls. Scale bar indicates 10 μm . For every condition the trajectory of the aster (the same one as in the image sequence) is plotted. In addition, for every combination of MT length and dynein amount a grey bar plot shows the percentage of the time that MT asters are

centered (+), calculated by $\frac{\sum_{i=1}^n T_{i,+}}{\sum_{i=1}^n T_{i,+/-}} \times 100\%$, where n is the number of events, T_+ is the time

per event, that the centrosome is centered, $T_{i,+/-}$ is the total observation time per event. The percentage of the time is also calculated for not-centered (-) centrosomes, where T_- replaces T_+ in the equation. The black bar plot shows the number of events in which the aster moves (+) and in which the aster does not move (-).

chamber (Fig. 5.2). In practice this corresponds to aster behaviors at early (1), intermediate (2), and late (3) times in the experiment. In the first regime there is no clear difference in aster behavior between different dynein amounts (Fig. 5.2A). For all three amounts the MT aster diffuses through the microfabricated chamber. Short MTs allow the aster to sample a large area of the microfabricated chamber so that the centrosome is only centered around 60% of the time. After some time the MTs, growing from the centrosomes, reach approximately the length of half the microfabricated chamber width. In this regime different dynein amounts result in very different behaviors (Fig. 5.2B). If dynein is not present, MTs can only exert pushing forces, and around 80% of the MT asters do not move. Around 60% of these “trapped” asters are found centered in the microfabricated chambers. Most MT ends are located in the corners of the microfabricated chambers and are not yet buckled. In this situation, MTs are quite stable and very few catastrophes are observed. The absence of movement and relatively inefficient centering in the absence of MT catastrophes is consistent with previous results [115, 117]. When dynein is present in the microfabricated chamber, MT and aster behavior are quite different. At intermediate dynein amounts asters move in almost half of the cases, but the movement is not very dramatic, with the aster typically located in the center. At high dynein amounts however, the movement of the MT aster is much more

dramatic: the aster moves throughout the whole microfabricated chamber, often in a directed rather than diffusive manner. This dramatic movement results in poorly centered asters in around 60% of the cases.

In the third and final regime the MTs are very long. When dynein is absent the MTs buckle around the microfabricated chamber and there is no observable movement. Around 70% of the asters are considered centered, similar to the situation with shorter MTs (the 2nd regime). Surprisingly, in this regime pulling forces improve the centering. At intermediate dynein amounts around 90% of the asters are centered, and at high dynein amounts, all the observed centrosomes are centered and immobile. And strikingly, especially at high dynein amounts, the MTs do not buckle, but are straight, which is in strong contrast to the long buckled MTs in the absence of dynein. This shows that in this well-centered case dynein generates pulling forces on the dynamic MT ends, while regulating the MT length, as shown in chapter 4.

We can conclude that pulling forces decrease the centering, compared to the pushing forces, if the MTs are just long enough to reach the edges of the microfabricated chamber. In this case, antagonistic pushing forces generate long enough contacts (in time) of MTs with the chamber edges to allow for capture by dynein motors and the generation of pulling forces. Because initially only a single or a few MTs are captured by a motor, the pulling forces generated by this MT(s) can result in dramatic movement of the aster. However, if more MTs become captured by a motor protein, the pulling forces by the different MTs balance each other. And interestingly, if many MT are pulled upon, the centering by pulling and pushing is more efficient than by pushing alone.

So how can pulling forces enhance the reliability of centering of a MT aster? In existing models pulling forces do not contain positional information that leads to centering, as discussed above [118, 148]. To explain our experimental results, we introduce in the next section a new model in which pulling forces center due to positional information that arises from geometrical effects.

5.3 Theory

The theoretical description of our system consists of a dynamic MT aster situated in a microfabricated chamber with dynein motors specifically attached to the walls. The description includes known physical properties of the main components of our system, which are the dynamics of MTs, pushing forces generated by growing MTs,

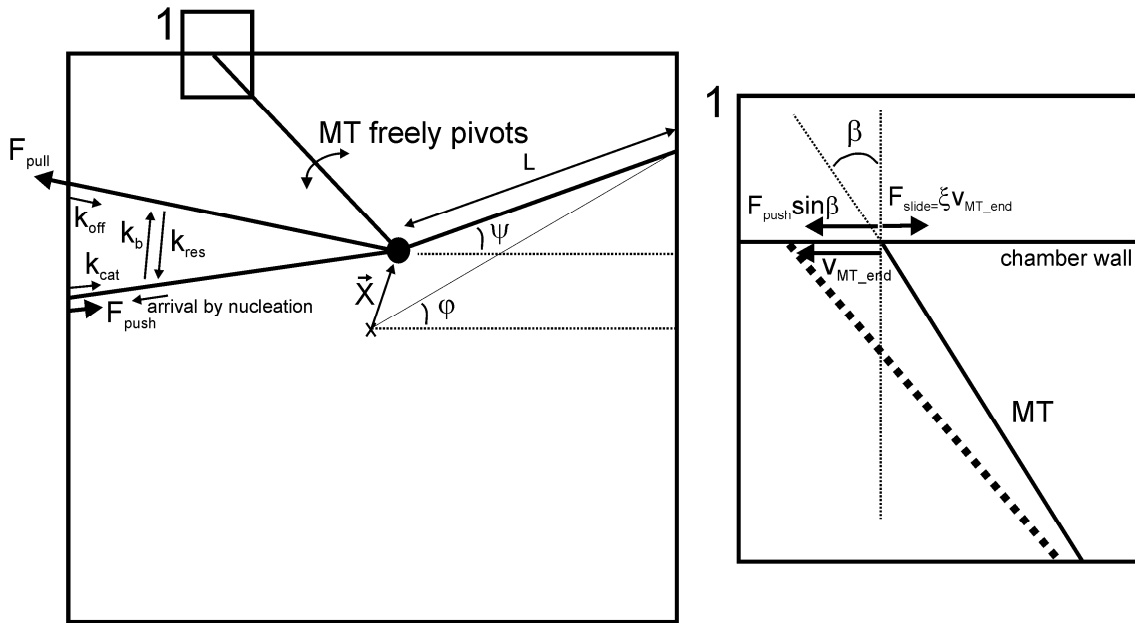


Figure 5.3

Schematic drawing of the parameters. A centrosome is located at position \bar{x} from the center; the parameter ψ denotes the angle between the MT and the chamber wall; ϕ denotes the angle between the MT end and the center of the chamber; L denotes the distance between the MT end and the centrosome. MTs, after nucleation, arrive at the chamber wall and generate a pushing force while growing. The growing MTs can undergo catastrophe with a rate k_{cat} , or they can bind to motor with a rate k_b and generate a pulling force. MTs that are shrinking and pulling can be rescued and switch to the growing state with a rate k_{res} , or can unbind and shrink away with a rate k_{off} . The sliding mechanism is drawn in detail 1. Due to MT length increase the MT slides along the chamber wall. The friction, ξ , multiplied with the velocity of the sliding MT, v_{MT_end} , is in balance with the component of the pushing force parallel to the wall, $F_{push} \sin \beta$.

capturing of MT ends by dynein motors, pulling forces exerted by dynein motors on shrinking MTs, and isotropic MT nucleation at the centrosome (see parameters in figure 5.3). We in addition assume that MTs, which extend from the centrosome, can pivot freely around their nucleation point. MTs change their orientation without affecting the other MTs in the aster.

How do the ingredients introduced above lead to efficient centering? Initially, we assume that the centrosome is de-centered, as shown in figure 5.4A, and that MTs have an isotropic distribution due to their isotropic nucleation at the centrosome. If these MTs are captured by dynein motors at the position where the first contact with the wall of the chamber is made, then pulling forces will be

isotropically distributed and the net pulling force will be zero (Fig. 5.4A, left figure). However, in practice there will be a time delay between the first contact of the growing MT with the wall and capturing of that MT by dynein. During this time the MT continues to grow and slides along the wall. Consequently, the MT changes its orientation, which affects the angular distribution of MTs: more MTs will be oriented towards the distal corners. Eventually, the redistributed MTs attach to dynein motors and a net pulling force on the centrosome is directed towards the distal corners, i.e. towards the center (Fig. 5.4A, right figure). Since the net pulling force is always directed towards the center, the central position in the chamber is the stable position for the centrosome. A rigorous description of the forces acting on a dynamic aster in this scenario is provided below.

The position of the centrosome within the two-dimensional plane of the microfabricated chamber is denoted by the position vector \bar{x} . The orientation of astral MTs is defined with respect to the horizontal line and is denoted by the angle ψ . This angle is a function of ϕ , where ϕ is the orientation of the line which connects the center of the microfabricated chamber and the end of the MT at the wall (Fig. 5.3). We distinguish two populations of MTs that are in contact with the wall: (i) MTs that are not bound to a motor and are growing and pushing. Their angular density is denoted by $N^+(\phi)$, and (ii) MTs that are bound to a motor and are shrinking and pulling. Their angular density is denoted by $N^-(\phi)$. MTs that are not in contact with the wall do not contribute to force generation and thus are not considered in this model. The time evolution of the two populations of MTs can be written as follows:

$$\frac{\partial N^+(\phi)}{\partial t} = \frac{v}{2\pi} \frac{\partial \psi}{\partial \phi} - k_{cat} N^+(\phi) - k_b N^+(\phi) + k_{res} N^-(\phi) - \frac{\partial}{\partial \phi} J_\phi, \quad (1)$$

$$\frac{\partial N^-(\phi)}{\partial t} = k_b N^+(\phi) - k_{off} N^-(\phi) - k_{res} N^-(\phi). \quad (2)$$

Here k_{cat} denotes the rate of switching to the shrinking state followed by shrinking away from the wall, k_b denotes the rate of binding to a motor followed by motor-induced switching to the shrinking state, k_{res} denotes the rate of unbinding from a motor followed by switching to the growing state, and k_{off} denotes the rate of unbinding from the motor followed by shrinking away from the wall. The rate for nucleation of new MTs is defined as

$$\nu = \nu_0 \left\{ N_{\max} - \int_0^{2\pi} d\phi [N^+(\phi) + N^-(\phi)] \right\}, \quad (3)$$

where ν_0 is nucleation rate for single MTs and N_{\max} the total number of nucleation sites. ν is multiplied with $\partial\psi/\partial\phi$ because ν is isotropic around ψ however the N^+ is defined around ϕ . J_ϕ denotes the angular current of growing MTs at the wall due to sliding (see below). For simplicity, the remaining calculations are made for a fixed centrosome position, $\dot{x} = 0$, and for MT populations in steady state, $\partial_t N^+ = \partial_t N^- = 0$ (the static response).

MTs that are not captured by a dynein motor, and are therefore growing, can change their orientation by pivoting around the centrosome. For this population of MTs we define the angular current, J_ϕ , as follows:

$$J_\phi = \dot{\phi} N^+(\phi), \quad (4)$$

where $\dot{\phi} = (\partial\phi/\partial\psi)\dot{\psi}$. In order to calculate this current, we need to describe the sliding of the MT end along the wall. For simplicity we assume that friction between the MT end and the wall depends linearly on the velocity of the MT end. The friction force is in balance with the component of the pushing force, f_{push} , parallel to the wall, $\xi v_{ip} = f_{push} \sin\beta$ (see detail 1 in figure 5.3). Here ξ denotes the friction coefficient between the MT end and the wall, and β denotes the angle between the MT and the wall. The velocity of the end is defined as $v_{ip} = L\dot{\psi}/\cos\beta$, where L denotes the distance between the centrosome and the MT end.

The pushing force for growing MTs is defined as $f_{push} = \min\{f_g, f_b\}$, where f_g stands for the pushing force derived from the (approximate) force velocity curve, $f_g = -f_0 \ln(\dot{L}/v_g)$ [88], and f_b stands for the buckling force of a MT with two pivoting ends, $f_b = \pi^2 k_B T L_p / L^2$ [175]. Here f_0 is the MT force constant, v_g is the growth velocity under zero load, k_B is the Boltzmann constant, T is the temperature, and L_p is the MT persistence length. MT growth is related to MT pivoting as $\dot{L} = L\dot{\psi} \tan\beta$. The pulling force on motor-attached shrinking MTs, f_{pull} , is considered to be constant and equal to the motor stall force for a fixed centrosome

position. To determine the total force on the centrosome we finally calculate the net pulling force on the centrosome:

$$\vec{F}_{pull} = \int_0^{2\pi} d\varphi N^-(\varphi) f_{pull} \vec{n}_\psi \quad (5)$$

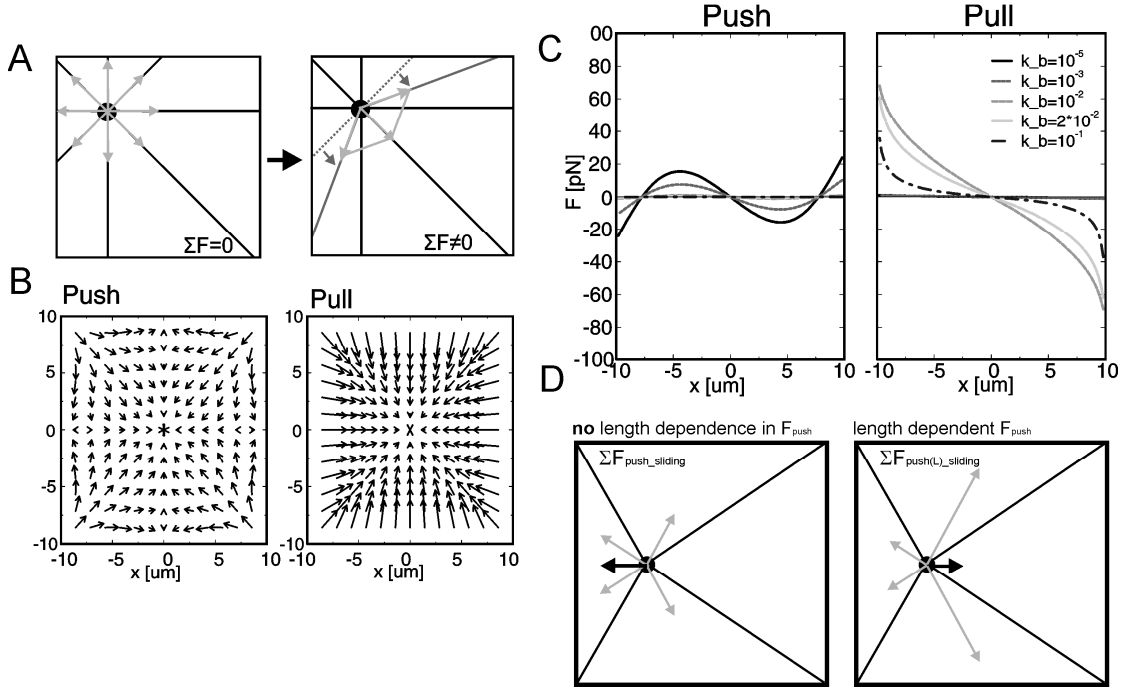


Figure 5.4

MT asters center by pulling forces upon redistribution of MT ends due to sliding. (A) Schematic picture of the sliding mechanism. If the MTs do not slide, the MT distribution remains isotropic and the sum of the pulling forces is zero. However if pushing MTs slide before they bind to a motor, the MT distribution becomes anisotropic and the subsequent sum over all pulling forces is directed towards the center. (B) Positional diagram of the static response due to pushing forces (left graph) and to pulling forces (right graph), where k_b is set to $2 \cdot 10^{-3} \text{ sec}^{-1}$. (C) Line profile for pushing as well as pulling forces in the microfabricated chamber. Pulling forces center the centrosome for every position in the microfabricated chamber. Pushing forces only center in positions away from the chamber edges. (D) Sliding results in a de-centering mechanism in the case of pushing forces if the magnitude of the pushing force is not length dependent (left picture), if the pushing force is length dependent the pushing force center in most of the positions in the microfabricated chamber.

and the net pushing force on the centrosome:

$$\vec{F}_{push} = - \int_0^{2\pi} d\varphi N^+(\varphi) f_{push} \vec{n}_\psi. \quad (6)$$

Here \vec{n}_ψ is the unit vector from the position of the centrosome to the end of the MT. We combine eq. 1-6 to numerically calculate the static response of the centrosome in various locations in the microfabricated chamber using a simple Euler method. In the calculation of the static response the centrosome is maintained at a fixed position and the steady state forces on the centrosome are calculated by first calculating the MT distribution. This distribution is calculated by numerically solving Eq. 1 and 2 for $\partial_t N^+ = \partial_t N^- = 0$. The values of parameters in the equations are obtained from known properties of MTs and dynein, and from our experimental observations (see section 5.6.5). In our analysis we only vary k_b , which corresponds effectively to varying the dynein amounts in the experiment. In figure 5.4B the positional diagrams of the static response of the centrosome due to pushing and pulling forces are shown for $k_b = 2 \cdot 10^{-3} \text{ sec}^{-1}$. In this case the majority of the MTs slide towards the corners. The pulling forces center the MT aster in every position in the microfabricated chamber (Fig. 5.4B, right graph). The pushing forces only center the centrosome if the MT aster is positioned sufficiently far from the chamber edges. Pushing forces show different behavior in different areas, because two different effects influence the pushing force. The first is the length dependence of the magnitude of force due to buckling, which centers, and is dominant in the center region. The second is the sliding mechanism, which influences the direction of the pushing force leading to de-centering (for the same reason that pulling forces lead to centering). Close to the edges of the microfabricated chamber the sliding mechanism dominates the buckling effect resulting in de-centering by pushing forces (Fig. 5.4D).

To quantify the role of sliding in the generation of centering forces, we calculate the static linear response (dF/dx in steady state) at the center position for different k_b for the pushing and the pulling force (Fig. 5.5A) and compare it to the accompanying MT distribution (Fig. 5.5B). At low k_b all MTs slide to the corners, and pushing forces are predominant, because the motor binding is low compared to the other rates. At higher k_b most MTs still reach the corners before a motor binds them. Yet in the corners the MTs eventually bind to a motor and an efficient centering force by pulling is generated ($k_b \sim 2 \cdot 10^{-2} \text{ sec}^{-1}$). At very high k_b the MTs are immediately bound by a motor when they hit the chamber wall, and therefore do not slide. In this case the net pulling force approaches zero because the MT distribution

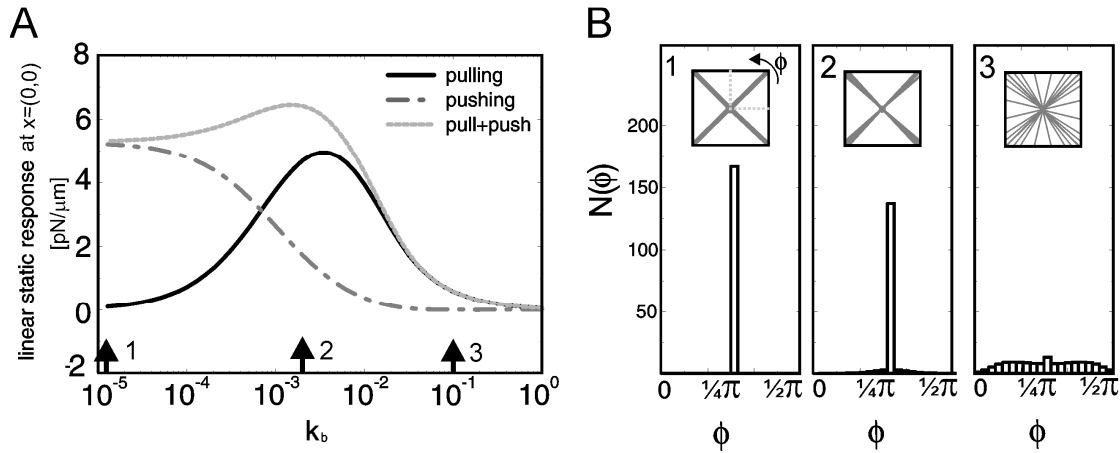


Figure 5.5

The role of k_b on the pushing force, the pulling force and the MT distribution. (A) Plot of the static linear response at the chamber center for different values of k_b in sec^{-1} . (B) Plot of MT density as a function of ϕ from 0 to $\frac{1}{2}\pi$ for the three different values of k_b . The inset shows cartoons of the MT distribution in a microfabricated chamber.

becomes close to isotropic ($k_b \sim 1 \text{ sec}^{-1}$). The pushing forces are also zero because all MTs are bound to a motor.

5.4 Comparison of experiments and theory

To verify whether this model is consistent with our experiments, we examine the MT distribution in our microfabricated chambers. We compare the MT density in the corner regions (Fig. 5.6A indicated in light grey) to the MT density in between the corners, the middle regions (Fig. 5.6A, indicated in dark grey) of a microfabricated chamber that contains a MT aster. We calculate the difference in intensity between the corner regions and the middle regions, normalized by the intensity in the middle regions. If this intensity ratio is larger than zero, then there are more MTs in the corner regions. We find that both with and without pulling forces more MTs lay in the corner regions of the microfabricated chamber (Fig. 5.6B,C,D). As expected, the effect is strongest if MTs are never bound by a motor and in principle can slide all the way to the corners. Nevertheless, with motor attachment there is also a redistribution of MT density. The difference is not due to uneven background or due to an anisotropic nucleation, because centrosomes nucleate MTs isotropically if they are not confined in a microfabricated chamber (Fig. 5.6B,E,F). We compared the MT distribution in the experiment with the theory

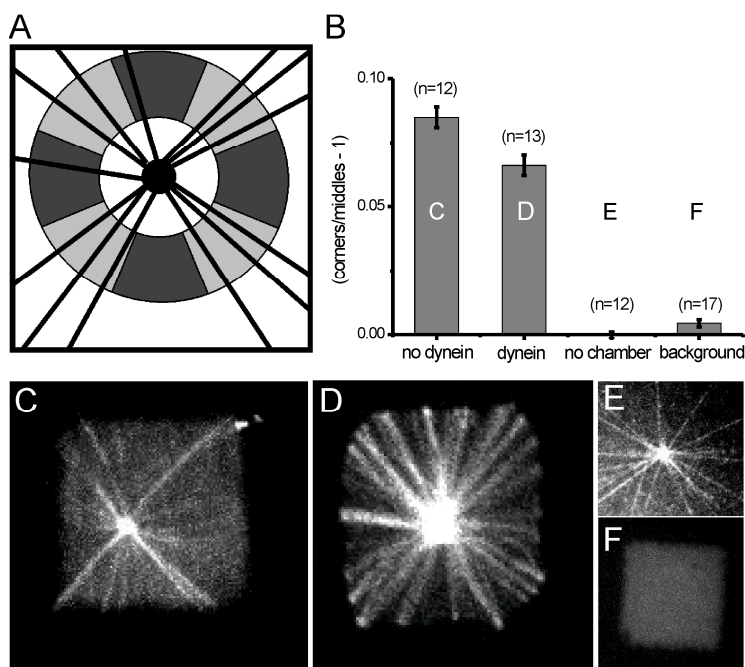


Figure 5.6

Sliding of MTs in microfabricated chambers. (A) Schematic picture of the analysis performed to measure sliding. The areas indicated in dark grey form the middle regions of the microfabricated chamber. The areas indicated in light grey form the corner regions of the microfabricated chamber. By comparing the intensity in the corner regions with the middle regions the presence of sliding in the experiment was measured. (B) Bar plot in which the intensity of the (corners/middles - 1) is plotted for different cases, the error is the SE. For all these cases a spinning disk fluorescence confocal microscopy image is shown. The cases are: (C) a MT aster in a microfabricated chamber without dynein, (D) a MT aster in a microfabricated chamber with a high dynein concentration, (E) a MT aster on a surface, which is not confined in a microfabricated chamber, and (F) an empty microfabricated chamber.

and estimate that our experiments at high dynein amounts are in the regime around $k_b \sim 0.1 \text{ sec}^{-1}$ (Fig. 5.5B, right).

5.5 Discussion

In our theory the length dependence of pushing forces is due to buckling. The arrival time of newly nucleated MTs can also generate a length dependence, as previously described [117]. This mechanism however cannot by itself lead to simultaneous

centering by pushing and pulling forces. Both forces would depend on the arrival time in the same way, but with opposite signs, resulting in an opposite effect on centering. One mechanism will center but the other mechanism will de-center. In principle the same holds for our sliding mechanism. The redistribution of MTs leads to centering by pulling forces, but de-centering by pushing forces. In this case however the de-centering of the pushing forces is compensated due to the length dependence of the pushing force due to buckling (Fig. 5.5). This length dependent mechanism only affects the pushing forces, but does not affect the pulling forces.

The combined results of our experiments and theory show that pulling forces can center a MT aster through a sliding mechanism facilitated by pushing forces. Interestingly this centering mechanism depends heavily on the geometry of the confining space. In a square geometry the MTs slide towards the corners, allowing for a dramatic redistribution of MTs, resulting in efficient centering forces (Fig.

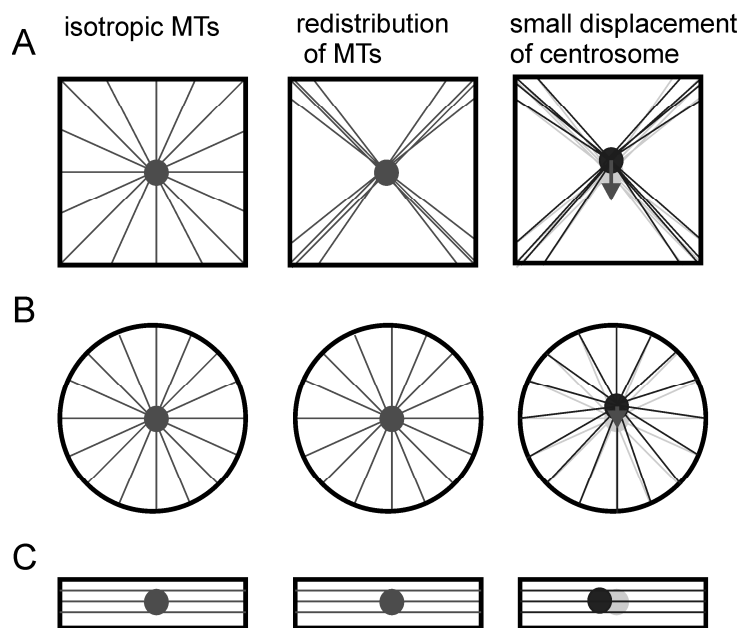


Figure 5.7

Cartoons of the possible role of the sliding mechanism in different geometries. (A) In a square geometry the sliding induces dramatic redistribution of MTs, which results in a centering force due to pulling if the centrosome is displaced. (B) In a circular geometry MTs do not redistribute due to sliding, resulting in a less efficient pulling force by a small displacement of the centrosome. (C) In a one dimensional geometry, with dynein only localized to the left and right extremity, MTs do not redistribute and displacement of the centrosome does not result in a centering force due to pulling.

5.7A). One can speculate that, for example, in a circular geometry, sliding will be much less pronounced, when the centrosome is close to the center. The static linear response due to pulling forces will be much weaker because MTs, radiating from the aster, will be perpendicular to the circular walls resulting in inefficient sliding (Fig. 5.7B). The most extreme case will be a 1D environment, where MTs align in parallel with the elongated confinement and motors only pull from the extremities. In this situation there will be no sliding and therefore no centering by pulling forces (Fig. 5.7C). Future mathematical calculations will be necessary to verify these speculations.

In the first cell stage embryo of *C. elegans* pulling forces are responsible for spindle positioning. The confining geometry of this embryo is oval, which in our model will lead to centering. It would be interesting to analyze the MT distribution during this positioning process of the spindle to study the possible role of the geometry-dependent mechanism. In the meiotic preprophase in *S. pombe* MTs interact with dynein, which is mostly located on the cell ends, and induce nuclear oscillations. This situation is very similar to figure 5.7C, where we indeed do not expect centering by pulling forces. However, to conclude whether our model is relevant for this cellular process, it will be necessary to study the dynamics of our model, instead of the static response, and check whether we can also reproduce the nuclear oscillations.

In summary, our *in vitro* experiments have shown that pulling forces can contribute to centering processes. MT asters, with long MTs, center more reliably in microfabricated chambers with motor proteins bound to the sidewalls. We can explain our data with a simple model where pulling forces depend on MT redistribution in a confining geometry. In the future it would be interesting to perform similar *in vitro* experiments using different geometries.

5.6 Materials and methods

5.6.1 Biological materials

The dynein construct used in this study was the biotinylated GST-dynein331 construct, which was tested in a gliding assay using a simple flow cell. The gliding speeds found were 130 +/- 35 (29) nm/sec, very similar to numbers reported before. Centrosomes were purified with generous help of Claude Celati from human lymphoblastic KE37 cell lines according to Ref. [173].

5.6.2 Sample preparation

Microfabricated chambers were constructed and activated as described in chapter 2. The sample was made as described in section 2.3.3. The biotinylated protein that was introduced, was the biotinylated dynein as described in section 4.5.1 at 20 nM.

5.6.3 Data analysis

The position of the centrosome in the microfabricated chamber was tracked using the automatic ImageJ plugin spot tracker made by D. Sage, F.R. Neumann, F. Hediger, S.M. Gasser and M. Unser [177]. In a home-written program in Matlab the edges of the chamber are manually tracked and are compared to the centrosome position to define whether the centrosome is centered. We define a centrosome to be centered, if the center position of the centrosome is within 30% of the chamber radius. A centrosome that moves can be centered for example for 38% of the time and not centered for 62% of the time. A centrosome is defined to move, if it moves more than 1 pixel per 150 sec, movement slower than this we attribute to noise, because by eye this movement appears to be due to stage drift.

5.6.4 Data analysis of the distribution of microtubules in a microfabricated chamber

The samples were tested for sliding by a home-written program in Matlab. In this program only the immobile asters, with long MTs (not yet buckled) were analyzed. In the analysis first the images of the microfabricated chamber were rotated such that the horizontal walls were parallel to the 0° axes. The position of the corners of the microfabricated chambers was tracked manually. From the center of the centrosome a circle, with the maximum size that still fits in the microfabricated chamber, was defined (Fig. 5.6A). Within this circle, a smaller circle, with the same geometrical center, but with a radius that is decreased with five pixels, was defined. The region between the two circles was divided into 8 equally sized regions, all 45° , starting at -22.5° , resulting in “corner” (indicated in light grey) and “middle” (indicated in dark grey) regions. For every area the total intensity was calculated. The total intensity in the corner regions was compared to the intensity in the middle regions (Fig. 5.6A). If the MTs slide, it is expected that there are more MTs in the corners than in the middles, which should result in a ratio of (corners-

middles)/middles larger than zero (Fig. 5.6B). This is indeed the case (Fig. 5.6B), indicating that there is sliding in the experiment.

5.6.5 Parameter choices

Parameter:	value:	based on:
v	$= 0.01 \text{ sec}^{-1}$	rough estimate from experiments where MTs were grown from centrosomes under similar experimental conditions
N_{max}	$= 50 \text{ MTs}$	rough estimate from experiments where MTs were grown from centrosomes under similar experimental conditions
k_{cat}	$= 10^{-4} \text{ sec}^{-1}$	estimated from the dynamics of MTs in the microfabricated chambers
k_{res}	$= 10^{-4} \text{ sec}^{-1}$	rough estimate from the dynamics of MTs in the microfabricated chambers even though it is difficult to identify a rescue in our microfabricated chamber experiments, nevertheless there are indications that proteins that regulate MT shrinkage induce rescues [108]
k_{off}	$= 10^{-3} \text{ sec}^{-1}$	rough estimate from chapter 4 and from the dynamics of the MTs in the microfabricated chambers
v_0	$= 5 \text{ } \mu\text{m}/\text{min}$	taken from [176]
F_{motor_stall}	$= 5 \text{ pN}$	taken from [170]
v_g	$= 2 \text{ } \mu\text{m}/\text{min}$	rough estimate from experiments under similar experimental conditions.
F_{MT_0}	$= 6 \text{ pN}$	unknown, roughly based on measurements in buckling experiments [72, 88]
v_d	$= 10^{-2}$	$\mu\text{m}/\text{min}$ taken from [88]
k_B	$= 1.38 \cdot 10^{-23} \text{ J K}^{-1}$	
T	$= 300 \text{ K}$	room temperature
D	$= 20 \text{ } \mu\text{m}$	measured
L_p	$= 8 \text{ mm}$	taken from [178]
ζ	$= 1 \text{ pN sec}/\mu\text{m}$	arbitrarily taken value

5.7 Acknowledgements

I would like to thank Guillaume Romet-Lemonne and Chris Rétif for help and advice on the microfabrication, and Samara Reck-Peterson and Ron Vale for supplying the dynein. The theory was developed in collaboration with Nenad Pavin and Frank Jülicher.

Chapter VI:

Reconstitution of a microtubule plus-end tracking system *in vitro*

The microtubule cytoskeleton is essential to cell morphogenesis. Growing microtubule plus-ends have emerged as dynamic regulatory sites in which specialized proteins, called plus-end-binding proteins (+TIPs), bind and regulate the proper functioning of microtubules [46, 49, 179, 180]. However, the molecular mechanism of plus-end association by +TIPs and their ability to track the growing end are not well understood. Here we report the in vitro reconstitution of a minimal plus-end tracking system consisting of the three fission yeast proteins Mal3, Tip1 and the kinesin Tea2. Using time-lapse total internal reflection fluorescence microscopy, we show that the EBI homologue Mal3 has an enhanced affinity for growing microtubule end structures as opposed to the microtubule lattice. This allows it to track growing microtubule ends autonomously by an end recognition mechanism. In addition, Mal3 acts as a factor that mediates loading of the processive motor Tea2 and its cargo, the Clip170 homologue Tip1, onto the microtubule lattice. The interaction of all three proteins is required for the selective tracking of growing microtubule plus-ends by both Tea2 and Tip1. Our results dissect the collective interactions of the constituents of this plus-end tracking system and show how these interactions lead to the emergence of its dynamic behaviour. We expect that such in vitro reconstitutions will also be essential for the mechanistic dissection of other plus-end tracking systems.

This chapter has been published:

Peter Bieling*, [Liedewij Laan*](#), Henry Schek, E.Laura Munteanu, Linda Sandblad, Marileen Dogterom, Damian Brunner, Thomas Surrey,
Reconstitution of a microtubule plus-end tracking system *in vitro*,
Nature **450**, 1100-1105 (2007) (*equal contribution)

6.1 Introduction

Microtubules (MTs) are polar, dynamic tubulin polymers that have a variety of functions in eukaryotic cells [17]. The dynamics and the spatial organization of MTs are regulated by several highly conserved MT-associated proteins. An important class of these proteins, called +TIPs, accumulates selectively at growing MT plus-ends in living cells. A wealth of fluorescence microscopy studies in various organisms have identified numerous +TIPs that belong to conserved subfamilies: CLIP-170 [45], APC [181], EB1 [182], CLASPs [183], p150 [184] and spectraplakins [185]. In the fission yeast *Schizosaccharomyces pombe*, classical genetics combined with real-time fluorescence microscopy [186] demonstrated that multiple aspects of cellular organization depend on a defined distribution of MTs [68, 187]. This distribution is mediated by, among others, three +TIPs: the EB1 homologue Mal3 [59], the Clip170 homologue Tip1 [70] and the kinesin Tea2 [188, 189]. A hierarchy of molecular events required for plus-end tracking has been established from observations inside living yeast cells: the motor Tea2 and its putative cargo Tip1 move along the MT lattice towards its growing plus-ends, where they accumulate [59, 188]. Efficient recruitment to MTs and the plus-end accumulation of Tea2 and Tip1 depend on the presence of Mal3, which itself tracks the MT plus-ends independently of Tea2 and Tip1 [59, 188, 190]. It is not yet known whether additional factors or post-translational modifications are required, or whether Mal3, Tea2 and Tip1 constitute a minimal system that is sufficient to show plus-end tracking. In fact, a mechanistic understanding of plus-end tracking is still missing, in part because of the lack of an *in vitro* assay in which plus-end tracking can be reconstituted with a minimal set of pure components [191].

6.2 Results on end-tracking *in vitro*

Here we reconstitute MT plus-end tracking of the three purified proteins, namely Mal3, Tea2 and Tip1, *in vitro*. Initially experiments were performed with Spinning Disk Confocal Fluorescence Microscopy in the presence of all three +TIP proteins in an assay as described in section 6.4.2.1. These first experiments showed that TIP1-GFP can track the growing ends of dynamic MTs, but only in the presence of Mal3 and Tea2 (Fig. 6.1). To dissect the mechanism of the tip-tracking of Tip1-GFP we subsequently observed +TIPs and dynamic MTs on chemically functionalized surfaces by two-colour total internal reflection fluorescence (TIRF) microscopy [192] (Fig. 6.2a) individually and in all different combinations of the three proteins.

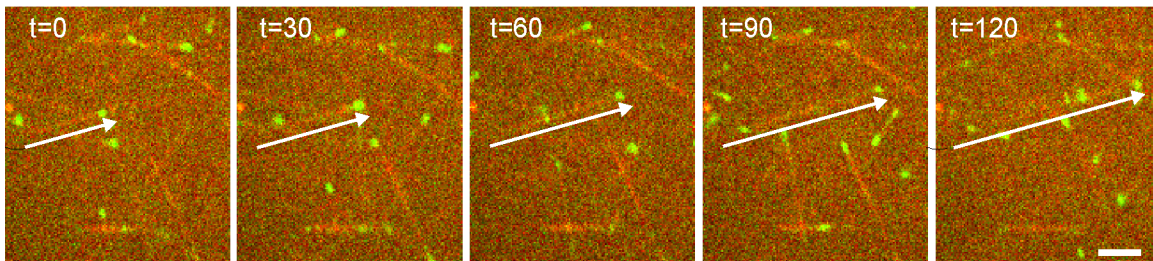


Figure 6.1

Tip1-GFP tracks dynamic MT ends in the presence of Mal3 and Tea2. Scale bar indicates 3 μm . White arrow indicates a growing MT with TIP1-GFP localized to the end. Time is indicated in seconds.

6.2.1. Mal3 autonomously tracks the growing microtubule end *in vitro*

Only one of the three proteins, the EB1 homologue Mal3, was able to bind efficiently to dynamic MTs in the absence of the others. Alexa 488-labeled Mal3 selectively accumulated at growing MT ends at considerable ionic strength (Fig. 6.2b) over a wide range of protein concentrations (Fig. 6.3a). Movie sequences and the corresponding kymographs (time–space plots), revealed that Mal3 was tracking the fast-growing plus-ends and the more slowly growing minus-ends (Fig. 6.2c). However, Mal3 did not accumulate at the ends of depolymerizing MTs (Fig. 6.2c) or static MTs (Fig. 6.4a). Selective tracking of free, polymerizing MT ends is therefore an inherent property of Mal3. Mal3–Alexa 488 also bound weakly along the entire length of MTs (Fig. 6.2b, c), a behavior that was enhanced at lower ionic strength (Fig. 6.3a). This binding might reflect the previously shown preferential association of Mal3 with the lattice seam of Taxol-stabilized MTs [193].

Two fundamentally different molecular mechanisms can be envisaged for how Mal3 accumulates at the growing MT end. Mal3 could co-polymerize in a complex with tubulin to the growing MT end, and subsequently be released. Alternatively, instead of binding to free tubulin, Mal3 could recognize a characteristic structural feature at the MT end. This structural feature could either be a collective property of several tubulin subunits such as the previously observed protofilament sheet [194] or a property of individual tubulin dimers that are in a GTP-bound versus a GDP-bound state [195]. To distinguish between a co-polymerization mechanism and an end-recognition mechanism, we measured the spatial distribution of Mal3 along MT plus-ends that were growing in the presence of various tubulin concentrations but a constant Mal3 concentration.

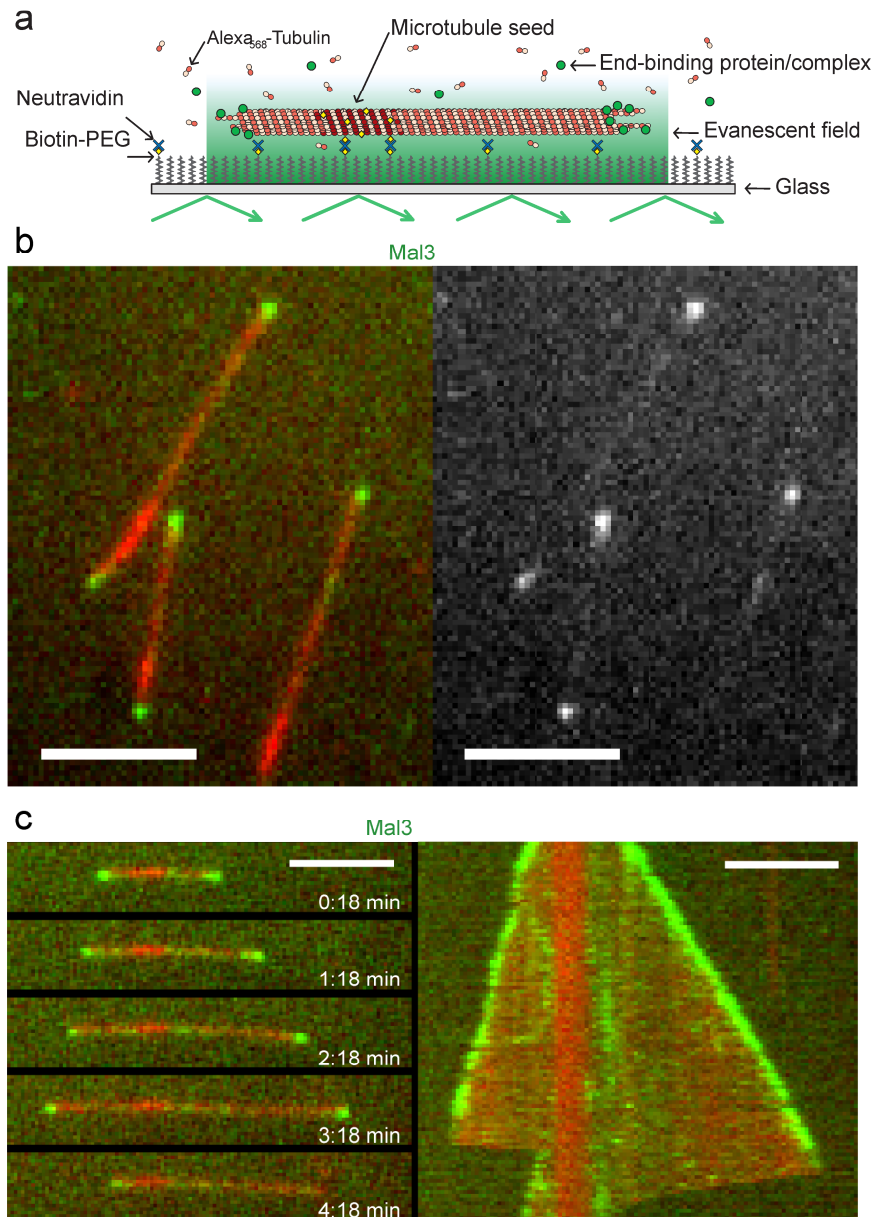


Figure 6.2

Tracking of growing microtubule ends by Mal3 *in vitro*. (A) Diagram of the experimental setup. Dynamic microtubules were grown in the presence of free Alexa 568-labeled tubulin and fluorescently labeled +TIPs from short stabilized microtubule seeds attached to a PEG-passivated glass surface by means of biotin-neutravidin links. Bright microtubule seeds, dim (non-biotinylated) microtubules extending from the seeds, and +TIPs were observed by TIRF microscopy in the evanescent field close to the glass surface. (B) Overlaid TIRF images of Mal3–Alexa 488 (green) and dynamic Alexa 568-labeled microtubules (red) (left), and for comparison the image of Mal3–Alexa 488 alone (right). (C) Time sequence of overlaid images of Mal3–Alexa 488 (green) and a dynamic Alexa 568-labeled microtubule (red) taken at the indicated times in min:sec (left), and the corresponding kymograph of the same microtubule (right). Mal3 was used at 200 nM in all end-tracking experiments, unless otherwise stated. The kymograph displays a period of 5 min. Scale bars, 5 μm.

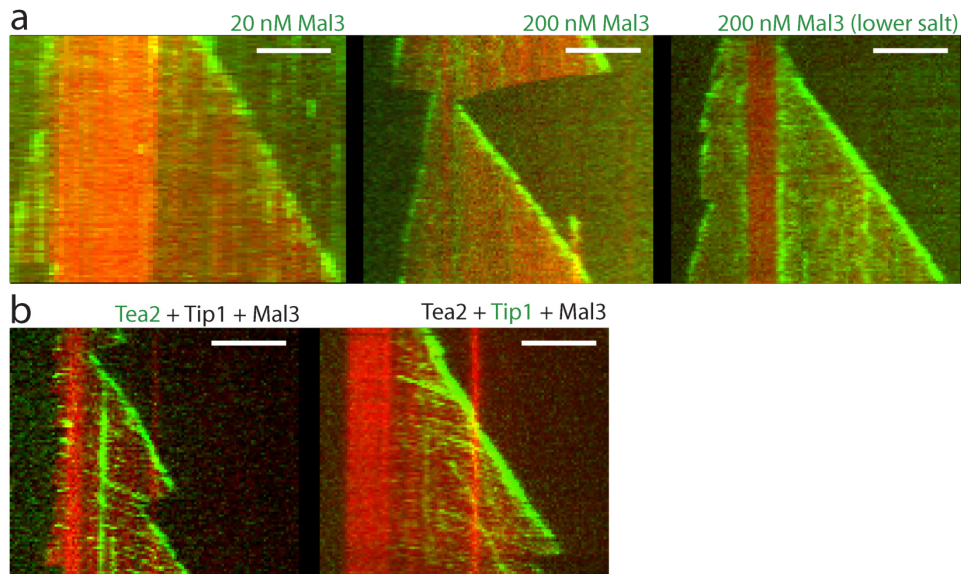


Figure 6.3

Kymographs of dynamic microtubules (red) and labeled +TIPs (green) (A) Mal3 autonomously tracks the growing microtubule end in the absence of Tea2 and Tip1 over a range of conditions: Kymographs showing end-tracking of Mal3-Alexa488 at concentrations of 20 nM (left) and 200 nM (middle) in assay buffer (same buffer that was used for experiments with dynamic microtubules). The excitation intensity was higher for the experiment with the lower Mal3 concentration, and the time-lapse was recorded with a 2-fold higher binning because of the lower level of fluorescence intensity. The kymograph with 200 nM Mal3-Alexa488 in 'lower salt assay buffer' (containing 50 mM instead of 85 mM KCl) shows also end tracking of Mal3 and increased binding to the microtubule lattice (right). The signal intensities of the two kymographs with 200 nM Mal3 can be compared (identical detection sensitivities). (B) Tea2 and Tip1 do not localize to depolymerizing microtubule ends: Kymographs showing the behaviour of Tea2-Alexa488 in the presence of Mal3 and Tip1 (left) and showing the behaviour of Tip1-GFP in the presence of Mal3 and Tea2 (right). Experimental conditions are the same as in Fig. 6.8a and Fig. 6.8c, respectively. All kymographs are projected over 5 min.

Increased MT growth velocities resulting from increased tubulin concentrations led to a more comet-shaped accumulation of Mal3–Alexa 488 at growing MT plus-ends (Fig. 6.5a). Averaged fluorescence intensity profiles of Mal3–Alexa 488 comets demonstrated that after an initial peak in fluorescence the signal decreased exponentially towards the basal lattice signal (Fig. 6.5a). The peak fluorescence of

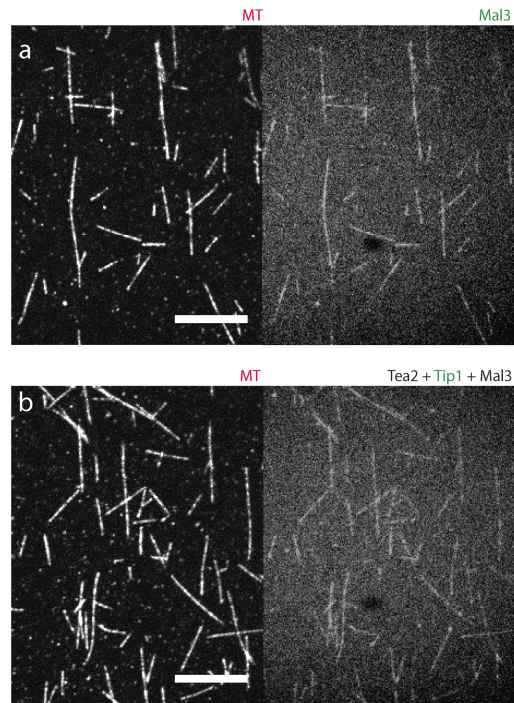


Figure 6.4

+TIPs do not accumulate at ends of static microtubules. Tetramethylrhodamine-labeled microtubules (left top and bottom) with (A) 200 nM Mal3-Alexa488 alone (right top) and (B) 8 nM Tip1-GFP in the presence of 200 nM Mal3 and 50 nM Tea2 (right bottom). To record these images, a flow chamber was first filled with 8 μ l PLL-PEG-biotin (1 mg/ml in BRB80) for 5 minutes. After washing with 100 μ l BRB80, the following washing and incubation sequence was then performed: 25 μ l streptavidin (1 mg/ml in BRB80), 5 min incubation, 25 μ l BRB80, 25 μ l κ -casein (1 mg/ml in BRB80), 5 min, 25 μ l taxol stabilised biotinylated GMPCPP microtubules (containing 15% biotinylated and 5% tetramethylrhodamine-labeled tubulin), 5 min, 25 μ l 10 μ M taxol in BRB80, 15 μ l proteins in assay buffer without tubulin and with additional 10 μ M taxol. Temperature was 28°C. Images were taken on a Leica microscope equipped with a spinning disk confocal setup (Visitech). Scale bar is 5 μ m.

Mal3 was largely insensitive to changes in the tubulin/Mal3 ratio (Fig. 6.5b). This argues against a simple co-polymerization mechanism, because such a mechanism would lead to peak signals that varied with the tubulin/Mal3 ratio. Furthermore, gel-filtration experiments showed that Mal3 does not bind to unpolymerized tubulin (Fig 6.6a). This agrees with the observation that the amount of Mal3 binding along the MT lattice is also independent of the tubulin concentration (Fig. 6.5b). Together these data

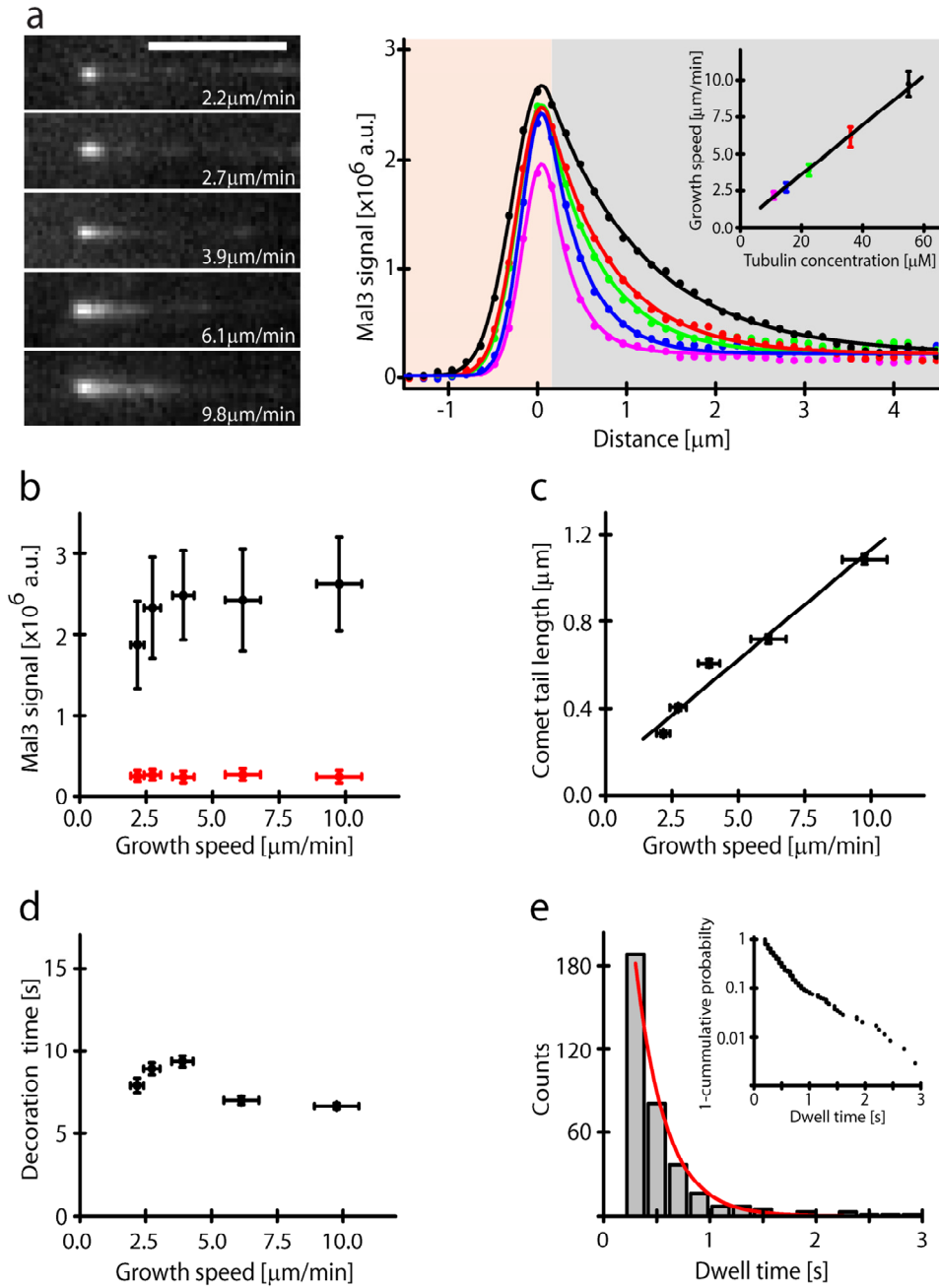


Figure 6.5

Mechanism of plus-end tracking by Mal3. (A) Images of individual Mal3–Alexa 488 comets at the indicated growth velocities (in $\mu\text{m min}^{-1}$) (left) and averaged intensity profiles of the comets (right).

Chapter VI

The Mal3–Alexa 488 concentration was 200 nM. The data (dots) were fitted (lines) using gaussian (pink area) and exponential (grey area) functions (section 6.4). The inset shows the dependence of the growth velocities on tubulin concentrations. Error bars indicate S.D. (B) The Mal3–Alexa 488 signal at the peak of the Mal3 comet (black symbols) and the signal on the MT lattice behind the comet (red symbols) as quantified separately from intensity line scans. Error bars indicate the S.D. of the maximum tip intensity and the s.d. of the averaged line scans for the lattice intensity. (C) Mal3 comet tail lengths as obtained from single-exponential fits to the averaged intensity profiles. Error bars indicate standard errors as obtained from the exponential fits. (D) The characteristic decoration time of the Mal3 signal in the Mal3 comet tail at different MT growth speeds as obtained by dividing the comet tail length by the MT growth speed. Errors were calculated by error propagation. (E) Histogram of dwell times of single Mal3–Alexa 488 events at growing MT plus-ends. The inset shows the ‘1 – cumulative probability’ distribution of dwell times. The Mal3–Alexa 488 concentration was 1 nM. The red line shows a single-exponential fit to the distribution of the individual dwell times.

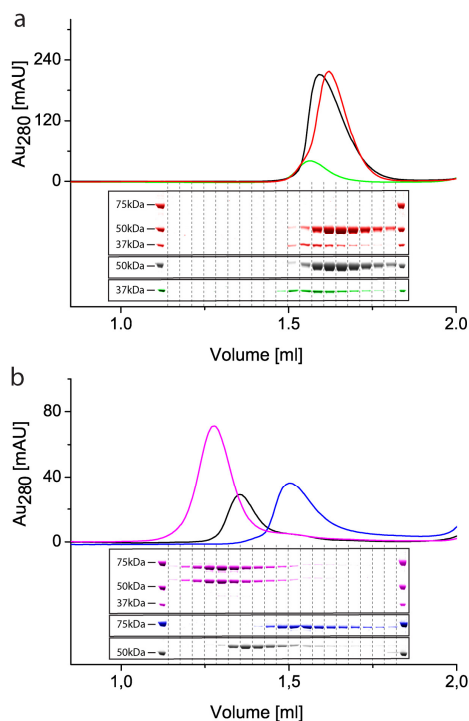


Figure 6.6

Elution profiles and Coomassie-stained SDS gels of the fractions eluted from analytical size exclusion chromatography (Superose 6) runs. (A) 60 nM tubulin alone (black), 10 nM Mal3 alone (green) or a mixture of the two proteins (red) were. Both proteins retain their position in the profile when mixed together indicating that Mal3 and tubulin do not interact in solution. (B) 10 nM Tea2 (blue) and 10 nM Tip1 (black) were loaded. When mixed (magenta), both proteins are upshifted relative to their position in the absence of the other protein, indicating that Tea2 and Tip1 form a stable complex in solution.

support a mechanism in which Mal3 tracks MT ends by recognizing a structural feature.

The characteristic comet tail length obtained from exponential fits to the decays of the averaged Mal3 fluorescence intensity profiles increased linearly with the MT growth velocity (Fig. 6.5c). This suggests that MT ends are decorated with Mal3 for a characteristic time of about 8 s, independent of MT growth velocity (Fig. 6.5d). In contrast, the dwell time of individual Mal3–Alexa 488 molecules at growing MT plus-ends, measured with greater temporal resolution under single-molecule imaging conditions, was only 0.282 ± 0.003 s (Fig. 6.5e). This indicates that individual Mal3 molecules turn over rapidly on a plus-end-specific structure that has a lifetime of about 8 s before it transforms into a normal MT lattice structure. A similarly fast turnover of Mal3 was also observed *in vivo* [190].

6.2.2 Tea2 and Tip1 are interdependent and need Mal3 to track the growing microtubule plus-end *in vitro*

In contrast to Mal3, green fluorescent protein (GFP)-tagged Tip1 and Alexa 488-labeled Tea2 did not bind significantly to the MTs in conditions under which selective end tracking of Mal3 was observed (Fig. 6.7a). Under single-molecule imaging conditions, however, rare interactions of the kinesin Tea2 with the MT could be observed at low ionic strengths with the use of higher frame rates. A gaussian fit to the velocity distribution yielded a mean velocity of $4.8 \pm 0.3 \mu\text{m min}^{-1}$, and a single-exponential fit to the ‘1 – cumulative probability’ distribution of the measured run lengths yielded an average run length of $0.73 \pm 0.01 \mu\text{m}$ (Fig. 6.7b). Because Tea2 binds *in vivo* [59] and *in vitro* (Fig. 6.6b) to Tip1, and because the motor might be auto-inhibited without its putative cargo, we tested whether Tip1 could enhance the binding of Tea2–Alexa 488 to dynamic MTs. However, this was not the case (Fig. 6.7a).

In vivo, the presence of Mal3 is needed for plus-end tracking of Tea2 and Tip1 [59, 188, 190]. Using our *in vitro* approach, we examined whether the autonomous plus-end tracking protein Mal3 is sufficient to mediate MT plus-end tracking of the processive motor Tea2 and its cargo Tip1. In the presence of Mal3 and Tip1, Tea2–Alexa 488 now strongly accumulated at growing MT plus-ends (Fig. 6.8a). No accumulation of Tea2–Alexa 488 was visible at growing minus-ends (Fig. 6.8a) or

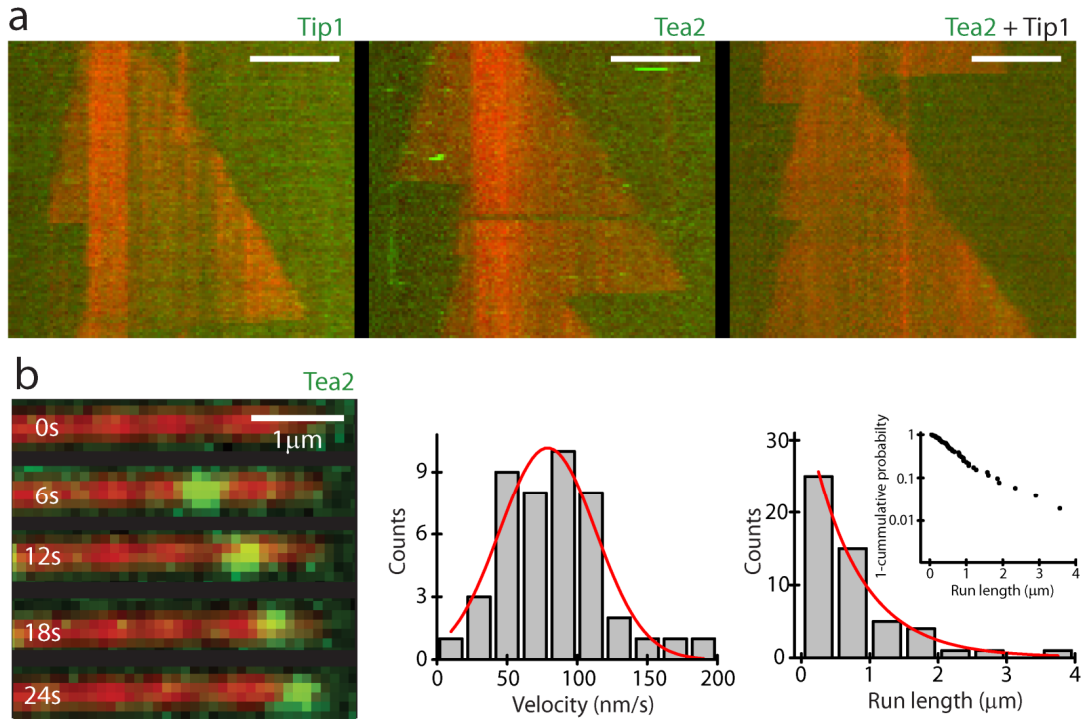


Figure 6.7

Tea2 and Tip1 individually and in combination do not track microtubule ends. (A) Kymographs of Tip1-GFP (left), Tea2-Alexa 488 (middle), and Tea2-Alexa 488 together with Tip1 (right) (labeled +TIPs in green) on dynamic Alexa 568-labeled microtubules (red). The sensitivity for GFP and Alexa 488 detection was strongly increased in comparison with that in Fig. 6.1b. Concentrations were 50 nM for Tip1 and 8 nM for Tea2 in all end-tracking experiments unless otherwise stated. The kymographs display a period of 5 min. Scale bars, 5 μm. (B) Time sequence of TIRF images of a processive run of a single Tea2-Alexa 488 moving on a stable Alexa 568-labeled microtubule, taken at the indicated times in seconds (left). The Tea2-GFP concentration was 0.5 nM. Histograms of velocities (centre) and run lengths (right) of single Tea2-Alexa 488 runs are shown; the inset shows the '1 - cumulative probability' distribution of run lengths. The red lines show a gaussian fit to the velocity distribution (centre) and a single-exponential fit to the distribution of the individual run lengths (right).

Reconstitution of a microtubule plus-end tracking system in vitro

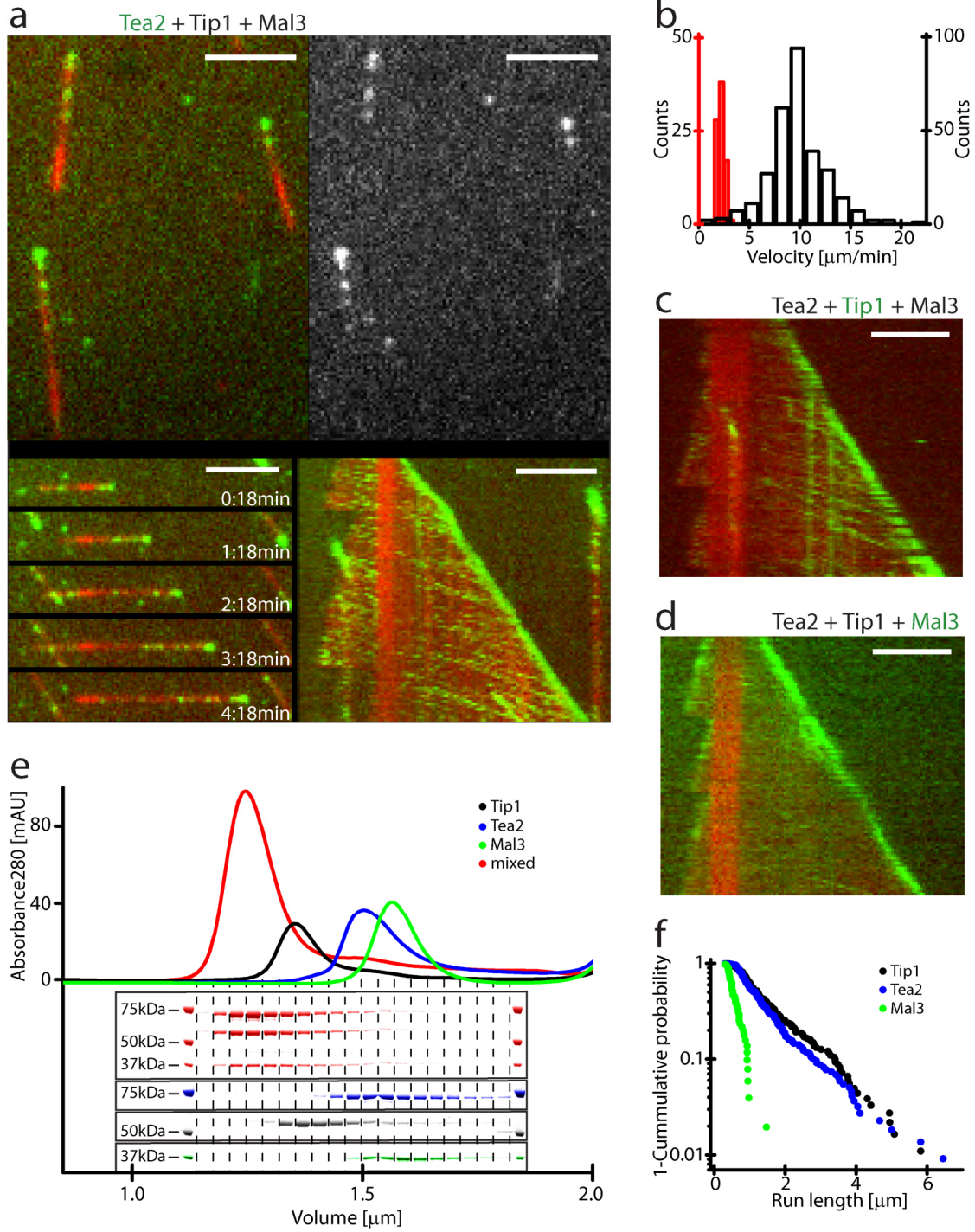


Figure 6.8

Efficient MT plus-end tracking of Tea2–Tip1 in the presence of Mal3. (A) Overlaid TIRF images showing Tea2–Alexa 488 (green) and Alexa 568-labeled MTs (red) in the presence of the two other +TIPs (top left), and for comparison an image with the signal of only Tea2–Alexa 488 (top right). Bottom left, time sequence of images (at the times shown, in min:sec); bottom right, the corresponding kymograph. Protein concentrations for Mal3 are as in figure 6.1 and for Tea2 and Tip1 as in figure 6.7a. Kymographs display periods of 5 min. Scale bars, 5 μm . (B) Histograms of the velocities of MT plus-end growth (red, left axis) and Tea2–Alexa 488 speckle movement along the MT lattice (black, right axis). The increased velocity of Tea2 speckles in comparison with single Tea2 molecules (Fig. 6.7b) is mostly a consequence of an increased temperature. (C) Kymograph showing Tip1–GFP in the presence of Tea2 and Mal3. (D) Kymograph showing Mal3–Alexa 488 (green) in the presence of Tea2 and Tip1. The signal intensity can be directly compared with figure 6.1b. (E) Gel filtrations of Mal3, Tea2 and Tip1: elution profiles and SDS gels of the corresponding eluted fractions of individual runs of Mal3 alone (green), Tea2 alone (blue), Tip1 alone (black) and an equimolar mixture of all three +TIPs (red). (F) Run-length distribution of Mal3–Alexa 488 (green), Tip1–GFP (black) and Tea2–Alexa 647 (blue) moving along the MT lattice, always in the presence of the other two +TIPs. Concentrations were 100 nM Mal3, 50 nM Tip1 and 8 nM Tea2.

depolymerizing ends (Fig 6.3b). Furthermore, Tea2–Alexa 488 speckles appeared along the MT lattice and moved towards the plus-end (Fig. 6.8a). The speed of these particles was on average $9.8 \pm 2.9 \mu\text{m min}^{-1}$ and therefore 4.4-fold faster than the velocity of MT growth ($2.2 \pm 0.3 \mu\text{m min}^{-1}$; Fig. 6.8b). Tip1–GFP moved similarly along the MT lattice and also tracked growing MT plus-ends (Fig. 6.8c), but not depolymerizing ends (Fig 6.3b) or the ends of static MTs (Fig. 6.4b). Mal3–Alexa 488, in contrast, was not observed to move along the MT to the same extent as Tea2 and Tip1 (Fig. 6.8d). These observations very closely mimic the situation *in vivo* [59, 188, 190].

Gel filtrations demonstrated that in solution Mal3, Tea2 and Tip1 exist as a stable ternary complex (Fig. 6.8e). It is therefore most likely that the formation of this complex is required for efficient binding of Tea2–Tip1 to the MT. However, the three proteins do not behave in the same way once bound to the MT. Imaging the movements of the three proteins on the MT lattice with greater temporal resolution showed that Tip1–GFP and Alexa 647-labeled Tea2 co-migrate, indicating that Tea2 indeed transports Tip1. Consistent with this was our observation that the average run lengths for Tea2 and Tip1 were very similar, at 0.90 ± 0.01 and $1.10 \pm 0.01 \mu\text{m}$, respectively (Fig. 6.8f). In contrast, Mal3–Alexa 488 showed only short runs with an

average run length of $0.29 \pm 0.01 \mu\text{m}$ (Fig. 6.8f). This demonstrates that Mal3 is initially transported by Tea2, but dissociates shortly after a productive binding event.

We confirmed that Mal3-mediated recruitment of Tea2–Tip1 to the MT lattice requires the interaction of Mal3 with the amino-terminal extension of the kinesin Tea2 [156]. Replacing full-length Tea2 with a construct lacking the N-terminal extension (ΔNTea2) abolished efficient binding of Tip1–GFP to the MT (Fig. 6.9a). In addition, Mal3-mediated recruitment of the Tea2–Tip1 complex requires the presence of both Tea2 and Tip1. Tea2–Alexa 488 was hardly present on MTs in the absence of Tip1 (Fig. 6.9b) and Tip1–GFP was not significantly bound to MTs in the absence of Tea2 (Fig. 6.9c), whereas binding of Mal3–Alexa 488 to MTs was unaffected in both cases (Fig. 6.9d and data not shown). The results with the double combinations of proteins (Fig. 6.7a, right, and Fig. 6.9b–d) exactly mimic the *in vivo* single-deletion mutants of *mal3*, *tea2* and *tip1* [59, 188, 190].

Replacing ATP with ADP eliminated the efficient binding of Tea2–Alexa 488 along the MT lattice and the tracking of MT plus-ends, despite the presence of all three proteins (Fig. 6.9e). Only a very weak fluorescence signal could be observed at growing MT ends, but without a preference for the plus-or minus-end (Fig. 6.9e). This demonstrates that *in vitro* the processive motor activity of Tea2 is essential for efficient MT-end tracking of Tea2–Tip1 and also for their plus-end preference.

6.3 Discussion

In living cells, single deletions of Mal3, Tea2 or Tip1 suggested that these three +TIPs mainly decrease the frequency of MT catastrophes without strongly affecting the other parameters of MT dynamic instability [59, 70, 189]. We tested the direct effects of Mal3 alone and of Mal3 with Tea2 and Tip1 on MT dynamics under conditions of selective end tracking. We imaged MTs in the presence of unlabeled +TIPs by differential interference contrast microscopy. Similar to the situation *in vivo*, neither Mal3 alone nor the combination of all three proteins had a strong effect on the growth and shrinkage velocities of MT plus-ends (Table 6.1). However, Mal3 alone increased the frequencies of catastrophes and rescues. The addition of Tea2–Tip1 counteracted these effects of Mal3 (Table 6.1). These results show that especially the effect of Mal3 on the catastrophe frequency is different from what would be expected from the corresponding deletion *in vivo*. This is not surprising, because several other proteins not studied here are known to affect the catastrophe frequency [196, 197]. By including these other modulators of MT dynamics in the future, our *in vitro* system

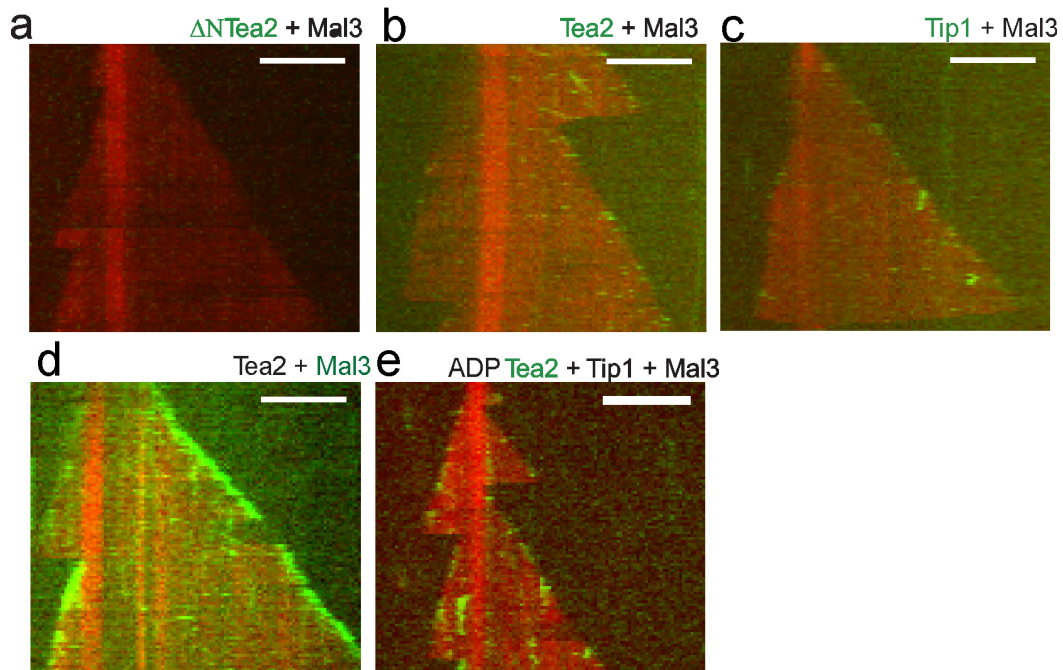


Figure 6.9

All three +TIPs and the motor activity of Tea2 are required for microtubule plus-end tracking of the Tea2/Tip1 complex. Kymographs of dynamic microtubules (red) and various combinations of +TIPs. (A) Tip1-GFP (green) cannot bind the microtubule or track ends efficiently in the presence of Δ NTea2 and Mal3. The signal intensity can be directly compared with Fig. 6.8c (identical detection sensitivity). (B) Tea2-Alexa488 (green) in the presence of Mal3 alone does not bind efficiently to microtubules. The fluorescence signal can be directly compared to Fig. 6.7 (C) Tip1-GFP (green) in the presence of Mal3 alone does not bind efficiently to microtubules. The fluorescence signal can be directly compared to Fig. 6.8a. (D) Mal3-Alexa488 (green) in the presence of Tea2 alone tracks growing microtubule ends. The fluorescence signal can be directly compared to Fig. 6.1b and Fig 6.8d. (E) The motor activity of Tea2 is required for its microtubule plus-end tracking ability: Tea2-Alexa488 (green) in the presence of Mal3, Tip1 and ADP instead of ATP. The signal intensity can be directly compared to Fig. 6.8a. Kymographs display periods of 5 min. Scale bars are 5 μ m.

promises also to lead to the identification of the more complex minimal system that reproduces physiological MT dynamics.

Thus, we have identified Mal3 as an autonomous tracking protein of growing MT ends *in vitro*. Mal3 most probably recognizes a structural feature at MT ends rather than co-polymerizing as a tubulin–Mal3 complex. As *in vivo*, the behavior of

+TIPs present	V_{growth} [μm/min] (n)	V_{shrink} [μm/min] (n)	T_{cat} [sec] (n)	N_{res} in total shrinkage time [sec]
none	1.2 ± 0.2 (62)	26 ± 9 (41)	650 ± 80 (69)	0 in 322
Mal3	1.3 ± 0.2 (63)	26 ± 8 (74)	230 ± 20 (132)	8 in 314
Mal3 Tip1 Tea2	1.3 ± 0.2 (54)	27 ± 9 (40)	410 ± 50 (61)	4 in 321

Table 6.1

Dynamic instability parameters of MTs in the absence and presence of +TIPs. 'V_{growth}' is the weighted

average growth time $\bar{V}_{growth} = \frac{\sum_{i=1}^N V_i T_i}{\sum_{i=1}^N T_i}$ with T_i being the time of growth event i. The error on

V_{growth} is the weighted standard deviation $sd = \sqrt{\frac{N}{N-1} \frac{\sum_{i=1}^N (V_i - \bar{V}_g)^2 T_i}{\sum_{i=1}^N T_i}}$. 'V_{shrink}' idem 'V_{growth}'. 'T_{cat}' is

the sum over all growth times divided by the number n of catastrophes observed. 'Error Tcat' is the statistical error $err = \frac{\bar{T}}{\sqrt{N}}$. N_{res} is the total number of rescues observed in the total shrinkage time.

Mal3 *in vitro* does not depend significantly on the presence of Tea2 or Tip1. Furthermore, we identified Mal3–Tea2–Tip1 as a minimal system producing plus-end tracking behavior of Tea2 and Tip1 *in vitro*. This suggests that *in vivo* Tea2, Tip1 and Mal3 may also work as a MT plus-end tracking system, independently of other +TIPs. However, *in vivo* part of the Mal3 pool might simultaneously function in 'parallel' end tracking systems. The role of Mal3 as a loading factor of Tea2–Tip1 involves the initial formation of a ternary complex that promotes productive encounters of Tea2–

Tip1 with the MT lattice. Tip1 is subsequently transported by the processive motor Tea2, whereas Mal3 rapidly dissociates and is transported for only short distances.

Our *in vitro* system provides a powerful new tool to test the proposed mechanisms for MT end targeting of different +TIPs [191, 198, 199] and to analyze the interplay between plus-end tracking and the dynamic properties of MTs that are ultimately responsible for the morphogenetic function of the MT cytoskeleton.

6.4 Materials and Methods

6.4.1 Protein Biochemistry

The full length *tea2* ORF from *S.pombe* and a *tea2* fragment lacking the initial 363 nucleotides were cloned into a modified pETM expression vector (gift of G. Stier) creating fusions of the *tea2* sequence separated by a short linker and a TEV protease cleavage site from an N-terminal z-tag (the IgG binding domain from Protein A) and a hexa-histidine tag (coding for z-Tea2 and z- Δ NTea2, respectively). For labelling with a cysteine reactive dye a similar construct with an additional glycine and cysteine at the C-terminus of Tea2 was generated (coding for z-Tea2-Cys). The recombinant fusion proteins were expressed in *E. coli* (BL21(DE3) CodonPlus-RIL induced with 0.2 mM IPTG for 16 h at 18°C). Harvested cells were resuspended in ice-cold buffer A (50 mM KPi with pH 8.0, 400 mM NaCl, 2 mM MgCl, 0.2 mM MgATP (adenosine-5'-triphosphate supplemented with equimolar MgCl₂), 5 mM mercaptoethanol) containing protease inhibitors (Roche) and lysed using an Emulsiflex C-5. Clarified lysates were loaded onto a Talon column (Clontech), the column was washed with buffer A containing 15 mM imidazole and proteins were eluted in buffer A containing 150 mM imidazole. The tag was cleaved off over night by His-tagged TEV protease at 4°C (1 mg protease per 50 mg substrate). The cleaved proteins (Tea2, Δ NTea2, Tea2-Cys) were dialyzed into buffer A, subsequently passed through a TALON column to remove the z-tag and the TEV protease and were frozen in liquid nitrogen. The storage buffer of the Tea2 constructs with the C-terminal cysteine contained 5 mM TCEP instead of β -mercaptoethanol.

To generate Tip1-GFP, the full length *tip1* ORF from fission yeast was PCR amplified and ligated into a modified pHAT2 expression vector, thereby fusing an eGFP-tag to its N-terminus. The protein was expressed in *E. coli* (BL21(DE3) induced with 0.2 mM IPTG for 16h at 22°C). Harvested cells were resuspended in ice-cold buffer B (50 mM KPi with pH 7.4 100 mM NaCl, 5 mM mercaptoethanol) containing protease inhibitors (Roche) and were lysed using an Emulsiflex C-5.

Clarified lysates were loaded onto a Talon column (Clontech), the column was washed with the corresponding buffer B containing 15 mM imidazole and proteins were eluted in buffer B containing 150 mM imidazole. After elution Tip1-GFP was dialyzed against buffer B and was frozen in liquid nitrogen.

Tip1-GST was cloned by PCR amplification of the full length tip1 ORF from a preexisting construct and was subsequently ligated into the expression vector pGEX-6P-1 (Amersham). The fusion protein was expressed and purified as described [70]. To remove the GST-tag, Precision protease (1 mg protease per 100 mg substrate, Amersham) was added to purified Tip1-GST and after 2h incubation on ice, the mix was passed twice over a glutathion Sepharose (Amersham) column. The purification of Mal3 [193] and of tubulin [200] were performed as previously described. Protein concentrations of +TIPs were determined by Bradford using BSA as standard, while tubulin concentrations were determined by measuring the absorbance at 280 nm.

6.4.2 Protein labeling

To generate fluorescently labeled Tea2, 20 μ M Tea2-Cys was incubated with 1.2 mM Alexa Fluor 488 C5 maleimide or Alexa Fluor 647 C2 maleimide (both Molecular Probes) for 4 h at 16°C. To generate fluorescently labeled Mal3, 200 μ M Mal3 was incubated with 6 mM Alexa Fluor 488 FTP ester (Molecular Probes) for 3 hr at 16°C. Excess dye was separated from protein by two consecutive passages of the reaction mix through Biospin 6 desalting columns. Functionality of labeled Mal3 was demonstrated in turbidity experiments. For single molecule experiments, fast dual-color imaging and run length determination in the presence of all +TIPs, proteins were gelfiltrated over a Superose 6 10/300 GL after labeling. The labeled proteins were frozen in liquid nitrogen. Labelling ratios ranged between 0.76 and 1.05 of dye per protein molecule. Labelling of tubulin with Alexa Fluor 568 carboxylic acid succinimidyl ester (Molecular Probes) and with 6((biotinoyl)amino)hexanoic acid, succinimidyl ester (Molecular Probes) was performed as described [201].

6.4.3 Analytical Gel filtration

50 μ l of 10 nM Mal3, Tea2, Tip1 and/or 60 nM tubulin were incubated in gel filtration buffer (80 mM K-PIPES at pH 6.8, 85 mM KCl, 4 mM MgCl, 1 mM GTP, 1 mM EGTA, 10 mM β -mercaptoethanol) either individually or in combinations, as indicated, on ice for 15 min before loading on a Superose6 PC 3.2/30 equilibrated in gel filtration

buffer using a SMART FPLC system (Amersham Biosciences). The absorbance of the eluted protein was measured at 280 nm. Fractions of 36 μ l were collected, supplemented with SDS sample buffer and separated on 4-12% bis-tris acrylamide gels (Invitrogen). Proteins were stained with Coomassie Brilliant Blue.

6.4.4 Turbidity measurements

To confirm that fluorescently labeled Mal3 is still functional, we measured the kinetics of the change of light scattering caused by a suspension of polymerizing MTs [202] in the presence or absence of Mal3, as previously described [193]. Briefly, polymerization of MTs was induced by heating a solution of 21 μ M tubulin with 4.2 μ M Mal3 or Mal3-Alexa488 to 37°C. The optical density was measured at 350 nm.

6.4.5 Glass surface treatment

To functionalize glass coverslips with biotin-PEG, coverslips were cleaned, silanized with (3-glycidyloxypropyl)trimethoxysilane (GOPTS), functionalized with diamino poly(ethylene glycol) (DAPEG) as described [203], and treated with 100 mM NHS-biotin in DMF for 1 h at 75°C. The biotin-PEG functionalized slides were washed two times in DMF, then five times in water, spin-dried and stored at 4° for up to two months. To generate passivated glass, 20 μ l PLL-PEG (1 mg/ml poly-L-lysine (20 kDa) grafted to polyethylenglycol (5 kDa) with 3.5 lysine units per PEG chain) in PBS was dried on a glass surface followed by extensive washing with water.

6.4.6.1 End-tracking assay 1

Coverslips and microscope slides were cleaned in chromosulphuric acid. A flow cell was constructed by drawing two parallel lines of vacuum grease approximately 5 mm apart on a clean microscope slide, and by mounting a clean coverslip on top. A solution of 10 μ l of 0.2 mg/ml PLL-PEG-biotin (SurfaceSolutions) was flown, so that 10 μ l filled the flow cell, and incubated for 5 minutes in order to form a good monolayer. The flowcell was washed with 150 μ l assay buffer (including 2 mM ATP). The flow cell was blocked with 0.5 mg/ml κ -casein in assay buffer for 5 minutes. Afterwards the flowcell was incubated with streptavidin (0.5 mg/ml streptavidin in assay buffer) for 5 minutes. The streptavidin was washed away with 50 μ l assay buffer. GMP-CPP MTs (containing 15% biotinylated tubulin) in 20 μ l assay buffer were flown in and incubated for 5 minutes. After washing the MTs away 20 μ l of the assay

mix was introduced (20 μM tubulin, 1 μM rhodamine tubulin, 0,1% methyl cellulose (4000cP; Sigma), 0.2 mg/ml α -casein, 0,2 mg/ml κ -casein, in MRB50 with 50 M KCl together with the +TIP proteins at indicated concentrations). The final concentrations of the +TIP proteins were 2.5 μM Mal3, 40 nM Tip1-GFP and 100 nM Tea2. The sample was sealed with candlewax. The experiments were performed at 25 °C. The MTs were imaged using a Spinning Disk Confocal Microscopy on an inverted Leica microscope with a spinning disk from Yokogawa. Images were taken every 3 seconds.

6.4.6.2 End-tracking assay 2

Flow chambers consisting of a biotin-PEG functionalized coverslip and a PLL-PEG passivated glass separated by double-sided tape (Tesa) were prepared in a heated room ($30 \pm 1^\circ\text{C}$). The chamber was then equilibrated with assay buffer (80 mM K-PIPES at pH 6.8, 85 mM KCl, 4 mM MgCl, 1 mM GTP, 1 mM EGTA, 10 mM β -mercaptoethanol and 2 mM MgATP or MgAMP-PNP or 5 mM MgADP) and potential residual non-specific binding sites were blocked by flowing in 1% Pluronic F-127 and 50 $\mu\text{g}/\text{ml}$ κ -casein in assay buffer. The channels were then incubated with 50 $\mu\text{g}/\text{ml}$ neutravidin and 50 $\mu\text{g}/\text{ml}$ κ -casein in assay buffer on ice for 5 min, washed with a minimum of 15 chamber volumes of assay buffer, and incubated with brightly labeled, short GMP-CPP MTs (containing 20% Alexa₅₆₈ labeled tubulin and 7.7% biotinylated tubulin) in assay buffer at room temperature for 5 min. MT growth was then initiated by flowing in 11 μM dimly labeled tubulin (containing 6.7% Alexa₅₆₈ labeled tubulin and no biotinylated tubulin) together with +TIP proteins at the indicated concentrations in assay buffer containing 0,1% methyl cellulose (4000cP; Sigma) and oxygen scavengers (20 mM glucose, 200 $\mu\text{g}/\text{ml}$ glucose oxidase, 400 $\mu\text{g}/\text{ml}$ catalase). In some experiments with Mal3, the tubulin concentration was varied in order to vary the MT growth rate (Fig. 6.4). If not stated otherwise, the final concentrations of the labeled and unlabeled +TIP proteins were 200 nM Mal3, 50 nM Tip1 and 8 nM Tea2. The temperature was maintained at $30 \pm 1^\circ\text{C}$. For the direct visualization of co-migration of Tea2 and Tip1 and for the measurements of the individual run lengths of +TIPs after landing as a ternary complex to the MT lattice, the Mal3 concentration was lowered to 100 nM in order to reduce the density of transport events on the MTs.

For the analysis of the individual run length of +TIPs after landing of the ternary complex, two sets of experiments were performed using combinations of Tea2-Alexa647 with either Tip1-GFP or Mal3-Alexa488 in the same flow cell. The run length of Tea2 was evaluated and found to be similar for both sets of experiments.

Since the Tea2 run length was the same in the presence of Mal3-Alexa 488 and unlabeled Mal3, we concluded that Mal3 labeling did not impair the function of the protein. For the determination of the dwell time of single Mal3 molecules at the MT plus-end, the Mal3-Alexa488 concentration was lowered to 1 nM to allow for the direct visualization of individual end-binding events. The tubulin concentration was set to 36 μ M to be able to visualize Mal3 end-binding over a larger tip region.

6.4.7 Tea2 single molecule assay on static microtubules

Single molecule studies utilize prepolymerized taxol-stabilized MTs (containing 5% Alexa-568 labeled tubulin and 5% biotinylated tubulin) immobilized on a coverslip surface in a manner identical to that used to link the GMPCPP MT seeds used in the dynamic MT studies. Following the immobilization of the MTs, the fluid in the chamber was exchanged for BRB80 (80 mM K-PIPES at pH 6.8, 2 mM MgCl, 1 mM EGTA) with 20 μ M taxol. The final experimental solution was 12 mM K-PIPES at pH 6.8, 50 mM KCl (for Tea2) or 100 mM KCl (for Mal3), 2 mM MgCl₂, 1 mM EGTA, 10 mM β -mercaptoethanol, 10 μ M taxol containing oxygen scavengers as above. The final protein concentrations were either 0.5 nM Tea2-Alexa-488 or 2 nM Mal3-Alexa488.

6.4.8 TIRF Microscopy

MTs and MT-associated proteins were visualized by two color total internal reflection fluorescence microscopy using a custom system constructed around an Olympus IX71 microscope chassis as described [204] with the exception that this work utilized a 100x TIRF objective (Olympus) and a Cascade II, cooled CCD camera (Photometrics/Roper Scientific). The laser power was adjusted using an acousto-optical filter (AOTF) depending on the available signal intensity under different experimental conditions. Therefore, fluorescence intensities are not directly comparable between experiments, if not stated otherwise.

Standard two color time-lapse imaging for the localization of +TIPs on dynamic MTs was performed at 1 frame/3 sec with a 100 ms exposure time. For one color experiments, the frame rate was increased to 2 frames/sec for the run length analysis of +TIPs on the lattice of dynamic MTs and to 20 frames/sec (with a 50 ms exposure time) for the dwell time analysis of single Mal3 molecules at the MT plus-end. The frame rate for single molecule imaging of Tea2 on static MTs was 2 frames/sec.

For the simultaneous dual-color TIRF imaging for colocalization of Tea2 and Tip1, the TIRF setup was modified to include two high speed filter wheels allowing excitation and emission filters to be removed from the central filter turret and placed external to the microscope. The central microscope turret-mounted wheel was held at a single position with a multi-band pass mirror and the external filter wheels were used to change emission and excitation filters. Interspersed time-lapse image sequences were recorded at 1 frame/sec.

6.4.9 Data analysis of Mal3 comets

To analyze the fluorescence intensity of Mal3 'comets' at growing MT plus-ends, intensity line-scan profiles of over fifty individual growing MT plus-ends were first aligned to each other. Each individual intensity line-scan profile started in solution at a distance of 1.5 μm from the MT plus-end and extended over 5 μm of the MT. Alignment was based on a Gaussian fit to the first part of the profile starting in solution and reaching the second pixel after the maximum value. The position of the maximum of the fit was set to zero and used to align the profiles. The data of all aligned intensity scans were then binned into single-pixel-sized bins and afterwards averaged by dividing the sum of values within individual bins by the total number of profiles. The part of the averaged intensity profile starting one pixel behind the maximum was found to decay exponentially. Simultaneous exponential fits ($I = I_0 \cdot \exp(x/d) + I_{\text{lattice}}$) to the decaying parts of the intensity profiles measured at different MT growth rates yielded the Mal3 comet tail lengths d and the lattice signal I_{lattice} that was a shared parameter for the fits. The characteristic decoration time for Mal3 at the MT end was determined by dividing comet length by growth speed for each growth velocity condition. The error of the comet tail length represents the standard error of the exponential fit. The error of the decoration time was calculated by error propagation from the standard errors of the growth rates and the fitted comet tail length.

The maximum intensity of Mal3 at the MT tip and the standard deviation were extracted from the averaged intensity profiles. The intensity of Mal3 on the MT lattice was quantified separately. Intensity line scans were performed along 6-16 μm long stretches of MT lattice and adjacent (1 μm away) to the analyzed MT to account for the background signal level. The difference between these two intensity scans yielded the Mal3 signal on the MT lattice. Mal3 signals from 15 stretches of MT lattice were

measured per tubulin concentration yielding the average Mal3 signal and the standard deviation.

6.4.9 Analysis of TIRF data with dynamic microtubules

For the determinations of the speeds of growing MT ends and of speckle of Tea2, Tip1 or Mal3 moving along MT and for run length analysis, movements were first analyzed with the ‘MultipleKymograph’ plug-in for ImageJ by Arne Seitz (<http://www.embl.de/eamnet/html/Kymogrph.html>). Average velocities of Tea2 speckles and growing Alexa568-MTs and their standard deviation (Fig. 6.8c) were obtained from velocity histograms generated from 70 MTs from three independent experiments.

Average run lengths of Tea2, Tip1 and Mal3 speckles and their standard error (Fig. 6.8f) were obtained from single exponential fits to cumulative probability distributions of the individual travel distances as determined by kymograph analysis from two independent experiments for each protein. The total number of events analyzed was $n=198$ for Mal3-Alexa488, $n=520$ for Tea2-Alexa647 and $n=182$ for Tip1-GFP. For the analysis of the dwell time of individual Mal3 end-binding events (Fig. 6.4e), continuously growing MT plus-ends were selected based on images of growing MTs taken directly (1s) before and after a fast Mal3 time-lapse sequence (Fig. 6.6). Dwell times of individual binding events within the tip region (1.5 μm from the very tip of the MT to the end of the comet tail), were extracted by kymograph analysis. The average dwell time and the standard error (Fig. 6.8f) were obtained from a single exponential fit to the cumulative probability distribution of the individual dwell times from three independent experiments. In total 351 events were analyzed.

6.4.10 Analysis of TIRF data with static microtubules

Single molecule motility of Tea2 was analyzed by kymograph analysis and by automated particle tracking implemented in a custom software environment [54]. Briefly, this routine uses a statistical algorithm to determine if spots of more intense signal are indeed above the background camera signal. Once identified, each bright area is fit to a Lorentzian function providing the location of the center of the object in the image. After all objects are found in each image a second algorithm determines which spots in each image are likely to be same motor protein in a subsequent image and based on this information assembles the particles into tracks. Under conditions where the particle’s landing on MTs are sparse, the algorithm determines tracks at

least as well as kymograph analysis and allows for the tracking of frame to frame displacement and object brightness in a straightforward and convenient manner. At several stages in the analysis, the performance of the algorithm is checked against kymographs. A best fit line was applied to the distance vs. time data for each track and the resulting slope was used as the average velocity. Run lengths were calculated by multiplying the track's duration with the average velocity of the fit thus preventing a single noisy data point at the end or beginning of a track from skewing the run length. For the purposes of creating the velocity distributions, only particles that moved a minimum of 200 nm (~4-8 times the positional uncertainty of a single particle tracked by the algorithm) were included because short runs, which consist of the fewest images and therefore the fewest measured particle positions, have the greatest chance of producing errant velocities.

6.4.11 DIC assay to determine microtubule dynamic instability parameters

Coverslips and microscope slides were cleaned in chromosulphuric acid. A flow cell was constructed by drawing two parallel lines of vacuum grease approximately 5 mm apart on a clean microscope slide, and by mounting a clean coverslip on top. A solution of 10 μ l of 0.2 mg/ml PLL-PEG-biotin (SurfaceSolutions) was flown, so that 10 μ l filled the flow cell, and incubated for 5 minutes in order to form a good monolayer. The flowcell was washed with 150 μ l assay buffer (including 2 mM ATP). The flow cell was blocked with 0.5 mg/ml κ -casein in assay buffer for 5 minutes. Afterwards the flowcell was incubated with streptavidin (0.5 mg/ml streptavidin in assay buffer) for 5 minutes. The streptavidin was washed away with 50 μ l assay buffer. GMP-CPP MTs (containing 15% biotinylated tubulin) in 20 μ l assay buffer were flown in and incubated for 5 minutes. After washing the MTs away 20 μ l of the assay mix was introduced (10 μ M tubulin, 0,1% methyl cellulose (4000cP; Sigma), 0.2 mg/ml α -casein, 0,2 mg/ml κ -casein, in assay buffer together with the +TIP proteins at indicated concentrations). The final concentrations of the +TIP proteins were 200 nM Mal3, 50 nM Tip1 and 8 nM Tea2. The sample was sealed with candlewax. The experiments were performed at 30 °C.

6.4.12 DIC microscopy

Samples were observed on an inverted microscope (DMIRB, Leica Microsystems, Rijswijk, the Netherlands) with a 100x 1.3 NA oil immersion objective by video-

enhanced differential interference contrast (VE-DIC) microscopy. The temperature in the sample was adjustable by a sleeve around the objective lens, which was controlled by thermoelectric coolers (Melcor). Images were recorded by a CCD camera (CF8/1, Kappa) and sent to an image processor (Argus 20, Hamamatsu). The resulting image stream was both burned on a DVD and digitized at a rate of 1 frame every 2 s online.

6.4.13 Analysis of DIC data

For the analysis of MT dynamics, for every condition DIC data was collected from three independent experiments and for every experiment at least 10 MTs were analyzed by kymographs. The growth or shrinkage velocities (V_{growth} or V_{shrink}) were measured from manual fits to the growth/shrinkage parts of kymographs. The average velocity is the average over all events weighed with the time of the individual events. The error is the weighted standard deviation. The catastrophe or rescues time (T_{cat} or T_{res}) was determined by dividing the total growth or shrinkage time by the total number of catastrophes or rescues observed. The error is the statistical error given by the catastrophe or rescues time divided by the square root of observed events.

6.5 Acknowledgements

The work presented in this chapter is a shared effort of Peter Bieling and Henry Schek the 3rd from the group of Thomas Surrey, Linda Sandblad from the group of Damian Brunner, and E. Laura Munteanu and myself from Marileen Dogterom's group. The groups of Thomas Surrey and Damian Brunner are located at the EMBL in Heidelberg, Germany. End-binding experiments using spinning disk confocal fluorescence microscopy and microtubule dynamics experiments using VE-DIC microscopy were performed at AMOLF. End-binding and single molecule experiments using TIRF microscopy and gel-filtration experiments were performed at the EMBL.

Chapter VII:

Concluding remarks and additional research directions

We have characterized how dynein, attached to a growth-opposing barrier, can regulate and pull on dynamic MT ends, mimicking a specific interaction at the cell cortex in chapter 4. Interestingly the cell exploits the cell boundary in many more ways for cellular organization. This chapter starts with concluding remarks about follow-up experiments, mainly focused on chapter 5 (section 7.1). Subsequently three mechanisms involving interactions of MTs with the cell cortex and the (preliminary) experiments that address them are described. In section 7.2 the influence of force on the regulation of MT dynamics by plus-end binding proteins is discussed. In vivo it has been suggested that MAPs (MT Associated Proteins) can act as a cell boundary sensor for MTs, by rapidly inducing catastrophe as soon as the MT grows against the cortex [64]. We show preliminary results on the effect of force on the regulation of MT dynamics by Mal3 (see also chapter 6). In section 7.3 the capture of dynamic MT ends by non-motor proteins is studied, which is thought to play an important role in cellular polarization [73, 74]. In vivo data suggest that the interaction of two proteins, IQGAP1, which is localized at the cortex, and CLIP170, which tracks the growing MT end, can capture and stabilize dynamic MTs [80, 205]. In section 7.4 we exploit our in vitro assay to study this interaction. The first steps towards reconstituting delivery of proteins at the tip of MTs to the cell cortex are described, a mechanism present in many different cells [46].

7.1 Positioning processes based on microtubule pulling forces

7.1.1 Studying the role of geometry in cellular organization in lipid droplets

In chapter 5 we have studied the role of pulling forces in positioning processes. In this experiment motor proteins are stably attached to a rigid microfabricated chamber wall. This is an appropriate model system for cells with a hard boundary where cortical anchors are embedded in the actin cortex and cannot move. In many cells however cortical attachment sites are not firmly bound, but can move through the membrane, for example in budding yeast cells [206]. In this situation the sliding mechanisms we presented in chapter 5 will be more complex because captured MTs will also reposition. It will be exciting to investigate what the effect of mobile capturing sites is on MT-based positioning processes. A possible approach to this question will be to confine MT asters in lipid droplets with, for example, dynein molecules specifically bound to the inside of the lipid layer. Droplets are small containers encapsulating aqueous solution, separated by a lipid monolayer from the surrounding oil. It has been shown that it is possible to encapsulate and anchor active proteins in lipid droplets [207]. By a well-designed micro fluidics system biotinylated lipid droplets can be merged [208], allowing for sequential introduction of, for example, streptavidin, biotinylated dynein and centrosomes with tubulin. By confining the lipid droplets in narrow micro fluidic channels the geometry of the droplet can then be manipulated [208]. This experiment may be the logical next step in understanding the role of pulling forces in MT positioning processes.

7.1.2 The role of geometry in spindle positioning in first cell stage *C. elegans* embryos

We have shown in chapter 5 that, pulling forces can center a MT aster in a microfabricated chamber when coupled to MT sliding. It is hard to anticipate how relevant this mechanism is *in vivo*. It would be fascinating to physically deform the *C. elegans* embryo and study the positioning of the mitotic spindle in this deformed embryo, similar to recent experiments with *S. pombe* cells, where the cells were physically forced to grow in a bent shape, and thereby reorganized their MT array [209, 210]. It is hard to predict how difficult or simple it will be to physically deform the *C. elegans* embryo, but it would be very interesting to study the role of geometry on the

MT organization in these more complex cells, and compare it to both *in vitro* experiments and theoretical models that describe MT based positioning processes.

7.2 Regulation of microtubule dynamics by a combination of force and +TIPs

7.2.1 Introduction

Recent studies in *S. pombe* cells in interphase showed that interaction with the cell cortex, particularly at the cell ends, regulates MT dynamics [64, 70]. There is increasing evidence that this regulation is partly due to compressive forces generated by MTs growing against the cell end [64, 113]. The compressive forces reduce the growth velocity, which possibly directly reduces the catastrophe rate, as observed *in vitro* [72]. In addition there are proteins, like the kinesin-8, KLP5/6, that regulate the MT dynamics at the cell cortex [64]. It is suggested that KLP5/6, which is a catastrophe-inducing motor protein, can sense the MT growth velocity. It accumulates at the MT plus-end of slower growing MTs and in this way enhances the catastrophe rate at the cell ends.

Our goal is to study the combined effect of force and +TIPs on the regulation of MT dynamics. We hope to unravel mechanisms that are relevant for many different cell types that exploit physical barriers and +TIPs to locally regulate MT dynamics [46, 211]. We use an *in vitro* assay where MTs are grown against glass barriers in the presence of one or more +TIPs [72, 88]. We are interested in the effect of force on the regulation of MT dynamics by Mal3, Tea2 or Tip1. Tip1 is an especially interesting candidate. *In vivo* studies suggest that Tip1 stabilizes MTs in the cytoplasm, but rapidly dissociates from the MT end when the MT contacts the cell end. After Tip1 dissociation the MT immediately undergoes catastrophe, giving rise to the speculation that Tip1 might act as a cell boundary sensor [70].

In this section the assay and preliminary results on the effect of force in the presence of Mal3 are presented.

7.2.2 Experiments

The experiment to measure the influence of force on MT dynamics in the presence of +TIPs is similar to experiments previously described [72, 88]. Guanylyl-(alpha, beta)-methylene-diphosphonate (GMPCPP [31]) stabilized biotinylated MT seeds are attached via biotin-streptavidin linkage to a surface coated with biotinylated-PLL-PEG [212]. Dynamic MTs are grown from this seeds against glass barriers made as

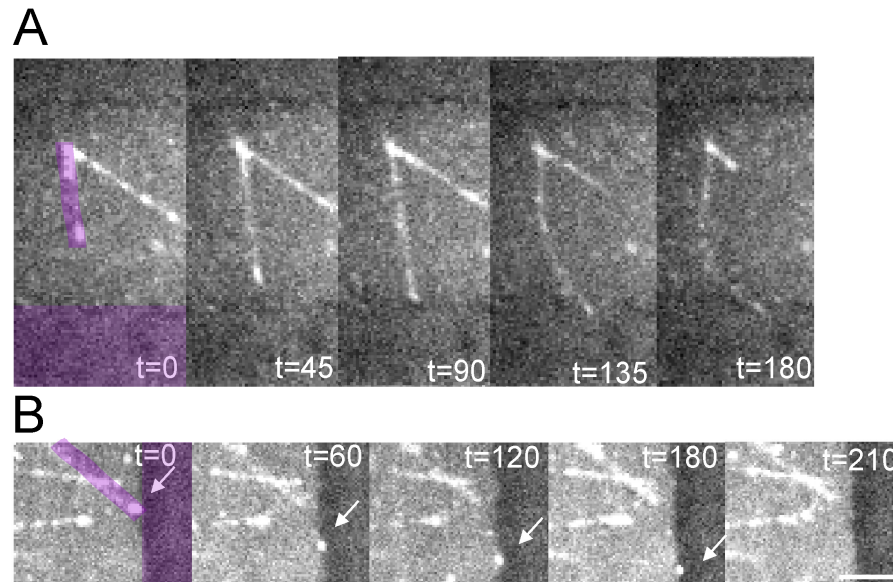


Figure 7.1

Time sequence of MT growing against glass barriers in the presence of Mal3-alexa488 (A) or Mal3, Tea2 and Tip1-GFP (B) against a glass barrier. The MTs of interest and the barrier are highlighted in the first image of the sequence. Scale bar indicates 2 μm .

described in section 2.1.1. Experiments are performed at 15 μM tubulin and at 25 $^{\circ}\text{C}$. To prevent MTs from growing over the barriers, a crowding agent, methyl-cellulose, is added. We have performed experiments to verify that the end of the MT can be detected while in contact with the barrier. Now we can correlate the dynamics of the +TIPs at the plus-tip with MT catastrophes. Indeed both when Mal3-Alexa488 is imaged (Fig. 7.1A) as well as when Tip1-GFP is imaged in the presence of Mal3 and Tea2 (Fig. 7.1B), the plus-end of the MT can be monitored while the MT grows against the barrier.

Subsequently we started with studying the effect of force on the regulation of MT dynamics by Mal3 in more detail, since Mal3 is essential for the tip-tracking of Tip1 and Tea2. We focus our analysis on MTs that stall in a straight conformation against the microfabricated barrier, in contrast to the image sequence in figure 7.1. We compare the average contact time, T_{contact} (the time that the MT stalls at the barrier until a catastrophe), in the presence and absence of Mal3 (Fig. 7.2). The contact time decreases from 100 ± 30 s in the absence of Mal3 to 15 ± 3 s at a 200 nM Mal3 concentration, a 7 ± 4 fold decrease. The decrease of the catastrophe time of freely growing MTs in the presence of 200 nM Mal3 was only 3 ± 1 under the same experimental conditions (measured in our group [41]).

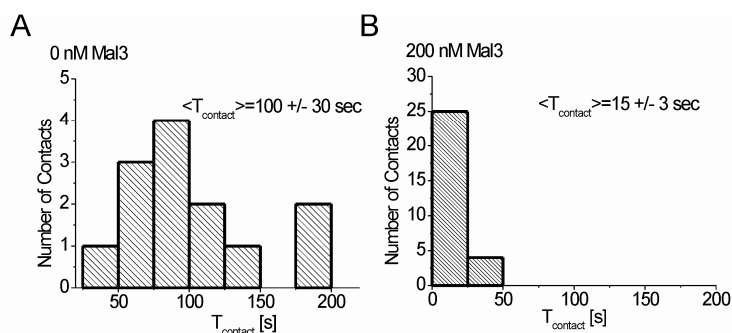


Figure 7.2

Contact times in the absence (A) and presence (B) of 200 nM Mal3.

7.2.3. Conclusion/Discussion

The fact that the difference in the reduction in catastrophe time is not the same for both situations mentioned above is intriguing. Recent high resolution electron microscopy and optical tweezers data suggest that Mal3 changes the MT end structure, so it is tempting to speculate that this modified structure is more prone to undergo catastrophe due to force [41, 213, 214]. Nevertheless more experiments are necessary

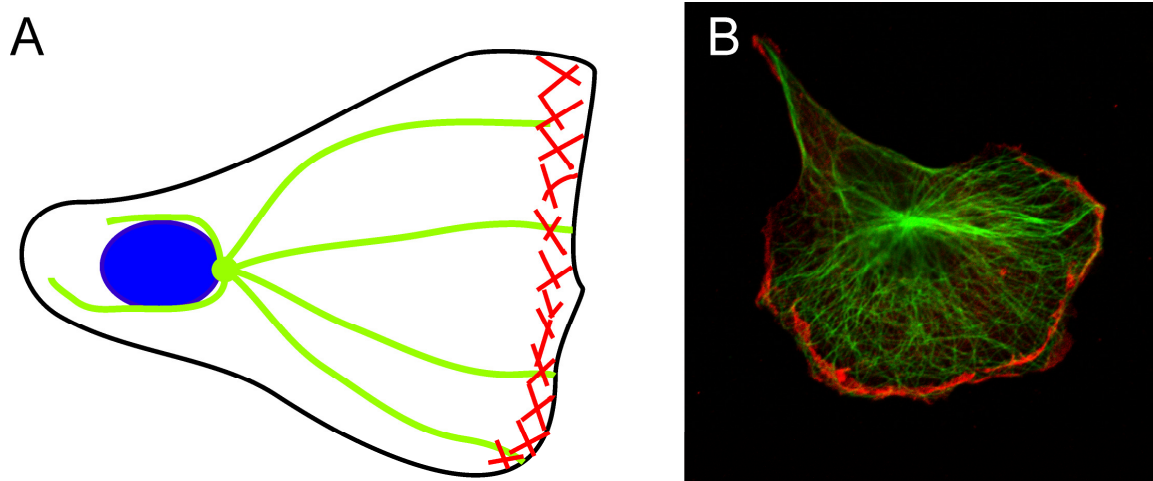


Figure 7.3

MT organization in a migrating cell. (A) Cartoon of the MT array (green) in migrating cells. MTs interact with actin (red) at the cortex of the leading edge, where they are locally stabilized, resulting in a polarized MT array. (B) Fluorescent microscopy picture of a polarized fibroblast. The MTs are stained in green, the cortical actin-binding protein IQGAP1 is stained in red. Image made by T. Watanabe, Nagoya University.

to show the significance of the effect of force.

Furthermore, since we can monitor the MT end in contact with the barrier, we would like to correlate the process of catastrophe at the barrier with the intensity of the +TIP at the MT end. Do all +TIPs simultaneously disappear from the plus-end before a catastrophe, or is there a typical sequence of events that precedes a catastrophe? In dual color experiments, Mal3 and Tea2 or Tip1 can be simultaneously measured, allowing for correlating the dynamics of Tea2, Tip1 and Mal3. Information about the sequence of events will shed light on the end-tracking mechanisms of Mal3, Tea2, Tip1, and thereby on end-tracking mechanisms in general. In addition we can obtain information about the MT catastrophe itself. As said above Mal3, and its homolog EB1 may alter the growing MT end structure, but maybe they also recognize this structure [41, 213, 214]. If this is true, the dynamics of Mal3 may reveal the dynamics of the MT end structure before a catastrophe, which could shed new light on the molecular mechanism underlying catastrophe.

7.3 Microtubule capture by non-motor proteins

7.3.1 Introduction

MT polymerization dynamics are important for cellular polarization [74, 215]. Dynamic instability allows MTs to search three dimensional space [116], so that they may find specific target sites within the cell [17]. If the sites are not homogenously distributed, capture of MTs at these target sites can generate an asymmetric MT array. For example, in migrating cells, MT plus-ends are thought to be stabilized and captured at specific cortical regions on the leading edge, leading to an asymmetric distribution of MTs in the cell, essential for directed cell migration (Fig. 7.3A) [73, 78].

In vivo studies in motile fibroblasts suggest that MTs are captured by the interaction of a plus-end tracking protein, CLIP170 [45], and an actin binding protein, IQGAP1, that is localized at the cortex and does not bind directly to MTs [77, 80]. These experiments show that IQGAP1 binds to CLIP170, and partially colocalizes with MTs at the leading edge [80] (Fig. 7.3B). However these *in vivo* experiments do

not show whether CLIP170 and IQGAP1 are sufficient for MT capture. Moreover they do not reveal the molecular mechanisms of this interaction. We have designed an *in vitro* reconstituted system to address these questions. Through our experiments we hope to learn about the capturing of MTs by CLIP170 and IQGAP1, however we also hope to shed more light on MT capturing mechanisms in general. Can non-motor proteins also capture MTs, and is the mechanism similar to what we have observed for dynein (chapter 4)? In this section we show our progress in developing this *in vitro* assay.

7.3.2 CLIP170 tracks growing microtubule ends in the presence of EB1

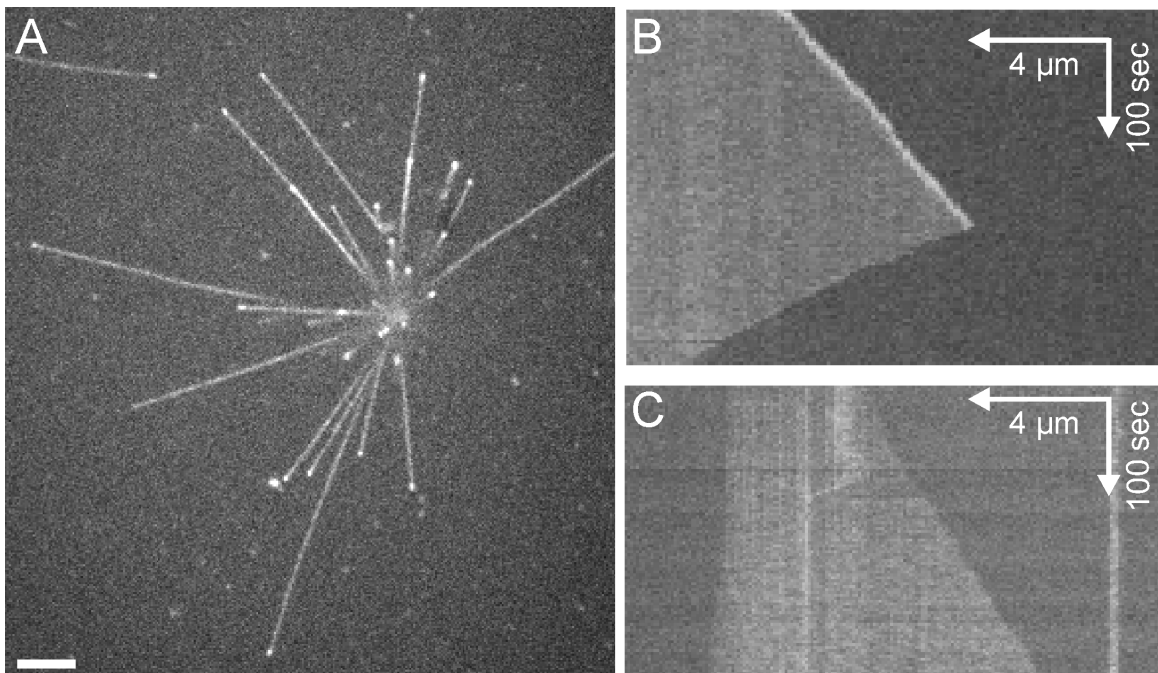


Figure 7.4

EB1 (in contrast to CLIP170) can autonomously track dynamic MT ends. (A) EB1-GFP localizes faintly on the MT lattice but is strongly enhanced on the tips of MTs growing from a centrosome. Scale bar indicates 3 μm. (B) Kymograph of a growing and shrinking MT in the presence of EB1-GFP. Clearly EB1-GFP tracks the growing but not the shrinking MT end. (C) Kymograph of a MT growing in the presence of CLIP170-GFP. CLIP170-GFP localizes on the MT lattice but is not autonomously enhanced at the growing MT end. Images taken with spinning disk confocal microscopy.

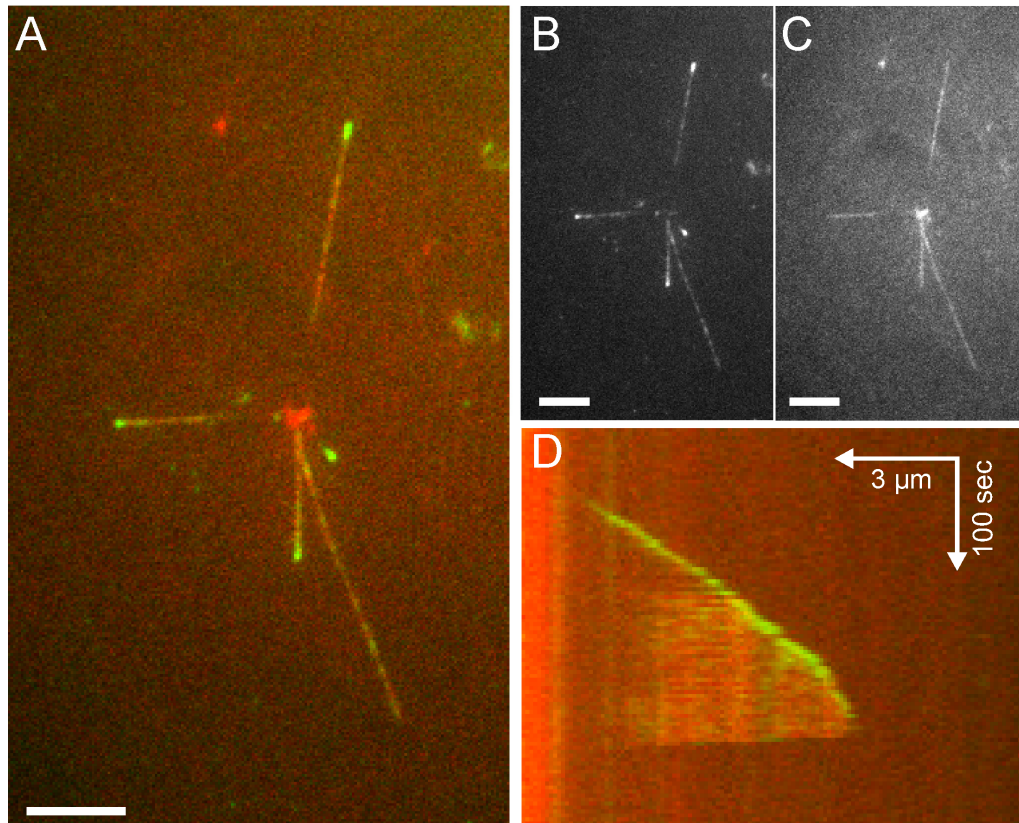


Figure 7.5

CLIP170 tracks growing MT ends in the presence of EB1. (A) Color merge of a TIRF image of the MTs in red and CLIP170 in green. (B) TIRF image of the CLIP170 (C) TIRF image of the MTs. (D) Kymograph showing that CLIP170 tracks the growing end but not the shrinking end of dynamic MTs.

We first reconstitute the end-tracking of CLIP170 to dynamic MT ends. It was previously shown that CLIP170 needs EB1 for end tracking [55, 58], so we exploit EB1 (full length), with and without GFP, in our assays. For CLIP170 we use a truncated construct, CLIP170-608, which is the H2 fragment [55, 58, 216] with an additional part of the coiled coil domain, with optionally a GFP attached (herein referred to as CLIP170 (-GFP)).

The plus-end tracking behavior of EB1 and CLIP170 is studied in the following *in vitro* experiments. Centrosomes are non-specifically attached to the glass surface of a flowcell, and subsequently the surface is blocked with 0.2 mg/ml PLL-PEG (SurfaceSolutions, Switzerland) and 1mg/ml κ -casein. Afterwards the solution

containing tubulin and optionally the +TIPs are added (30 μ M tubulin, 0.2 mg/ml κ -casein, 1 mM GTP, 0.1 % methyl cellulose, an oxygen scavenger system, 100 mM KCl, in MRB80 with optionally 1.5 μ M rhodamine tubulin, and/or 100 nM EB1, and/or 50 nM CLIP170). The sample is sealed and imaged at 25 °C with Spinning Disk Confocal Microscopy on an inverted Leica microscope equipped with a spinning disk from Yokogawa, or with TIRF microscopy, using a NIKON-Roper TIRF system.

Figure 7.4A and B show that similar to Mal3 [56], EB1 autonomously tracks MT plus-ends, and faintly stains the lattice [55-58]. CLIP170 in contrast does not autonomously track the growing plus-end but faintly stains the complete MT lattice (Fig. 7.4C). However in the presence of EB1, CLIP170 tracks the growing plus-end. It does not track the shrinking end and only faintly stains the MT lattice (Fig. 7.5).

7.3.3 IQGAP1 binds specifically to gold barriers

IQGAP1 is attached to a gold barrier as described in chapter 2.2. We use a truncated version of IQGAP1 in this assay, Strep-MBP-IQGAP1-CT-His, which is similar to the construct described in Ref. [80] as MBP-IQGAP1-CT, but extended with a strep-tag (Strep) and a his-tag (His). The strep-tag allows for specific binding to streptavidin

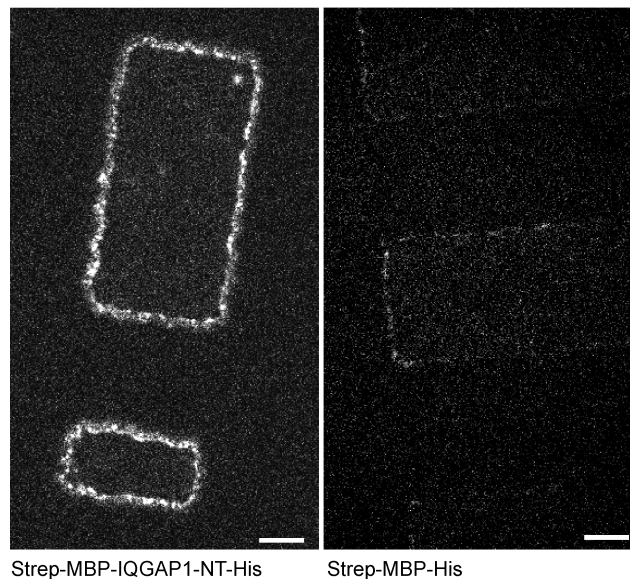


Figure 7.6

Strep-MBP-IQGAP1-CT-His specifically binds to a gold layer. A FITC antibody against IQGAP1 only localizes to the gold layer of a microfabricated chamber, where Strep-MBP-IQGAP1-CT-His is attached (left image). It does not localize to Strep-MBP-His which is similarly attached to the gold layer (right image).

[217], and the his-tag improves the purification, resulting in a more pure protein. We verified that this construct indeed localizes to gold barriers coated with biotin via gold-specific chemistry. First the IQGAP1 construct is attached to the activated gold barrier. Subsequently the presence of the IQGAP1 construct is detected by incubating the sample with FITC-antibodies against IQGAP1. Figure 7.6 (left image) shows that the antibodies specifically localize at the edges of the microfabricated chambers. In a negative control sample we coat the gold layer with strep-MBP-his and then incubate the sample with the FITC-antibodies against IQGAP1. In this case almost no binding of the antibodies to the gold layers can be detected (Fig. 7.6, right image). We conclude that we can specifically coat the gold barriers with Strep-MBP-IQGAP1-CT-His.

7.3.4 Preliminary results on microtubule capture by IQGAP1 and CLIP170 *in vitro*

We performed preliminary experiments where dynamic MT were grown from centrosomes in the presence of EB1 and CLIP170-GFP against IQGAP1-coated gold barriers, as described in section 2.3.1. In our first experiments we did not observe obvious capture of MTs by IQGAP1 and CLIP170, as observed in the presence of dynein (chapter 4). MTs that were in contact with the barrier shrank away from the barrier within a time that at first sight was comparable to the time MTs spend against a MBP-coated barrier (data not shown). A quantitative analysis and more statistics are however needed to investigate the precise effect of the IQGAP1-coated-barrier on MT dynamics. As a side remark: We sometimes observe MT nucleation from the barrier,

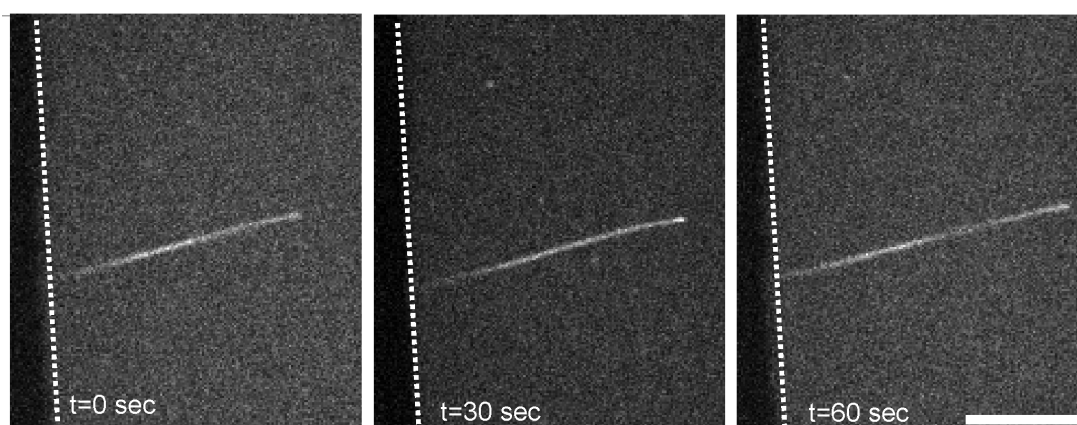


Figure 7.7

An IQGAP1-coated barrier nucleates MTs in the presence of EB1 and CLIP170-GFP. Scale bar indicates 5 μm . The white dotted line indicates the edge of the gold-barrier.

which we never observe in the absence of IQGAP1, confirming that IQGAP1 is present and active at the barrier in our experiments (Fig 7.7).

7.3.5 Conclusion/Discussion

We made the first steps towards reconstituting the capture of MTs by the interaction of non-motor proteins, CLIP170 and IQGAP1. More experiments are necessary to be able to draw conclusions about this potential capturing mechanism. In addition, in the literature a thorough analysis of the regulation of MT dynamics by CLIP170 is missing which is essential for interpreting the contact times at the barrier in the presence of CLIP170 and IQGAP1. Therefore it is recommendable to study also the effect of CLIP170 on free MT dynamics, which is an interesting study on its own.

From a more biophysical perspective it will be interesting to study how specific MT capture is to a particular protein. What is the minimal requirement for MT capture? Can any protein that is attached to a barrier and interacts with the MT end induce MT capture? How much does MT capture depend on the affinity of the capturing protein for the MT end? We can speculate that dynein binds strongly to the MT end, resulting in prolonged capture. In contrast CLIP170 rapidly exchanges on the MT tip [55, 58] and does not show prolonged capture in our preliminary experiments. The role of the binding affinity in MT capture can be studied by employing several biotinylated proteins that bind MTs with a different affinity in our *in vitro* assay.

7.4 Towards the role of microtubule-based transport in cortical pattern formation

7.4.1 Introduction

Many different cell types, from mobile fibroblasts [218] to fission yeast cells [68] (Fig. 7.8A-B), display non-homogenous protein patterns on their cell cortex. These patterns are important for cell morphogenesis: in fibroblasts the small G-protein Cdc42 localizes at the leading edge where motility is also initiated [218]. In fission yeast the cell-end marker protein Tea1 that among others is responsible for recruiting the actin-dependent cell-growth machinery, is specifically located at the cell ends [68] (Fig. 7.7A). MTs contribute to these non-homogenous protein patterns [219]. Tea1 travels to the cell ends at the tip of growing MTs, where it is deposited at the cortex (Fig. 7.8AB)[4]. The dynamics and organization of MTs are important for this protein delivery. If the MTs are too short they do not reach the cell end, if they are too long

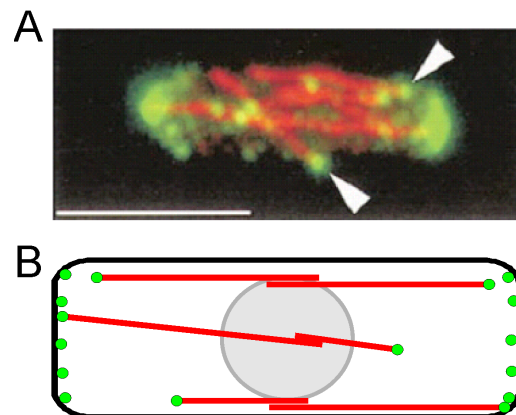


Figure 7.8

Teal1 forms a non-homogeneous protein pattern on the cell cortex of an *S. pombe* cell, and is localized at the tip of growing MTs. (A) Fluorescence image showing MTs in red and Teal1 in green, taken from [4]. (B) Schematic picture of protein patterning by MTs.

they buckle along the cell end. In both cases they do not deliver their cargo at the correct position. Interestingly, the proteins that are involved in transporting cell end markers are also involved in regulating MT dynamics [4, 70, 189].

Why are proteins transported on the tip of dynamic MTs? What is the advantage of this system over simple diffusion? Diffusion based processes can also generate non-homogenous protein patterns, as has been shown for example in *E. coli*. In *E. coli* Min proteins oscillate between the cell poles to select the cell center as the division site [220]. This non-homogeneous pattern has been reconstituted *in vitro*, and depends purely on reaction-diffusion processes [221]. Our aim is to study the role of MT based transport versus diffusive transport in cortical protein pattern formation. For this purpose we would like to set up a minimal *in vitro* system. This model system should allow us to perturb MT based transport and diffusion independently and evaluate the resulting protein patterns. We hope to learn what the advantages are of both strategies in terms of precision, speed and flexibility. In this section a possible future experiment is discussed. First results are shown and recommendations for continuation of these experiments are given.

7.4.2 Experimental plan

In the final *in vitro* experiments we would like to reconstitute non-homogenous protein patterns by MT-based delivery in microfabricated chambers. By growing MTs from a centrosome, and confining them in an elongated microfabricated chamber, we plan to

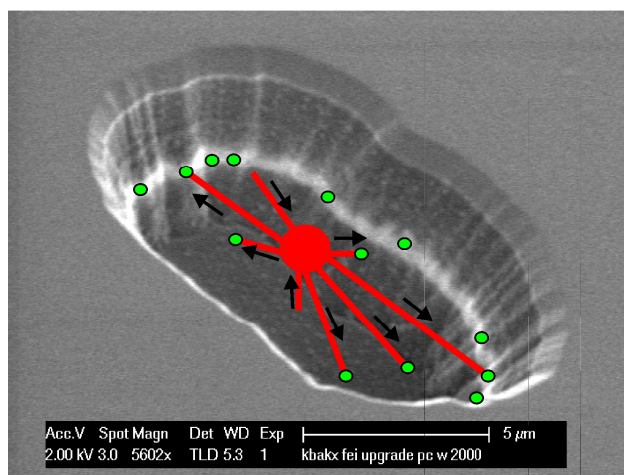


Figure 7.9

SEM image of a microfabricated chamber. A schematic MT array and the patterning proteins at the MT tips and walls are drawn in the microfabricated chamber.

manipulate the MT array to grow along the long axis of the chamber (Fig. 7.9). By varying the concentration of the patterning proteins in solution we plan to control the ratio of diffusing over transported protein. By exploiting surface chemistry and attaching protein tags to the patterning proteins we plan to control binding of the proteins to the microfabricated chamber walls. In this section the design considerations for the experiments are discussed step by step.

7.4.3 +TIPs travel with the end of growing microtubules and regulate their dynamics

One of the first hurdles in setting up these *in vitro* experiments consists of reconstituting transport at the tip of growing MTs *in vitro*. Fortunately this first hurdle has been recently taken, as shown in chapter 6. The plus-end tracking system that we use consists of three components, Mal3, Tea2 and Tip1. This allows for quite sophisticated manipulation of MT dynamics as well as patterning protein concentration. If, for example, Tip1 is the patterning protein, the concentration of Tip1 at the MT tip relative to the concentration in solution will depend on the Tea2 concentration. However, by varying the Tea2 concentration most likely the MT dynamics will change, but this effect potentially can be counteracted by varying the Mal3 or the tubulin concentration. Unfortunately at this point the regulation of MT dynamics by the combination of the three +TIPs is not yet well understood. Regulation of MT dynamics by Mal3 has been studied in depth [41], however a detailed study of

the effect of Tea2 and Tip1 is lacking. Therefore it is advisable to explore the effect of Tea2 and Tip1 more extensively, beyond the initial characterization in chapter 6.

7.4.4 Confining microtubules and patterning proteins in microfabricated chambers

In the experiments with microfabricated chambers performed so far, we ensured that the sealing prevents MTs from growing out of the microfabricated chamber. However in the ultimate patterning experiments the sealing of the microfabricated chamber should also inhibit diffusion of patterning proteins between different microfabricated chambers. Only then the total number of patterning proteins in the microfabricated chamber conserved. Thus are the diffusing fraction and the tip-tracking fraction of patterning proteins coupled. This is particularly important because one possible role of MT based transport is to effectively deplete proteins from the environment. In this case MTs act as “sticky tubes” that collect proteins from the environment and prevent them from binding at random positions, bringing the proteins to the proper position at the cell cortex.

So far we did not test whether the sealing of our microfabricated chambers inhibits diffusion. By performing FRAP (Fluorescence Recovery After Photobleaching) experiments the exchange of proteins between the microfabricated chamber and the environment can however easily be tested [61].

7.4.5 Protein binding with tunable affinities to microfabricated chamber walls

An important parameter in this experiment is the binding affinity of the patterning protein for the microfabricated chamber walls. The chambers will be quite small, 5-20 μm in length, on the order of a fission yeast cell. The time it will take for a typical protein to diffuse from the middle of the microfabricated chamber to the boundary can easily be calculated. The theoretical diffusion constant of a typical ~ 50 kD protein is on the order of $5 \cdot 10^{-11} \text{ m}^2/\text{s}$. Therefore it will take such a protein ~ 1 sec to reach the chamber boundary. If the protein has a high affinity for the walls all the binding sites on the chamber wall will be occupied by the diffusing proteins, immediately after the experiment starts. In this case one may expect that it is no longer possible to form a non-homogeneous protein pattern. In the other extreme case, if the binding affinity is very low, it may not be possible at all to bind proteins to the chamber walls. We therefore aim to bind proteins to the microfabricated chamber walls via a tag of which the affinity can be tuned. We chose the polyhistidine-tag, consisting of 6 histidines

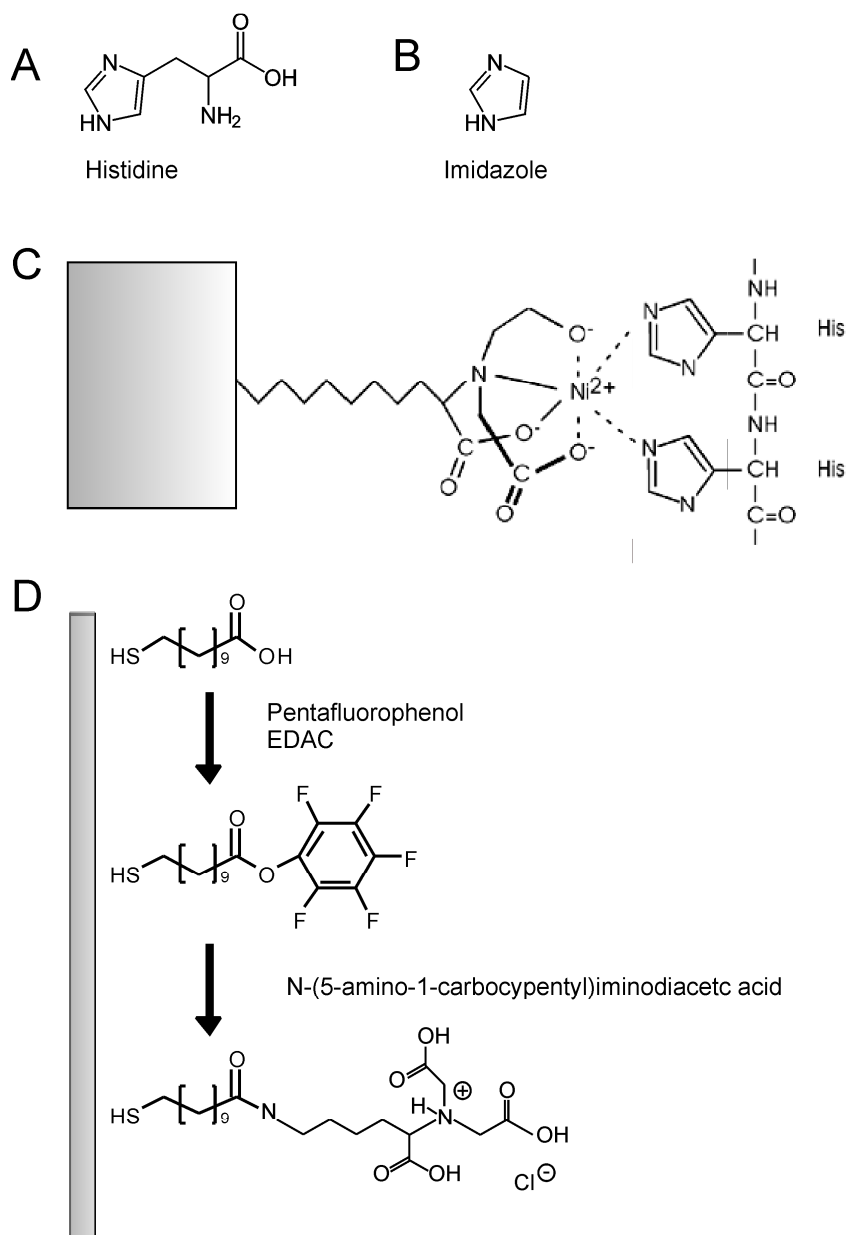


Figure 7.10

Activation of the gold surface with NiNTA. (A) molecular structure of histidine (B) molecular structure of imidazole (C) semi 3-d structure of histidine-tags bound to Ni-NTA. (C) Chemical reaction to bind Ni-NTA to a gold surface.

(Fig. 7.10A) usually referred to as His-tag, which specifically binds to Ni²⁺-nitrilotriacetic acid (Ni-NTA) (Fig. 7.10C) [210]. The affinity can be tuned by adding imidazole in solution (Fig. 7.10C), which reduces the affinity by competing for

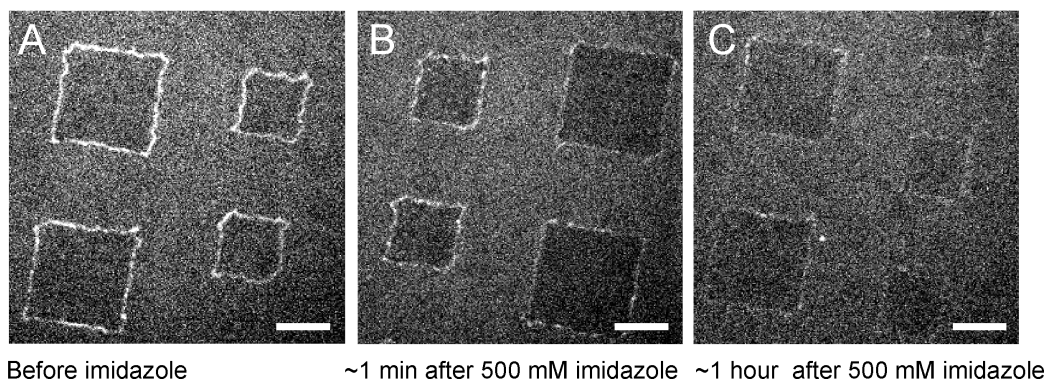


Figure 7.11

Specific association and dissociation of Tip1-GFP to gold barriers. (A) Tip1-GFP associates specifically to Ni-NTA that is attached to gold barriers. After imidazole is added the signal significantly reduces after one minute (B) and is almost completely removed after one hour (C).

binding sites. The Ni-NTA is attached specifically to the gold barriers in the microfabricated chambers via thiol-chemistry, as described for biotin (section 2.2.1, Fig. 7.10D) [222, 223].

Preliminary experiments in figure 7.11 show that Ni-NTA can be bound via thiol-chemistry to a gold barrier and that a His-tagged protein, in this case Tip1-GFP, associates with it. The affinity of Tip1-GFP to the Ni-NTA can strongly be reduced by adding imidazole in a high concentration (Fig. 7.11). After one minute the intensity of

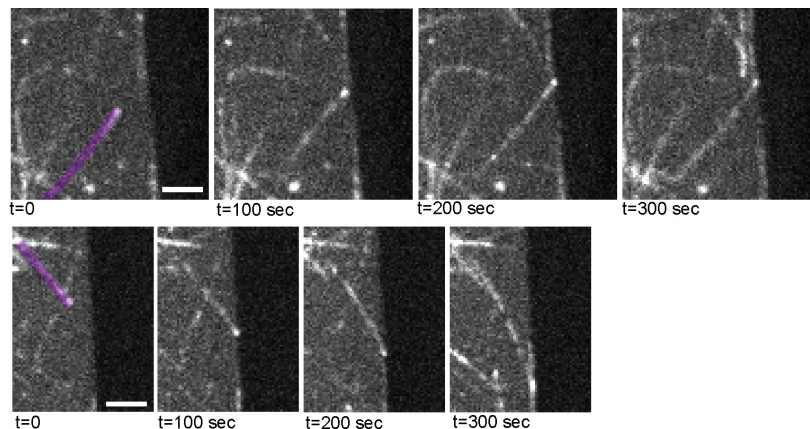


Figure 7.12

MT growing against gold barriers in the presence of Mal3, Tea2 and Tip1-GFP. Time sequences show that the end accumulation of Tip1-GFP is clearly visible when the MT grows against the gold barrier. The MT of interest is highlighted in the first image of the sequence. Scale bars indicate 2 μm .

the Tip1-GFP on the chamber walls has already decreased, and after one hour almost all Tip1-GFP has dissociated from the walls. We attribute the remaining fluorescent signal at the walls to non-specific absorption of proteins to the chamber walls, possibly enhanced by initial specific binding.

Considering the unbinding rates in the literature, the fast dissociation (visible after 1 minute) is probably unbinding of the His-tag from the Ni-NTA, the slow unbinding (on the time scale of one hour) is probably unbinding of non-specifically bound protein. Nevertheless, the clear decrease in intensity confirms that the affinity of the his-tag to the Ni-NTA can be regulated by imidazole, as has been shown previously [222, 223]. Control experiments in the absence of imidazole did not show this clear decrease. In the described experiments, Tip1-GFP was not present in solution and therefore there was no rebinding to the wall after imidazole addition. The next step in evaluating this interaction will be to measure the on- and off-rate of Tip1-GFP from the microfabricated chamber walls, with Tip1-GFP in solution and in the presence of different imidazole concentration. This can be measured by performing FRAP experiments on the chamber walls.

7.4.6 Conclusion/Discussion

We have jumped the first hurdles in reconstituting protein pattern formation *in vitro*. The big challenge will be to combine all the different aspects in one experiment. We think the next milestone towards this experiment will be to form protein patterns on microfabricated barriers instead of in microfabricated chambers. MTs should be grown in the presence of the +TIPs Mal3, Tea2 and Tip1-GFP, from surface attached nucleation sides against microfabricated gold barriers that are activated with Ni-NTA (an assay similar to section 2.3.1). When using barriers instead of chambers, the patterning protein concentration in solution can not be depleted, however this simplified experiment allows for extensive testing of the optimal binding affinities and the proper MT dynamics. As a first step we show that the end of the MT is visible if it grows against a (in this case bare) microfabricated gold barrier, (Fig. 7.12) so that if any patterns form, they should be detectable in these experiments.

7.5 Acknowledgements

The work on the effect of force on MT dynamics has been performed together with Inga Maria Tharun, and E. Laura Munteanu. The experiments on the *in vitro* reconstitution of MT capture by IQGAP1 and CLIP170 were performed in collaboration with Takashi Watanabe and Kozo Kaibuchi (Nagoya University, Japan). I would like to acknowledge Chris Rétif and Guillaume Romet-Lemonne for their help with the microfabrication, Joost te Riet for his advice on the attachment of Ni-NTA to a gold surface, and Martin Loose for discussions about studying positioning processes in lipid droplets.

Bibliography

1. Hill, T.L., *Theoretical problems related to the attachment of microtubules to kinetochores*. Proceedings Of The National Academy Of Sciences Of The United States Of America, 1985. **82**: p. 4404-4408.
2. Laan, L., et al., *Force-generation and dynamic instability of microtubule bundles*. Proc Natl Acad Sci USA, 2008. **105**(26): p. 8920-8925
3. Inoue, S. and E.D. Salmon, *Force Generation by Microtubule Assembly Disassembly in Mitosis and Related Movements*. Mol Biol Cell, 1995. **6**(12): p. 1619-1640.
4. Mata, J. and P. Nurse, *teal and the microtubular cytoskeleton are important for generating global spatial order within the fission yeast cell*. Cell, 1997. **89**(6): p. 939-949.
5. Kerssemakers, J.W.J., et al., *Assembly dynamics of microtubules at molecular resolution*. Nature, 2006. **442**(7103): p. 709-712.
6. Dogterom, M., et al., *Force generation by dynamic microtubules*. Curr Opin Cell Biol, 2005. **17**(1): p. 67-74.
7. Carminati, J.L. and T. Stearns, *Microtubules orient the mitotic spindle in yeast through dynein-dependent interactions with the cell cortex*. J Cell Biol, 1997. **138**(3): p. 629-641.
8. Tolic-Norelykke, I.M., *Push-me-pull-you: how microtubules organize the cell interior*. Eur Biophys J, 2008.
9. Yamamoto, A., et al., *Dynamic behavior of microtubules during dynein-dependent nuclear migrations of meiotic prophase in fission yeast*. Mol Biol Cell, 2001. **12**(12): p. 3933-3946.
10. Grill, S.W., et al., *Polarity controls forces governing asymmetric spindle positioning in the *Caenorhabditis elegans* embryo*. Nature, 2001. **409**(6820): p. 630-633.
11. Nguyen-Ngoc, T., K. Afshar, and P. Gonczy, *Coupling of cortical dynein and G alpha proteins mediates spindle positioning in *Caenorhabditis elegans**. Nat Cell Biol, 2007. **9**(11): p. 1294-U158.
12. Alberts, B., et al., *Molecular Biology of the Cell*. 4 ed. 2002, New York: Garland Publishing. 1400.
13. Savoian, M.S., M.L. Goldberg, and C.L. Rieder, *The rate of poleward chromosome motion is attenuated in *Drosophila* zw10 and rod mutants*. Nature Cell Biology, 2000. **2**(12): p. 948-952.

Bibliography

14. Sharp, D.J., G.C. Rogers, and J.M. Scholey, *Cytoplasmic dynein is required for poleward chromosome movement during mitosis in Drosophila embryos*. *Nat Cell Biol*, 2000. **2**(12): p. 922-930.
15. Varma, A. and K.D. Young, *FtsZ collaborates with penicillin binding proteins to generate bacterial cell shape in Escherichia coli*. *J Bacteriol*, 2004. **186**(20): p. 6768-74.
16. Yang, Z.Y., et al., *Kinetochore dynein is required for chromosome motion and congression independent of the spindle checkpoint*. *Curr Biol*, 2007. **17**(11): p. 973-980.
17. Desai, A. and T.J. Mitchison, *Microtubule polymerization dynamics*. *Annu Rev Cell Dev Biol*, 1997. **13**: p. 83-117.
18. McIntosh, J.R. and K.L. McDonald, *The Mitotic Spindle*. *Scientific American*, 1989. **261**(4): p. 48-56.
19. Burakov, A.V., E.S. Nadezhdina, and V.I. Rodionov, *The nature of the centering force*. *Molecular Biology of the Cell*, 2002. **13**: p. 199A-199A.
20. Vallee, R.B. and S.A. Stehman, *How dynein helps the cell find its center: a servomechanical model*. *Trends in Cell Biology*, 2005. **15**(6): p. 288-294.
21. Yeaman, C., K.K. Grindstaff, and W.J. Nelson, *New perspectives on mechanisms involved in generating epithelial cell polarity*. *Physiological Reviews*, 1999. **79**(1): p. 73-98.
22. Lye, R., Porter, ME, Scholey, JM and McIntosh, JR, *Identification of a microtubule-based cytoplasmic motor in the nematode C. elegans*. *Cell* 1987. **51**: p. 309-318.
23. Vale, R.D., *identification of a novel force generating protein, kinesin*. *Cell*, 1985. **42**: p. 39-50.
24. Svoboda, K. and S.M. Block, *Force and Velocity Measured for Single Kinesin Molecules*. *Cell*, 1994. **77**(5): p. 773-784.
25. Walker, R.A., et al., *Dynamic Instability of Individual Microtubules Analyzed by Video Light-Microscopy - Rate Constants and Transition Frequencies*. *Journal of Cell Biology*, 1988. **107**(4): p. 1437-1448.
26. Chretien, D., et al., *Lattice-Defects in Microtubules - Protofilament Numbers Vary within Individual Microtubules*. *Journal of Cell Biology*, 1992. **117**(5): p. 1031-1040.
27. Chretien, D. and R.H. Wade, *New Data on the Microtubule Surface Lattice*. *Biology of the Cell*, 1991. **71**(1-2): p. 161-174.
28. Gittes, F., et al., *Flexural Rigidity of Microtubules and Actin-Filaments Measured from Thermal Fluctuations in Shape*. *Journal of Cell Biology*, 1993. **120**(4): p. 923-934.

29. Mitchison, J. and M. Kirschner, *Microtubule assembly nucleated by isolated centrosomes*. *nature*, 1984. **312**: p. 232-237.
30. Mitchison, J. and M. Kirschner, *Dynamic instability of microtubule growth*. *nature*, 1984. **312**: p. 237-242.
31. Hyman, A.A., et al., *Role of Gtp Hydrolysis in Microtubule Dynamics - Information from a Slowly Hydrolyzable Analog, Gmpcpp*. *Mol Biol Cell*, 1992. **3**(10): p. 1155-1167.
32. Wang, H.W. and E. Nogales, *Nucleotide-dependent bending flexibility of tubulin regulates microtubule assembly*. *Nature*, 2005. **435**(7044): p. 911-915.
33. Janosi, I.M., D. Chretien, and H. Flyvbjerg, *Structural microtubule cap: Stability, catastrophe, rescue, and third state*. *Biophysical Journal*, 2002. **83**(3): p. 1317-1330.
34. Molodtsov, M.I., et al., *A molecular-mechanical model of the microtubule*. *Biophysical Journal*, 2005. **88**(5): p. 3167-3179.
35. Wang, H.W., et al., *Assembly of GMPCPP-bound tubulin into helical ribbons and tubes and effect of colchicine*. *Cell Cycle*, 2005. **4**(9): p. 1157-1160.
36. Schek, H.T., et al., *Microtubule assembly dynamics at the nanoscale*. *Current Biology*, 2007. **17**(17): p. 1445-1455.
37. VanBuren, V., L. Cassimeris, and D.J. Odde, *Mechanochemical model of microtubule structure and self-assembly kinetics*. *Biophysical Journal*, 2005. **89**(5): p. 2911-2926.
38. Tran, P.T., P. Joshi, and E.D. Salmon, *How tubulin subunits are lost from the shortening ends of microtubules*. *Journal of Structural Biology*, 1997. **118**(2): p. 107-118.
39. Dimitrov, A., et al., *Detection of GTP-Tubulin Conformation in Vivo Reveals a Role for GTP Remnants in Microtubule Rescues*. *Science*, 2008. **322**(5906): p. 1353-1356.
40. Fygenson, D.K., E. Braun, and A. Libchaber, *Phase-Diagram of Microtubules*. *Physical Review E*, 1994. **50**(2): p. 1579-1588.
41. Munteanu, E.M., *Dynamics and regulation at the tip*. PhD thesis, 2008.
42. Gadde, S. and R. Heald, *Mechanisms and molecules of the mitotic spindle*. *Current Biology*, 2004. **14**(18): p. R797-R805.
43. Schaap, I.A.T., et al., *Tau protein binding forms a 1 nm thick layer along protofilaments without affecting the radial elasticity of microtubules*. *Journal of Structural Biology*, 2007. **158**(3): p. 282-292.
44. Akhmanova, A. and M.O. Steinmetz, *Tracking the ends: a dynamic protein network controls the fate of microtubule tips*. *Nature Reviews Molecular Cell Biology*, 2008. **9**(4): p. 309-322.

Bibliography

45. Perez, F., et al., *CLIP-170 highlights growing microtubule ends in vivo*. Cell, 1999. **96**(4): p. 517-527.
46. Akhmanova, A. and C.C. Hoogenraad, *Microtubule plus-end-tracking proteins: mechanisms and functions*. Current Opinion in Cell Biology, 2005. **17**(1): p. 47-54.
47. Howard, J. and A.A. Hyman, *Dynamics and mechanics of the microtubule plus end*. Nature, 2003. **422**(6933): p. 753-758.
48. Lansbergen, G. and A. Akhmanova, *Microtubule plus end: A hub of cellular activities*. Traffic, 2006. **7**(5): p. 499-507.
49. Schuyler, S.C. and D. Pellman, *Microtubule "plus-end-tracking proteins": The end is just the beginning*. Cell, 2001. **105**(4): p. 421-424.
50. Howard, J. and A.A. Hyman, *Microtubule polymerases and depolymerases*. Curr Opin Cell Biol, 2007. **19**(1): p. 31-35.
51. Kinoshita, K., et al., *Reconstitution of physiological microtubule dynamics using purified components*. Science, 2001. **294**(5545): p. 1340-1343.
52. Brouhard, G.J., et al., *XMAP215 is a processive microtubule polymerase*. Cell, 2008. **132**(1): p. 79-88.
53. Kinoshita, K., B. Habermann, and A.A. Hyman, *XMAP215: a key component of the dynamic microtubule cytoskeleton*. Trends in Cell Biology, 2002. **12**(6): p. 267-273.
54. Helenius, J., et al., *The depolymerizing kinesin MCAK uses lattice diffusion to rapidly target microtubule ends*. Nature, 2006. **441**(7089): p. 115-119.
55. Bieling, P., et al., *CLIP-170 tracks growing microtubule ends by dynamically recognizing composite EB1/tubulin-binding sites*. Journal of Cell Biology, 2008. **183**(7): p. 1223-1233.
56. Bieling, P., et al., *Reconstitution of a microtubule plus-end tracking system in vitro*. Nature, 2007. **450**(7172): p. 1100-1105.
57. Komarova, Y., et al., *Mammalian end binding proteins control persistent microtubule growth*. J Cell Biol, 2009. **10**.
58. Dixit, R., et al., *Microtubule plus-end tracking by CLIP-170 requires EB1*. Proceedings of the National Academy of Sciences of the United States of America, 2009. **106**(2): p. 492-497.
59. Busch, K.E. and D. Brunner, *The microtubule plus end-tracking proteins mal3p and tip1p cooperate for cell-end targeting of interphase microtubules*. Current Biology, 2004. **14**(7): p. 548-559.
60. Bringmann, H., et al., *A kinesin-like motor inhibits microtubule dynamic instability*. Science, 2004. **303**(5663): p. 1519-1522.
61. McNally, J., *Quantitative FRAP analysis of molecular binding dynamics in vivo*. Methods Cell Biol, 2008. **85**: p. 329-351.

62. Gupta, M.L., et al., *Plus end-specific depolymerase activity of Kip3, a kinesin-8 protein, explains its role in positioning the yeast mitotic spindle*. Nature Cell Biology, 2006. **8**(9): p. 913-U33.
63. Stumpff, J., et al., *The kinesin-8 motor Kif18A suppresses kinetochore movements to control mitotic chromosome alignment*. Developmental Cell, 2008. **14**(2): p. 252-262.
64. Tischer, C., D. Brunner, and M. Dogterom, *Force-and kinesin-8-dependent effects in the spatial regulation of fission yeast microtubule dynamics* molecular systems biology, 2009.
65. Varga, V., et al., *Yeast kinesin-8 depolymerizes microtubules in a length-dependent manner*. Nature Cell Biology, 2006. **8**(9): p. 957-U60.
66. Athale, C.A., et al., *Regulation of Microtubule Dynamics by Reaction Cascades Around Chromosomes*. Science, 2008. **322**(5905): p. 1243-1247.
67. Li, R. and G.G. Gundersen, *Beyond polymer polarity: how the cytoskeleton builds a polarized cell*. Nature Reviews Molecular Cell Biology, 2008. **9**(11): p. 860-873.
68. Hayles, J. and P. Nurse, *A journey into space*. Nature Reviews Molecular Cell Biology, 2001. **2**(9): p. 647-656.
69. Snaith, H.A. and K.E. Sawin, *Fission yeast mod5p regulates polarized growth through anchoring of tea1p at cell tips*. Nature, 2003. **423**(6940): p. 647-651.
70. Brunner, D. and P. Nurse, *CLIP170-like tip1p spatially organizes microtubular dynamics in fission yeast*. Cell, 2000. **102**(5): p. 695-704.
71. Tran, P.T., et al., *A mechanism for nuclear positioning in fission yeast based on microtubule pushing*. J. Cell Biol., 2001. **153**(2): p. 397-411.
72. Janson, M.E., M.E.d. Dood, and M. Dogterom, *Dynamic instability of microtubules is regulated by force*. The Journal of Cell Biology, 2003. **161**(6): p. 1029-1034.
73. Watanabe, T., J. Noritake, and K. Kaibuchi, *Regulation of microtubules in cell migration*. Trends in Cell Biology, 2005. **15**(2): p. 76-83.
74. Goode, B.L., D.G. Drubin, and G. Barnes, *Functional cooperation between the microtubule and actin cytoskeletons*. Current Opinion in Cell Biology, 2000. **12**(1): p. 63-71.
75. Kaverina, I., K. Rottner, and J.V. Small, *Targeting, capture, and stabilization of microtubules at early focal adhesions*. Journal of Cell Biology, 1998. **142**(1): p. 181-190.
76. Manneville, J.B. and S. Etienne-Manneville, *Positioning centrosomes and spindle poles: looking at the periphery to find the centre*. Biology of the Cell, 2006. **98**(9): p. 557-565.

Bibliography

77. Hart, M.J., et al., *IQGAP1, a calmodulin-binding protein with a rasGAP-related domain, is a potential effector for cdc42Hs*. *Embo Journal*, 1996. **15**(12): p. 2997-3005.
78. Noritake, J., et al., *IQGAP1: A key regulator of adhesion and migration*. *Journal of Cell Science*, 2005. **118**(10): p. 2085-2092.
79. Fukata, M., et al., *Regulation of cross-linking of actin filament by IQGAP1, a target for Cdc42*. *Journal of Biological Chemistry*, 1997. **272**(47): p. 29579-29583.
80. Fukata, M., et al., *Rac1 and Cdc42 capture microtubules through IQGAP1 and CLIP-170*. *Cell*, 2002. **109**(7): p. 873-885.
81. Miller, R.K., et al., *The kinesin-related proteins, Kip2p and Kip3p, function differently in nuclear migration in yeast*. *Molecular Biology of the Cell*, 1998. **9**(8): p. 2051-2068.
82. Yeh, E., et al., *Dynamic positioning of mitotic spindles in yeast: Role of microtubule motors and cortical determinants*. *Molecular Biology of the Cell*, 2000. **11**(11): p. 3949-3961.
83. Dujardin, D.L. and R.B. Vallee, *Dynein at the cortex*. *Current Opinion in Cell Biology*, 2002. **14**(1): p. 44-49.
84. Heil-Chapdelaine, R.A., J.R. Oberle, and J.A. Cooper, *The cortical protein Num1p is essential for dynein-dependent interactions of microtubules with the cortex*. *Journal of Cell Biology*, 2000. **151**(6): p. 1337-1343.
85. Vogel, S.K., et al., *Interphase microtubules determine the initial alignment of the mitotic spindle*. *Current Biology*, 2007. **17**(5): p. 438-444.
86. Yamamoto, A., C. Tsutsumi, and Y. Hiraoka, *Microtubule behavior in meiotic prophase of fission yeast*. *Mol Biol Cell*, 1999. **10**: p. 248A-248A.
87. Schmidt, D.J., et al., *Functional analysis of cytoplasmic dynein heavy chain in *Caenorhabditis elegans* with fast-acting temperature-sensitive mutations*. *Molecular Biology of the Cell*, 2005. **16**(3): p. 1200-1212.
88. Dogterom, M. and B. Yurke, *Measurement of the force-velocity relation for growing microtubules*. *Science*, 1997. **278**(5339): p. 856-860.
89. Fygenson, D.K., J.F. Marko, and A. Libchaber, *Mechanics of microtubule-based membrane extension*. *Phys. Rev. Lett.*, 1997. **79**(22): p. 4497-4500.
90. Janson, M.E. and M. Dogterom, *Scaling of Microtubule Force-Velocity Curves Obtained at Different Tubulin Concentrations*. *Physical Review Letters*, 2004. **92**(24): p. 248101-4.
91. Hill, T.L., *Linear aggregation theory in cell biology*. 1987, New York, Berlin, Heidelberg: Springer-Verlag.
92. Hill, T.L. and M. Kirschner, *Bioenergetics and kinetics of microtubule and actin filament assembly and disassembly*. *Int. Rev. Cytol.*, 1982. **78**: p. 1-125.

93. van Doorn, G.S., et al., *On the stall force for growing microtubules*. European Biophysics Journal with Biophysics Letters, 2000. **29**(1): p. 2-6.
94. Janson, M.E., *Force Generation by Growing Microtubules*. PhD thesis, 2002.
95. Mogilner, A. and G. Oster, *The polymerization ratchet model explains the force-velocity relation for growing microtubules*. European Biophysics Journal with Biophysics Letters, 1999. **28**(3): p. 235-242.
96. Peskin, C.S., G.M. Odell, and G.F. Oster, *Cellular Motions and Thermal Fluctuations - the Brownian Ratchet*. Biophysical Journal, 1993. **65**(1): p. 316-324.
97. Kerssemakers, J.W.J., et al., *Optical trap setup for measuring microtubule pushing forces*. Applied Physics Letters, 2003. **83**: p. 4441.
98. Coue, M., V.A. Lombillo, and J.R. McIntosh, *Microtubule depolymerization promotes particle and chromosome movement in vitro*. J. Cell Biol., 1991. **112**(6): p. 1165-1175.
99. Grishchuk, E.L., et al., *Force production by disassembling microtubules*. Nature, 2005. **438**(7066): p. 384-388.
100. Koshland, D.E., T.J. Mitchison, and M.W. Kirschner, *Polewards Chromosome Movement Driven by Microtubule Depolymerization In vitro*. Nature, 1988. **331**(6156): p. 499-504.
101. Lombillo, V.A., R.J. Stewart, and J.R. McIntosh, *Minus-End-Directed Motion of Kinesin-Coated Microspheres Driven by Microtubule Depolymerization*. Nature, 1995. **373**(6510): p. 161-164.
102. Grissom, P., et al., *Kinesin-8 from fission yeast: a heterodimeric, plus-end-directed motor that can couple microtubule depolymerization to cargo movement*. Mol Biol Cell, 2009. **20**(3): p. 963-72.
103. Riemsdag, E.E.F., M.E. Janson, and M. Dogterom, *Active motor proteins can couple cargo to the ends of growing microtubules*. Physical Biology, 2004. **1**(4): p. C5-C11.
104. Cheeseman, I.M., et al., *Mitotic spindle integrity and kinetochore function linked by the Duo1p/Dam1p complex*. Journal of Cell Biology, 2001. **152**(1): p. 197-212.
105. Westermann, S., et al., *The Dam1 kinetochore ring complex moves processively on depolymerizing microtubule ends*. Nature, 2006. **440**(7083): p. 565-569.
106. Asbury, C.L., et al., *The Dam1 kinetochore complex harnesses microtubule dynamics to produce force and movement*. Proc Natl Acad Sci USA, 2006. **103**(26): p. 9873-9878.
107. Grishchuk, E.L., et al., *The Dam1 ring binds microtubules strongly enough to be a processive as well as energy-efficient coupler for chromosome motion (vol 105, pg 15423, 2008)*. Proc Natl Acad Sci USA, 2008. **105**(49): p. 19562-19562.

Bibliography

108. Franck, A.D., et al., *Tension applied through the Dam1 complex promotes microtubule elongation providing a direct mechanism for length control in mitosis*. Nat Cell Biol, 2007. **9**(7): p. 832-U171.
109. McIntosh, J.R., et al., *Fibrils Connect Microtubule Tips with Kinetochores: A Mechanism to Couple Tubulin Dynamics to Chromosome Motion*. Cell, 2008. **135**(2): p. 322-333.
110. Powers, A.F., et al., *The Ndc80 Kinetochore Complex Forms Load-Bearing Attachments to Dynamic Microtubule Tips via Biased Diffusion*. Cell, 2009. **136**(5): p. 865-875.
111. Daga, R.R. and F. Chang, *Dynamic positioning of the fission yeast cell division plane*. Proceedings of the National Academy of Sciences of the United States of America, 2005. **102**(23): p. 8228-8232.
112. Tolic-Norrelykke, I.M., et al., *Nuclear and division-plane positioning revealed by optical micromanipulation*. Current Biology, 2005. **15**(13): p. 1212-1216.
113. Foethke, D., et al., *Force and length-dependent catastrophe activities explain interphase microtubule organization in fission yeast*. Molecular systems biology, 2009: p. -.
114. Tolic-Norrelykke, I.M., et al., *Positioning and elongation of the fission yeast spindle by microtubule-based pushing*. Current Biology, 2004. **14**(13): p. 1181-1186.
115. Faivre-Moskalenko, C. and M. Dogterom, *Dynamics of microtubule asters in microfabricated chambers: The role of catastrophes*. Proceedings of the National Academy of Sciences of the United States of America, 2002. **99**(26): p. 16788-16793.
116. Holy, T.E., et al., *Assembly and positioning of microtubule asters in microfabricated chambers*. Proceedings of the National Academy of Sciences of the United States of America, 1997. **94**(12): p. 6228-6231.
117. Dogterom, M. and B. Yurke, *Microtubule dynamics and the positioning of microtubule organizing centers*. Physical Review Letters, 1998. **81**(2): p. 485-488.
118. Howard, J., *Elastic and damping forces generated by confined arrays of dynamic microtubules*. Physical Biology, 2006. **3**(1): p. 54-66.
119. Janson, M.E. and M. Dogterom, *A bending mode analysis for growing microtubules: Evidence for a velocity-dependent rigidity*. Biophysical Journal, 2004. **87**(4): p. 2723-2736.
120. Sharp, D.J., G.C. Rogers, and J.M. Scholey, *Microtubule motors in mitosis*. Nature, 2000. **407**(6800): p. 41-47.
121. Skibbens, R.V., V.P. Skeen, and E.D. Salmon, *Directional Instability of Kinetochore Motility during Chromosome Congression and Segregation in*

- Mitotic Newt Lung-Cells - a Push-Pull Mechanism.* Journal of Cell Biology, 1993. **122**(4): p. 859-875.
122. Kapitein, L.C., et al., *The bipolar mitotic kinesin Eg5 moves on both microtubules that it crosslinks.* Nature, 2005. **435**(7038): p. 114-118.
 123. Rieder, C.L. and E.D. Salmon, *Motile Kinetochores and Polar Ejection Forces Dictate Chromosome Position on the Vertebrate Mitotic Spindle.* Journal of Cell Biology, 1994. **124**(3): p. 223-233.
 124. Brouhard, G.J. and A.J. Hunt, *Microtubule movements on the arms of mitotic chromosomes: Polar ejection forces quantified in vitro.* Proceedings of the National Academy of Sciences of the United States of America, 2005. **102**(39): p. 13903-13908.
 125. Funabiki, H. and A.W. Murray, *The Xenopus chromokinesin Xkid is essential for metaphase chromosome alignment and must be degraded to allow anaphase chromosome movement.* Cell, 2000. **102**(4): p. 411-424.
 126. Maiato, H., et al., *The dynamic kinetochore-microtubule interface.* Journal of Cell Science, 2004. **117**(23): p. 5461-5477.
 127. Burbank, K.S., T.J. Mitchison, and D.S. Fisher, *Slide-and-cluster models for spindle assembly.* Current Biology, 2007. **17**(16): p. 1373-1383.
 128. Gardner, M.K. and D.J. Odde, *Modeling of chromosome motility during mitosis.* Current Opinion in Cell Biology, 2006. **18**(6): p. 639-647.
 129. Joglekar, A.P. and A.J. Hunt, *A Simple, Mechanistic Model for Directional Instability during Mitotic Chromosome Movements.* Biophys J, 2002. **83**(1): p. 42-58.
 130. Liu, J., et al., *An integrated mechanobiochemical feedback mechanism describes chromosome motility from prometaphase to anaphase in mitosis.* Proceedings of the National Academy of Sciences of the United States of America, 2008. **105**(37): p. 13752-13757.
 131. Mogilner, M., et al., *Modeling mitosis.* Trends in Cell Biology, 2006. **16**(2): p. 88-96.
 132. Nedelec, F.J., et al., *Self-organization of microtubules and motors.* Nature, 1997. **389**(6648): p. 305-308.
 133. Surrey, T., et al., *Physical properties determining self-organization of motors and microtubules.* Science, 2001. **292**(5519): p. 1167-1171.
 134. Wollman, R., et al., *Reverse engineering of force integration during mitosis in the Drosophila embryo.* Molecular Systems Biology, 2008. **4**: p. -.
 135. Grill, S.W., et al., *The distribution of active force generators controls mitotic spindle position.* Science, 2003. **301**(5632): p. 518-521.
 136. Grill, S.W. and A.A. Hyman, *Spindle positioning by cortical pulling forces.* Dev Cell, 2005. **8**(4): p. 461-465.

Bibliography

137. Grill, S.W., K. Kruse, and F. Julicher, *Theory of mitotic spindle oscillations*. Phys Rev Lett, 2005. **94**(10): p. -.
138. Kozlowski, C., M. Srayko, and F. Nedelec, *Cortical microtubule contacts position the spindle in C. elegans embryos*. Cell, 2007. **129**(3): p. 499-510.
139. Pecreaux, J., et al., *Spindle oscillations during asymmetric cell division require a threshold number of active cortical force generators*. Current Biology, 2006. **16**(21): p. 2111-2122.
140. Brangwynne, C.P., et al., *Microtubules can bear enhanced compressive loads in living cells because of lateral reinforcement*. Journal of Cell Biology, 2006. **173**(5): p. 733-741.
141. Gittes, F. and C.F. Schmidt, *Signals and noise in micromechanical measurements*. Methods in Cell Biology, Vol 55, 1998. **55**: p. 129-156.
142. Romet-Lemonne, G., M. VanDuijn, and M. Dogterom, *Three-dimensional control of protein patterning in microfabricated devices*. Nano Letters, 2005. **5**(12): p. 2350-2354.
143. Ashkin, A., *Acceleration and trapping of particles by radiation pressure*. Physical Review Letters, 1970. **24**(4): p. 156-159.
144. Svoboda, K. and S.M. Block, *Biological applications of optical forces*. Annual Review of Biophysics and Biomolecular Structures, 1994. **23**: p. 247-285.
145. Tselutin, K., F. Seigneurin, and E. Blesbois, *Comparison of cryoprotectants and methods of cryopreservation of fowl spermatozoa*. Poultry Science, 1999. **78**(4): p. 586-590.
146. Visscher, K., S.P. Gross, and S.M. Block, *Construction of Multiple-Beam Optical Traps with Nanometer-Resolution Position Sensing*. IEEE Journal of Selected Topics in Quantum Electronics, 1996. **2**(4): p. 1066-1076.
147. Mitchison, T. and M. Kirschner, *Dynamic instability of microtubule growth*. Nature, 1984. **312**: p. 237-241.
148. Dogterom, M., et al., *Force generation by dynamic microtubules*. Current Opinion in Cell Biology, 2005. **17**(1): p. 67-74.
149. Dogterom, M. and B. Yurke, *Measurement of the force-velocity relation for growing microtubules*. Science, 1997. **278**: p. 856-860.
150. McIntosh, J.R., E.L. Grishchuk, and R.R. West, *Chromosome-microtubule interactions during mitosis*. Annual Review of Cell and Developmental Biology, 2002. **18**: p. 193-219.
151. Rieder, C.L. and E.D. Salmon, *The vertebrate cell kinetochore and its roles during mitosis*. Trends in Cell Biology, 1998. **8**(8): p. 310-318.
152. Grishchuk, E.L. and J.R. McIntosh, *Microtubule depolymerization can drive poleward chromosome motion in fission yeast*. Embo Journal, 2006. **25**(20): p. 4888-4896.

153. Skibbens, R.V., V.P. Skeen, and E.D. Salmon, *Directional Instability of Kinetochore Motility during Chromosome Congression and Segregation in Mitotic Newt Lung Cells: A Push-Pull Mechanism*. Journal of Cell Biology, 1993. **122**(4): p. 859-875.
154. Gibbons, I.R.a. and F. E., *A latent adenosine triphosphatase form of dynein I from sea urchin sperm flagella*. J. Biol. Chem., 1979. **254**: p. 187-196.
155. Schek, H.T. and A.J. Hunt, *Micropatterned structures for studying the mechanics of biological polymers*. Biomedical Microdevices, 2005. **7**(1): p. 41-46.
156. Browning, H. and D.D. Hackney, *The EBI homolog Mal3 stimulates the ATPase of the kinesin Tea2 by recruiting it to the microtubule*. Journal of Biological Chemistry, 2005. **280**(13): p. 12299-12304.
157. Doorn, G.S.v., et al., *On the stall force for growing microtubules*. European Biophysics Journal with Biophysics Letters, 2000. **29**(1): p. 2-6.
158. Footer, M.J., et al., *Direct measurement of force generation by actin filament polymerization using an optical trap*. Proceedings of the National Academy of Sciences of the United States of America, 2007. **104**(7): p. 2181-2186.
159. Campas, O., et al., *Collective dynamics of molecular motors pulling on fluid membranes*. 2006.
160. Civelekoglu-Scholey, G., et al., *Model of Chromosome Motility in Drosophila Embryos: Adaptation of a General Mechanism for Rapid Mitosis*. Biophys J, 2006. **90**(11): p. 3966-3982.
161. Gardner, M.K. and D.J. Odde, *Modeling of chromosome motility during mitosis. Cell division, growth and death / Cell differentiation*, 2006. **18**(6): p. 639.
162. VandenBeldt, K.J., et al., *Kinetochores use a novel mechanism for coordinating the dynamics of individual microtubules*. Current Biology, 2006. **16**(12): p. 1217-1223.
163. Waters, J.C., R.V. Skibbens, and E.D. Salmon, *Oscillating mitotic newt lung cell kinetochores are, on average, under tension and rarely push*. Journal of Cell Science, 1996. **109**: p. 2823-2831.
164. Levesque, A.A. and D.A. Compton, *The chromokinesin Kid is necessary for chromosome arm orientation and oscillation, but not congression, on mitotic spindles*. Journal of Cell Biology, 2001. **154**(6): p. 1135-1146.
165. Maresca, T.J., et al., *Xnf7 contributes to spindle integrity through its microtubule-bundling activity*. Current Biology, 2005. **15**(19): p. 1755-1761.
166. Dujardin, D.L. and R.B. Vallee, *Dynein at the cortex*. Curr Opin Cell Biol, 2002. **14**(1): p. 44-49.

Bibliography

167. Manneville, J.-B., et al., *Activity of transmembrane proteins induces magnification of shape fluctuations of lipid membranes*. Phys Rev Lett, 1999. **82**(21): p. 4356-4359.
168. Adames, N.R. and J.A. Cooper, *Microtubule interactions with the cell cortex causing nuclear movements in Saccharomyces cerevisiae*. J Cell Biol, 2000. **149**(4): p. 863-874.
169. Reck-Peterson S. L , A.Y., Andrew P. Carter, Arne Gennerich, Nan Zhang, and a.R.D. Vale, *Single-Molecule Analysis of Dynein Processivity and Stepping Behavior*. Cell, 2006. **126**: p. 335–348.
170. Gennerich, A., et al., *Force-induced bidirectional stepping of cytoplasmic dynein*. Cell, 2007. **131**(5): p. 952-965.
171. Janson, M.E., M.E. de Dood, and M. Dogterom, *Dynamic instability of microtubules is regulated by force*. J Cell Biol, 2003. **161**(6): p. 1029-1034.
172. Cho, C., S.L. Reck-Peterson, and R.D. Vale, *Regulatory ATPase sites of cytoplasmic dynein affect processivity and force generation*. J Biol Chem, 2008. **283**(38): p. 25839-25845.
173. Moudjou, M., Bornens,M. , *Isolation of Centrosomes From Cultured Animal Cells*. Cell Biology: A Laboratory Handbook, ed. J.E.Celis Academic Press, New York.1994: p. 595-604.
174. Grill, S.W., K. Kruse, and F. Julicher, *Theory of mitotic spindle oscillations*. Physical Review Letters, 2005. **94**(10): p. -.
175. Howard, J., *Elastic and damping forces generated by confined arrays of dynamic microtubules*. Phys Biol, 2006. **3**(1): p. 54-66.
176. Reck-Peterson, S.L., et al., *Single-molecule analysis of dynein processivity and stepping behavior*. Cell, 2006. **126**(2): p. 335-348.
177. Sage, D., et al., *Automatic Tracking of Individual Fluorescence Particles: Application to the Study of Chromosome Dynamics*. IEEE Transactions on Image Processing, 2005. **14**(9): p. 1372-1383.
178. Mickey, B. and J. Howard, *Rigidity of Microtubules Is Increased by Stabilizing Agents*. Journal of Cell Biology, 1995. **130**(4): p. 909-917.
179. Mimori-Kiyosue, Y. and S. Tsukita, *"Search-and-capture" of microtubules through plus-end-binding proteins (+TIPs)*. Journal of Biochemistry, 2003. **134**(3): p. 321-326.
180. Wittmann, T. and A. Desai, *Microtubule cytoskeleton: A new twist at the end*. Current Biology, 2005. **15**(4): p. R126-R129.
181. Mimori-Kiyosue, Y., N. Shiina, and S. Tsukita, *Adenomatous polyposis coli (APC) protein moves along microtubules and concentrates at their growing ends in epithelial cells*. Journal of Cell Biology, 2000. **148**(3): p. 505-517.

182. Mimori-Kiyosue, Y., N. Shiina, and S. Tsukita, *The dynamic behavior of the APC-binding protein EBI on the distal ends of microtubules*. *Current Biology*, 2000. **10**(14): p. 865-868.
183. Akhmanova, A., et al., *CLASPs are CLIP-115 and-170 associating proteins involved in the regional regulation of microtubule dynamics in motile fibroblasts*. *Cell*, 2001. **104**(6): p. 923-935.
184. Vaughan, P.S., et al., *A role for regulated binding of p150(Glued) to microtubule plus ends in organelle transport*. *Journal of Cell Biology*, 2002. **158**(2): p. 305-319.
185. Kodama, A., et al., *ACF7: An essential integrator of microtubule dynamics*. *Cell*, 2003. **115**(3): p. 343-354.
186. Ding, D.Q., et al., *Oscillatory nuclear movement in fission yeast meiotic prophase is driven by astral microtubules, as revealed by continuous observation of chromosomes and microtubules in living cells*. *Journal of Cell Science*, 1998. **111**: p. 701-712.
187. Brunner, D. and P. Nurse, *New concepts in fission yeast morphogenesis*. *Philosophical Transactions of the Royal Society of London Series B-Biological Sciences*, 2000. **355**(1399): p. 873-877.
188. Browning, H., D.D. Hackney, and P. Nurse, *Targeted movement of cell end factors in fission yeast*. *Nature Cell Biology*, 2003. **5**(9): p. 812-818.
189. Browning, H., et al., *Tea2p is a kinesin-like protein required to generate polarized growth in fission yeast*. *Journal of Cell Biology*, 2000. **151**(1): p. 15-27.
190. Busch, K.E., et al., *Tea2p kinesin is involved in spatial microtubule organization by transporting Tip1p on microtubules*. *Developmental Cell*, 2004. **6**(6): p. 831-843.
191. Carvalho, P., J.S. Tirnauer, and D. Pellman, *Surfing on microtubule ends*. *Trends in Cell Biology*, 2003. **13**(5): p. 229-237.
192. Axelrod, D., *Total internal reflection fluorescence microscopy in cell biology*. *Traffic*, 2001. **2**(11): p. 764-774.
193. Sandblad, L., et al., *The Schizosaccharomyces pombe EBI homolog Mal3p binds and stabilizes the microtubule lattice seam*. *Cell*, 2006. **127**(7): p. 1415-1424.
194. Chretien, D., S.D. Fuller, and E. Karsenti, *Structure of Growing Microtubule Ends - 2-Dimensional Sheets Close into Tubes at Variable Rates*. *Journal of Cell Biology*, 1995. **129**(5): p. 1311-1328.
195. Drechsel, D.N. and M.W. Kirschner, *The Minimum Gtp Cap Required to Stabilize Microtubules*. *Current Biology*, 1994. **4**(12): p. 1053-1061.

Bibliography

196. Ohkura, H., M.A. Garcia, and T. Toda, *Dis1/TOG universal microtubule adaptors - one MAP for all?* Journal of Cell Science, 2001. **114**(21): p. 3805-3812.
197. West, R.R., T. Malmstrom, and J.R. McIntosh, *Two related kinesins, klp5(+) and klp6(+), foster microtubule disassembly and are required for normal chromosome movement in fission yeast.* Molecular Biology of the Cell, 2001. **12**: p. 436A-436A.
198. Folker, E.S., B.M. Baker, and H.V. Goodson, *Interactions between CLIP-170, tubulin, and microtubules: Implications for the mechanism of CLIP-170 plus-end tracking behavior.* Molecular Biology of the Cell, 2005. **16**(11): p. 5373-5384.
199. Tirnauer, J.S., et al., *EB1-microtubule interactions in Xenopus egg extracts: Role of EB1 in microtubule stabilization and mechanisms of targeting to microtubules.* Molecular Biology of the Cell, 2002. **13**(10): p. 3614-3626.
200. Castoldi, M. and A.V. Popova, *Purification of brain tubulin through two cycles of polymerization-depolymerization in a high-molarity buffer.* Protein Expression and Purification, 2003. **32**(1): p. 83-88.
201. Hyman, A., et al., *Preparation of modified tubulins.* Methods Enzymol, 1991. **196**: p. 478-85.
202. Gaskin, F., C.R. Cantor, and M.L. Shelanski, *Turbidimetric studies of the in vitro assembly and disassembly of porcine neurotubules.* J Mol Biol, 1974. **89**(4): p. 737-55.
203. Lata, S. and J. Piehler, *Stable and functional immobilization of histidine-tagged proteins via multivalent chelator headgroups on a molecular poly(ethylene glycol) brush.* Analytical Chemistry, 2005. **77**(4): p. 1096-1105.
204. Seitz, A.T.S., *Processive movement of single kinesins on crowded microtubules visualized using quantum dots.* EMBO, 2006: p. 1-11.
205. Fukata, M., et al., *Role of IQGAP1, an effector of Rac1 and Cdc42, in the regulation of cell polarity acting through CLIP-170.* Molecular Biology of the Cell, 2001. **12**: p. 47A-47A.
206. Vorvis, C., S.M. Markus, and W.L. Lee, *Photoactivatable GFP tagging cassettes for protein-tracking studies in the budding yeast Saccharomyces cerevisiae.* Yeast, 2008. **25**(9): p. 651-659.
207. Merkle, D., N. Kahya, and P. Schwille, *Reconstitution and Anchoring of Cytoskeleton inside Giant Unilamellar Vesicles.* Chembiochem, 2008. **9**(16): p. 2673-2681.
208. Loose, p.c.w.M.
209. Minc, N.D., et al., *Establishing new sites of polarization by microtubules.* Current Biology, 2008: p. 83-94.

210. Terenna, C.R., et al., *Physical Mechanisms Redirecting Cell Polarity and Cell Shape in Fission Yeast*. Current Biology, 2008. **18**(22): p. 1748-1753.
211. Jaworski, J., C.C. Hoogenraad, and A. Akhmanova, *Microtubule plus-end tracking proteins in differentiated mammalian cells*. International Journal of Biochemistry & Cell Biology, 2008. **40**(4): p. 619-637.
212. Huang, N.P., et al., *Biotin-derivatized poly(L-lysine)-g-poly(ethylene glycol): A novel polymeric interface for bioaffinity sensing*. Langmuir, 2002. **18**(1): p. 220-230.
213. des Georges, A., et al., *Mal3, the Schizosaccharomyces pombe homolog of EB1, changes the microtubule lattice*. Nature Structural & Molecular Biology, 2008. **15**(10): p. 1102-1108.
214. Vitre, B., et al., *EB1 regulates microtubule dynamics and tubulin sheet closure in vitro*. Nature Cell Biology, 2008. **10**(4): p. 415-U81.
215. Waterman-Storer, C.M. and E.D. Salmon, *Positive feedback interactions between microtubule and actin dynamics during cell motility*. Current Opinion in Cell Biology, 1999. **11**(1): p. 61-67.
216. Arnal, I., et al., *CLIP-170/tubulin-curved oligomers coassemble at microtubule ends and promote rescues*. Current Biology, 2004. **14**(23): p. 2086-2095.
217. Skerra, A. and T.G.M. Schmidt, *Applications of a peptide ligand for streptavidin: the Strep-tag*. Biomolecular Engineering, 1999. **16**(1-4): p. 79-86.
218. Heasman, S.J. and A.J. Ridley, *Mammalian Rho GTPases: new insights into their functions from in vivo studies*. Nature Reviews Molecular Cell Biology, 2008. **9**(9): p. 690-701.
219. Sawin, K.E. and P. Nurse, *Regulation of cell polarity by microtubules in fission yeast*. Journal of Cell Biology, 1998. **142**(2): p. 457-471.
220. Deboer, P.A.J., R.E. Crossley, and L.I. Rothfield, *A Division Inhibitor and a Topological Specificity Factor Coded for by the Minicell Locus Determine Proper Placement of the Division Septum in Escherichia-Coli*. Cell, 1989. **56**(4): p. 641-649.
221. Loose, M., et al., *Spatial regulators for bacterial cell division self-organize into surface waves in vitro*. Science, 2008. **320**(5877): p. 789-792.
222. Lauer, S.A. and J.P. Nolan, *Development and characterization of Ni-NTA-bearing microspheres*. Cytometry, 2002. **48**(3): p. 136-145.
223. Sigal, G.B., et al., *A self-assembled monolayer for the binding and study of histidine tagged proteins by surface plasmon resonance*. Analytical Chemistry, 1996. **68**(3): p. 490-497.

Bibliography

Summary

The MT cytoskeleton is essential for cellular organization. Interestingly, the MT cytoskeleton is very dynamic; it dramatically changes shape throughout the cell cycle. This dramatic reorganization of the MT array depends on a property of MTs termed “dynamic instability”: the intrinsic ability of MTs to rapidly switch between a growing and a shrinking state. Regulation of the parameters that govern dynamic instability throughout the cell cycle, allows for flexibility in the organization of MTs. An important role of the MT array is the generation of forces needed for the proper positioning of various cellular organelles. Interactions of motor proteins with dynamic MTs are partly responsible for this force generation; however MTs themselves are also capable of generating forces, while interacting with physical barriers, such as the cell cortex.

In this thesis we study force generation by MT assembly as well as disassembly, while MTs interact with a physical barrier. We also study how these physical forces regulate MT dynamics, in combination with MT associated (motor) proteins (MAPs), which regulate MT dynamics biochemically. More on the cellular level, we study the role of MT force generation in cellular organization. As stated in the title: “Force generation at microtubule ends: An *in vitro* approach to cortical interactions”, we use *in vitro* techniques. In *in vitro* experiments minimal functional modules are isolated. This is in large contrast to *in vivo* experiments where many processes occur simultaneously in a small confining space, and are often entangled.

In chapter 2 we describe the *in vitro* assays that we use to study MT-cortex interactions. We exploit microfabrication techniques to make physical barriers. These microfabricated structures are incorporated in four different assays. In the first assay MTs, with one end attached to the surface, are grown with their other end against rigid gold barriers. We use gold barriers to, via thiol-chemistry, specifically bind proteins that interact with MTs, to the barriers. In the second assay MTs are also attached to the surface at one end, but they are grown against glass barriers. This assay allows us to study the effect of MT pushing forces on MT dynamics, for example in the presence of MT associated proteins. In the third assay we use microfabricated chambers to study the role of pulling forces compared to pushing forces in cellular organization. Here, a MT aster is confined in a microfabricated chamber. Pulling forces arise from interactions between MT ends and motor proteins that are specifically attached to the chamber walls. Pushing forces result from MT assembly against the walls of the microfabricated chamber and from elastic restoring forces of the MT array. In the last

Summary

assay an optical trap is used in combination with microfabricated structures. Either a single MT or multiple MTs (depending on the specific experimental conditions) are grown from an axoneme, a rigid bundle of MTs. The axoneme is attached to a bead, held in an optical trap, and positioned in front of a microfabricated barrier. MT growth and shrinkage against the barrier results in displacement of the bead in the optical trap. The usage of an optical trap allows us to measure MT based forces quantitatively. In all four assays the microfabricated barriers function as a minimal system to mimic the cell cortex. In the case of pushing forces the essential function of the barrier is to oppose growth. In the case of pulling forces the barrier is specifically coated with proteins that connect the barrier to the shrinking MT and therefore transmit the generated pulling forces.

Several *in vitro* studies have shown that MT growth can generate pushing forces on the order of several pN [88, 94]. In cells however, MTs often function in bundles. For example in the mitotic spindle, a bundle of MTs interacts with the kinetochore. A collection of MTs is also responsible for force generation at the chromosome arms. In chapter 3 we use the above-described optical trap assay to study the dynamics and force generation of a growing MT bundle. We find that MTs that grow in a parallel bundle and are only coupled at their base can generate much higher forces than individual MTs. The maximum pushing force generated by a MT bundle scales linearly with the number of MTs in the bundle. This is in contrast to previous experiments on actin bundles that suggest that the forces generated by an actin bundle do not scale with the number of actin filaments in the bundle. Interestingly the force generated by a MT bundle couples the dynamics of the MTs in the bundle. The bundle can cooperatively switch to a shrinking state, due to a force induced coupling of the dynamic instability of single MTs. We can reproduce these cooperative switches with a simple computer simulation.

Where growing MTs generate pushing forces, shrinking MTs can generate pulling forces, as has been shown in *in vitro* experiments [99, 101]. Pulling forces are complicated because a link has to be made and maintained with a shrinking MT in order to transmit the generated force to an object. *In vivo* experiments have suggested that the motor protein dynein, located both at the cortex and at the kinetochore may play an important role in forming the link to a shrinking MT. In chapter 4 we study *in vitro* whether the motor protein dynein is sufficient to form a link between a physical barrier (mimicking the cortex or the kinetochore) and a shrinking MT, and whether this link withstands an opposing pulling force. MTs are grown against a rigid barrier specifically coated with dynein. The dynamics and the forces generated by the interaction of the MT end and the dynein-coated barrier are studied. We find that

dynein, when mechanically attached to a growth-opposing barrier, can hold on to a shrinking MT end and generate pulling forces up to ~ 5 pN. In addition, dynein, 'cortex'-attached dynein captures MT ends, induces catastrophes and slows down subsequent MT shrinkage. Our results provide a mechanistic explanation for observations in living cells and provide new information for theoretical models describing cellular organization by pulling forces.

In vivo experiments have shown that pulling forces play an important role in the positioning of organelles, such as the mitotic spindle, in the cell. In chapter 5 we study the role of pulling forces in positioning processes in an experimental model system. MT asters are grown in microfabricated chambers (as described above) and pulling forces are introduced by specifically attaching dynein to the chamber walls. The position of the aster is measured (a) when only pushing forces are present (no dynein at the wall), (b) when the pulling to pushing ratio is low (low dynein amounts at the wall), (c) when the pulling to pushing ratio is high (high dynein amounts at the wall). Surprisingly, and in contrast with previous theoretical speculations, pulling forces center a MT aster more reliably in a microfabricated chamber than pushing force alone. We developed a simple mathematical description for this improved centering, in which pulling forces center an aster due to an anisotropic distribution of MTs in the microfabricated chamber. The anisotropic distribution is due to MT growth-induced sliding. MTs are initially nucleated isotropically. However their increasing length forces them to slide along the microfabricated chamber wall when they grow against it. Eventually the MTs are captured by a motor protein and pulling forces are generated by the anisotropic MT array. The net force generated by this MT array reliably centers the MT aster.

So far we have mainly focused on MT force generation and the regulation of MT dynamics by these forces. However MT dynamics are also biochemically regulated by MAPs. One large class of these MAPs are the +TIPs: proteins that are known from *in vivo* observations to specifically track the growing MT plus-end. In chapter 6 we reconstitute the plus-end tracking of three +TIPs from fission yeast, Mal3, Tea2, and Tip1, *in vitro*. We find that Mal3 autonomously tracks both ends of the MT. Single molecule studies show that Mal3 very transiently binds to the MT end and therefore most likely does not end-track by copolymerization but by recognition of the MT end. Tea2, a motor-protein, and Tip1 need Mal3 and each other to track the MT end, and they specifically track the MT plus-end. Mal3 is needed to load Tea2 and Tip1 on the MT lattice. This complex then moves together processively to the MT plus-end (for which Mal3 is not needed).

Summary

In chapter 7 we present additional research directions. In the first section two new experiments are described to test the theory developed in chapter 5. In the first experiment we propose to grow MT asters in lipid droplets which should allow for very dramatic sliding. In the second experiment we propose to deform a *C. elegans* embryo. In this system the mitotic spindle is positioned by pulling forces. Deforming the embryo would allow us to evaluate how much geometry affects the positioning of the mitotic spindle in *C. elegans*. This should elucidate the biological relevance of our sliding model. In the second section we study the combined effect of physical and biochemical regulation of MT dynamics. MTs are grown in the presence of Mal3 against glass barriers. Our preliminary results show that force might enhance the destabilizing effect of Mal3 on MTs. In the third section the assay and preliminary results on MT capture by non-motor proteins are presented. *In vivo*, capture by (non-motor) proteins at the cortex is thought to play an important role in cell polarization. In the fourth section we describe the first steps in developing an *in vitro* assay to study the delivery of proteins to the cell cortex by transport at the end of MTs compared to simple diffusion of these proteins. Delivery of proteins to the cell cortex is thought to be important for cell polarization as well.

In conclusion, we have studied mechanisms of force generation by dynamic MTs. On a more cellular level we have studied the consequence of this force generation on the positioning of cellular objects in a confining space. All the experiments in this thesis have been performed *in vitro*. The next step will be to investigate how we can extrapolate the concepts we learned from *in vitro* experiments to the complexity of an *in vivo* system.

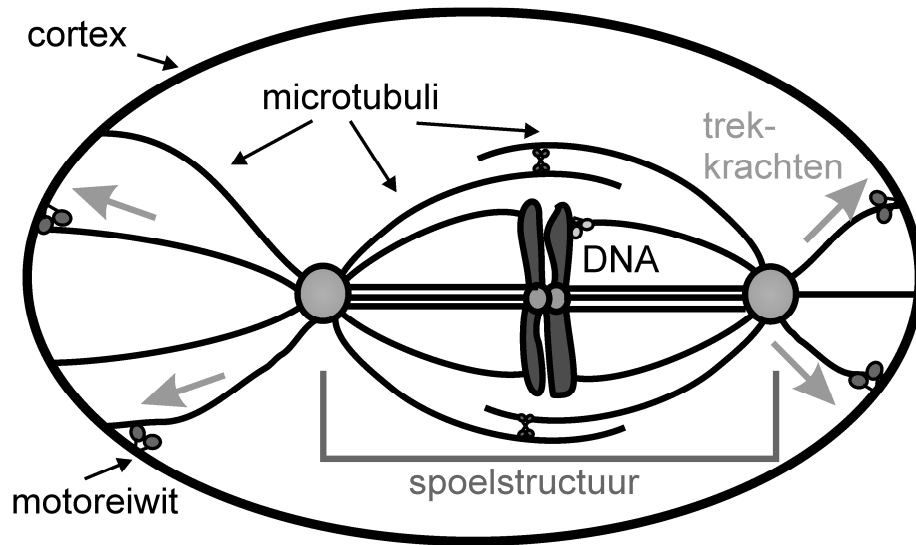
Samenvatting

Cellen, de bouwstenen van ons lichaam, zijn verrassend goed georganiseerde systemen. Verrassend, aangezien cellen erg klein zijn. Een typische cel in ons lichaam is tientallen micrometer in doorsnede, duizend keer zo klein als de doorsnede van een dobbelsteen. Op deze schaal staan de bouwstenen van een cel (eiwitten) niet stil, ze bewegen zich continu. Stel je voor dat je een huis hebt gebouwd en dat je een dag later terugkomt en dat blijkt dat geen enkele steen nog op zijn plek staat. Een van de vragen waar we ons in de biofysica dan ook mee bezighouden is: hoe kan het dat binnen deze veranderlijke omgeving de meeste processen juist heel georganiseerd verlopen? In ons lichaam vinden bijvoorbeeld per dag vele miljoenen celdelingen plaats, waarvan het overgrote deel goed verloopt: het DNA, het erfelijk materiaal, wordt verdubbeld en netjes over de twee nieuwe cellen verdeeld, waarna de cel in tweeën splitst.

De celdeling is ook een goed voorbeeld van het nut van de dynamiek van een cel. Tijdens de cel cyclus moet een cel namelijk dramatische veranderingen ondergaan. Het merendeel van de tijd moet de cel zijn functie uitvoeren, een spiercel moet bijvoorbeeld samentrekken. Op een gegeven moment moet de cel echter delen. Op dit moment moet de hele interne organisatie van de cel dramatisch veranderen, om de machinerie te bouwen die nodig is om het DNA over de twee nieuwe cellen te verdelen.

De structuur die (mede) verantwoordelijk is voor de interne organisatie van een cel is het skelet van de cel, het cytoskelet. Het cytoskelet bestaat uit verschillende eiwit filamenten waaronder microtubuli. Microtubuli zijn holle eiwit buisjes die opgebouwd zijn uit tubuline eiwitten. Het gedrag van microtubuli staat aan de basis van de dynamiek van het cytoskelet. Microtubuli zijn namelijk dynamisch, ze schakelen continu tussen groei en krimp, wat we dynamisch instabiliteit noemen. Deze dynamiek maakt het mogelijk om binnen korte tijd zeer verschillende structuren met microtubuli te bouwen. Zo zijn de microtubuli in de fase voor celdeling lang en groeien ze vanaf de kern naar de rand van de cel. Tijdens de fase van celdeling vormen de microtubuli een spoelstructuur om het DNA over de twee nieuwe cellen te verdelen (Figuur 1).

Hoe verdeelt een spoelstructuur van microtubuli het DNA nu over twee nieuwe cellen? Dit is een vraag, die een heel vakgebied bezighoudt en waar (nog) geen simpel antwoord op is. Het moge echter duidelijk zijn dat om iets te verplaatsen krachten uitgeoefend moeten worden. De laatste jaren zijn verschillende mechanismen geïdentificeerd, die bijdragen aan het leveren van deze krachten. Zo spelen motoreiwitten, eiwitmachientjes, die aan microtubuli kunnen duwen en trekken, een



Figuur 1

De spoelstructuur, gemaakt van microtubuli verdeelt het DNA over de cel, waardoor, na deling de twee nieuwe cellen beiden DNA bevatten. Trekkkrachten door microtubuli en motoreiwitten op de cortex zorgen ervoor dat de spoelstructuur op de juiste plek in de cel blijft.

rol. Recente biofysische experimenten hebben echter laten zien dat microtubuli zelf ook krachten kunnen uitoefenen terwijl ze groeien en krimpen. Een microtubule groeit door de aanhechting van nieuwe tubuline eiwitten aan het eind van de microtubule. Als je nu een voorwerp voor de groeiende microtubule plaatst, zal dit voorwerp vooruit geduwd worden. Als je een voorwerp weet te verbinden met het eind van een krimpende microtubule zal dit met de krimpende microtubule mee getrokken worden.

In de spoelstructuur oefenen microtubuli krachten uit om het DNA te verplaatsen. Om de spoelstructuur zelf op de goede plek in de cel te houden oefenen ze krachten uit op de wand van de cel, de cortex (Figuur 1). Om een analogie te geven: stel, je stopt een knikker in een ronde vissekom en je gaat schudden. De knikker zal zich dan door de hele kom bewegen. (Je geeft de knikker “thermische energie”: In een cel zorgt thermische energie ervoor dat alle eiwitten en organellen bewegen als ze niet actief vastgehouden worden). Nu plakken we echter touwtjes op de knikker die we met verschillende punten op de rand van de vissekom verbinden en we trekken deze vervolgens strak. Als je nu aan de kom schudt blijft de knikker op zijn plek. Er wordt gespeculeerd dat microtubuli op vergelijkbare wijze de spoelstructuur op zijn plek kunnen houden.

En zo zijn we bijna aangekomen bij het onderwerp van mijn proefschrift: “kracht-generatie aan microtubule-einden: een *in vitro* benadering van interacties met de cortex.” Ik heb uitgelegd wat microtubuli zijn, dat ze krachten kunnen uitoefenen,

en hoe een kracht, uitgeoefend op de cortex, kan zorgen voor interne organisatie. Maar wat bedoel ik nou met een “*in vitro* benadering”? In *in vitro* experimenten probeer je een minimale module te isoleren die nog steeds de gewenste functie vervult. Dit doen we omdat het vaak moeilijk is om een individuele module binnen de complexiteit van een compleet systeem te bekijken. In hoofdstuk 4 heb ik bijvoorbeeld gekeken of het motor-eiwit dynein kan trekken aan krimpende microtubuli. In mijn minimale modelsysteem zijn slechts dynamische microtubuli, dynein, en een muurtje dat de cortex nabootst aanwezig. In dit model experiment kun je, door dynein wel of niet toe te voegen, gemakkelijk concluderen of dynein wel of niet kan trekken aan microtubuli. Als ik echter in een cel, in een *in vivo* experiment, dezelfde tactiek volg, is het trekken van een conclusie niet zo gemakkelijk. Stel, ik verwijder dynein uit de cel en ik zie dat er nog steeds trekkrachten op microtubuli worden uitgevoerd, wat betekent dit dan? Het kan zijn dat dynein geen rol speelt. Het kan echter ook zijn dat verschillende mechanismen dezelfde rol vervullen, en dat er een back-up mechanisme in werking is gesteld. Nu is natuurlijk wel het zo dat je bij een *in vitro* experiment nooit zeker weet of het gevonden mechanisme zich *in vivo* ook daadwerkelijk voordoet. Het is dus belangrijk continue terug te koppelen tussen *in vivo* en *in vitro* experimenten.

In hoofdstuk 2 van dit proefschrift staan de verschillende *in vitro* experimenten beschreven, die ik heb uitgevoerd. In elk experiment laten we microtubuli tegen muurtjes, die de cortex nabootsen, groeien en krimpen. Ik beschrijf hoe we deze muurtje maken, hoe we microtubuli hier tegenaan laten groeien en krimpen en tenslotte hoe we de krachten en de dynamiek van de microtubuli meten. Een van de technieken die we gebruiken is het optisch pincet. Het optisch pincet is een gefocuseerde laserbundel waarmee je kleine bolletjes kunt vasthouden. Tegelijkertijd kun je de kracht, die op het bolletje wordt uitgeoefend, meten. Door zo’n bolletje aan een microtubule te plakken en dit geheel voor een muurtje te plaatsen kunnen we de duwkrachten, die microtubuli kunnen generen, meten. Als we eiwitten, die een link met krimpende microtubuli kunnen vormen, op de muur plakken kunnen we ook de trekkrachten van krimpende microtubuli meten. In een ander experiment voeren we eigenlijk het eerder beschreven gedachte experiment met de knikker en de vissekom uit. We groeien microtubuli van een centrosome (de knikker) in een gemicrofabriceerde kamer (de vissekom) en kijken of trekkrachten op de microtubuli vanaf de muren van de kamer zorgen dat de centrosome in het midden van de kamer blijft.

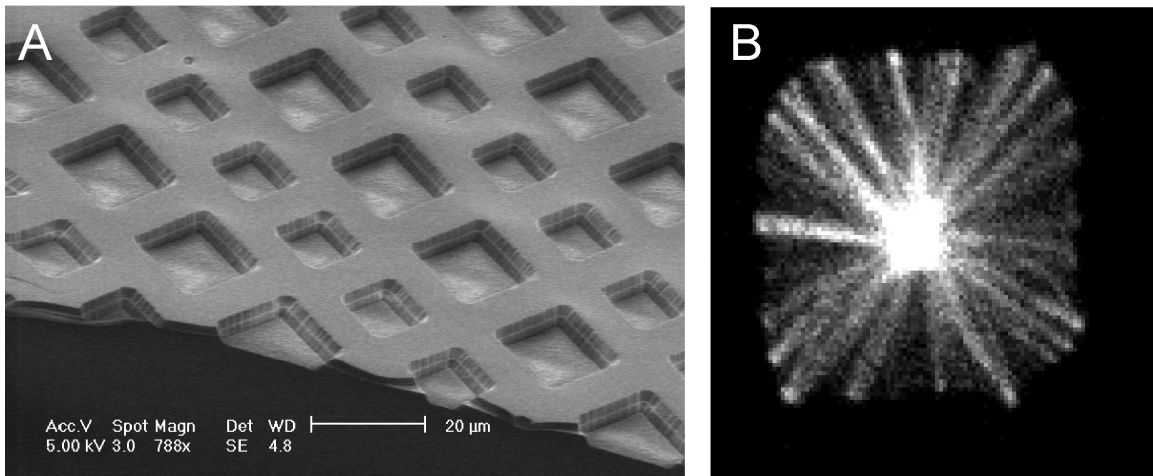
In hoofdstuk 3 staat beschreven hoe bundels van microtubuli krachten genereren. Met onze optische pincet techniek hebben we gevonden dat de kracht die een bundel van microtubuli kan uitoefenen lineair schaal met het aantal microtubuli in

Samenvatting

de bundel. Verder hebben we ontdekt dat een kracht, uitgeoefend op de microtubule bundel, de dynamica van de microtubuli in de bundel kan reguleren. Dit betekent dat de bundel zich als een geheel in de groei of in de krimp toestand kan bevinden. Dit is verrassend, aangezien het schakelen tussen groei en krimp een toevallig proces is.

In hoofdstuk 4 hebben we, zoals hierboven al beschreven, aangetoond dat het motor-eiwit dynein, als het aan een muurtje vastgeplakt zit, samen met krimpende microtubuli trekkrachten kan uitoefenen. Verder laten we zien dat dynein, door aan het eind van krimpende microtubule te binden, de dynamica van de microtubule verandert. Verrassend genoeg doet dynein dit alleen als het aan een muurtje vast zit. Onze *in vitro* experimenten kunnen *in vivo* data verklaren en geven input voor theoretische modellen.

In hoofdstuk 5 hebben we gekeken naar de positionering, door trekkrachten, van een microtubule aster (een centrosome, die als een ster microtubuli in alle richtingen groeit) in een gemicrofabriceerde kamer (Figuur 2A). Op de wanden hebben we het motor eiwit dynein geplakt dat aan de microtubuli trekt. Tot onze verrassing vinden we dat de centrosome altijd naar het midden van de kamer wordt getrokken en hier ook blijft (Figuur 2B). Om deze bevindingen te verklaren hebben we een wiskundig model opgesteld, dat onze resultaten goed kan beschrijven. De volgende stap wordt om te kijken of het mechanisme, dat we ontdekt hebben ook een belangrijke rol speelt *in vivo*.



Figuur 2

Het centreren van een microtubule aster in een gemicrofabriceerde kamer. (A) Plaatje, gemaakt met een electronen microscoop, waarin gemicrofabriceerde kamertjes te zien zijn. (B) Plaatje, gemaakt met fluorescentie microscopie, waarin een microtubule aster (in wit) te zien is, die door motoreiwitten op de rand van de kamer (niet zichtbaar in dit plaatje) naar het midden van de kamer is getrokken.

In hoofdstuk 6 hebben we onderzocht hoe het kan dat in de verschillende fases van de cel cyclus de microtubuli zo'n verschillende lengte hebben. Dit komt waarschijnlijk o.a. doordat er eiwitten zijn die de dynamica van microtubuli kunnen veranderen. Een groep eiwitten, die hiervoor in aanmerking komt, zijn de +TIPs: eiwitten die zich specifiek aan het eind van groeiende microtubuli bevinden. We hebben in een *in vitro* experiment laten zien dat sommige +TIPs autonoom (zonder hulp van andere eiwitten) het eind van de microtubule kunnen herkennen en dat zij tegelijkertijd inderdaad de dynamica van microtubuli kunnen beïnvloeden.

Ten slotte staan in hoofdstuk 7 verschillende experimenten beschreven die pas net opgestart zijn of nog opgestart moeten worden. In de eerste sectie staat beschreven welke experimenten uitgevoerd zouden kunnen worden om het mechanisme dat wij *in vitro* hebben ontdekt in hoofdstuk 5, *in vivo* te testen. In de tweede sectie staan de eerste resultaten beschreven van experimenten waarin we kijken hoe +TIPs (zie hoofdstuk 6) in combinatie met kracht, de dynamica van microtubuli beïnvloeden. Het lijkt erop dat kracht het effect van +TIPs op de dynamica van microtubuli versterkt. Er zijn echter meer experimenten nodig om dit zeker te kunnen stellen. In de derde sectie bestuderen we of andere eiwitten dan dynein ook in staat zijn krimpende microtubuli vast te houden. En ten slotte beschrijf ik in sectie vier de opzet van een experiment om te bestuderen of er andere rollen zijn voor het specifiek localiseren van eiwitten aan het eind van microtubuli. Er wordt namelijk gedacht dat microtubuli eiwitten specifiek aan hun eind meenemen om ze vervolgens aan de celwand af te geven. Op deze manier kunnen namelijk waarschijnlijk niet-homogene eiwit patronen in cellen gevormd worden.

Al het werk beschreven in dit proefschrift is deel van fundamenteel onderzoek en draagt bij aan onze begripsvorming van de interne organisatie van cellen. Afgezien van het feit dat het fascinerend is om beter te begrijpen hoe cellen werken, zal beter begrip van de werking van cellen er hopelijk in de toekomst voor zorgen dat we beter begrijpen waarom sommige cellen (gezonde cellen) wel goed functioneren en andere cellen (zieke cellen) niet.

Dankwoord

Als eerste wil ik Marileen bedanken. Marileen, voor mij was je een ideale promotor, bedankt voor je vertrouwen en al je goede adviezen! Op een goede tweede komen de mensen uit de bio-assembly groep. Special thanks to: Laura Munteanu, who taught me all the “ins and outs” of *in vitro* microtubule research; Jacob Kerssemakers en Astrid van der Horst, voor jullie hulp met de “optical trap” opstelling; Guillaume Romet-Lemonne, for introducing the microfabricated chamber experiment to me; Julien Husson, the trapping magician, for performing the optical trap experiments together with me; Paige Shaklee, for proofreading all the chapters of my thesis and for being my paranimf; Inga Maria Tarun for the work you did as a student in our group; Chris Retif voor je advies en hulp met nanofabricage. And thanks to Gerbrand Koster, Christian Tischer, Gertjan Verhoeven, Nienke Geerts, and Svenja-Marei Kalisch. Additionally, I would like to thank all my colleagues and friends at AMOLF for generating such a good atmosphere, also after work, during the last five years! Ik wil ook graag de ondersteuning bedanken, die ervoor zorgt dat alles zo soepel verloopt.

There are also people outside AMOLF, I would like to thank: Thomas Surrey and his group, for teaching me how to handle and purify proteins, essential skills for a biophysicist; Kozo Kaibuchi and Takashi Watanabe, who purified many proteins for our collaborative project and Damian Brunner, who participated in both collaborations. I would like to thank Frank Jülicher and Nenad Pavin for collaborating on the positioning project and teaching me how to do theory. My attendance at the Physiology Course made a big impact on my PhD research. I like to thank the organizers, Ron Vale and Tim Mitchison for selecting me to participate in this course. In addition, I would like to thank Ron Vale and Sam Reck-Peterson for sharing their proteins with us, a collaboration that started at the Physiology Course.

Bedankt: “Vadsige zeemeerminnen“, voor jullie vriendschap, laten we onze oud en nieuw traditie nog lang voortzetten; Laura, voor de briljante cover; Maartje, voor (bijna) 25 jaar vriendschap! Familie van Dijk, het is fijn zo’n gemakkelijke schoonfamilie te hebben! Valentijn en Anne, Wijnand en Marlijne, het is goed te weten dat ik altijd op jullie kan bouwen, lieve papa en mama, dank jullie wel voor jullie onvoorwaardelijke steun en liefde! Dorothee, bedankt dat je er altijd voor me bent, ik kan me geen passendere paranimf wensen! Sven, voor jou de laatste woorden: Dank je wel voor je humor, liefde, zorg en geduld met mij. Ik weet dat jouw onvoorwaardelijke steun verre van vanzelfsprekend is!

Curriculum Vitae

Liedewij Laan werd geboren op 7 december 1980 te Hengelo (o). Na het behalen van het gymnasium diploma in 1999 aan de ‘Openbare Scholengemeenschap de Bataafse Kamp’ te Hengelo (o) begon zij haar studie technische natuurkunde aan de Universiteit Twente. Tijdens deze opleiding studeerde ze een semester aan de University of Limerick, Ierland, waar ze vakken volgde in de toegepaste biologie. Zij ronde haar studie in 2005 met lof af met een afstudeer onderzoek in de experimentele biofysica in de groep van Prof. Dr. M. Dogterom, aan het FOM Instituut voor Atoom- en Molecuulfysica (AMOLF), te Amsterdam. In mei 2005 begon zij haar promotie onderzoek, ook in de groep van Prof. Dr. M. Dogterom op het AMOLF. De resultaten van haar promotie onderzoek staan beschreven in dit proefschrift. Na het behalen van haar graad van doctor zal Liedewij als postdoctoraal onderzoeker werken aan het FAS Institute for Systems Biology aan Harvard in Boston, in de VS. Zij zal onderzoek gaan doen naar cel morfologie en evolutie in de groep van Prof. Dr. A. Murray.

Liedewij Laan was born in Hengelo (o), the Netherlands on the 7th of December 1980. After obtaining her high school diploma at the ‘Openbare Scholengemeenschap de Bataafse Kamp’ in Hengelo (o) in 1999, she studied applied physics at Twente University. During her study she spent one semester at the University of Limerick, Ireland, to follow courses in applied biology. She finished her studies with honors with a master project in the group of Prof. Dr. M. Dogterom at the FOM Institute for Atomic and Molecular Physics (AMOLF) in Amsterdam in 2005. Starting in May 2005 she worked as a PhD student, also in the group of Prof. Dr. M. Dogterom, at AMOLF. The results of this work are presented in this dissertation. Upon receiving her PhD, Liedewij will work as a post-doctoral fellow at the FAS Institute for Systems Biology at Harvard in Boston, USA. She will study cell morphology and evolution in the group of Prof. Dr. A. Murray.